PORTOFOLIU DE LUCRĂRI
ÎN DOMENIUL DE DOCTORAT VIZAT

1. Mazaherifar, M.H.; Hiziroglu, S.; **Brenci L.M.***; Coşereanu, C. Properties of Insulation-Type Green Composite Panels Manufactured from Recycled Cardboard. Applied Science, 2025, 15(19), 10378
https://doi.org/10.3390/app151910378

2. Nicolau, A., Baba, M.N., Cerbu, C., Cioacă, C., **Brenci, L.M. ***, Coşereanu, C.* Evaluation of 3D-Printed Connectors in Chair Construction: A Comparative Study with Traditional Mortise-and-Tenon Joints. Materials 2025, 18(1), 201.
https://doi.org/10.3390/ma18010201

3. **Brenci, L.M.;** Gurău, L. A Stratified Characterization of Surface Quality of Beech Processed by Profile Milling. Applied Sciences, 2024, 14(1) 129.
https://doi.org/10.3390/app14010129

4. Lungu, A.; Ispas, M.; **Brenci, L.M.;** Răcăsan, S.; Coşereanu. C. Comparative Study on Wood CNC Routing Methods for Transposing a Traditional Motif from Romanian Textile Heritage into Furniture Decoration. Applied Sciences-Basel, 2021. 11(15), 6713. WOS:00068198970000.
https://doi.org/10.3390/app11156713

5. Zeleniuc, O.; **Brenci, L.M.*;** Coşereanu, C.; Fotin, A. Influence of Adhesive Type and Content on the Properties of Particleboard Made from Sunflower Husks. BioResources, 2019. 14(3):7316-7331. DOI: 10.15376/biores.14.3.7316-7331.
http://doi.org/10.15376/biores.14.3.7316-7331

6. Georgescu, S.V.; Coşereanu, C.; Fotin A.; **Brenci L.M.;** Costiuc, L. Experimental thermal characterization of timber frame exterior wall using reed straws as heat insulation materials. Journal of Thermal Analysis and Calorimetry, 2019. 138:2505–2513. DOI: 10.1007/s10973-019-08325-2.
https://link.springer.com/article/10.1007%2Fs10973-019-08325-2

7. **Brenci, L.M.;** Coşereanu, C.; Zeleniuc, O.; Georgescu, S.V.; Fotin, A. Thermal conductitity of wood with ABS waste core sandwich composites subject to various core modification. Bioresoures Journal, 2018. 13(1): pp 555-568. ISSN: 1930-2126.
http://doi.org/10.15376/biores.13.1.555-568

8. Coşereanu, C., **Brenci, L.M.,** Zeleniuc, O., Fotin, A. Effect of particle size and geometry of single-layer and three-layer particleboard made from sunflower seed husks. BioResources Journal, 2015. 10(1):pp 1127-1136. ISSN: 1930-2126. DOI:10.15376/biores.10.1.1127-1136

9. Nicolau, A.; Coşereanu, C.; Brenci, L.M.; Pop, M.A.; Cioaca, C. Evaluation of tensile and compression bending moment of I-type joints with 3D printed connectors. Bulletin of the Transilvania University of Brasov, Series II: Forestry, Wood Industry, Agricultural Food Engineering, 2024. Vol. 17(66) No. 2 – 2024. CABI Index
https://webbut.unitbv.ro/index.php/Series_II/article/view/8661

10. Brenci L.M. Eco-composites designed for thermal and acoustic insulation of buildings. Bulletin of the Transilvania University of Braşov, 2016. Vol. 9 (58) No.2, pp: 45-52, ISSN 2065-2135 (Print), ISSN 2065-2143 (CD-ROM). CABI Index
https://webbut.unitbv.ro/index.php/Series_II/article/view/815

Data: Conf.dr.ing. Luminita-Maria BRENCI
30.10.2025

Article

Properties of Insulation-Type Green Composite Panels Manufactured from Recycled Cardboard

Mohammad Hassan Mazaherifar [1] , **Salim Hiziroglu** [2] , **Luminita Maria Brenci** [1,]* and **Camelia Cosereanu** [1]

[1] Faculty of Furniture Design and Wood Engineering, Transilvania University of Brasov, B-dul Eroilor nr. 29, 500036 Brasov, Romania; mohammad.mazaherifar@unitbv.ro (M.H.M.); cboieriu@unitbv.ro (C.C.)

[2] Department of Natural Resource Ecology and Management, Oklahoma State University, Stillwater, OK 74078-6013, USA; salim.hiziroglu@okstate.edu

* Correspondence: brenlu@unitbv.ro

Abstract

This study investigates the influence of two processing methods, namely wet and dry, on the structural, physical, mechanical, and acoustic performance of green lignocellulosic fiber-based composite panels. A comprehensive evaluation was carried out to compare the vertical density profile, affinity to water, thermal insulation and sound absorption, microstructural features, and mechanical performance of two types of experimental panels. The dry-processed samples exhibited 24% more prominent vertical density profile and superior dimensional stability, with lower thickness swelling (TS) and water absorption (WA) due to their more compact fiber arrangement compared to those of the specimens made using the wet process. However, the wet-processed panel demonstrated significantly enhanced mechanical properties, including 36% higher modulus of elasticity (MOE), 61% modulus of rupture (MOR), and 67% internal bonding strength (IB). Such findings could be attributed to their increased fibrillation and improved inter-fiber bonding compared with those of the panels made using the dry process. The thermal conductivity values of the wet- and dry-processed panels were found to be 0.053 W/mK and 0.057 W/mK, respectively. Acoustic analysis of the samples revealed that while the dry-processed panel slightly outperformed in terms of low-frequency sound absorption, the wet-processed panel exhibited superior high-frequency absorption, particularly when perforations were introduced. Microscopic examination of the samples confirmed that wet processing produced a more homogenous and fibrillated microstructure, correlating well with the observed enhancements in mechanical and acoustic performance. In conclusion, it can be stated that the processing strategies of such panels could be applied for diverse engineering applications, including thermal insulation, acoustic damping, and sustainable structural materials.

Keywords: recycled cardboard; green composite panels; lignocellulosic fiber; acoustic absorption behavior; mechanical properties

1. Introduction

Improving the energy efficiency of buildings has emerged as a critical strategy for mitigating global energy consumption and reducing greenhouse gas emissions. The building sector alone accounts for a substantial portion of worldwide energy use, primarily due to heating, cooling, and ventilation requirements. To address this issue, passive design approaches, particularly thermal and sound insulation, have gained prominence as cost-effective and sustainable solutions for minimizing energy losses and enhancing indoor

comfort [1]. Generally, insulating materials offer benefits such as low density, a large specific surface area, and adaptable raw material profiles [2,3].

Thermal and sound insulation play a pivotal role in maintaining a stable indoor environment by reducing heat transfer and sound transmission through the building envelope. Conventional insulation materials encompass a range of inorganic and synthetic options, including fiberglass, vermiculite, expanded polystyrene (EPS), and polyurethane foams [4–6]. These materials exhibit favorable thermal performance. However, their production often relies on non-renewable resources, involving energy-intensive manufacturing processes, creating challenges for end-of-life disposal due to poor biodegradability and toxic emissions [7–9].

Consequently, there is a growing impetus to explore environmentally benign alternatives that align with the principles of sustainable development and the circular economy. Research has increasingly focused on insulation materials derived from renewable, biodegradable, and recycled sources. Lignocellulosic biomass, including agricultural residues, wood fibers, and recycled paper products, has shown promise as a sustainable insulation feedstock due to its low cost, high availability, and favorable thermal and mechanical properties [2,9]. Among recycled materials, paper and cardboard stand out as particularly attractive, given their high cellulose content, biodegradability, and widespread post-consumer availability. Furthermore, it results in optimizing resource consumption due to the utilization of recycled materials [1].

Corrugated cardboard, a primary component of global packaging systems, is largely composed of recycled cellulose fibers and exhibits excellent mechanical strength, low density, and good recyclability [10]. Globally, more than 50 million metric tons of corrugated cardboard are produced annually, with recycling rates approaching 90% in many countries [11]. While such a resource can be recycled up to 25 times [12], fiber degradation and environmental burdens associated with cardboard manufacturing and waste disposal, such as high water and energy consumption and methane emissions from landfills, remain persistent challenges [13,14].

Valorizing recycled cardboard into high-performance insulation composites offers a compelling solution to extend the lifecycle of paper-based materials while addressing environmental concerns. Previous studies have demonstrated the integration of recycled cardboard into structural components such as fiber-reinforced concrete [15], sandwich beams manufactured by using cardboard in the core [16,17], and gypsum-based insulation boards [18]. However, applications in thermal and acoustic insulation remain underexplored, particularly using low-energy, non-toxic manufacturing methods.

One emerging approach involves combining recycled cardboard fibers with foaming and leavening agents, such as sodium bicarbonate and yeast, to create lightweight, porous insulation composites. These agents promote gas formation during processing, resulting in materials with low thermal conductivity and enhanced sound absorption. In a recent study, eco-panels made from recycled cardboard, sodium bicarbonate, and baking powder achieved a thermal conductivity coefficient near 0.05 W/mK and sound absorption coefficient of 0.85 at 700 Hz [19].

However, cellulose can also serve as the sole structural component for producing lightweight, porous materials without the need for an additional supporting matrix. Cellulose-based foams are commonly fabricated via a two-step wet processing route. In the first stage, an aqueous fiber suspension is transformed into a wet foam by introducing gas bubbles through mechanical agitation or air sparging, thereby generating a highly aerated structure. The second stage involves removing the liquid phase, typically achieved through freeze-drying, evaporation, or supercritical drying, to preserve the porous architecture and achieve the desired density and structural stability [20,21].

Despite these promising outcomes, there is still limited information on the characteristics of such panels, and further research is needed to optimize the composition, processing parameters, and performance characteristics of cardboard-based insulation materials to meet regulatory and functional standards. In particular, understanding how foaming agents interact with recycled fibers to influence porosity, mechanical integrity, and moisture resistance is important for the practical use of these materials.

Therefore, the objective of the present study is to develop lightweight, eco-friendly insulation-type composites by repurposing recycled corrugated cardboard and incorporating commonly available foaming and leavening agents. The research focuses on evaluating the thermal, acoustic, physical, and mechanical properties of the proposed composites through a simplified, sustainable manufacturing process. The data and information from the results of this work are expected to provide us with a better understanding of circular, biodegradable insulation alternatives with the potential to reduce dependence on conventional inorganic and synthetic materials in the construction industry.

2. Materials and Methods

2.1. Preparation of the Raw Materials

Unprinted cardboard was obtained from the recycling bin of a local store. Two distinct wet and dry defibration methods were employed to process the material. For the wet defibration method, the cardboard was first manually torn into smaller fragments before being immersed in water for two hours to facilitate softening. Once sufficiently saturated, the material was mechanically defibrated using a high-speed blender operating at 9000 rpm for one minute. A cardboard-to-water ratio of 1:12 by weight was maintained throughout this process. In the dry defibration method, the unprinted cardboard was also manually pre-torn into small fragments. Subsequently, the material was processed using a mechanical impact mill operating at approximately 1500 rpm to achieve fiber separation. The physical [22], chemical [23,24], and morphological [25,26] characteristics of the fibers defibrated from the cardboard are displayed in Table 1.

Table 1. Properties of cardboard fibers.

	Physical Properties	Morphological Properties			Chemical Properties				
Cellulose Fibers	Density (kg/m^3)	Length (µm)	Width (µm)	Diameter (µm)	Cellulose %	Hemicellulose %	Lignin %	Ash %	Additives %
	1500–1600	192	53	10–50	40–80	5–15	10–15	15	15

To manufacture the experimental panels, both wet- and dry-defibrated fibers were used in a formulation comprising four components: 500 g of processed unprinted cardboard, 2.5 L of water, sodium bicarbonate 12% by weight of the total mixture, and yeast 8% by weight of the total mixture.

2.2. Manufacturing of the Panels

Two types of green composite samples were manufactured under controlled laboratory conditions using defibrated fibers derived from unprinted cardboard. These fibers, as primary material, were prepared for both dry and wet defibration techniques, as illustrated in Figures 1a and 1b, respectively. Prior to shaping, sodium bicarbonate and yeast were incorporated into the mixture to aid in the expansion and structuring of the composite matrix. The prepared mixtures were then poured onto mold-lined trays covered with baking paper, as depicted in Figure 1c. Manufacturing was carried out by baking in an oven for 15 h at a temperature of 150 °C. Following thermal treatment, the composites were cooled off at ambient temperature, as shown in Figure 1d.
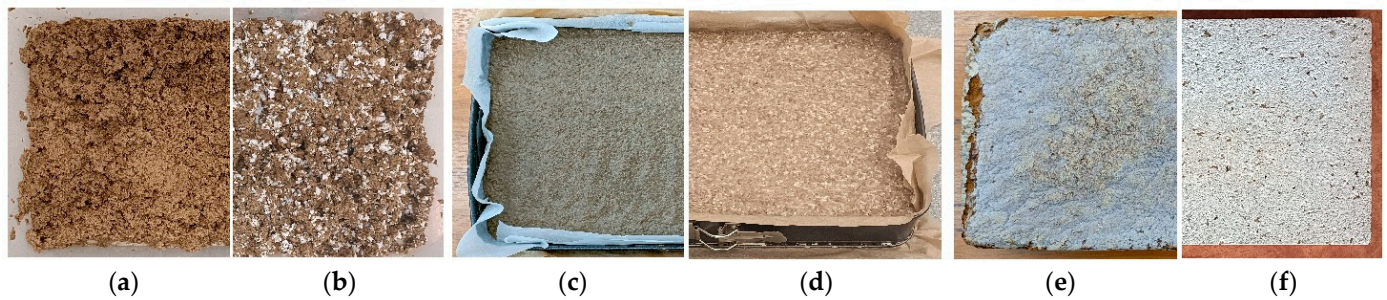
Figure 1. Panel manufacturing phases: defibrated fibers via dry (**a**) and wet (**b**) techniques; prepared mixture for dry (**c**) and wet (**d**) method; composite panel before cutting (**e**); composite panel after cutting (**f**).

To ensure dimensional consistency and eliminate any overcooked or uneven surface layers, the panels were planed and cut to achieve uniform thickness (Figure 1e). For both wet and dry processing methods, four rectangular panels measuring 320 mm × 250 mm (length × width) were manufactured. After final trimming and surface preparation, the average thickness of each panel was reduced to 30 mm.

2.3. Vertical Density Profiles (VDPs) of the Samples

The VDPs of the resulting composites were determined using the IMAL X-ray density profiler DPX300 (San Damaso, Italy). Eight square specimens (50 mm × 50 mm) were cut from the panels for this purpose. Measurements were taken across the entire thickness of each specimen to assess the internal density distribution. Prior to profiling, each sample was weighed with a high-precision balance, model EU C-LCD made by Gibertini Elettronica (Novate Milanese, Italy). The analyzer's built-in measurement system was also used to confirm the sample dimensions, ensuring accurate density evaluation.

2.4. Affinity to Water

The absorption of water (WA) and the swelling in thickness (TS) were assessed according to the European standard SR EN 317:1996 [27] by immersing the specimens in distilled water. Five square specimens with nominal dimensions of 50 × 50 mm were sectioned from the experimental panels and subsequently subjected to a conditioning phase of 24 h at 20 ± 2 °C and 65 ± 5% relative humidity. The water absorption assessment was conducted in a controlled bath, wherein the specimens were fully submerged in distilled water maintained at 20 ± 1 °C for a duration of 24 h. Dimensional measurements were taken using a digital caliper with an accuracy of 0.01 mm. The mass of each sample was recorded at three specific intervals, namely before immersion, after 2 h, and after 24 h, employing an electronic balance with an accuracy of 0.01 g. The samples' thicknesses were measured at the central point along the diagonal of each specimen during every weighing phase to ensure consistency.

2.5. Thermal Conductivity Coefficient (λ) of the Samples

The thermal conductivity coefficient (λ) of the composite specimens was determined using a heat flow meter, model HFM436 Lambda made by Netzsch manufacturer from Selb, Germany. Two experimental composite configurations were tested in accordance with the guidelines of ISO 8301 [28] and DIN EN 12667 [29]. The sample was positioned between two flat plates, one that was heated up to 20 °C and the other that was cooled to as low as −10 °C, to measure the heat flux. The instrument calculated thermal conductivity automatically based on Fourier's Law, utilizing the temperature gradient between the plates. Before conducting the measurements, the system was calibrated following standard

protocols, which accounted for both the temperature difference (ΔT) and the average temperature (Tm) across the specimen (Table 2).

Table 2. Set parameters for the determination of λ.

Number of Tests	Temperature 1 Lower Plate	Temperature 2 Upper Plate	ΔT $T_2 - T_1$	Average $(T_1 + T_2)/2$
1	−10	20	30	5
2	−5	20	25	7.5
3	0	20	20	10
4	5	20	15	12.5
5	10	20	10	15
6	15	20	5	17.5

2.6. Sound Absorption Coefficient of the Samples

The sound absorption performance of the composite panels was evaluated across both low- and high-frequency ranges using impedance tube methods adapted to each frequency domain. To ensure accuracy and standardization, each method adhered to the relevant international testing standards.

2.6.1. Low-Frequency Sound Absorption Coefficient (α) Measurement

Low-frequency α-coefficient measurements were performed using a SCS80 FA impedance tube, from Vibro-Acoustic S.R.L. (Campodarsego PD, Italy), equipped with a two-microphone configuration. The procedure followed the guidelines of ISO 10534-2:1998 [30], which specifies the sound transfer method under normal incidence. α-coefficient was measured over a frequency range of 50 to 1390 Hz, with an incident sound pressure level of 75 dB.

For each type of composite, two specimens were tested. The maximum α-values for each specimen were calculated by the system's analysis software, and the average of these maximum values was used to assess the performance of the corresponding panel. This approach enabled effective comparison between the wet- and dry-processed composites within the low-frequency domain.

2.6.2. High-Frequency Sound Absorption Measurement

The high-frequency α-coefficient was evaluated using the impedance tube Brüel & Kjær (model 4206, Nærum, Denmark) based on the transfer function method with two microphones (TFM), in accordance with ISO 11654:1997, ISO 10534-2:1998, and ASTM E1050-12:1998 [30–32]. The measurements were performed under normal incidence conditions (0° angle) over a controlled frequency range of 100 Hz to 6400 Hz.

Each circular sample had a diameter of 29 mm and was tested using the sample holder of the impedance tube. Acoustic signals generated by the internal speaker were transmitted through the tube, and two microphones captured the responses. A data acquisition (DAQ) board and a signal conditioner processed and then analyzed the sound through a computer interface equipped with specialized acoustic analysis software.

To investigate the acoustic behavior of the samples under the effect of perforations, in addition to the standard wet- and dry-processed samples, modified versions of the same samples featuring seven uniformly distributed holes (each 3 mm in diameter) were also tested under identical conditions.

All measurements were conducted in a controlled laboratory environment, with ambient temperature of 22 ± 2 °C and 55 ± 5% relative humidity. This setup ensured repeatable and reliable characterization of the materials' sound absorption performance of the samples across the high-frequency spectrum.

2.7. Sample Porosity

The porosity volume of the specimens was measured using AccuPyc III 1350 Gas Pycnometer. For this analysis, five rectangular samples measuring 10 mm × 10 mm × 35 mm were prepared for each type. Precise dimensional measurements were obtained using a digital caliper with a resolution of 0.01 mm. The AccuPyc provides the true density (ρ_{true}) by displacing gas within the solid material, excluding interparticle voids but including closed pores. It also measures the bulk density (ρ_{bulk}) of the sample, accounting for pores and interparticle spaces. Porosity is calculated with Equation (1):

$$Porosity\ (\%) = \frac{\rho_{bulk}}{\rho_{true}} \cdot 100 \tag{1}$$

2.8. Microscopic Evaluation of the Samples

Stereo-microscopic observations were conducted using a Nikon SMZ18-LOT2 stereomicroscope manufactured by Nikon Corporation (Tokyo, Japan). This analysis facilitated the visual assessment and measurement of fiber dispersion, inter-fiber spacing, yeast incorporation within the composite matrix, and the integrity of fiber bonding. Images were acquired at a magnification of 120× on the two different composite types, selecting for this evaluation three samples cut from each composite.

2.9. Mechanical Properties of the Samples

Mechanical tests were conducted in accordance with applicable European standards, adhering to the specified procedures for sample preparation, including quantity, shape, and size. The MOE and MOR of the samples were measured by the universal testing machine Zwick/Roell Z010 (Ulm, Germany), with a loadcell with a capacity of 10,000 N, following the methodology described in EN 310:1993 [33]. Eight test specimens were prepared per composite type according to the specifications outlined in EN 326-1 [34].

IB strength, measured perpendicular to the panel surface, was evaluated according to EN 319 [35] using the Zwick/Roell Z010 testing system. For this test, eight square samples (50 mm × 50 mm) cut from each composite were examined.

2.10. Statistical Analysis

Statistical analyses were conducted to assess the significance of the differences between the composite groups. Standard deviations were calculated in Microsoft Excel, applying a 95% confidence interval with a significance threshold of $\alpha = 0.05$ ($p < 0.05$). To examine the effect of the two defibration techniques on the primary material properties, a two-sample *t*-test was performed using Minitab statistical software, version 19.2020.1. The analysis compared the mean values of the key parameters, including the vertical density profile, dimensional stability, thermal conductivity, MOE, MOR, and IB strength across the composite types.

3. Results and Discussion

The physical and mechanical properties of the samples are displayed in Table 3.

Table 3. Physical and mechanical properties of the samples.

Panel Type	Density (Kg/m^3)	WA (%)		TS (%)		λ (W/mK)	α_{max}	Porosity (%)	Flexural (N/mm^2)		IB (N/mm^2)
		2 h	24 h	2 h	24 h				MOE	MOR	
Wet	155.5	507.07	526.38	6.44	7.41	0.053	0.89	90	42.48	0.26	0.06
Dry	204.94	376.07	395.77	4.76	5.36	0.057	0.94	86.3	27.23	0.10	0.02

The performance of green lignocellulosic fiber-based insulation composites manufactured from recycled corrugated cardboard is fundamentally governed by the interplay between fiber morphology, degree of fibrillation, porosity, and gas expansion dynamics during the manufacturing process. Among these factors, the processing route, whether wet or dry, plays a decisive role in shaping the microstructural characteristics of the material, thereby exerting a direct influence on its physical, mechanical, thermal, and acoustic behavior. The choice of method is therefore not merely a processing decision but rather a key determinant of the functional performance and sustainability of the final product.

From a physical standpoint, the density and porosity of these composites are strongly dictated by the preparation method. Dry processing, typically involving hammer milling, produces coarser and less fibrillated fibers. These fibers exhibit reduced surface area and a more rigid morphology, which allows for denser packing during panel formation. As a result, the dry-processed composites generally attain a higher bulk density and lower void fraction. High porosity is obtained by accommodating enhanced gas retention and expansion when foaming agents, such as sodium bicarbonate and yeast, are activated during thermal treatment. The outcome is a foam-like, lightweight structure with improved open-cell architecture, reduced density, and the potential to optimize both thermal insulation and high-frequency acoustic absorption.

The degree of fibrillation achieved during wet processing holds particular significance. It increases the available surface area for hydrogen bonding between fibers and fines, thereby strengthening inter-fiber adhesion without relying on synthetic binders. Beyond simple adhesion, the fibrillated fibers act as reinforcement points within the matrix, distributing stress more uniformly and limiting crack initiation and propagation. Refining through wet processing further contributes to the regulation of pore size distribution, creating a more homogeneous structure that balances mechanical integrity with functional properties. Such improvements are directly reflected in mechanical indices, including flexural MOE, MOR, and IB strength. Composites characterized by finer fibers and uniform porosity are therefore anticipated to display superior stiffness, greater resistance to bending-induced fracture, and stronger cohesion through enhanced inter-fiber bonding.

The acoustic performance of these composites is similarly governed by the interaction between density and pore architecture. Panels with a higher density and compact structure typically exhibit improved absorption at lower frequencies, where mass-related damping and panel resonance dominate. On the other hand, higher-porosity panels with finely interconnected pore structures are more effective at attenuating high-frequency sound. This is achieved through viscous and thermal dissipation mechanisms occurring as sound waves penetrate the pore network. The balance between these two behaviors highlights a unique opportunity for design flexibility; by adjusting processing parameters and pore structure, cardboard-based composites can be tuned to target either low-frequency or high-frequency sound absorption or engineered to perform across a wider frequency range. Additional structural modifications, such as controlled surface perforation, may further expand the acoustic response, potentially enabling nearly total absorption at certain frequencies, which is a characteristic highly desirable for architectural and industrial noise-control applications.

Thermal conductivity, a key criterion for insulation materials, is closely correlated with density and porosity. Lower-density composites with higher void fractions contain a larger proportion of entrapped air, which functions as an efficient thermal barrier and minimizes heat transfer. Conversely, higher-density composites, while offering enhanced mechanical stability, facilitate greater solid-phase conduction pathways, thereby raising thermal conductivity. However, once their porosity exceeds 80%, the differences in density or porosity have only a minor influence on thermal conductivity, since heat transfer occurs mainly through stagnant air rather than the solid matrix.

From the perspective of sustainable material engineering, these interrelationships highlight a critical opportunity to tailor recycled cardboard-based insulation products to diverse functional applications without the need for synthetic polymers, formaldehyde-based adhesives, or energy-intensive binders. This advantage directly supports global efforts to reduce dependency on petroleum-derived construction materials while aligning with circular economy principles. Wet processing, owing to its ability to generate lightweight, mechanically resilient, and acoustically efficient panels, can be prioritized for applications emphasizing energy efficiency and sound management in building envelopes. In contrast, dry processing offers value in contexts requiring mass-related damping or enhanced low-frequency acoustic response, where the trade-off of higher density may be beneficial.

Equally important, the utilization of recycled corrugated cardboard as a feedstock confers significant environmental benefits. With global cardboard recycling rates already approaching 90%, redirecting this abundant post-consumer resource into high-value insulation products extends its lifecycle and mitigates the environmental burdens of landfilling or incineration. Moreover, integrating foaming and leavening agents, such as sodium bicarbonate and yeast, introduces a low-energy, non-toxic manufacturing pathway that avoids the challenges of conventional insulation production, such as high embodied energy, poor biodegradability, and hazardous emissions.

All in all, the influence of fiber morphology, processing method, and pore architecture demonstrates the versatility of green lignocellulosic fiber-based composites in advancing sustainable construction materials. By leveraging simple yet effective manufacturing strategies, it becomes possible to design insulation products with tailored combinations of mechanical, thermal, and acoustic performance, thereby offering viable, biodegradable alternatives to conventional inorganic and synthetic insulations widely used in the construction sector. A summary of the statistics for the measured properties of the samples is shown in Table 4.

Table 4. Statistical significance of the measured properties of the samples.

Property	Wet (Mean $\pm$ SD)	Dry (Mean $\pm$ SD)	*p*-Value	Significance
Density (Kg/m^3)	155.5 $\pm$ 13.83	204.94 $\pm$ 8.70	0.000	Significant
WA 2 h (%)	507.07 $\pm$ 95	376.07 $\pm$ 38	0.132	Not Significant
WA 24 h (%)	526.38 $\pm$ 91	395.77 $\pm$ 41	0.055	Not Significant
TS 2 h (%)	6.44 $\pm$ 0.5	4.76 $\pm$ 0.4	0.010	Significant
TS 24 h (%)	7.41 $\pm$ 0.5	5.36 $\pm$ 0.4	0.024	Significant
λ (W/mK)	0.053 $\pm$ 0.001	0.057 $\pm$ 0.003	0.048	Significant
MOE (N/mm^2)	42.48 $\pm$ 2	27.23 $\pm$ 3	0.000	Significant
MOR (N/mm^2)	0.26 $\pm$ 0.01	0.10 $\pm$ 0.02	0.000	Significant
IB (N/mm^2)	0.06 $\pm$ 0.005	0.02 $\pm$ 0.005	0.001	Significant

3.1. Vertical Density Profiles (VDPs) of the Samples

The VDPs of the panels made using the wet and dry processing methods exhibited distinct differences reflecting the influence of manufacturing conditions on panel compaction and internal structure. The dry-processed panel demonstrated a significantly higher average density of 204.94 kg/m^3, whereas the wet-processed panel showed a relatively lower density of 155.5 kg/m^3. Statistical analysis has shown that this difference was significant ($p < 0.05$), indicating a strong influence of the processing method on the bulk density of the panels.

This variation can be primarily attributed to differences in fiber morphology [20] and gas expansion behavior [36,37] during processing rather than compaction efficiency. The dry-processed fibers, obtained from the hammer mill, were coarser and less fibrillated, enabling denser packing and reducing void formation, which is consistent with the lower porosity value of 86.3%.

In contrast, the wet-processed fibers, prepared with a blender, underwent significant fibrillation and water-induced swelling, promoting a looser fiber network. Additionally, the water-induced swelling likely enhanced CO_2 evolution from the sodium bicarbonate and yeast system during baking, generating a more foamed structure. Consequently, the wet-processed panel exhibited a markedly higher porosity (90%), resulting in a 24% lower bulk density compared to its dry-processed counterpart.

The VDP curves in Figure 2 further illustrate the density distribution across the panel thickness for both processing methods. The wet-processed panel in Figure 2a also exhibited a more irregular density profile, characterized by a lower and relatively uniform core density with a value of ~155 kg/m³. The smoother transition from surface to core density indicates an integrated structure, consistent with the higher porosity and greater water absorption behavior observed for this panel.

(**a**) (**b**)
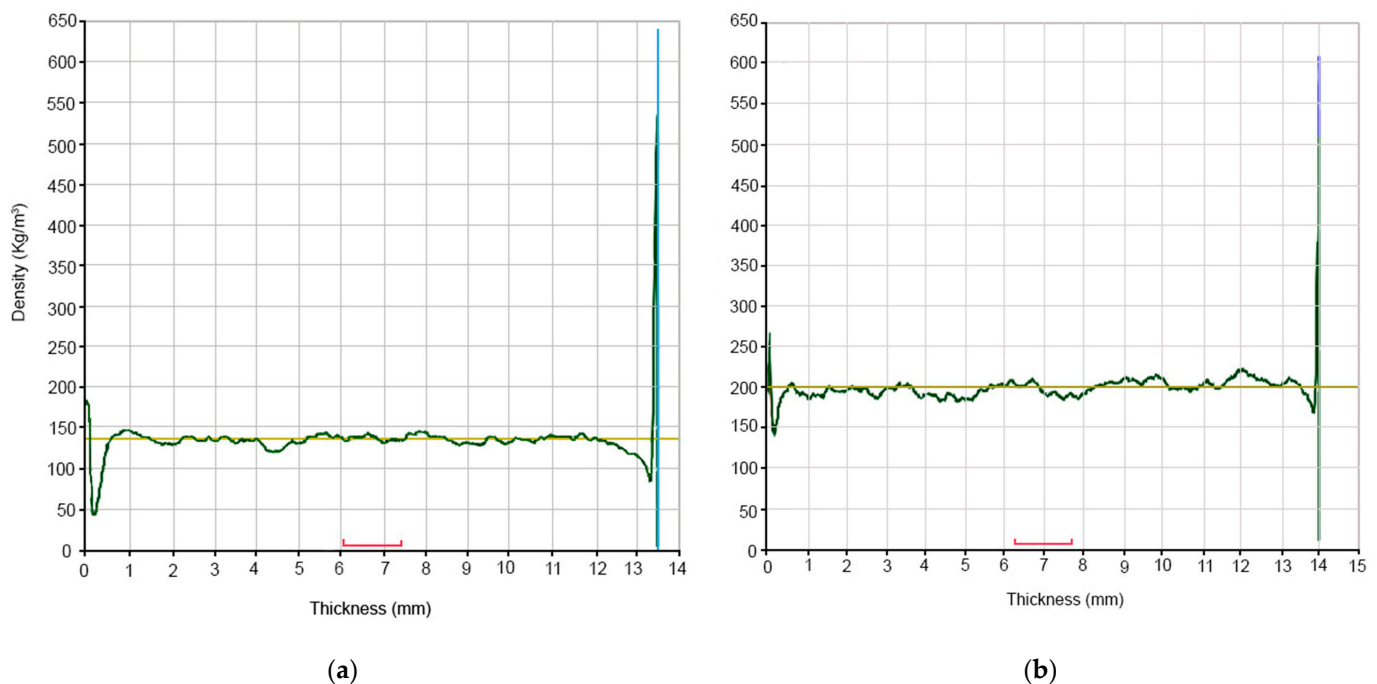
Figure 2. Typical vertical density profiles of the wet-processed (**a**) and dry-processed (**b**) samples.

In contrast, the dry-processed panels shown in Figure 2b exhibited a relatively stable density profile, maintaining values close to the average of ~205 kg/m³ across the core region, with slight fluctuations between 180 and 220 kg/m³.

3.2. Water Affinity of the Composites

The affinity to water, evaluated in terms of water absorption and thickness swelling, exhibited significant differences between the wet- and dry-processed composites ($p < 0.05$ for TS; $p > 0.05$ for WA), as illustrated in Figure 3. The wet-processed panel demonstrated markedly higher water absorption values, reaching 507.07% after 2 h and increasing slightly to 526.38% after 24 h. In contrast, the dry-processed panel absorbed substantially less water, with water absorption values of 376.07% and 395.77% after 2 and 24 h, respectively. However, the differences in water absorption between the two panels were not statistically significant, with $p > 0.05$, group A in Figure 3. This pronounced difference can be attributed to the greater porosity and open-cell structure of the wet-processed panel, with 90% porosity compared to the corresponding value of 86.3% for the denser and more compact dry-processed samples. The highly fibrillated and water-swollen fibers generated during wet processing likely created interconnected voids, promoting rapid water penetration and

retention, whereas the coarser, less fibrillated fibers of the dry-processed panel contributed to reduced capillary water uptake.
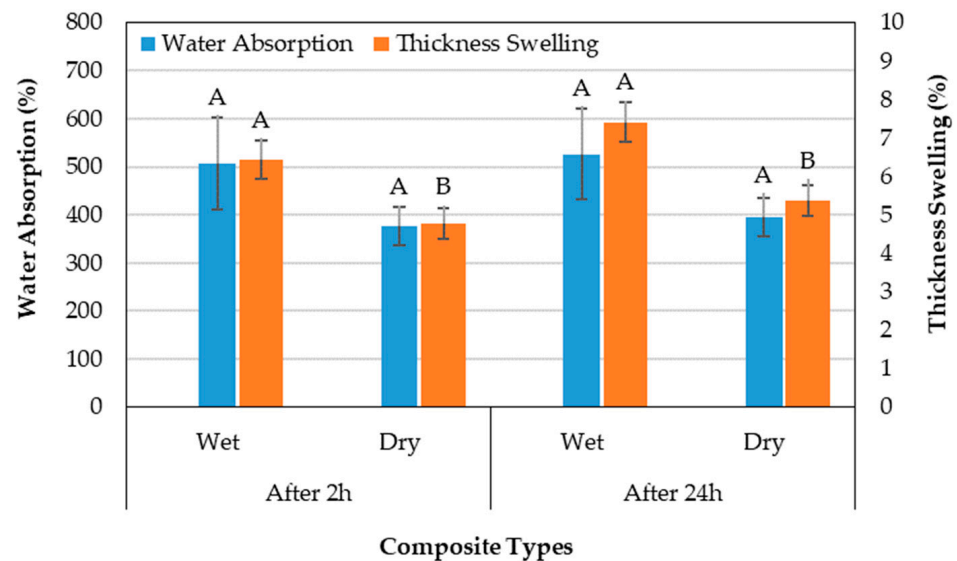

Figure 3. WA and TS after 2 h and 24 h of water immersion.

Similarly, TS followed the same trend, with the wet-processed panel exhibiting higher swelling values of 6.44% after 2 h and 7.41% after 24 h, compared to 4.76% and 5.36% for the dry-processed panel for the same time intervals. Unlike water absorption, the differences in TS were statistically significant at both time intervals, with $p < 0.05$, (groups A and B). The greater thickness swelling in the wet-processed panel is consistent with its higher water absorption and its less consolidated fiber network, which undergoes more significant expansion when saturated. The dry-processed panel, with its denser internal structure, exhibited better resistance to swelling, highlighting its superior dimensional stability under humid conditions.

These findings indicate that while the wet-processed panel may offer potential advantages for applications where low density and high porosity are desirable (e.g., thermal or acoustic insulation), its poor dimensional stability limits its suitability for structural or load-bearing applications. In contrast, the dry-processed panel demonstrates better dimensional stability, making it more appropriate for applications requiring improved resistance to moisture-induced deformation.

3.3. Thermal Conductivity Coefficient (λ) of the Samples

The panels exhibited a significant difference between the wet- and dry-processed composites ($p < 0.05$) in terms of λ-values, highlighting the influence of processing method and resulting microstructural characteristics on the heat transfer behavior, as shown in Figure 4. The wet-processed panels demonstrated a lower thermal conductivity value of 0.053 W/mK, whereas the dry-processed panel had a λ value of 0.057 W/mK. Although this absolute difference appears small, it is statistically meaningful (groups A and B) and consistent with the distinct structural features of the two panels.

The lower λ-value of the wet-processed panel can be attributed to its higher porosity (90%) and lower bulk density (155.5 kg/m^3), which are consequences of extensive fiber fibrillation and gas expansion during wet processing. The open, foam-like structure likely entrapped more air within the panel matrix, and since air is a poor thermal conductor, this resulted in reduced heat transfer. Conversely, the dry-processed panel, with its denser fiber packing (204.94 kg/m^3) and lower porosity (86.3%), provided increased solid–solid contact

between fibers, enhancing conduction pathways and thus increasing thermal conductivity. A direct relationship between density and thermal conductivity has been consistently documented in previous research [1,38], underscoring the critical role that bulk density plays in governing heat transfer behavior within lignocellulosic composites. However, both panels are highly porous, and the dominant contributor to thermal insulation is still the entrapped air phase, which has very low thermal conductivity (0.025 W/mK). In such low-density composites, once the porosity exceeds 80%, further changes in density or porosity have only a minor influence on thermal conductivity, since heat transfer occurs mainly through the entrapped air, rather than the solid matrix [39]. Several researchers have emphasized that thermal transport in porous media is largely dictated by the characteristics of the pore network. In agreement with this, Clarke [40] reported that the decrease in thermal conductivity is critically influenced by the pore volume fraction, the aspect ratio, and the spatial distribution of the pores. Other properties, such as mechanical strength and water absorption, are more strongly influenced by these structural differences.
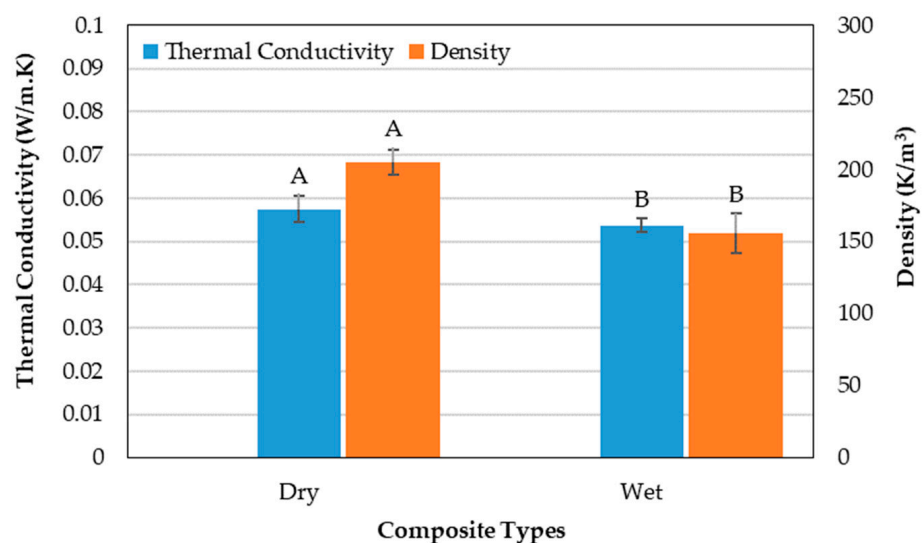
Figure 4. Thermal conductivity coefficient versus density of the samples.

These findings suggest that the wet-processed panel, due to its superior thermal insulation capability, may be more suitable for non-structural applications, such as thermal or acoustic insulation. In contrast, the dry-processed panel, despite its slightly higher thermal conductivity, is more appropriate for applications requiring enhanced mechanical performance and dimensional stability.

3.4. Sound Absorption Coefficient (α) of the Samples

The sound transfer through the panels was evaluated over both low-frequency (50–1390 Hz) and high-frequency (100–6400 Hz) domains, revealing distinct effects of processing method and panel configuration on acoustic performance.

In the low-frequency range (Figure 5), both panels exhibited high sound absorption potential, with the dry-processed panel slightly outperforming the wet-processed one. Specifically, the dry-processed panel achieved a maximum sound absorption coefficient (α_{max}) of 0.94, compared to 0.89 for the wet-processed panel at 700 Hz frequency. Despite the wet-processed panel's higher porosity and fibrillated structure, the more compact structure of the dry-processed panel appears to favor the dissipation of low-frequency acoustic waves, potentially due to better impedance matching with the surrounding air.
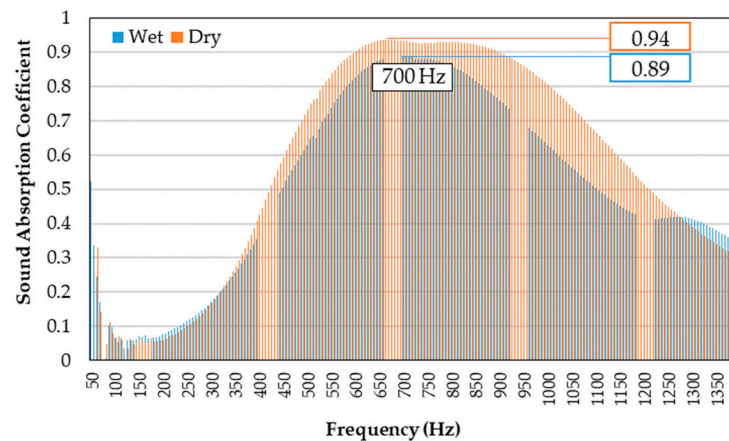
Figure 5. α-coefficient of the samples (measured for low-frequency range).

In the high-frequency range (Figure 6), the results indicated a clear advantage for the wet-processed panels, especially when modified with perforations. Among the unperforated samples, the wet-processed panel recorded an α_{max} of 0.84, outperforming the dry-processed counterpart, which reached 0.75. This enhancement is attributed to the highly porous and interconnected fiber network of the wet-processed composite, which promotes efficient absorption through viscous losses and internal friction mechanisms [41].
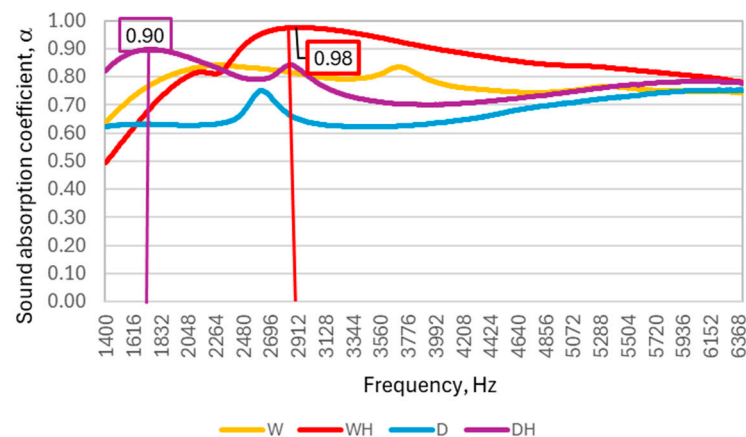
Figure 6. α-coefficient of the samples (measured for high-frequency range).

When perforations were introduced, sound absorption performance improved significantly for both processing methods. The wet-processed panel with holes had an α_{max} of 0.98, the highest among all the samples, while the dry-processed panel with holes reached 0.90. The presence of perforations likely facilitates multiple acoustic wave reflections and longer travel paths within the panel matrix, amplifying energy dissipation. The combination of wet processing and structural perforation proved particularly effective, suggesting a strong synergistic effect between fiber morphology and design optimization. Composite density is influenced by substrate choice, processing method, and post-treatment [42]. Foam layer performance improves with higher pore density and contact area achieved through optimized geometry, finer fibrils, and controlled density [42]. Resonance tuning is possible by adjusting thickness and perforation design, including cavity number, size, depth, and distribution [43].

These findings demonstrate that both material processing and structural modification have a substantial influence on acoustic behavior. While the dry-processed panel offered slightly better low-frequency absorption, wet-processed panels, especially with

perforations, exhibited superior broadband sound absorption, making them well-suited for applications requiring effective acoustic damping across a wide frequency spectrum.

3.5. Mechanical Behavior of the Samples

The performance of the composite panels (Figure 7) was assessed through measurements of flexural MOE, MOR, and IB strength. All three properties of the wet- and dry-processed panels exhibited statistically significant differences ($p < 0.05$) between them (different groups A and B), indicating that the processing method plays a pivotal role in determining their mechanical performance.
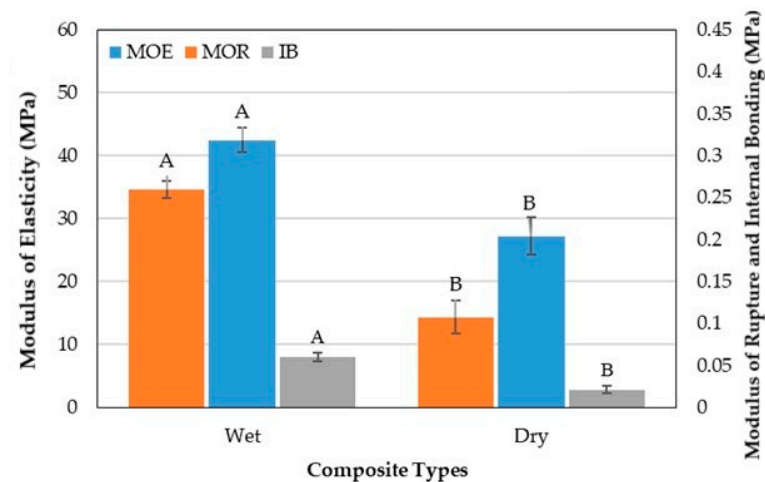
Figure 7. Mechanical properties of the samples.

The wet-processed panel demonstrated a superior MOE of 42.48 MPa, significantly higher than the 27.23 MPa observed for the dry-processed panel. This 36% increase in stiffness is attributed to the finer, more fibrillated fibers generated during the wet process, which likely created more extensive fiber–fiber contact areas and improved stress transfer within the composite matrix.

Similarly, the MOR of the wet-processed panel reached 0.26 MPa, more than double that of the dry-processed panel, with a value of 0.10 MPa, reflecting its greater resistance to failure for 61% under bending stress. The increased MOR further supports the hypothesis that the wet processing method leads to a better-integrated fiber network with improved structural cohesion.

Internal bonding strength followed the same trend. The wet-processed panel achieved a value of 0.06 N/mm^2, compared to 0.02 MPa for the dry-processed sample. This substantial difference (67%) may result from the improved fiber surface area and bonding potential induced by mechanical fibrillation in the wet processing stage, which promotes stronger inter-fiber adhesion during thermal cooking.

These improvements are primarily attributed to the finer, more fibrillated fibers produced during wet processing, which increase fiber–fiber contact areas, facilitating stress transfer within the composite matrix, and enabling additional hydrogen bonds between fibers and fines. Furthermore, the refining effect inherent to wet processing can regulate and control foam microstructure, leading to more uniform stress distribution and enhanced load-bearing capacity. Such synergistic effects of fiber morphology modification and microstructural optimization provide a clear mechanistic basis for the superior mechanical performance of wet-processed panels [20].

Collectively, these results indicate that the wet processing method produces composite panels with significantly enhanced mechanical properties, suggesting its potential for use in applications where flexural strength and internal cohesion are critical. In contrast, the

lower mechanical performance of the dry-processed panels may limit their suitability for structural uses, but they could be acceptable in applications where the mechanical demands are less stringent.

3.6. Microscopic Evaluation of the Samples

A microscopic investigation was conducted using stereo-microscopy at a magnification of 120× to evaluate the morphological characteristics of fibers within the composite structure, providing insight into how processing methods influenced fiber dispersion and surface texture (Figure 8). The dry-processed composite (Figure 8a) revealed a network of coarser fibers with minimal fibrillation and relatively smooth surfaces. The fiber diameters ranged from approximately 15.38 µm to 42.28 µm, with most fibers appearing intact and less mechanically degraded. This morphology is indicative of the hammer milling process used in dry preparation, which preserves the structural integrity of the fibers but limits surface area exposure and matrix interlocking. The observed compact fiber arrangement is consistent with the lower porosity (86.3%) and higher density (204.94 kg/m^3) measured for the dry-processed panels.

(a)

(b)
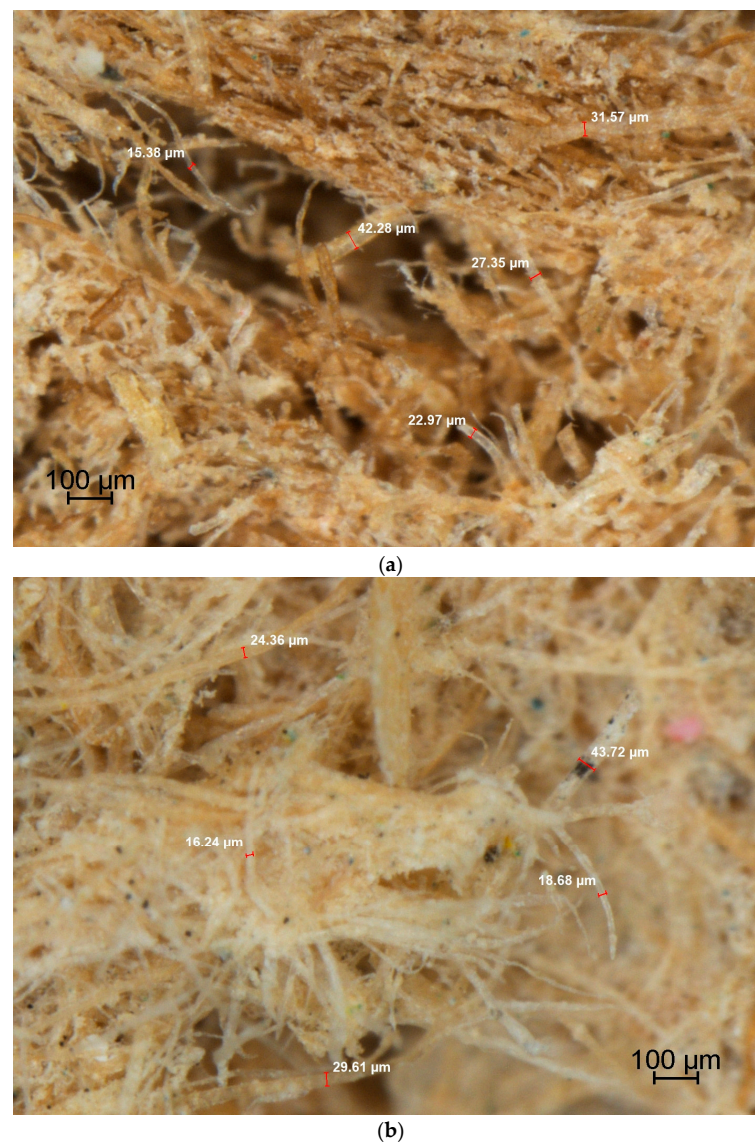
Figure 8. Microscopic investigation of the samples at 120× magnification; (**a**) dry-processed composite; (**b**) wet-processed composite.

In contrast, the wet-processed composite (Figure 8b) exhibited a markedly different microstructure. The fibers were significantly more fibrillated and entangled, with finer elements distributed throughout the matrix. Fiber diameters ranged from 16.24 μm to 43.72 μm, but many fibers appeared fragmented, with frayed ends and delaminated surfaces. These features are a direct result of the high-shear blending and water-induced swelling that occur during wet processing. The enhanced fibrillation leads to an open and more porous network, in line with the measured porosity of 90% and reduced density (155.5 kg/m^3) for the wet-processed panels. Moreover, this loose fiber architecture is believed to facilitate greater gas expansion during foaming and higher water absorption due to increased capillary pathways.

These microstructural features are consistent with the superior mechanical performance observed for the wet-processed panel. These substantial improvements are attributed to enhanced fibrillation, increased fiber surface area, and stronger inter-fiber bonding potential resulting from the wet processing method. Statistical analysis of the mechanical properties confirmed that these differences were significant ($p < 0.05$), further supporting the positive influence of fiber morphology and microstructural refinement on the mechanical behavior of binder-less fiber composites.

4. Conclusions

This study comprehensively investigated the influence of wet and dry processing techniques on the structural, physical, mechanical, thermal, and acoustic performance of binder-less natural fiber composites. The results clearly indicate that the processing method plays a pivotal role in defining the internal microstructure and, consequently, the overall behavior of the panels across multiple performance domains.

The dry-processed panels with a higher density value of 204.94 kg/m^3 and lower porosity value of 86.3% demonstrated superior dimensional stability, particularly in terms of their thickness swelling. Although the water absorption differences between the two methods were not statistically significant from each other, the dry-processed samples maintained better structural integrity under moisture exposure. In the case of thermal conductivity, the wet-processed panel showed a significantly lower thermal conductivity value of 0.053 W/mK versus 0.057 W/mK for the dry samples, reflecting enhanced insulation performance due to its more porous internal architecture.

Contrary to expectations based on their lower density, the wet-processed panels exhibited superior mechanical properties, achieving statistically significant increases in MOE, MOR, and IB strength compared to the dry-processed panel. Such enhancement could be attributed to improved and homogeneous fibrillation and inter-fiber bonding facilitated by the wet processing method. Microscopic examination supported these observations, revealing a more compact, homogeneous, and well-bonded fiber network in the wet-processed panel, while the dry-processed composite appeared to be more heterogeneous, with poorly integrated fiber bundles and voids. These microstructural differences can also be directly contributed to the observed variation in mechanical strength of the samples.

The acoustic performance of the panels further highlighted the nuanced impact of processing methods. In the low-frequency range (50–1390 Hz), the dry-processed panel achieved a slightly higher maximum sound absorption coefficient, with α_max reaching 0.94, compared to 0.89 for the wet-processed sample. However, in the high-frequency range (100–6400 Hz), the wet-processed panel outperformed its dry counterpart, with α_max recorded at 0.84 versus 0.75. The perforations with seven holes and 3 mm diameter in both panel types further enhanced the overall high-frequency absorption, with the wet-processed perforated panels attaining an α_max of 0.98, while the dry-processed perforated

panels reached 0.90. These results emphasize the potential of structural modifications to improve acoustic performance and tailor composites for targeted frequency ranges.

In conclusion, wet processing, despite yielding composites with lower dimensional stability, resulted in materials with improved mechanical strength, thermal insulation, and high-frequency sound absorption capabilities. Conversely, dry processing favored dimensional stability and low-frequency acoustic performance. These findings offer valuable insights for engineering multifunctional, eco-friendly composites and demonstrate how processing routes can be chosen strategically to meet the diverse requirements of applications in building materials, acoustic insulation, and sustainable construction systems.

References

1. Mathews, J.M.; Vivek, B.; Charde, M. Thermal insulation panels for buildings using recycled cardboard: Experimental characterization and optimum selection. *Energy Build.* **2023**, *281*, 112747. [CrossRef]
2. Bi, L.J. Research on corrugated cardboard and its application. *Adv. Mater. Res.* **2012**, *535*, 2171–2176. [CrossRef]
3. Lohtander, T.; Herrala, R.; Laaksonen, P.; Franssila, S.; Österberg, M. Lightweight lignocellulosic foams for thermal insulation. *Cellulose* **2022**, *29*, 1855–1871. [CrossRef]
4. Antunes, M.D.S.P.; Cano, Á.; Realinho, V.C.D.R.; Osuna, D.A.; Perero, J.I.V. Compression properties and cellular structure of polyurethane composite foams combining nanoclay and different reinforcements. *Int. J. Compos. Mater.* **2014**, *4*, 27–34.
5. Kausar, A. Polyurethane composite foams in high-performance applications: A review. *Polym.-Plast. Technol. Eng.* **2018**, *57*, 346–369. [CrossRef]
6. Yucel, K.; Basyigit, C.; Ozel, C. Thermal insulation properties of expanded polystyrene as construction and insulating materials. In Proceedings of the 15th Symposium in Thermophysical Properties, Boulder, CO, USA, 22–27 June 2003.
7. Benallel, A.; Tilioua, A.; Ettakni, M.; Ouakarrouch, M.; Garoum, M.; Hamdi, M.A.A. Design and thermophysical characterization of new thermal insulation panels based on cardboard waste and vegetable fibers. *Sustain. Energy Technol. Assess.* **2021**, *48*, 101639. [CrossRef]
8. Benallel, A.; Tilioua, A.; Mellaikhafi, A.; Babaoui, A.; Hamdi, M.A.A. Thermal characterization of insulating materials based on date palm particles and cardboard waste for use in thermal insulation building. In Proceedings of the AIP Conference Proceedings, Virtual, 26–28 April 2021; AIP Publishing: Melville, NY, USA, 2021; Volume 2345, p. 020024.
9. Cintura, E.; Nunes, L.; Esteves, B.; Faria, P. Agro-industrial wastes as building insulation materials: A review and challenges for Euro-Mediterranean countries. *Ind. Crops Prod.* **2021**, *171*, 113833. [CrossRef]
10. Xie, M.; Qiao, Q.; Sun, Q.; Zhang, L. Life cycle assessment of composite packaging waste management—A Chinese case study on aseptic packaging. *Int. J. Life Cycle Assess.* **2013**, *18*, 626–635. [CrossRef]
11. FAO. *World Production Cardboard*; Food and Agriculture Organization: Rome, Italy, 2021.
12. Mazaherifar, M.H.; Coşereanu, C.; Timar, C.M.; Georgescu, S.V. Physical and mechanical properties of foam-type panels manufactured from recycled cardboard. *Constr. Build. Mater.* **2024**, *411*, 134685. [CrossRef]
13. Miller, M.; Justiniano, M.; McQueen, S. *Energy and Environmental Profile of the US Pulp and Paper Industry*; Energetics, Inc.: Columbia, MD, USA, 2005.
14. Virtanen, Y.; Nilsson, S. *Environmental Impacts of Waste Paper Recycling*; Routledge: Abingdon, UK, 2013.

15. Mahdi, S.; Xie, T.; Venkatesan, S.; Gravina, R.J. Mechanical characterisation and small-scale life-cycle assessment of polypropylene macro-fibre blended recycled cardboard concrete. *Constr. Build. Mater.* **2023**, *409*, 133902. [CrossRef]

16. Betts, D.; Sadeghian, P.; Fam, A. Structural behavior of sandwich beams with flax fiber–reinforced polymer faces and cardboard cores under monotonic and impact loads. *J. Archit. Eng.* **2020**, *26*, 04020013. [CrossRef]

17. McCracken, A.; Sadeghian, P. Corrugated cardboard core sandwich beams with bio-based flax fiber composite skins. *J. Build. Eng.* **2018**, *20*, 114–122. [CrossRef]

18. Sair, S.; Mandili, B.; Taqi, M.; El Bouari, A. Development of a new eco-friendly composite material based on gypsum reinforced with a mixture of cork fibre and cardboard waste for building thermal insulation. *Compos. Commun.* **2019**, *16*, 20–24. [CrossRef]

19. Mazaherifar, M.H.; Timar, M.C.; Georgescu, S.V.; Coșereanu, C. Sustainable thermal and acoustic insulating panels from recycled cardboard. *BioResources* **2025**, *20*, 4115–4135. [CrossRef]

20. Li, J.; Yang, X.; Xiu, H.; Dong, H.; Song, T.; Ma, F.; Ji, Y. Structure and performance control of plant fiber based foam material by fibrillation via refining treatment. *Ind. Crops Prod.* **2019**, *128*, 186–193. [CrossRef]

21. Liuzzi, S.; Rubino, C.; Martellotta, F.; Stefanizzi, P. Sustainable Materials from Waste Paper: Thermal and Acoustical Characterization. *Appl. Sci.* **2023**, *13*, 4710. [CrossRef]

22. Woodhams, R.; Thomas, G.; Rodgers, D. Wood fibers as reinforcing fillers for polyolefins. *Polym. Eng. Sci.* **1984**, *24*, 1166–1171. [CrossRef]

23. Nair, A.S.; Al-Battashi, H.; Al-Akzawi, A.; Annamalai, N.; Gujarathi, A.; Al-Bahry, S.; Sivakumar, N. Waste office paper: A potential feedstock for cellulase production by a novel strain Bacillus velezensis ASN1. *Waste Manag.* **2018**, *79*, 491–500. [CrossRef]

24. Xu, H.; Huang, L.; Xu, M.; Qi, M.; Yi, T.; Mo, Q.; Zhao, H.; Huang, C.; Wang, S.; Liu, Y. Preparation and properties of cellulose-based films regenerated from waste corrugated cardboards using [Amim] $Cl/CaCl_2$. *ACS Omega* **2020**, *5*, 23743–23754. [CrossRef] [PubMed]

25. Chinga-Carrasco, G. Cellulose fibres, nanofibrils and microfibrils: The morphological sequence of MFC components from a plant physiology and fibre technology point of view. *Nanoscale Res. Lett.* **2011**, *6*, 417. [CrossRef]

26. Wang, X.; Sotoudehniakarani, F.; Yu, Z.; Morrell, J.J.; Cappellazzi, J.; McDonald, A.G. Evaluation of corrugated cardboard biochar as reinforcing fiber on properties, biodegradability and weatherability of wood–plastic composites. *Polym. Degrad. Stab.* **2019**, *168*, 108955. [CrossRef]

27. *EN 317:1996*; Particleboards and Fibreboards—Determination of Swelling in Thickness after Immersion in Water. European Committee for Standardization: Brussels, Belgium, 1996.

28. *ISO 8301:1991*; Determination of Steady-State Thermal Resistance and Related Properties. Heat Flow Meter Apparatus. International Organization for Standardization: Geneva, Switzerland, 1991.

29. *BS EN 12939:2001*; Thermal Performance of Building Materials and Products: Determination of Thermal Resistance by Means of Guarded Hot Plate and Heat Flow Meter Methods: Products of High and Medium Thermal Resistance. British Standards Institution: London, UK, 2001.

30. *ISO 10534:1998*; Acoustics—Determination of Sound Absorption Coefficient and Impedance in Impedance Tubes: Part 1: Method Using Standing Wave Ratio. Part 2: Transfer-Function Method. International Organization for Standardization: Geneva, Switzerland, 1998.

31. *ASTM E1050:1998*; Standard Test Method for Impedance and Absorption of Acoustical Materials Using a Tube, Two Microphones and a Digital Frequency Analysis System. ASTM International: West Conshohocken, PA, USA, 1998.

32. *ISO 11654:1997*; Acoustics: Sound Absorbers for Use in Buildings. Rating of Sound Absorption. International Organization for Standardization: Geneva, Switzerland, 1997.

33. *EN 310:1993*; Wood-Based Panels—Determination of Modulus of Elasticity in Bending and of Bending Strength. European Committee for Standardization: Brussels, Belgium, 1993.

34. *EN 326-1:1994*; Wood-Based Panels. Sampling, Cutting and Inspection. Part 1: Sampling and Cutting of Test Pieces and Expression of Test. European Committee for Standardization: Brussels, Belgium, 1994.

35. *EN 319:1993*; Particleboards and Fibreboards: Determination of Tensile Strength Perpendicular to the Plane of the Board. European Committee for Standardization: Brussels, Belgium, 1993.

36. Fauzi, M.S.; Lan, D.N.; Osman, H.; Ghani, S.A. Effect of sodium bicarbonate as blowing agent on production of epoxy shape memory foam using aqueous processing method. *Sains Malays.* **2015**, *44*, 869–874. [CrossRef]

37. Hussein, M.S.; Leng, T.P.; Rahmat, A.R.; Zainuddin, F.; Keat, Y.C.; Suppiah, K.; Alsagayar, Z.S. The effect of sodium bicarbonate as blowing agent on the mechanical properties of epoxy. *Mater. Today Proc.* **2019**, *16*, 1622–1629. [CrossRef]

38. Benallel, A.; Tilioua, A.; Garoum, M. Development of thermal insulation panels bio-composite containing cardboard and date palm fibers. *J. Clean. Prod.* **2024**, *434*, 139995. [CrossRef]

39. Janssen, H.; Van De Walle, W. The impact of pore structure parameters on the thermal conductivity of porous building blocks. *Constr. Build. Mater.* **2022**, *324*, 126681. [CrossRef]

40. Clarke, D.R. Materials selection guidelines for low thermal conductivity thermal barrier coatings. *Surf. Coat. Technol.* **2003**, *163–164*, 67–74. [CrossRef]

41. Gokulkumar, S.; Thyla, P.R.; Prabhu, L.; Sathish, S. Measuring methods of acoustic properties and influence of physical parameters on natural fibers: A review. *J. Nat. Fibers* **2020**, *17*, 1719–1738. [CrossRef]

42. Mamtaz, H.; Fouladi, M.H.; Al-Atabi, M.; Namasivayam, S.N. Acoustic Absorption of Natural Fiber Composites. *J. Eng.* **2016**, e5836107. [CrossRef]

43. Sun, W.; Strässle Zúñiga, S.H.; Philippe, V.; Rinaldi, L.; Abitbol, T. Mycelium-Bound composites from agro-industrial waste for broadband acoustic absorption. *Mater. Des.* **2025**, *250*, 113591. [CrossRef]

Article

Evaluation of 3D-Printed Connectors in Chair Construction: A Comparative Study with Traditional Mortise-and-Tenon Joints

Antoniu Nicolau [1], **Marius Nicolae Baba** [2], **Camelia Cerbu** [2], **Cătălin Cioacă** [3], **Luminița-Maria Brenci** [1,*] **and Camelia Cosereanu** [1,*]

1 Faculty of Furniture Design and Wood Engineering, Transilvania University of Brasov, B-dul Eroilor, nr. 29, 500036 Brasov, Romania; antoniu.nicolau@unitbv.ro
2 Faculty of Mechanical Engineering, Transilvania University of Brasov, B-dul Eroilor, nr. 29, 500036 Brasov, Romania; mariusbaba@unitbv.ro (M.N.B.); cerbu@unitbv.ro (C.C.)
3 Department of Management and Military Sciences, "Henri Coanda" Air Force Academy, Str. Mihai Viteazul 160, 500183 Brasov, Romania; catalin.cioaca@afahc.ro
* Correspondence: brenlu@unitbv.ro (L.-M.B.); cboieriu@unitbv.ro (C.C.)

Abstract: The present paper investigates the possibility of replacing the traditional L-type corner joint used in chair construction with a 3D printed connector, manufactured using the Fused Filament Fabrication (FFF) method and black PLA as filament. The connector was designed to assemble the legs with seat rails and stretchers, and it was tested under diagonal tensile and compression loads. Its performance was compared to that of the traditional mortise-and-tenon joint. Stresses and displacements of the jointed members with connector were analyzed using non-linear Finite Element Method (FEM) analysis. Both connector and mortise-and-tenon joint were employed to build chair prototypes made from beech wood (*Fagus sylvatica* L.). Digital Image Correlation (DIC) method was used to analyze the displacements in the vicinity of the jointed members of the chairs. Seat and backrest static load tests were carried out in order to verify if the chairs withstand standard loading requirements. Results indicated that the 3D printed connector exhibited equivalent mechanical performance as the traditional joint. The recorded displacement values of the chair with 3D-printed connectors were higher than those of the traditional chair reaching 0.6 mm on the X-axis and 1.1 mm on the Y-axis, without any failures under a maximum vertical load of approximately 15 kN applied to the seat. However, it successfully withstood the loads for seating and backrest standard tests, in accordance with EN 1728:2012, without any structural failure. This paper presents a new approach for the chair manufacturing sector, with potential applicability to other types of furniture.

Keywords: 3D printed connector; PLA; Fused Filament Fabrication; chair; mortise-and-tenon joint; L-type corner joint; digital image correlation; finite element method

1. Introduction

Additive manufacturing (AM), also known as 3D printing technology is a fabrication method where an object is created by successively depositing layers of material [1] based on computer-aided design, and it is used to build prototypes or series products [2]. Before printing, the virtual model is segmented into cross-sectional planes of the designed part, which are then transmitted to the 3D printer. This technology is distinct from subtractive processes, where raw materials are processed to form the final product through techniques like turning, milling, or drilling [1].

After three decades of development, 3D printing technology has emerged as a leading method that does not require any additional processing devices or auxiliary resources. Its ability to produce custom parts on demand has made it increasingly popular over the last decade. 3D printing has evolved into a viable technique for rapid prototyping, mass manufacturing and the production of customized parts [3–5].

The Fused Filament Fabrication (FFF) method involves applying material under constant pressure through a nozzle. The extruded material is deposited at a constant rate, solidifying after passing through the nozzle, thereby adhering to the previous material layer [4,6,7]. Complex shapes may require support during the printing process [8]. Additive manufacturing is capable of producing fully functional components using a wide range of materials, including ceramics, metals, and polymers, as well as combinations in hybrid or composite forms [9,10]. Among the diverse polymers available in the market are nylon, polycarbonate, high-density polyethylene, and polystyrene; however, polylactic acid (PLA) is the most commonly used filament due to its average tensile strength of 56.6 MPa, affordability, and suitability for a variety of applications [11]. These materials offer outstanding high thermal resistance, high rigidity and excellent resistance to a wide range of chemicals [2,12–14] and properties such as ultraviolet (UV) resistance, bio-compatibility, transparency or hardness. These features make them perfect for industries producing special purpose components [15].

PLA is a thermoplastic aliphatic polyester derived from corn and can be considered as an eco-friendly material. PLA is versatile, and PLA-based composites have been investigated in the literature, including composites with various reinforcements [11].

In the traditional furniture manufacturing industry, designing wooden components is often constrained by the execution of joints between parts [16]. Consequently, the design possibilities are frequently limited to L-type corner joints connecting wooden components, typically involving the joining of no more than two pieces in a single joint [13]. The integration of AM technology, whether independently or combined with traditional methods, allows for the creation of complex and visually appealing geometries that cannot be achieved solely through conventional techniques [17]. Hybrid design is a rapidly growing area of research that provides new hardware and software tools for crafting aesthetically appealing furniture products, enabling creative approaches in furniture design and construction. Generally, hybrid practices aim to expand producers' creative horizons while overcoming the limitations of traditional furniture making [13]. Moreover, by combining reverse design with additive manufacturing, it becomes possible to quickly conceptualize and produce custom products [18].

Over the last few years, numerous studies [19–22] have focused on determining the mechanical properties of L-type corner joints in furniture. The concepts of dismountable and modular furniture are becoming increasingly relevant, allowing end-users to engage directly in creating personalized designs [23,24]. Dismountable joints facilitate custom designs with press-fit systems, eliminating the need for adhesives or screws, enhancing fit, and simplifying the production and assembly of parts [25,26]. With FFF technology, these plastic connectors of various sizes and shapes can be produced in a single additive manufacturing process step [12]. The utilization of 3D printing technology reduces waste compared to traditional methods, as the 3D printer applies material only as needed to shape the final design made in software such as *AutoCAD*, *Rhino*, or *SOLIDWORKS* [27].

Various methods are being researched to improve joint solutions for modular furniture elements, replacing traditional ones [28]. Although mortise-and-tenon joints remain prevalent in furniture manufacturing, they are irreplaceable for certain types of constructions, particularly chairs. Chairs are subjected to various direct and indirect loads throughout their lifespan. Different mechanical load types—tensile, compression, bending, shear, and

torsion—impact the joints in the chair's structure. These loads can lead to negative effects, such as bending, cracking, or breaking in the connection elements. Static analysis conducted on the load-carrying capacity of chairs suggests that adding stretchers between legs is a suitable solution for users with a weight exceeding 150 kg [29].

Research involving diagonal compression and tensile testing of L-type corner joints has demonstrated that the mechanical performance of these joints significantly depends on the type of joint [30,31]. Bending moment testing of L-type corner joints connected with 3D printed connectors has been explored in other studies [32–36], and recent research has increasingly concentrated on designing and testing connectors for furniture part junctions, focusing particularly on case furniture [5,24,28,37]. FEM analysis, followed by experiments are utilized to characterize the mechanical performance of the raw material as well as the behavior of the joint in other application fields [36].

This study aims to investigate a specially designed connector for chair construction through testing it in the L-type corner joint under diagonal tensile and compression loads, and comparing it with a traditional mortise-and-tenon joint. Mechanical testing simulation via FEM highlighted the potential damage locations for the newly designed connectors. The research continued with the analysis of the chairs constructed with both traditional mortise-and-tenon joints and connectors for comparative results. Both prototypes underwent tests for seat and backrest strength following EN 1728:2012 [38], and optical analysis assessed 3D deformations in the areas of seat assembly using the DIC method. Both chairs met the standard requirements without structural or joint damage.

The DIC analysis enabled visualization of displacements in the joint area, demonstrating that the chair with connectors withstood a seating load of nearly 15 kN without sustaining damage. The advantages of this chair with 3D printed connectors compared to the traditional model include: disassembly, leading to reduced costs in packaging and transport; transferring assembly operations to the end-user; streamlining the wood-working process by eliminating machining operations for joints and gluing; and reducing the dimensions of seat rails and stretchers, positively impacting solid wood resource utilization. Other advantages of 3D printing in furniture construction over classic manufacturing technology are related to the approach to a new design without restrictions on shape, geometry and joint angle, as well as the use of ecological and biodegradable materials for the additive manufacturing.

2. Materials and Methods

Beech wood (*Fagus sylvatica* L.) with a density of 698 kg/m^3 and a moisture content of 8.5% was used as raw material for the wooden parts of the L-type corner joints and for the chairs, two constructed traditionally with mortise-and-tenon joints and the other two with connectors. The L-type corner joints and the chairs built with the traditional mortise-and-tenon joints serve as a reference. The bonding adhesive used for these structures was the commercial Novobond D2 polyvinyl acetate. However, screws were used to secure the connectors to the chair legs.

The experimental model of L-type corner joint includes three members, one for the leg, with cross-section of 35 mm × 35 mm and length of 50 mm, and two members for the stretchers/seat rails with cross-sections of 35 mm × 22 mm and lengths of 180 mm for the joints with connectors and 222 mm for the reference specimens. The tenon of the reference sample was executed with dimensions (L × l × g) of 12 mm × 13 mm × 8 mm. These joints are marked on the 3D models of the chairs designed for this research in Figure 1a for the reference and in Figure 1b for the proposed chair with connectors.
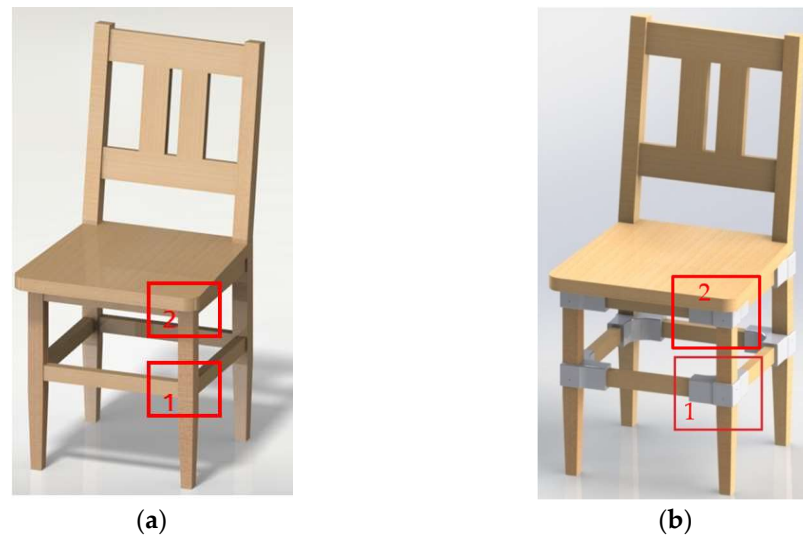
(**a**)　　　　　　　　　　　　　(**b**)

Figure 1. The joints considered in the experimental research: (**a**) Reference chair with traditional joints; (**b**) Proposed chair with 3D printed connectors. (1—leg and stretcher joint; 2—leg and seat rail joint).

The connector was 3D printed with the sizes and shape presented in Figure 2.
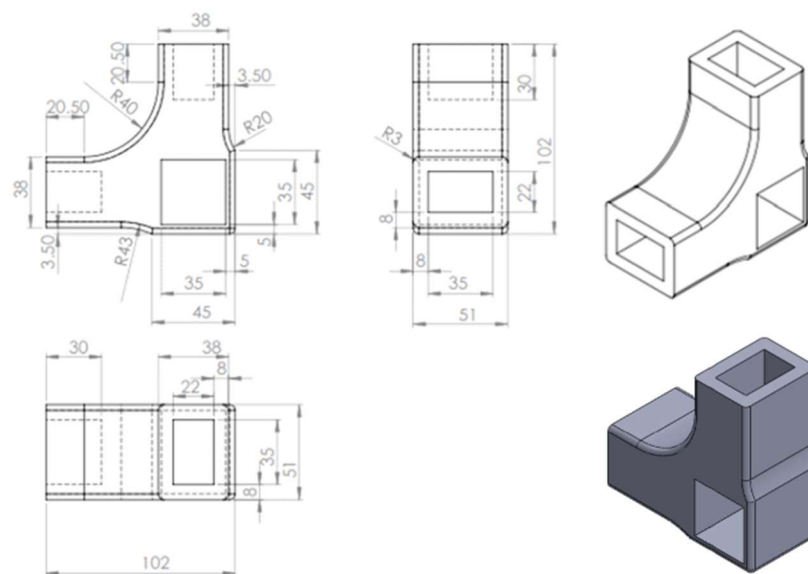

Figure 2. Dimensions and shape of the 3D printed connector.

The software utilized to create the 3D model was *SOLIDWORKS 3D CAD*, version 2016, developed by Dassault Systèmes, France. The (.stl) file of the model was exported to the printer. FFF technology was employed in the additive manufacturing process using the Ultimaker S5 printer (manufactured by UltiMaker, Utrecht, The Netherlands), which has a buildable volume of 330 mm × 240 mm × 300 mm, and operates with its own software, UltiMaker Cura 4.3. The printer deposited filament layers inclined at 45 degrees to the exterior perimeter and at 90 degrees to the previous layer (Figure 3a). The position of the connector on the build platform is displayed in Figure 3b. This position required additional support, which was removed once the connector was fully printed. Previous research has indicated that the horizontal position of parts during the build process tends to be unfavorable for the mechanical resistance of connectors subjected to diagonal compression and tensile loads in a L-type corner joint assembly [33,39].
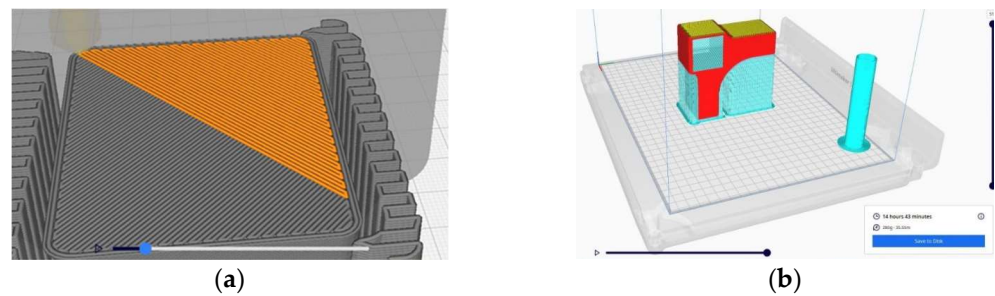
Figure 3. Description of the printing process: (**a**) Adjacent layers deposition; (**b**) Position of the sample on the build platform, displayed by the software.

The filament used for the FFF method was black polylactic acid (PLA) sourced from FORM Futura (Nijmegen, The Netherlands), characterized by a diameter of 2.85 mm, specific gravity of 1.24 g/cm^3, print temperature range of 190 °C to 225 °C, and a melting temperature around 210 °C, PLA is a bio-plastic, made up of a repeating chain of lactic acid and it is recyclable using conventional methods. Specifically, PLA is a thermoplastic aliphatic polyester derived from corn and can even be composted like other organic materials [11]. With a tensile modulus of 3310 MPa and a flexural modulus of 2364.3 MPa, black PLA demonstrates higher rigidity compared to other filaments, such as white PLA or fiberglass-reinforced PLA, as observed in preliminary experimental research. The selected print parameters were, as follows: print speed of 50 mm/s, print temperature of 250 °C, layer height of 0.2 mm, and 100% fill density. The printing parameters were selected according to the manufacturer recommendations and as result of the preliminary research on this topic [33,39]. Three pieces were printed simultaneously, with a total execution time of 14 h and 43 min.

For new models of 3D printed furniture and connectors, it is essential to analyze mechanical properties before bringing the products to market [2]. Following methodologies described in the literature [16,19,20], mechanical tests were conducted on L-type corner joints subjected to diagonal tensile (Figure 4a) and compression (Figure 4b) loads. A Zwick/Roell Z010 universal testing machine (Ulm, Germany) was employed to test five specimens of each category (one group with connectors and the other as the reference group). As depicted in Figure 4a, the tensile force (*F*) tends to open the joint, while the compression force tends to close it.
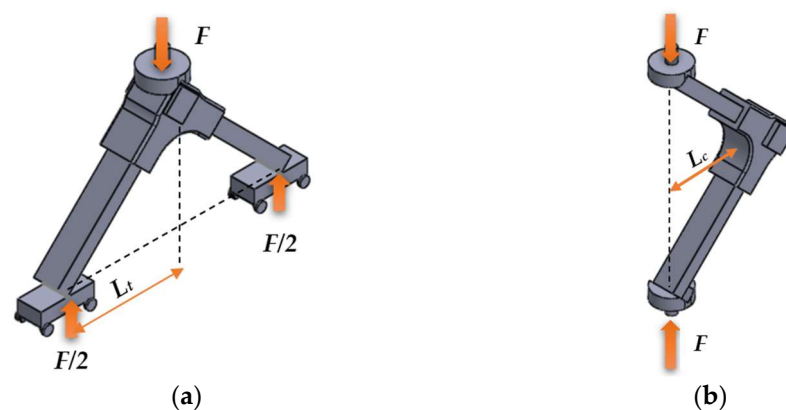

Figure 4. The models of the mechanical tests: (**a**) under tensile load; (**b**) under compression load.

The bending moments were calculated with Equation (1) for the tensile test and (2) for the compression test.

$$M_t = \frac{F}{2} \times L_t, \text{ in N·m} \tag{1}$$

$$M_c = F \times L_c, \text{ in N·m} \qquad (2)$$

where M_t and M_c are the moments under tensile and compression loads; L_t and L_c are the moment arms under tensile and compression loads, in m; F is the maximum failure load, in N.

The models shown in Figure 4 were analyzed using the finite element method (FEM), to simulate how the specimen reacts to applied diagonal tensile and compression forces, resulting in a field of displacements and specific stresses and strains in the connector. The FEM analysis was conducted using the *Simcenter 12.0* simulation software from Siemens PLM Software package, developed by Siemens Industry Software, Brașov, Romania. The initial step involved transferring the (.stl) models from the *SOLIDWORKS 3D CAD* software version 2016to the *Simcenter12.0* for discretization (Figure 5a).
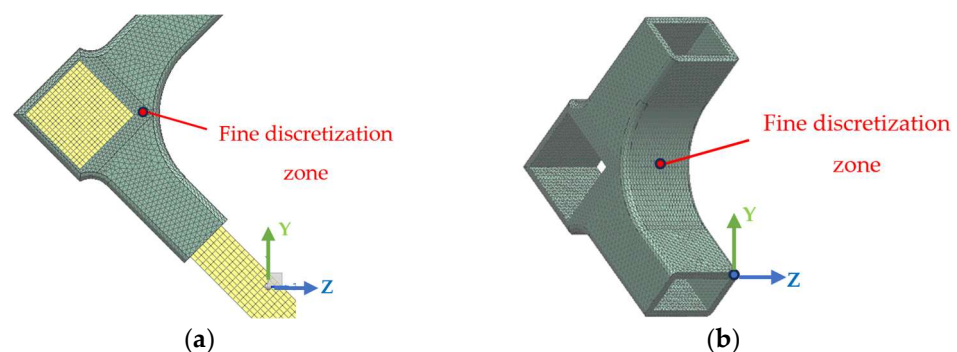

(**a**)   (**b**)

Figure 5. Mesh of the model in FEM analysis: (**a**) detail of the discretization of the L-type corner joint; (**b**) detail of the discretization of the connector.

Through discretization, the structure characterized by an infinite number of points is transformed into a simplified model with a finite number of nodes. The discretization was done differently for the solid wood elements and for the connector (Figure 5a). A more complex and finer network with numerous numbers of nodes was applied to some parts of the connector, in order to evaluate better the values of the specific displacements, stresses and strains in the areas of direct contact with the wooden members of the L-type corner joint (Figure 5a,b). The next step was to define rigid connections between the leg segment and the connector. The elastic properties of the beech wood and of the black PLA are presented in Table 1.

Table 1. Elastic properties of the materials used for FEM analysis *.

Material	Young's Modulus, in MPa			Shear Modulus, in MPa			Poisson's Ratio					
	E_L	E_R	E_T	G_{LR}	G_{LT}	G_{RT}	ν_{TR}	ν_{RT}	ν_{LT}	ν_{TL}	ν_{RL}	ν_{LR}
Wood	14,000	2280	1160	1970	950	467	0.36	0.75	0.51	0.044	0.073	0.45
PLA	3149			1287			0.36					

* Note: *L* indicates the longitudinal section; *T* denotes the transverse (crosscut) section, and *R* represents the radial section.

To evaluate the connector in the final product, four prototypes of chairs were manufactured—two for each type presented in Figure 6. Eight connectors were used to assemble the legs with the seat rails and the four stretchers of the experimental chair. The second type of chair was constructed traditionally with mortise-and-tenon joints and deemed the reference chair, subjected to the same tests as the experimental chair. Both types of prototypes were made from beech wood and had identical component parts,

with the exception of the seat rails and the stretchers, which were shorter for the chair with connectors.

Figure 6. The two types of chairs subjected to final tests (experimental chair with 3D printed connectors on the right, and the reference one on the left).

The objective of the final tests was to compare the performances of the two chairs—the first built with connectors and the second assembled in the traditional method. The initial test involved an optical analysis of the 3D deformations around the joints using the DIC method, followed by the assessment of the seat and backrest strengths according to EN 1728:2012 standard [38].

The equipment for DIC analysis belong to the Laboratory of Mechanical Testing (Research Center of Numerical Simulation, Testing and Mechanics of Composite Materials) in Research & Development Institute of Transilvania University of Brasov (Figure 7), and comprised two main systems:

- A system for analyzing structural behavior in fatigue tests (series 1451, K22305, manufactured by Walter & Bai, Löhningen, Switzerland), featuring actuators capable of moving vertically and horizontally with forces of 100 kN, and 63 kN respectively; piston strokes reaching 100 mm, and DION 7 version 1.6 software for static and dynamic tests.
- The optical analysis system of 3D deformations for materials and components ARAMIS SRX (manufactured by ZEISS GOM Metrology, Braunschweig, Germany), equipped with high-resolution 3D cameras, software, and hardware tailored to determine 3D displacements, strains, strain tensor directions, test point trajectories through digital image correlation methods. It incorporates two optical sensors (CMOS 2×12 mega pixels), attaining a resolution of 4096×3068 pixels; blue light technology with LED lighting; and GOM Correlate Professional software.

The ARAMIS SRX is a high-resolution 3D camera system capable of full-field and point measurements. It has a potential of capturing 2000 frames per second with two cameras measuring deformation. The blue light technology harnesses a narrowband blue ambient light that interacts during image capture, offering optimal illumination with short exposure times for measurement areas and high accuracy in point-based motion analysis. The DIC method functions by comparing digital images of the tested piece at various deformation stages, thus measuring displacements along the axes.

The monitored surfaces of the tested chairs were painted black and white to create a grid of black points (markers) that visualize the deformations. The GTM force transducer with a nominal load of 100 kN manufactured by GTM—GLASSMANN Testing and Metrology, Bickenbach from Germany was utilized for compression loading. The set parameters were, as follows:

- The vertical movement of the force transducer was fixed at 5 mm;
- Travel speed: 0.02 mm/s;
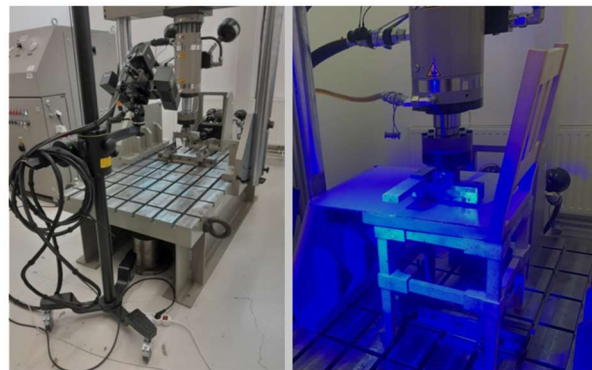- Fixed frame rate of 2 Hz, resulting in a total of 400 frames.

Figure 7. Equipment used for DIC analysis (system for analyzing the behavior of structures in fatigue tests on the left, optical analysis system for 3D deformations on the right).

The value of the load force on the seats will be determined once the final vertical movement of 5 mm is attained. In the jointing area between the legs and the seat rail and stretcher (monitored surfaces), 16 points were selected for the chair with connectors (Figure 8a), while 18 points were chosen for the reference chair (Figure 8b) to analyze their displacements on the X and Y axes.
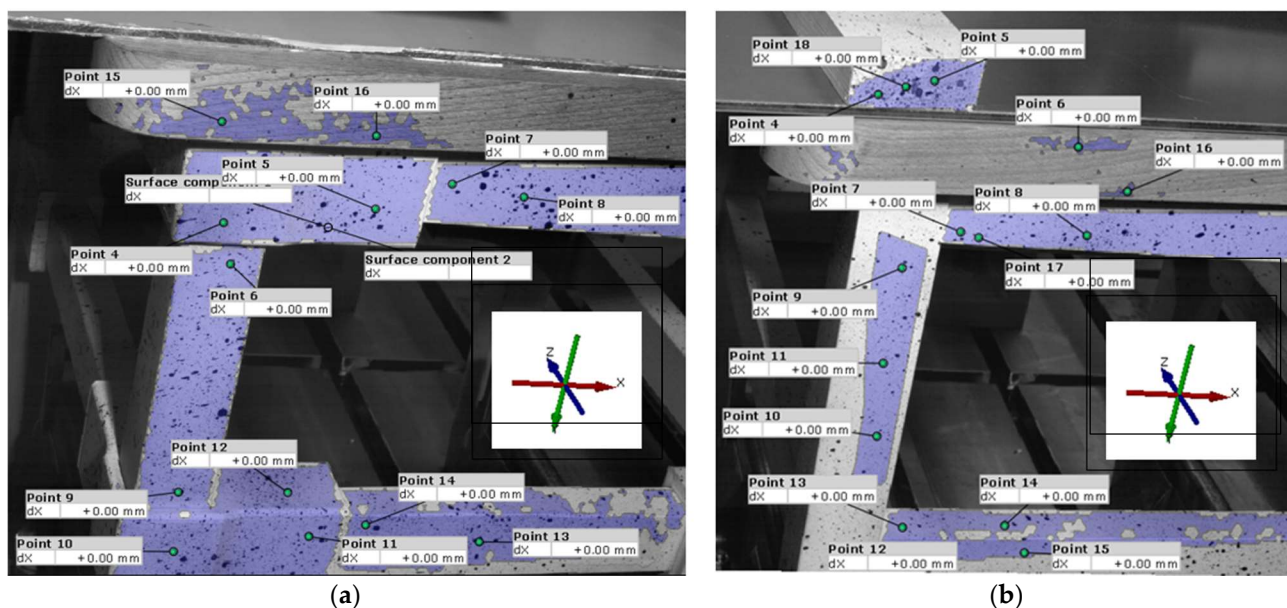

(**a**)   (**b**)

Figure 8. The selected points to follow the displacements on the horizontal and vertical axes: (**a**) For the chair with connector; (**b**) For the reference chair.

The second set of chairs (one with connectors and one as a reference) were tested on a furniture test rig from Hegewald & Peschke Meß- und Prüftechnik GmbH (Nossen, Germany), situated in the Design, Prototyping and Testing Laboratory (Cluj Innovation Park, Regional Center of Excellence for Creative Industries, Cluj-Napoca, Romania), which is certified by the National Accreditation Organization (RENAR). The test rig comprises two axes with 2.5 kN force cells each and is capable of performing cyclic durability tests, fatigue resistance tests on furniture components, and finished furniture products, operated

by SIMATIC HMI visualization software from Siemens AG (Munich, Germany). The chairs underwent testing according to the [38] standard for static loads, specifically:

- Seat static load of 1300 N and back static load test of 430 N, (test 6.4);
- Leg forward static load test (test 6.15), by applying a seat vertical load of 1000 N and a horizontal force of 400 N centrally to the rear of the seat, directed forward;
- Leg sideways static load test (test 6.16), by applying a seat vertical load of 1000 N and a horizontal force of 300 N centrally to the unrestrained side of the seat, at seat level, in a direction towards the restrained feet.

Tests were carried out for 10 cycles, following several stages: positioning the chairs on the rig and attaching the locking devices (Figure 9—position 1), setup of the pressing devices for the seat (Figure 9—position 2) and backrest (Figure 9—position 3).
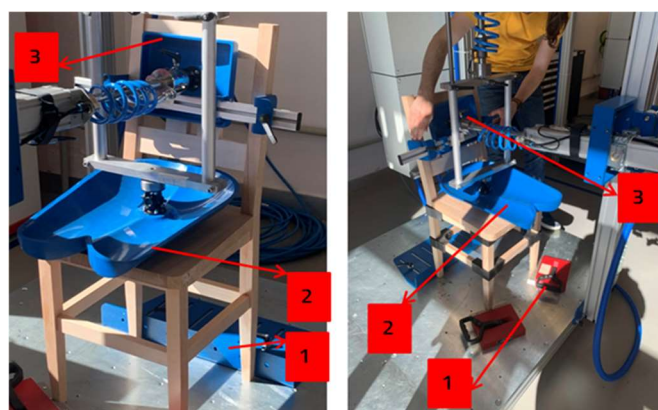

Figure 9. Chairs preparation on the test rig (reference chair on the left and chair with connectors on the right).

The test was conducted to determine whether the chair with connectors meets the minimum strength requirements under the same conditions as a traditionally manufactured chair. This method has also been applied by other researchers in their study of 3D-printed connectors designed for chairs [34].

3. Results and Discussion

3.1. FEM Analysis

The displacement fields of the L-type corner joint systems subjected both to compression and tensile loads, as well as the strain and stresses in the connector, were delineated through a non-linear FEM analysis. The results are illustrated in Figure 10 for displacements, in Figure 11 for stresses, and in Figure 12 for strains.

Figure 10 displays the deformed shapes of the L-type corner joints corresponding to displacements of 31.8 mm under tensile load and 76.77 mm under compression load, respectively. Deformed meshed geometry (as seen in Figure 10b) of the joint under compression load, accompanied by the loss of its initial position was highlighted also by [36], where numerical simulation was included. The maximum displacements occurred in the connector under tensile load (Figure 10a) at the upper section contacting the pressing device of the testing machine. Significant displacements (around 28 mm) are also indicated at the contact points between the rails and connector, indicating a tendency for the rail to detach from the connector. This tendency influences stress distribution in the connector's opposite corners and the corresponding outer face of the connector, where stress values reached approximately 90 MPa (Figure 11a). These areas are likely to fracture during experimental testing.
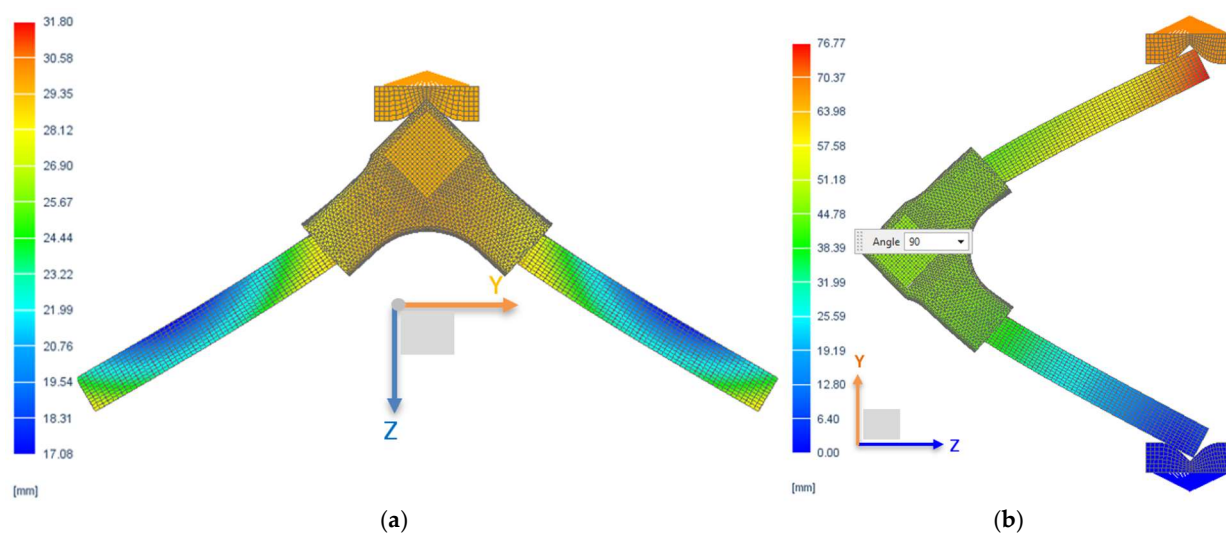
Figure 10. Field of displacements: (**a**) Simulation under the tensile load; (**b**) Simulation under the compression load.
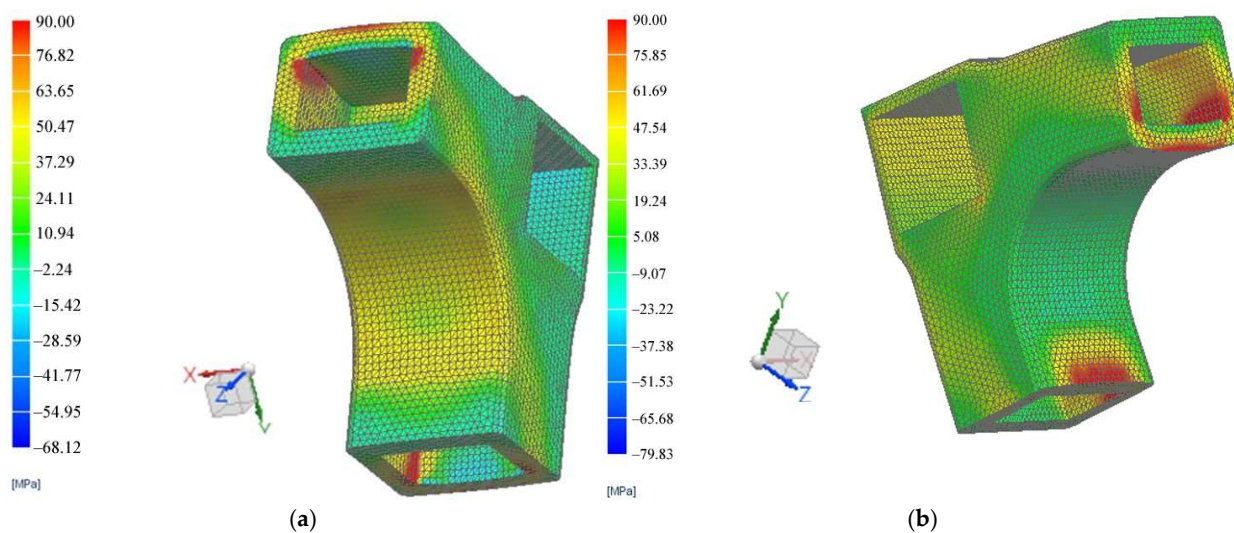

Figure 11. Field of stresses: (**a**) Simulation under the tensile load; (**b**) Simulation under compression load.
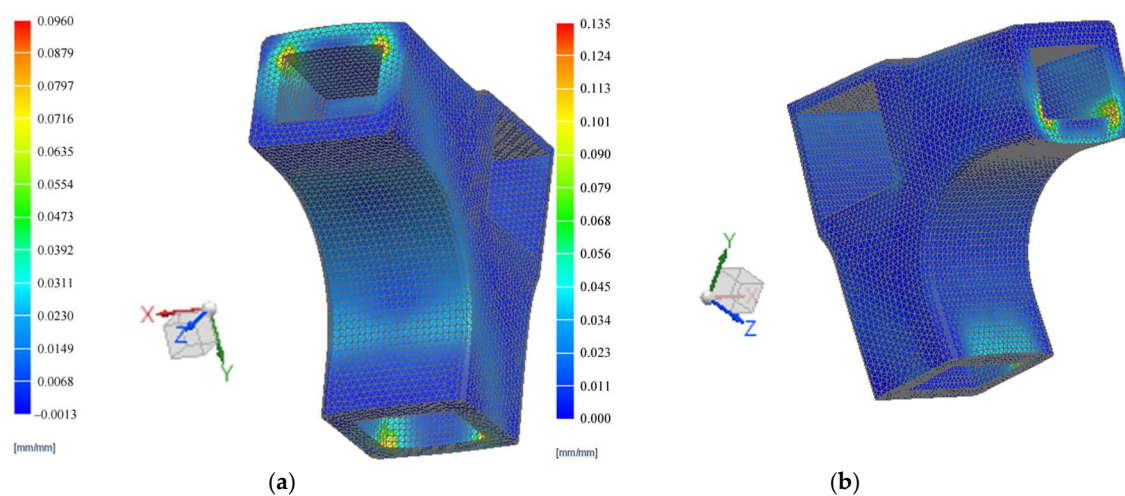

Figure 12. Field of strains: (**a**) Simulation under tensile load; (**b**) Simulation under compression load.

Figure 11b illustrates the maximum stress field in the connector under compression load. The most vulnerable surfaces are the interior corners in contact with the stretchers (or seat rails) that correspond to the connector's concave surface. The red color on the concave area indicates a stress value of 90 MPa, which is also susceptible to damage the connector during the mechanical testing.

Figure 12 shows the strain fields in the connector resulting from the FEM simulation of the diagonal tensile (a) and compression (b) tests applied to the L-type corner joints. The same corners with maximum stress values also exhibited the highest strain values, reaching 0.096 mm/mm under tensile load and 0.135 mm/mm under compression.

Similar simulations were conducted by other researchers [34] for 3D printed connectors manufactured using fused deposition modelling 3D printers with ABS filament. Their model simulated a compression test, where the force was applied at the end of the horizontal rail while the vertical rail was clamped. Maximum stresses of 26.9 MPa were recorded at the corners of the connectors with wall thickness of 5 mm, at the contact with wooden rails, where failures ultimately occurred after testing. The higher stresses of 90 MPa observed after FEM simulation in this study can be at-tributed to the thicker walls of the newly designed connector, measuring 8 mm, which demand greater pressing forces for deformation.

3.2. Mechanical Testing

The comparative graphs in Figure 13 demonstrate that the L-type corner connector joint performed better than the reference mortise-and-tenon joint assembly.
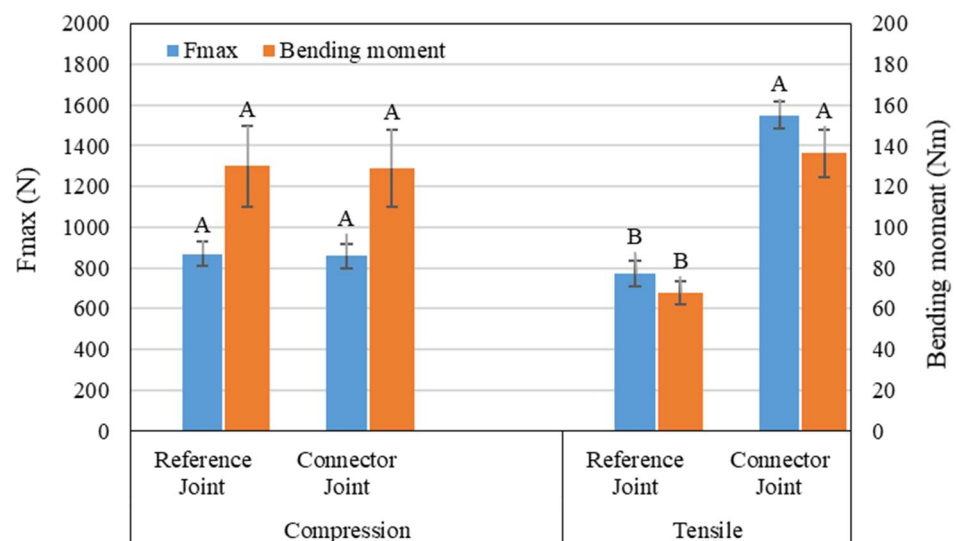

Figure 13. Results of the mechanical tests.

An initial observation from Figure 13 is that the bending moment under compression load is greater than that under tensile load for the mortise-and-tenon joint, consistent with trends reported by other researchers for wooden-based panels joints [16]. Testing mortise-and-tenon L-type corner joints composed of beech wood [19], the bending mo-ment under compression load was nearly twice that of the present work, while under tensile load, it was five times greater than the values resulting from the reference samples. These discrepancies can be explained by differences in specimen cross-sectional area and dimensions, corresponding moment arms, tenon sizes, and adhesive characteristics: larger cross-sections and tenon dimensions yield higher bending moments.

In the case of using the connectors, higher forces were recorded under tensile loads in comparison to compression loads (Figure 13). This trend has been noted by other researchers [20,32] investigating L-type corner joints made from beech wood, medium density fiberboard, and particleboard using various 3D printed fasteners designed for case furniture assembly. However, these types of joints typically demonstrate much lower bending moments compared to those recorded in the current study—approximately 12.3 Nm under tensile load and 8.6 Nm under compression load for assemblies made from beech wood [32] and 44.16 Nm under compression load for plywood joints [21]. Additionally, the bending moment values for L-type joints between two components made from glued HDF panels with a cross-section of 40 mm × 40 mm were roughly half of those obtained in this research [23], where 3D printed connectors made of acrylonitrile butadiene styrene (ABS) were used for the joints.

When comparing the bending moment capacity values determined in this study against those produced by other researchers [22] for similar samples constructed from beech wood and assembled with beech Domino dowels, consistency is evident in results. Other mortise-and-tenon corner-joints made of beech wood also exhibited similar bending moment values under compression when compared with the current study; however, higher tensile load bending moment values were recorded [31].

From the above results, one initial conclusion emerges: the values of bending moments under diagonal tensile and compression rely on both the material of the specimens and the joint type. For beech wood, the mortise-and-tenon joint generally exhibited higher values than other joint types [19,31], and tenon size significantly influences the tensile bending moment value: larger tenon sizes yield higher bending moment results. This conclusion applies to 3D printed connectors and fasteners as well. In this instance, the shape, material of the fastener, and the applied method collectively impact the joint's strength [27]. For example, dowel pins produced using the FFF method with PLA filament achieved mechanical performance comparable to wooden dowels in L-type corner joints con-structed from beech wood [26], highlighting PLA's suitability as a replacement for traditional wooden joints.

The statistical analysis for the data presented in Figure 13 included the calculation of the standard deviation using *Microsoft Excel* to establish a 95% confidence interval and a significance level of 0.05 ($p < 0.05$). A two-sample *t*-test was conducted using the *Minitab* software package, version 19.2020.1 to evaluate whether the mean tensile and compressive strengths were significantly influenced by the implementation of the connector joint in comparison to the reference case. The *p*-value > 0.9 indicates no significant difference between the connector and reference joints for the maximum force and bending moments under compression. The *p*-value $< 9 \times 10^{-5}$, much smaller than the standard significance level (0.05), indicates a statistically significant difference in bending moments under tensile conditions and demonstrates a higher tensile force capacity of the connector joint compared to the reference joint. According to the statistical results, the connector joint shows superior performance in tensile conditions, making it a better choice for applications involving significant tensile stress. For compressive conditions, there is no meaningful difference between the two joint types, suggesting that either joint could be used interchangeably for such applications.

FEM analysis serves as an important approach to simulate joint behavior under bending loads, evaluating displacement magnitudes, stresses, strains, and identifying vulnerable areas of the joint [20,23,28,32,34]. Accordingly, in the present case, the material failure occurred exclusively at the connector within the joint area adjoining the rails, as depicted by FEM analysis (Figure 14), leaving no cracks or other damages on the wooden parts.

| (a) | (b) |

Figure 14. Connector failure: (**a**) Under tensile load; (**b**) Under compression load.

From comparisons made, a consistent correlation appears between FEM simulation analyses and real mechanical testing outcomes regarding sensitive areas subjected to maximum stresses and strains, as well as system displacements. Experimental mechanical testing of the L-type corner joint with the connector indicated a maximum displacement value of around 25 mm for diagonal tensile loads and 60 mm for diagonal compression, with maximum forces of 1070 N and 719 N, respectively. These values are closely aligned with those highlighted by the FEM analysis

3.3. Optical Analysis of Displacements by DIC Method

To visualize the continuous displacements of the selected points, images captured by the two cameras were downloaded every 50th frame, resulting in a total of 9 images for each set of displacements on the X and Y axes for the 16 and 18 selected points, respectively. Graphical representation of the displacements of points in the jointing area is shown in Figure 15 for both the chair with connectors and the reference chair with traditional joints.

As can be observed in Figure 15, the behaviors of the two chairs differ under the pressing load applied at the center of the seat, until a vertical movement of 5 mm is reached. Initially, the displacements of the reference chair at the selected points are more homogeneous compared to those observed with the chair equipped with connectors. Furthermore, displacement values are higher in the chairs with connectors than in the reference chair, measuring 0.600 mm compared to 0.150 mm on the X axis and 1.100 mm versus 0.210 mm on the Y axis, indicating that the mortise-and-tenon joint exhibits increased rigidity relative to the connector joint. Following the displacements of the points selected on the reference chair, the ones selected on the leg (points 9, 10 and 11) recorded the highest displacements in both the X and Y axes. In contrast, points 7, 13, and 14 located near the mortise-and-tenon joints on the stretcher and seat rail displayed the lowest displacement values, evidencing the high rigidity of these joints (Figure 15a,c).

Conversely, for the chair with connectors, the displacement of points along the X axis occurred oppositely compared to the reference chair, yielding negative values in this instance (Figure 15b). The highest displacement values were noted for points situated on the connector of the seat rail and the seat rail adjacent to this connector (points 4–8), whereas the lowest values originated from points aligned on the connector of the stretcher (points 9–12). This phenomenon can be explained by the tendency of the seat rail to bend under the compression load applied at the chair seat, causing the connector to rise along the Y axis while simultaneously pushing the leg outward, signaling it could disengage from the joint. This action is substantiated by the graph in Figure 15d, which illustrates the negative displacement of point 4 situated on the connector, alongside the peaks in displacements for points 7 and 8 located on the seat rail. In this case, the connector joint may be classified as elastic, allowing movement within the joint system.
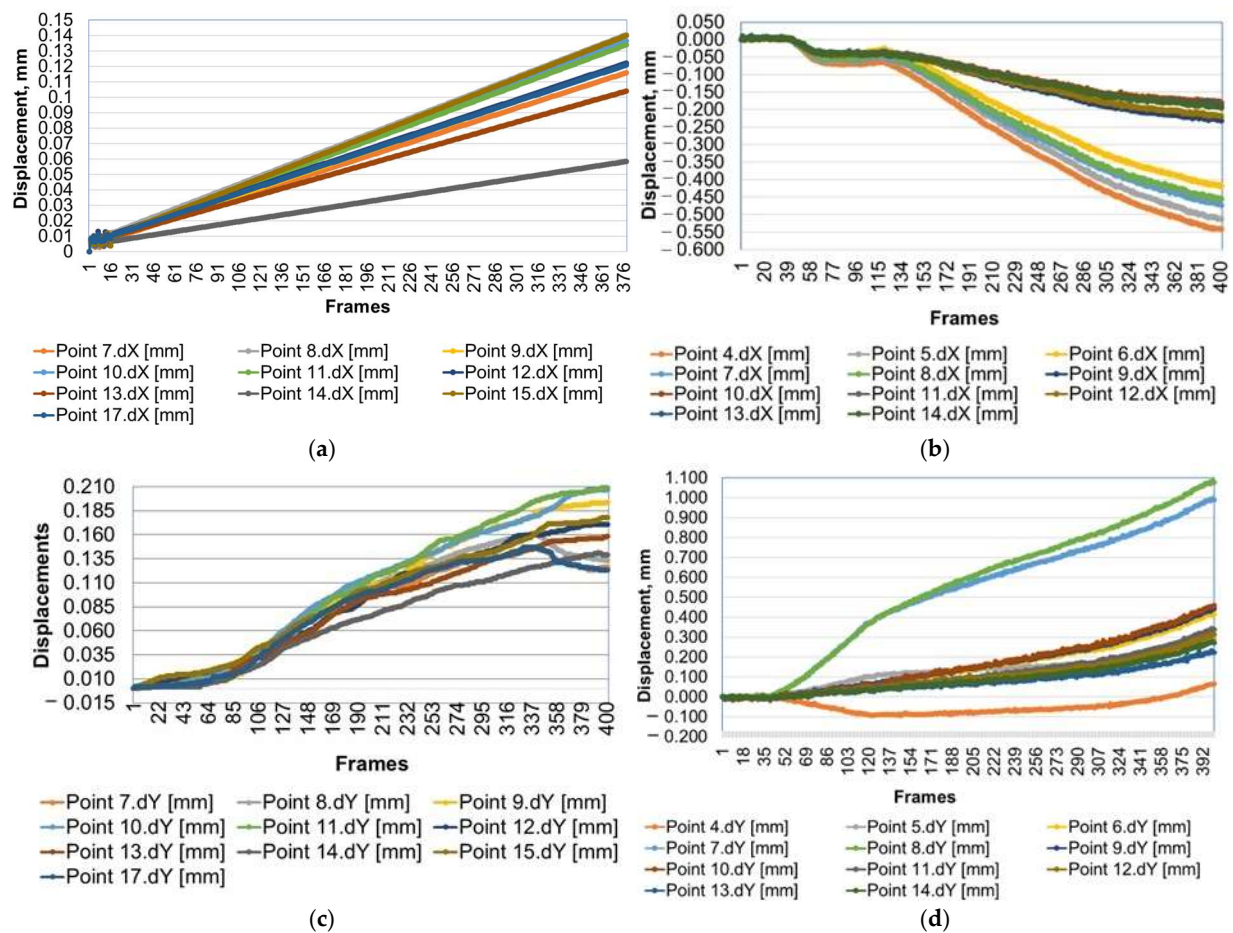
(**a**)

(**b**)

(**c**)

(**d**)

Figure 15. Displacements along X and Y axis, as resulted from DIC analysis: (**a**) points of reference chair along X axis; (**b**) points of chair with connectors along X axis; (**c**) points of reference chair along Y axis; (**d**) points of chair with connectors along Y axis.

Upon completing the optical analysis through the DIC method, both the reference chair and the chair with connectors were able to withstand loads of 19.69 kN (Figure 16a) and 14.95 kN (Figure 16b), respectively, without damaging the wooden components or connectors. As noted in another study [29], the inclusion of stretchers significantly increases of the chairs' load-bearing capacity. The presence of the four stretchers within the designed chair contributed to the high values of the loads recorded at the end of the test.
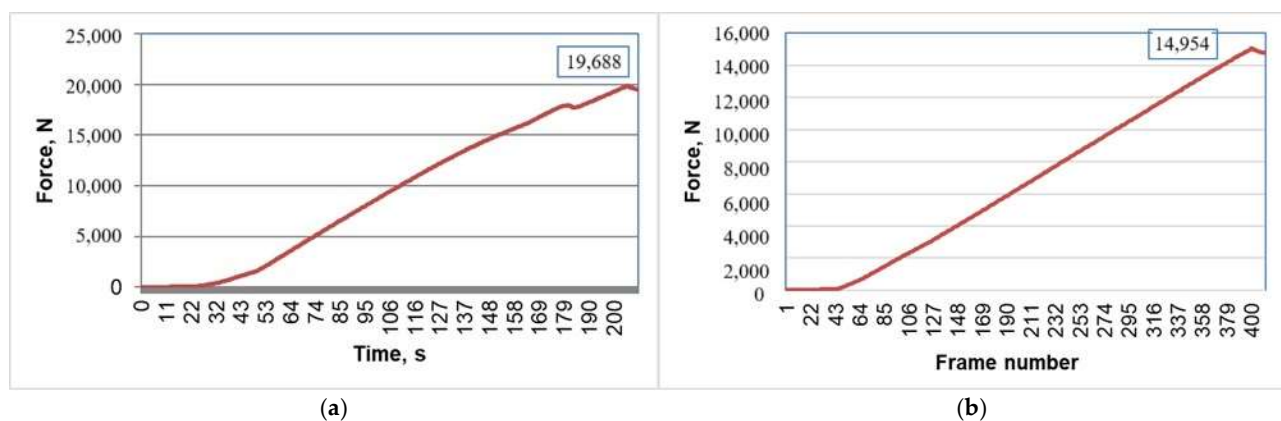

(**a**)

(**b**)

Figure 16. Load sizes corresponding to the 5 mm travel stroke during DIC analysis: (**a**) For the reference chair; (**b**) For the chair with connectors.

Another example can be found in the study [28], where a chair seat was subjected to bending test. 3D printed connectors made from Polyethylene Terephthalate (PETG) using FDM fabrication method were utilized to construct a chair capable of withstanding loads up to 7300 N. However, its structure was relatively simple, without stretchers.

The DIC optical displacement analysis results presented in this section indicate that the 3D printed connectors can effectively replace traditional mortise-and-tenon joints in chair structures while meeting equivalent performance standards, as evidenced by a load-carrying capacity exceeding 1495 kg, which far surpasses functional requirements. Future research could explore optimizing the chair and connector structures to enhance mechanical strength regarding load-carrying capacity and economic efficiency.

3.4. Static Load Tests

Static load tests for the seat and back were conducted first. The seat sustained a load of 1300 N, while the backrest supported a load of 430 N, both without damaging the wooden parts or connectors. Subsequently, a vertical seat load of 1000 N, accompanied by a horizontal force of 400 N, was centrally applied to the rear part of the seat, while a vertical seat load of 1000 N and a horizontal force of 300 N were applied centrally to the side of the seat, towards the restrained feet. Both chairs held the applied loads without failures or ruptures. It is crucial to note that the test rig utilized for this research is homologated, and the testing laboratory holds accreditation. As expected, the results of the performed tests revealed that the joint with connector offers the chair the resistance required by the standards in force. No difference was noted during and after the test between the strength of the chair with traditional joints and the chair with the 3D printed connectors.

Another attempt at using 3D printed connectors for chair construction was documented in [34]. In this instance, connectors were fabricated using FDM technology with ABS filament. The static load test applied to the chair's seat and backrest in accordance with [38] resulted in the backrest failing under load along a 3D printed layer at the connector.

This subject remains open to discovering the best solutions regarding materials and additive manufacturing methods that align with optimal design and economic efficiency.

4. Conclusions

- 3D printed connectors present a viable solution for chair construction.
- Joints with 3D-printed connectors made of PLA filament using the FFF additive manufacturing method exhibited greater strength under diagonal compression and tensile loads compared to traditional wooden mortise-and-tenon joints made from beech wood.
- FEM analysis of diagonal compression and tensile loads applied to L-type corner joints with connectors identified the susceptible zones of the connectors under maximum strain and stress.
- Experimental testing have shown that the connectors failed at the zones revealed by FEM analysis under maximum forces without damaging the wooden parts. Optical displacement analysis using the DIC method had as result higher values of the displacements for the chair with connectors compared to the reference chair, reaching values of 0.6 mm along the X axis and 1.1 mm along the Y axis under maximum vertical load on the seat of about 15 kN without failures of the chair structure.
- The reference chair exhibited uniform and consisten displacement patterns near the joints, highlighting the rigidity of the structure.
- The chair with connectors displayed varying displacement trends, attributed to the connector elasticity, which allowed movement between the wooden parts and the connectors without inflicting damage.

- Compressive loads applied to the chair seats achieved notable values of 19.6 kN for the reference chair and approximately 15 kN for the chair with connectors, without compromising their structural integrity. Both chairs withstood loads of 1300 N for the seat and 400 N for the backrest, meeting the mandatory requirements set forth by relevant standards.
- The chair with 3D-printed connectors is a reliable alternative to traditionally manufactured chair and a sustainable solution: it is an ecological option, ensures the product's disassembly, and allows for replacement to extend chair lifespan.
- The estimated cost of € 9.6 per connector can be reduced by further research, which could aim at optimizing both the chair and connector designs to align the mechanical strength of the chair with its load-carrying capacity while considering economic benefits.

References

1. Groth, C.; Kravitz, N.; Jones, P.; Graham, M.; Redmond, R. Three-Dimensional Printing Technology. *J. Clin. Orthod.* **2014**, *XLVIII*, 275–285.
2. Aydin, M. Additive Manufacturing: Is It a New Era for Furniture Production? *J. Mech. Eng. Autom.* **2015**, *5*, 338–347. [CrossRef]
3. Singh, T.; Kumar, S.; Sehgal, S. 3D printing of engineering materials: A state-of-the-art review. *Mater. Today: Proc.* **2020**, *28 Pt 3*, 1927–1931. [CrossRef]
4. Azlin, M.N.M.; Ilyas, R.A.; Zuhri, M.Y.M.; Sapuan, S.M.; Harussani, M.M.; Sharma, S.; Nordin, A.H.; Nurazzi, N.M.; Afiqah, A.N. 3D Printing and Shaping Polymers, Composites, and Nanocomposites: A Review. *Polymers* **2022**, *14*, 180. [CrossRef]
5. Jarža, L.; Čavlović, A.O.; Pervan, S.; Španić, N.; Klarić, M.; Prekrat, S. Additive Technologies and Their Applications in Furniture Design and Manufacturing. *Drv. Ind.* **2022**, *74*, 115–128. [CrossRef]
6. Sai Kalyan, M.V.D.; Kumar, H.; Nagdeve, L. Latest trends in Additive manufacturing. *IOP Conf. Ser. Mater. Sci. Eng.* **2021**, *1104*, 012020. [CrossRef]
7. Gade, S.; Vagge, S.; Rathod, M. A Review on Additive Manufacturing—Methods, Materials, and its Associated Failures. *Adv. Sci. Technol. Res. J.* **2023**, *17*, 40–63. [CrossRef] [PubMed]
8. Rouf, S.; Raina, A.; Irfan, M.; Ul Haq, M.I.; Naveed, N.; Jeganmohan, S.; Kichloo, A.F. 3D printed parts and mechanical properties: Influencing parameters, sustainability aspects, global market scenario, challenges and applications. *Adv. Ind. Eng. Polym. Res.* **2022**, *5*, 143–158. [CrossRef]
9. Shahrubudina, N.; Leea, T.; Ramlana, R. An Overview on 3D Printing Technology: Technological, Materials, and Applications. *Procedia Manuf.* **2019**, *35*, 1286–1296. [CrossRef]
10. Ranjan, R.; Kumar, D.; Kundu, M.; Moi, S. A critical review on Classification of materials used in 3D printing process. *Mater. Today Proc.* **2022**, *61*, 43–49. [CrossRef]
11. Pringle, A.; Rudnicki, M.; Pearce, J. Wood Furniture Waste–Based Recycled 3-D Printing Filament. *For. Prod. J.* **2022**, *68*, 86–95. [CrossRef]

12. Smardzewski, J.; Rzepa, B.; Kılıç, H. Mechanical Properties of Externally Invisible Furniture Joints Made of Wood-Based Composites. *BioResources* **2016**, *11*, 1224–1239. [CrossRef]

13. Magrisso, S.; Mizrahi, M.; Zoran, A. Digital Joinery for Hybrid Carpentry. In Proceedings of the 2018 CHI Conference on Human Factors in Computing Systems (CHI '18), Montreal, QC, Canada, 21–26 April 2018; Association for Computing Machinery: New York, NY, USA, 2018; pp. 1–11, Paper 167. [CrossRef]

14. Top, N.; Şahin, I.; Gökçe, H. Topology Optimization for Furniture Connection Part and Production with 3D Printer Technology. In Proceedings of the 29th International Conference on Research for Furniture Industry, Ankara, Turkey, 19–20 September 2019; pp. 671–677.

15. Saad, R. The revolution of Materials used in 3D Printing applications in Furniture & Interior Design. *Int. Des. J.* **2016**, *6*, 143–163. [CrossRef]

16. Derikvand, M.; Eckelman, C. Bending Moment Capacity of L-Shaped Mitered Frame Joints Constructed of MDF and Particleboard. *BioResources* **2015**, *10*, 5677–5690. [CrossRef]

17. Felek, S.Ö. A new Era in Furniture Production: 3D Printer. In Proceedings of the International Conference on Knowledge & Innovation in Engineering, Science &Technology, Berlin, Germany, 15–17 December 2020. Available online: www.kiconf.org (accessed on 7 November 2024).

18. Wang, C.; Zhang, C.; Zhu, Y. Reverse design and additive manufacturing of furniture protective foot covers. *BioResources* **2024**, *19*, 4670–4678. [CrossRef]

19. Demirci, S.; Diler, H.; Kasal, A.; Erdil, Y. Bending moment resistances of L-shaped furniture frame joints under tension and compression loadings. *Wood Res.* **2020**, *65*, 975–988. [CrossRef]

20. Krzyżaniak, Ł.; Smardzewski, J. Impact damage response of L-type corner joints connected with new innovative furniture fasteners in wood-based composites panels. *Compos. Struct.* **2021**, *255*, 113008. [CrossRef]

21. Petrova, B.; Jivkov, V. Application of 3D Printing Technology in Furniture Construction. *Materials* **2024**, *17*, 4848. [CrossRef]

22. Bas, S.; Denes, L.; Csiha, C. Mechanical Properties of Furniture Joints Using Loose Tenons and Connectors. *Forests* **2024**, *15*, 343. [CrossRef]

23. Podskarbi, M.; Smardzewski, J. Numerical modelling of new demountable fasteners for frame furniture. *Eng. Struct.* **2019**, *185*, 221–229. [CrossRef]

24. Chen, C.C.; Yang, W.Z.; Teng, H.M.; Liao, S.S.; Tsao, C.C. Study on the application of 3D printing to wooden furniture connectors. *J. Phys. Conf. Ser.* **2023**, *2631*, 012006. [CrossRef]

25. Yang, S.; Du, P. The Application of 3D Printing Technology in Furniture Design. *Sci. Program.* **2022**, *1*, 1960038. [CrossRef]

26. Demirel, S.; Kuvel, N.; Çava, K.; Aslan, M. The performance of 3d printed dowel with three different surface designs in furniture joints. *Turk. J. For.* **2023**, *25*, 100–106. [CrossRef]

27. Baharuldin, K.; Abdullah, M.E.Z.; Anwar, M.F.M.; Harun, M.H. Sustainable Furniture Joints: Leveraging Fused Deposition Modeling (FDM) for Eco-Friendly Design. *BIO Web Conf.* **2024**, *131*, 05015. [CrossRef]

28. Aiman, A.F.; Sanusi, H.; Haidiezul, A.H.M.; Cheong, H.Y. Design and structural analysis of 3D-printed modular furniture joints. *IOP Conf. Ser. Mater. Sci. Eng.* **2020**, *932*, 012101. [CrossRef]

29. Hitka, M.; Joščák, P.; Langová, N.; Krišťák, L.; Blašková, S. Load-carrying capacity and the size of chair joints determined for users with a higher body weight. *BioResources* **2018**, *13*, 6428–6443. [CrossRef]

30. Zacal, J.; Dostál, P.; Šustr, M.; Barboutis, I. Design and Testing of Low Cost Chair with Round Mortise and Tenon Joints. *Acta Univ. Agric. Silvic. Mendel. Brun.* **2016**, *64*, 567–572. [CrossRef]

31. Ayrilmis, N.; As, N.; Dündar, T.; Şendağ, A. Determination of Bending Moment of L-Type Corner Joints Used in Chair Production and Their Effects on Mechanical Performance of Chairs. *Mat. Int.* **2020**, *2*, 0318–0323. [CrossRef]

32. Krzyźaniak, Ł.; Kuşkun, T.; Kasal, A.; Smardzewski, J. Analysis of the Internal Mounting Forces and Strength of Newly Designed Fastener to Joints Wood and Wood-Based Panels. *Materials* **2021**, *14*, 7119. [CrossRef] [PubMed]

33. Nicolau, A.; Pop, M.A.; Coşereanu, C. 3D Printing Application in Wood Furniture Components Assembling. *Materials* **2022**, *15*, 2907. [CrossRef] [PubMed]

34. Hajdarevic, S.; Kitek Kuzman, M.; Obucina, M.; Vratuša, S.; Kušar, T.; Kariž, M. Strength and stiffness of 3D-printed connectors compared with the wooden mortise and tenon joints for chairs. *Wood Mater. Sci. Eng.* **2022**, *18*, 870–883. [CrossRef]

35. Janíková, N.; Šimek, M.; Kořený, A.; Gaff, M.; Hlavatý, J. Comparative study on the bending moment capacity and stiffness of innovative and traditional furniture corner joints. *Wood Mater. Sci. Eng.* **2024**, 1–9. [CrossRef]

36. Giannopoulos, G.I.; Georgantzinos, S.K. A Tunable Metamaterial Joint for Mechanical Shock Applications Inspired by Carbon Nanotubes. *Appl. Sci.* **2021**, *11*, 11139. [CrossRef]

37. Kasal, A.; Smardzewski, J.; Kuşkun, T.; Güray, E. Analyses of L-Type Corner Joints Connected with Auxetic Dowels for Case Furniture. *Materials* **2023**, *16*, 4547. [CrossRef] [PubMed]

38. *EN 1728*; Furniture—Seating—Test Methods for the Determination of Strength and Durability. European Committee for Standardization: Brussels, Belgium, 2012.

39. Nicolau, A.; Pop, M.A.; Georgescu, S.V.; Coșereanu, C. Application of Additive Manufacturing Technology for Chair Parts Connections. *Appl. Sci.* **2023**, *13*, 12044. [CrossRef]

Article

A Stratified Characterization of Surface Quality of Beech Processed by Profile Milling

Luminița-Maria Brenci and Lidia Gurău *

Faculty of Furniture Design and Wood Engineering, Transilvania University of Brasov, B-dul Eroilor 29, 500036 Brasov, Romania; brenlu@unitbv.ro
* Correspondence: lidiagurau@unitbv.ro

Abstract: The evaluation of surface quality after milling still represents a challenge due to the stratified structure of wood. In this paper, the surface quality of beech wood obtained by profile milling was analyzed differentiating between tool marks, fuzzy grain, and accidental surface gaps overlapped onto the deep anatomical cavities. The samples were milled at two rotation speeds, 3308 rpm (n_1) and 6594 rpm (n_2), and two feed speeds of 6.53 m/min (v_{f1}) and 23.74 m/min (v_{f2}). After the samples were cut, approximately 600 m of beech wood were further processed before measuring the surface quality again. The surface waviness measured by Wa increased more than double when the feed speed increased from v_{f1} to v_{f2}. Rk increased with the feed speed (with the feed per tooth, f_z, for a constant n, respectively) for n_2 by a significant 57%. An increase in the rotation speed from n_1 to n_2 has reduced Rk, but the effect was not significant. The processing quality, Rk, measured at different depths did not differ statistically, in spite of the local differences in the cutting speed. The moment of measuring the surface roughness, such as immediately after sharpening or after a working period, influenced the surface quality. After the tool processed 600 m of beech material, the surface quality improved by 30%. The statistical analysis showed that the most important factor affecting the surface quality was the feed speed (implicitly f_z, for constant n and number of cutters).

Keywords: beech wood; profiled milling; surface quality; roughness; waviness; tool marks; raised fibers; anatomical cavities

1. Introduction

The assessment of the surface quality following wood processing is very important in order to establish the impact of various processing parameters combinations [1–3]. The optimization of milling operations by considering the surface quality will reduce the amount of further sanding and can contribute to a reduction in the finishing costs. Therefore, it is important to find a combination of processing parameters suitable for a minimum surface roughness. Furthermore, the surface roughness of wood is very complex and represents a superposition of morphological features, such as waviness, raised fibers, tool marks, wood anatomical voids, as well as possible processing surface defects, such as material detached from the surface [4–9]. In this respect, the most used roughness parameters such as Ra or Rz are not enough to give a complete picture of the origin of the different irregularities present on a processed surface.

According to the studies performed by Gawroński [10], Sutcu [11], and Koc et al. [12], the cutting parameters affect the surface roughness of beech wood. The study performed by Gürgen et al. [13] on *Pinus sylvestris* after CNC milling showed that the surface roughness decreased with increasing rotation speed and decreased with decreasing the feed speed for all machining parameters. The evaluation of surface roughness for different depths of cut revealed that the maximum surface roughness value was registered for the highest depth of cut. Jiang et al. [14] have found that the cutting speed has not significantly influenced the surface roughness of walnut processed by straight-tooth milling, but the depth of cut

was significant. Costes and Larricq [15] stated that the quality of beech, when routed on a CNC machine, improves with an increase in the cutting speed. Piernik et al. [16] concluded that an increase in the feed speed and the chip thickness increases the surface roughness of beech milled by CNC, while the cutting speed had no effect on surface roughness, but just on the cutting power.

Most researchers have used Ra and Rz [11–13,17–19] to assess the quality of wood after milling, but these parameters do not consider the nature of wood irregularities and include the inherent wood anatomical gaps in the evaluation. The roughness parameters Ra and Rz decreased with a lower feed rate and a higher spindle speed in a study by Kok et al. [12] on beech (*Fagus orientalis*), Ayous (*Triplochiton Scleroxylon*), and MDF processed by CNC. Similarly, in another study of Rabiei and Yaghoubi [18], the surface roughness evaluated by Ra decreased with increasing the spindle speed and decreasing the feed rate as well as the depth of cut when beech wood was milled on a CNC machine. However, these two parameters employed by the researchers are not sufficient to correctly interpret the quality of wood and wood-based surfaces, which means that they must be evaluated together with other roughness parameters [7].

Kilic et al. [20] evaluated the effect of milling on the surface roughness of beech and aspen wood. On the basis of statistical analysis, they found no significant difference between the surface roughness determined on the tangential and radial surfaces. They observed that a number of roughness parameters, such as Ra, Rz, Rk, Rpk, and Rvk roughness are useful, to be used together, to evaluate the surface quality of wood.

Magoss [21] studied the influence of the wear of the cutting edges on the surface roughness for several species (oak, larch, beech, and pine wood) processed on CNC milling machines. The experimental results showed that the Rk parameter, which measures the core roughness and is the closest approximation of the tool marks, may be an important indicator of the tool edge wear. In the case of beech wood, the Rk value after milling with a blunt tool was approximately twice the value of milling with a sharp tool.

Gurău et al. [22] investigated the surface roughness of larch wood (*Larix decidua* Mill.) cut through by laser and CNC routing at different feed speeds, by parameters Ra, Rp, Rv, Rsk, Wa, Pa, Pt and the Abbot-curve parameters, Rk, Rpk, and Rvk, in order to find a more comprehensive understanding of the effect of processing on wood surface topography.

Learning from the above studies, it can be concluded that a complex surface such as that of wood requires a larger set of roughness parameters capable of differentiating between the various layers of irregularities present on a processed surface.

Therefore, this study uses a comprehensive set of standard parameters for surface characterization, such as Ra, Rv, Rsk, and Wa [23], and the Abbot curve parameters, Rk, Rpk, Rvk, A1, and A2 [24]. These parameters allow the analysis of surface quality on stratified levels of irregularities differentiating between tool marks, fuzzy grain, and accidental surface gaps overlapping onto the deep anatomical cavities of the wood, such as pores from earlywood. Such analysis will provide a more in-depth understanding and quantification of the tool interaction with the wood material and will help for a reliable selection of the most appropriate processing parameters. Furthermore, in a calculation of those parameters, a robust Gaussian regression filter tested and found suitable for wood was used in order to avoid the bias caused by the simple Gaussian filter contained in the majority of measuring instruments [9,25].

2. Materials and Methods

2.1. Wood Samples

Beech wood (*Fagus sylvatica* L.), with a mean density of 745 kg/m^3 and 7% moisture content, was processed by profiled milling in two processing passes in order to obtain profiles with 16 mm maximum depth (Figure 1).
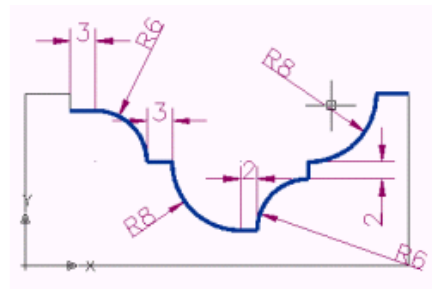
Figure 1. The samples' profile.

The milling was carried out on 1000 mm × 50 mm × 20 mm strips, along the grain direction, by using various cutting parameter combinations, which will be further detailed.

2.2. Processing by Profiled Milling

A vertical milling machine was used to process the beech strips with a profile cutterhead made of C45 steel [26], with 4 new and sharp cutters, made of C120 steel [27] (Figure 2). The dimensions and geometry of the cutting tool and the cutters are presented in Tables 1 and 2, respectively.

Figure 2. The profile cutterhead used in the milling process.

Table 1. Geometric parameters of the cutterhead.

D (mm)	B (mm)	d (mm)	Clearance Angle α (°)	Rake Angle γ (°)
178	40	30	25	18

Table 2. The dimensions of the cutters.

Length (mm)	Width (mm)	Thickness (mm)	Height (mm)
58	40	7.2	16

The profiled milling was performed with two rotation speeds, such as 3308 rpm (n_1) and 6594 rpm (n_2), and two feed speeds, 6.53 m/min (v_{f1}) and 23.74 m/min (v_{f2}), respectively. The cutting parameters combinations were n_1-v_{f1}, n_1-v_{f2}, n_2-v_{f1}, and n_2-v_{f2}. This provided a first set of samples. A second set of samples was prepared by using the same cutting parameter combinations, but after the tool milled 600 m of beech wood. The intention was to observe the impact of the cutting distance, as it further shows the influence of the cutting tool wear [28] on the surface quality, when the same working variables are used.

The strips of each cutting case combination were further shortened to 60 mm × 50 mm × 20 mm specimens available for inspection. The samples were labeled to identify their cutting parameters combination. Three samples were selected from the first set of data (sharpened tool) and two samples from the second set of data (after tool has cut 600 m), for each rotation speed and feed speed combination (n_1-v_{f1}, n_1-v_{f2}, n_2-v_{f1}, and n_2-v_{f2}), for

both tool conditions: sharpened and after 600 m cutting distance. This meant 20 processed samples were available for the surface quality measurement.

Table 3 summarizes the machining parameters used during the milling experiments with indication of the local cutting speed and feed per tooth values in 4 regions/profile depths, marked in Figure 3, and in which the surface quality was further checked.

Table 3. The machining parameters.

Tool Rotation Speed n (rpm)		Feed Rate v_f (m/min)		Measured Point	Profile Depth (mm)	Cutting Speed v_c (m/s)	Feed per Tooth f_z (mm/Tooth)	
n_1	3308	v_{f1}	6.53	Point 1	2	28.39	f_{z11}	0.49
		v_{f2}	23.74				f_{z12}	1.79
n_2	6594	v_{f1}	6.53			56.59	f_{z21}	0.25
		v_{f2}	23.74				f_{z22}	0.90
n_1	3308	v_{f1}	6.53	Point 2	8	29.43	f_{z11}	0.49
		v_{f2}	23.74				f_{z12}	1.79
n_2	6594	v_{f1}	6.53			58.66	f_{z21}	0.25
		v_{f2}	23.74				f_{z22}	0.90
n_1	3308	v_{f1}	6.53	Point 3	16	30.82	f_{z11}	0.49
		v_{f2}	23.74				f_{z12}	1.79
n_2	6594	v_{f1}	6.53			61.43	f_{z21}	0.25
		v_{f2}	23.74				f_{z22}	0.90
n_1	3308	v_{f1}	6.53	Point 4	10	29.78	f_{z11}	0.49
		v_{f2}	23.74				f_{z12}	1.79
n_2	6594	v_{f1}	6.53			59.35	f_{z21}	0.25
		v_{f2}	23.74				f_{z22}	0.90
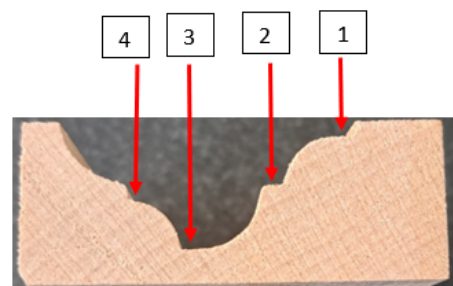
Figure 3. Sample cross-section with four zones of linear measurement.

From Table 3, note that the f_z is directly influenced by the feed speed v_f for a constant n and for the same number of cutters (a single type of tool was used in this research). Another notable observation is that the cutting speed, v_c, differs very slightly with the local tool diameter (depth of cut, respectively), for a given rotation speed, n. Therefore, the interpretation of the results will be mainly focused on variations in v_f, respectively, n.

2.3. Roughness Measurement

The surface morphology of the beech samples was measured with MarSurf XT20 equipment manufactured by MAHR Gottingen GMBH, Göttingen, Germany (Figure 4a). It used an MFW 250 scanning head with a tracing arm in the range of ±750 μm, and a stylus with 2 μm tip radius and 90° tip angle, as shown in Figure 4b.

(**a**)   (**b**)

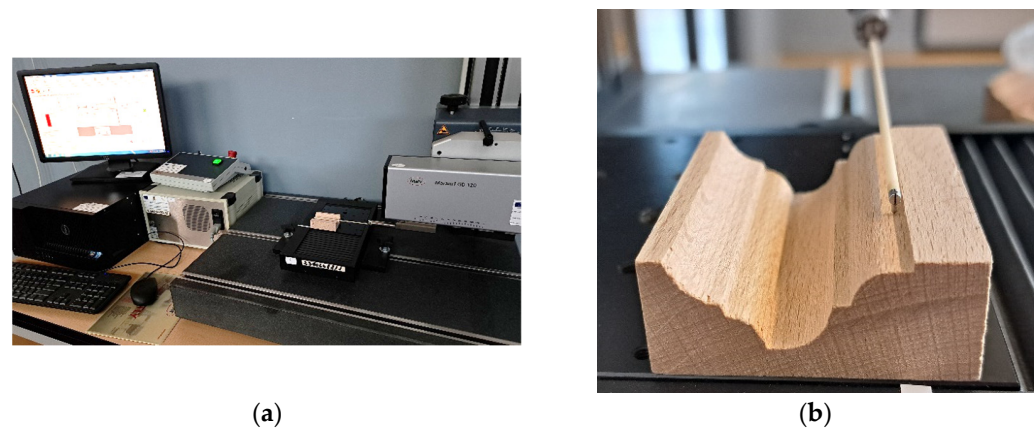**Figure 4.** Measurements of surface morphology. (**a**) MarSurf XT20 profilometer and data acquisition; (**b**) linear surface scanning by stylus (zone 1 in Figure 3).

For measuring the beech milled profiles, only the straight zones were considered, as marked by red arrows in Figure 3. The depth for the marked points were 2 mm for point 1, 8 mm for point 2, 16 mm for point 3, and 10 mm for point 4. This decision was drawn from the requirement that the stylus remains normal in relation to the processed surface. Further studies will take into consideration the possibility of measuring round profiles as well, by using adequate supports. Four profiles, 30 mm long, were measured from the numbered zones (Figure 3) along the milling direction with a speed of 0.5 mm/s, a scanning force of 0.7 mN, and a resolution of 5 μm. This meant 4 profiles were taken from each sample. In case of the first set of samples, there were 12 profiles for one parameters combination. For all 4 parameter combinations (ex. $n_1 - v_{f1}$; $n_1 - v_{f2}$; etc.), the total number of measurements reached 48. Similarly, for the second set of samples, there were 32 measurements.

Data acquired were further processed with MARWIN XR20 software provided together with the measuring equipment. Data evaluation began with removing any unwanted form errors, followed by a procedure of filtering with a robust Gaussian regression filter, contained in ISO/TS 16610-31 [25]. This filter was tested and it was recommended for wood surfaces because it reduces the distortions associated with deep grouped valleys in the profiles and it is more reliable in comparison with a simple Gaussian filter, common in most measuring instruments [9,29–32]. In this way, the measured data were separated by filtering the wavelengths of irregularities in waviness profiles and roughness profiles, corresponding to W parameters for the longest wavelengths, while R parameters evaluated the shortest wavelengths. The cut-off length used for filtering was 2.5 mm, recommended for wood surfaces [30,32]. After filtering, a number of useful parameters were calculated, such as Ra (arithmetic mean deviation of the roughness profile), Rv (the largest absolute profile valley depth), Rsk (skewness of the profile), and Wa (arithmetic mean deviation of the waviness profile) according to ISO 4287 [23]. In addition, Rk (the core roughness depth), Rpk (the reduced peak height), Rvk (the reduced valley depth), A1 (peak area in μm^2/mm), and A2 (valley area in μm^2/mm) were employed according to ISO 13565-2 [24].

The parameters from ISO 13565-2 [24] are particularly useful to characterize the stratified structure of a processed surface. Compared with other parameters, Rk depends the least on the wood anatomical structure and measures the height of the core roughness, the region defined by the highest concentration of data points in a measured profile, which excludes isolated peaks and valleys. For a milling process, it can be an approximation of the tool marks left on wood. Instead, Rpk is defined by the isolated peaks, which for a wood species, according to Westkämper and Riegel [4], can be considered an evaluation of wood raised grain and fuzziness of the surface. The fuzziness is caused by groups of fibers that are attached to the surface at only one end. Rvk is defined by isolated valleys, which in the case of wood can be caused by accidental material pull-out during processing and/or deep anatomical cell lumens.

Another test was conducted to monitor the surface quality after the tool has milled 600 m of the same profile and species, in order to see which is the effect of the tool condition.

Surface profiles were measured in the same way as in the case when the tool was sharpened, but on two specimens. This meant there were 8 measured profiles for analysis of each of the 4 parameters combination, making a total of 32 measurements. The surface morphology measurement and evaluation followed the same steps as for the sharpened tool.

2.4. Stereo-Microscopy Analysis

A stereo-microscope NIKON SMZ 18-LOT2 (Nikon Instruments, Melville, NY, USA) was used for the microscopic investigations of the profile milled beech samples. The straight zone 1 from Figure 2 was in focus. In order to better observe the occurrence of the raised fibers and possible surface defects such as material detachment, the samples were tilted by approximately $45°$.

2.5. Statistical Analysis

The surface quality parameters were tested for their significance for all processing combinations (rotation speed–feed speed). The software used was an IBM SPSS Statistics version 23.

3. Results and Discussion

The mean values and standard deviation for parameters evaluated in this analysis are contained in Table 4.

Table 4. The mean values roughness parameters (in μm). Standard deviation is presented in parentheses.

Tool Condition	Processing Parameters	Ra	Rk	Rpk	Rvk	Rv	Rsk	Rpk/Rvk	Rk+Rpk+Rvk	A1/A2	Wa
sharpened	$3308-6.53$ (n_1-v_{f1})	5.74 (0.94)	12.10 (1.70)	6.81 (2.19)	18.43 (5.30)	46.02 (13.25)	−2.02 (0.58)	0.37 (0.41)	37.34 (6.62)	0.18 (0.22)	6.79 (1.18)
	$3308-23.74$ (n_1-v_{f2})	7.4 (0.88)	14.99 (3.41)	16.51 (6.21)	20.77 (3.24)	46.98 (5.12)	−0.71 (0.91)	0.79 (1.92)	52.27 (5.48)	0.54 (1.11)	14.81 (2.20)
	$6594-6.53$ (n_2-v_{f1})	4.83 (0.67)	10.19 (1.94)	7.54 (2.30)	11.64 (2.52)	30,40 (7.52)	−1.08 (1.00)	0.64 (0.91)	29.37 (4.49)	0.48 (0.79)	5.38 (0.90)
	$6594-23.74$ (n_2-v_{f2})	6.59 (0.82)	16.02 (2.38)	10,68 (3.35)	16.39 (3.29)	42.29 (10.06)	−1.01 (0.89)	0.65 (1.02)	43.09 (5.32)	0.39 (0.50)	11.83 (2.99)
after 600 m milling length	$3308-6.53$ (n_1-v_{f1})	4.46 (0.63)	10.15 (1.38)	6.24 (1.83)	12.27 (3.17)	30.43 (8.02)	−1.34 (0.97)	0.51 (0.61)	28.66 (3.71)	0.28 (0.34)	10.28 (1.85)
	$3308-23.74$ (n_1-v_{f2})	4.93 (0.63)	12.26 (2.09)	8.67 (4.00)	13.54 (2.71)	35.37 (4.93)	−1.15 (0.87)	0.64 (1.48)	34.46 (5.33)	0.42 (1.58)	12.35 (5.65)
	$6594-6.53$ (n_2-v_{f1})	5.03 (1.62)	10.93 (2.11)	9.71 (4.72)	14.24 (8.02)	36.09 (14.57)	−0.99 (1.49)	0.68 (0.59)	34.89 (11.90)	0.47 (0.45)	10.44 (2.31)
	$6594-23.74$ (n_2-v_{f2})	4.97 (0.70)	11.43 (1.15)	7.12 (3.60)	14.42 (3.67)	36.38 (9.79)	−1.50 (0.88)	0.49 (0.98)	32.96 (4.66)	0.29 (0.59)	10.47 (4.20)

The surface morphology was first studied by considering the largest wavelengths irregularities produced by milling on the surface, namely the surface waviness. This can

be observed directly by comparing primary profiles, which contain both roughness and waviness (Figure 5), selected for the four groups/combinations of rotation speeds and feed speeds.
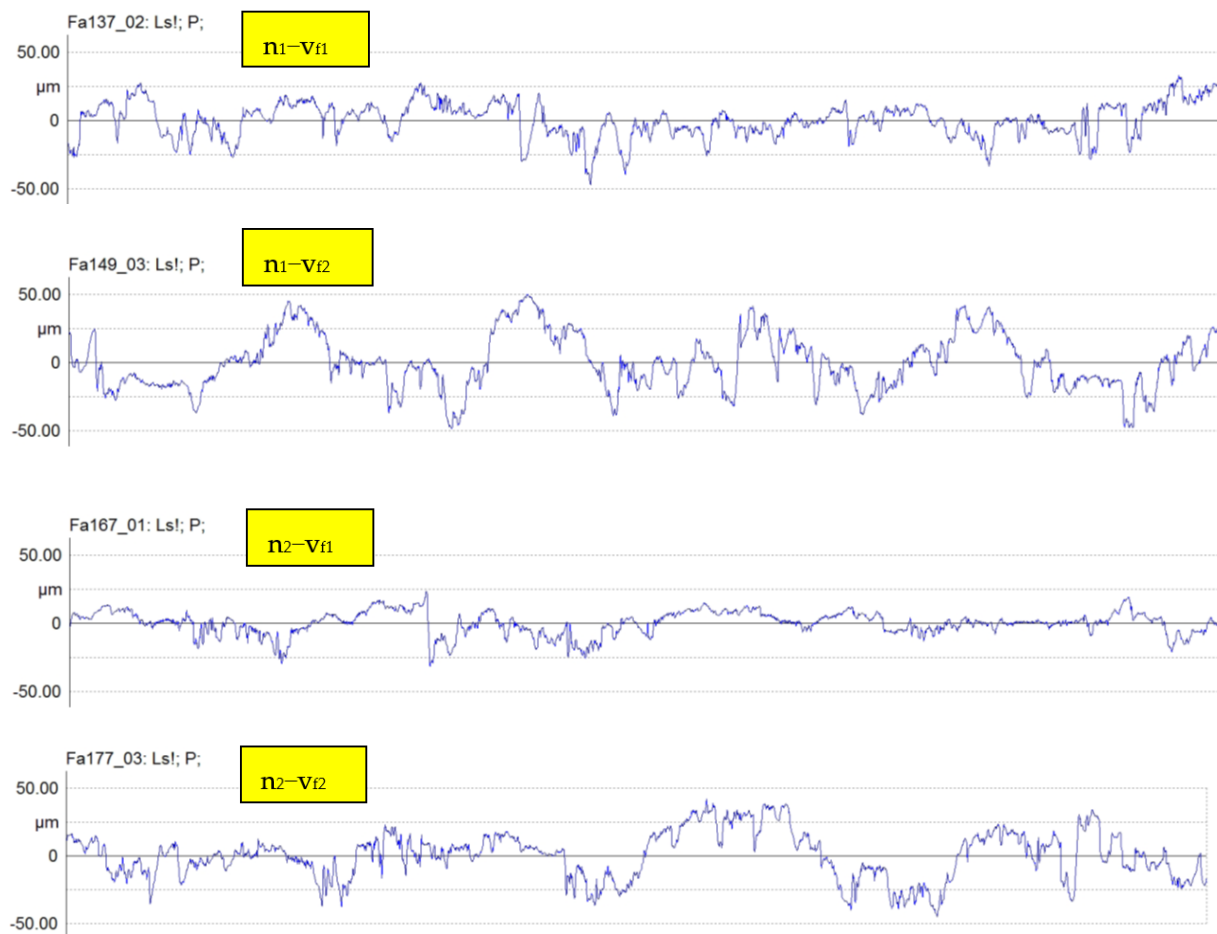

Figure 5. Primary profiles containing waviness and roughness together, for the four combinations of rotation speeds and feed speeds, when the tool was sharpened.

It can be seen from Figure 5 that an increase in the feed speed from v_{f1} to v_{f2} (3.6 times) has increased surface waviness, in the primary profiles, for both rotation speeds. The profiles are considerably wavier, containing large undulations, which can be spotted as patterns repeated at almost regular distance (approximately 6 mm), in Figure 5 and by a waviness profile overlapped on the ridged beech surface, in Figure 6. This observation is in agreement with the values of Wa parameter, which doubled in the case of both rotation speeds (Figure 7).

This result was statistically significant for $p < 0.05$ (test ANOVA, followed by Dunnett T3 multiple comparisons) (Tables 5 and 6). An explanation may be that an increase in the feed speed increases tool vibration, which leaves deeper waves in the surface. When the rotation speed almost doubled from n_1 to n_2, a decrease of 20% in surface waviness was measured, but this reduction had no statistical support (Table 6).

Table 5. Dependent variable Wa—Test between groups' effects.

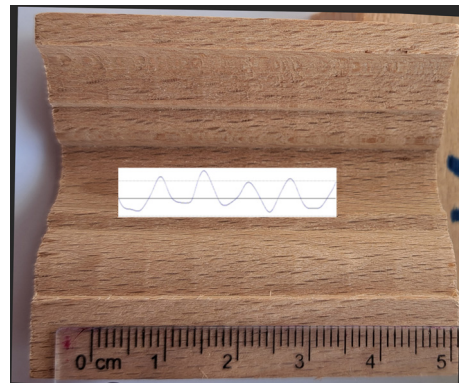| Source	Sum of Squares	df	Mean Square	F	Sig
Groups	693.397	3	231.132	51.894	0.000

Figure 6. Beech surface processed by n_1-v_{f2} parameters combination with a waviness profile overlapped.
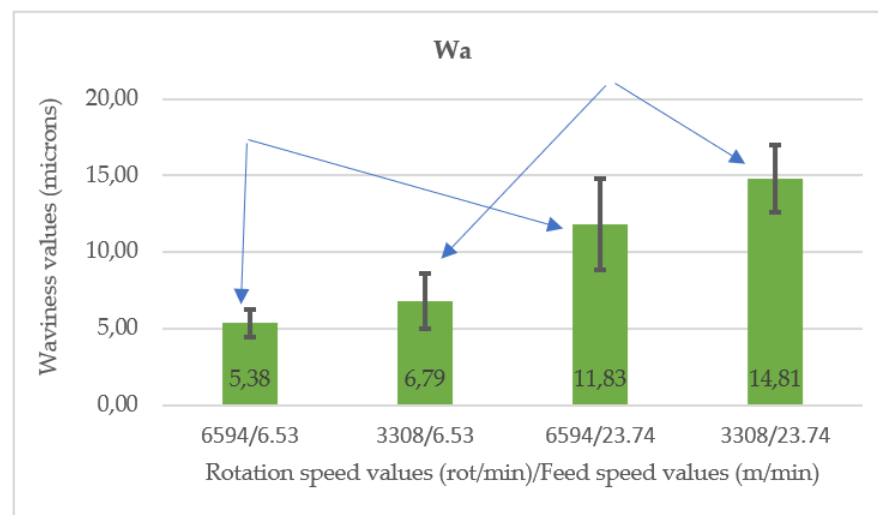

Figure 7. The variation of waviness parameter, Wa, with combinations of the rotation speed with the feed speed. With blue arrows, pair means that differ statistically are marked.

Table 6. Dependent variable Wa− Dunnet T3 Post Hoc Test for multiple comparisons between groups rotation speed–feed speed.

Groups		Mean Difference	Std. Error	Sig
n_1-v_{f1}	n_1-v_{f2}	−8.017 [1]	0.82	0.000
	n_2-v_{f1}	1.415	0.58	0.141
n_2-v_{f2}	n_1-v_{f2}	−2.98	1.07	0.063
	n_2-v_{f1}	6.45 [1]	0.90	0.000

[1] The error term is Mean Square (Error) = 4.454. The mean difference is significant at the 0.05 level.

Figure 8 displays the roughness profiles measured for each pair rotation speed–feed speed. Isolated raised fibers are marked with red ellipses, while the yellow ellipses indicate isolated deep valleys. From definition, the core roughness of the roughness profiles does not contain the isolated deep valleys associated with the deep pores from earlywood or isolated detached wood material, nor the isolated raised fibers or surface fuzziness. Instead, it can be viewed as the density of data above and below the zero line. Therefore, it appears that an increase in the feed speed (respectively, in f_z, for a constant n and z) is causing more dispersion above and below the zero line (Figure 6), which translated in an increase in Rk. These visual observations are confirmed by the measured Rk values, which increased, when the feed speed (respectively, f_z) increased 3.6 times, by 24% for n_1 and by a significant

57% for n_2 (from 10.19 μm to 16.02 μm) (Figure 9). The conclusion is that an increase in the feed speed (respectively, in f_z, for a constant n and z) increases the core roughness Rk and is more pronounced when the rotation speed increases as well (Figure 9).

Figure 8. Roughness profiles of each group combination, rotation speed–feed speed. Raised fibers are marked with red; deep isolated valleys are marked with yellow ellipses.

Figure 9. The variation of the core roughness parameter, Rk, with combinations of the rotation speed with the feed speed. With blue arrows, pair means that differ statistically are marked.

Since Rk is the parameter that approximates the best the tool marks (processing roughness), a supplementary statistical test was performed with the direct cutting parameters v_c–f_z on local profile depths D_1–D_4 (as in Table 3), when the rotation speed n was kept constant and the variable was the feed speed v_f (consequently, f_z). The conclusion from

Table 7 was the same, respectively, for a constant n; the increase in the feed speed vf (respectively, f_z) was statistically significant for Rk, even at different cutting levels (D_1-D_4) and mostly for the n_2 rotation speed.

Table 7. Pairwise comparison of parameters combinations (v_c/f_z) for Rk and the level of significance for an increase in v_f (f_z, respectively).

Parameters Combination 1 (v_c/f_z)	Parameters Combination 2 (v_c/f_z)	*p*-Value	Significance of an Increase in v_f, and in f_z, Respectively, at Different Profile Depths (Having Very Slight Changes in v_c in between Them)
$n_2-v_{f1}-D_1$ 56.59/0.25	$n_2-v_{f2}-D_1$ 56.59/0.90	0.00	Increase of v_f significant for n_2
$n_2-v_{f1}-D_2$ 58.66/0.25	$n_2-v_{f2}-D_2$ 58.66/0.90	0.015	Increase of v_f significant for n_2
$n_2-v_{f1}-D_3$ 61.43/0.25	$n_2-v_{f2}-D_4$ 59.35/0.90	0.019	Increase of v_f significant for n_2
$n_2-v_{f1}-D_4$ 59.35/0.25	$n_2-vf_2-D_4$ 59.35/0.90	0.002	Increase of v_f significant for n_2
$n_1-v_{f1}-D_1$ 28.39/0.49	$n_1-v_{f2}-D_1$ 28.39/1.79	0.229	Increase of v_f not significant for n_1
$n_1-v_{f1}-D_2$ 29.43/0.49	$n_1-v_{f2}-D_2$ 29.43/1.79	0.275	Increase of v_f not significant for n_1
$n_1-v_{f1}-D_3$ 30.82/0.49	$n_1-v_{f2}-D_3$ 30.82/1.79	0.02	Increase of v_f significant for n_1
$n_1-v_{f1}-D_4$ 29.78/0.49	$n_1-v_{f2}-D_4$ 29.78/1.79	0.03	Increase of v_f significant for n_1

Also, a visual examination of the roughness profiles in Figure 8 shows a reduction in Rk when the feed speed was kept constant while the rotation speed increased. For example, an increase in the rotation speed from n_1 to n_2 decreased Rk by approximately 16% for the vf1 feed speed. However, the effect on Rk of changing the rotation speed was not overall significant. This result was also confirmed by testing the local significance for the local profile depths (D_1-D_4) in Table 8.

Similar trends to Rk were observed in the values of Ra parameter (Figure 10), for which an increase in the feed speed has caused a significant increase no matter which rotation speed was used.
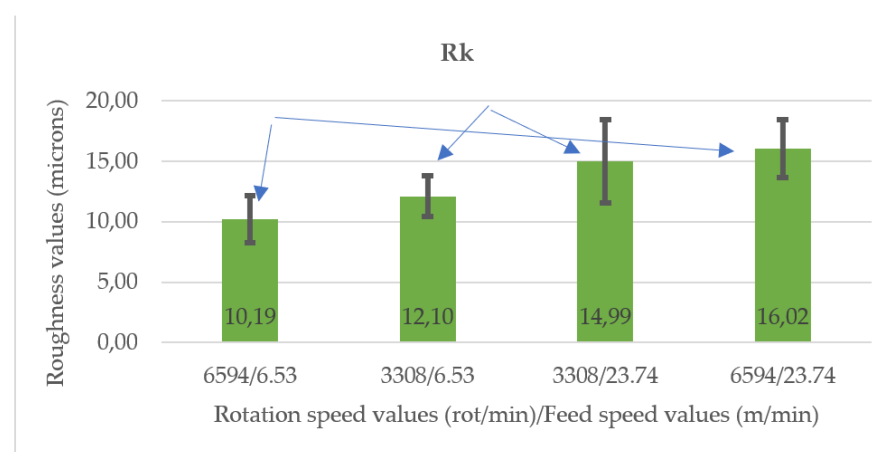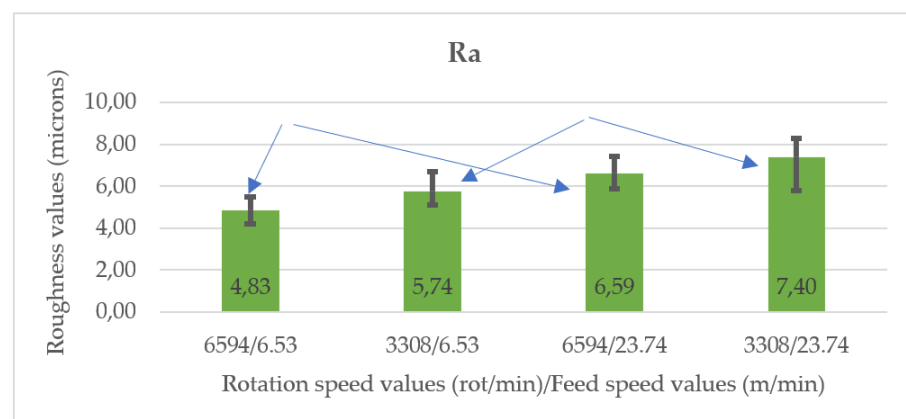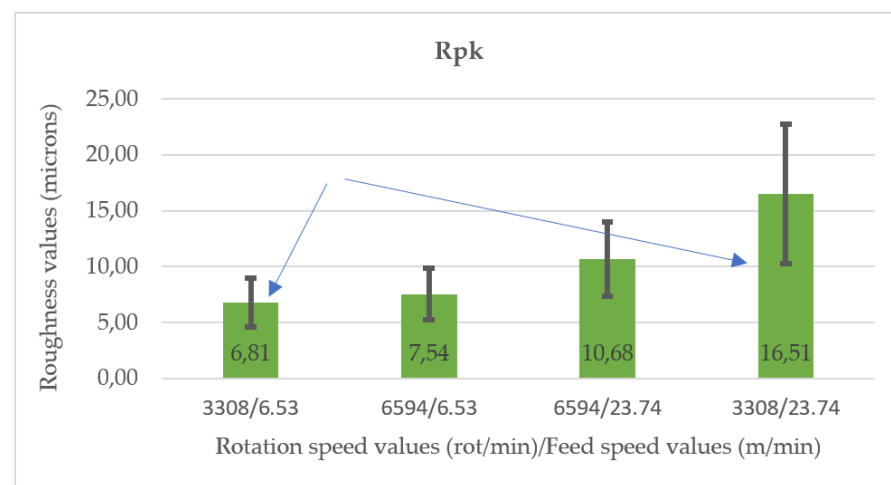

Figure 10. The variation of the mean roughness parameter, Ra, with combinations of the rotation speed with the feed speed. With blue arrows, pair means that differ statistically are marked.

Table 8. Pairwise comparison of parameters combinations (vc/fz) for Rk and the level of significance for an increase in n (and local v_c, respectively).

Parameters Combination 1 (v_c/f_z)	Parameters Combination 2 (v_c/f_z)	*p*-Value	Significance of an Increase in n, When v_f (f_z) is Kept the Same
$n_1-v_{f1}-D_1$ 28.39/0.49	$n_2-v_{f1}-D_1$ 56.59/0.25	0.03	Increase of n significant for v_{f1}
$n_1-v_{f1}-D_2$ 29.43/0.49	$n_2-v_{f1}-D_2$ 58.66/0.25	0.05	Increase of n significant for v_{f1}
$n_1-v_{f1}-D_3$ 30.82/0.49	$n_2-v_{f1}-D_3$ 61.43/0.25	0.752	Increase of n not significant for v_{f1}
$n_1-v_{f1}-D_4$ 29.78/0.49	$n_2-v_{f1}-D_4$ 59.35/0.25	0.792	Increase of n not significant for v_{f1}
$n_1-v_{f2}-D_1$ 28.39/1.79	$n_2-v_{f2}-D_1$ 56.59/0.90	0.001	Increase of n significant for v_{f2}
$n_1-v_{f2}-D_2$ 29.43/1.79	$n_2-v_{f2}-D_2$ 58.66/0.90	0.559	Increase of n not significant for v_{f2}
$n_1-v_{f2}-D_3$ 30.82/1.79	$n_2-v_{f2}-D_3$ 61.43/0.90	0.598	Increase of n not significant for v_{f2}
$n_1-v_{f2}-D_4$ 29.78/1.79	$n_2-v_{f2}-D_4$ 59.35/0.90	0.934	Increase of n not significant for v_{f2}

Another morphological aspect studied in relation to the processing parameters was the raised fiber. For the rotation speed n_1 = 3308 rot/min, the increase more than 3.6 times in the feed speed from v_{f1} = 6.53 m/min to v_{f2} = 23.74 m/min has caused Rpk to increase 2.4 times (from 6.81 µm to 16.51 µm) which was statistically significant (ANOVA followed by Dunnett T3). This means, that an increase in the feed speed is raising the wood fiber (Figure 11). This increase can also be observed from the microscopical images in Figure 12c,d, illustrating a detail of zone 1, zone depicted with red arrows in Figure 12a,b. The raised fibers also appear in the roughness profiles, where they are encircled in red (Figure 8). For the rotation speed n_2, although Rpk increased by 42% when the high feed speed was used and some raised fibers are visible in the roughness profiles, this had no statistical support. The increase in the rotation speed does not produce any significant effect regarding fuzziness or raised fiber.

Figure 11. The variation of the reduced peak heights parameter, Rpk, with combinations of the rotation speed with the feed speed. With blue arrows, pair means that differ statistically are marked.
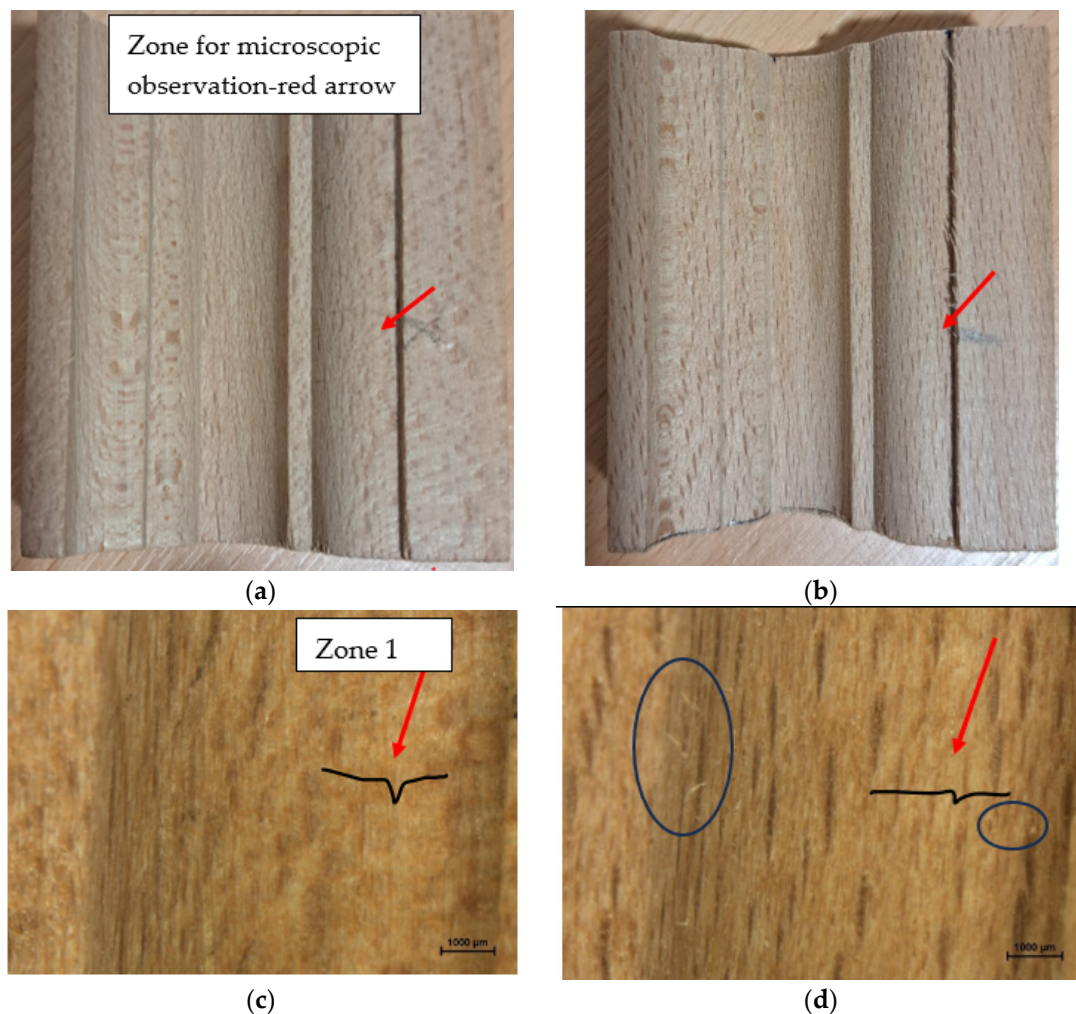
Figure 12. Images of beech milled profiles (**a**,**b**) and microscopic details (**c**,**d**) at magnification 22.5×. (**a**,**c**) Processing by n_1-v_{f1}; (**b**,**d**) processing by n_1-v_{f2}. Examples of raised fibers are marked with blue ellipses.

Wood is a stratified heterogeneous material and apart from outliers located above the core roughness it also has outliers located below the core roughness. They can be seen as surface gaps, exemplified by yellow ellipses in Figure 8. Their origin can be deep anatomical cavities going below the marks caused by the cutting tool, but can also include accidental surface gaps when wood material is detached leaving unwanted voids in the material. Both of them will depend on the type and proportion of anatomical cells encountered by the cutting plane. The weakest zones should be those from the earlywood and those coinciding with the wood rays (radial surfaces). The processed samples did not consider a certain top wood surface orientation, which varied from radial to tangential and combinations like semi-radial and semi-tangential. For the above-mentioned reasons, the parameter Rv, which measures the deepest valley in the profile, had a high standard deviation (Table 4) in comparison with the core roughness Rk, depending on the local wood anatomy. Furthermore, Rv had values in the range of earlywood pores cavities reported for beech (8–45–85 μm) [33] (p. 107) with the majority of them around the mean values given in the literature (45 μm), while some of the deepest valleys were below 70 μm. These observations can lead to the assumption that the isolated deep valleys seen in the roughness profiles, in most cases, belong to inherent wood anatomical cavities and are not processing defects. An exception was made in the situations in which the cutter encountered radial surfaces and this caused detachment of some ray tissues, as can be seen in Figure 13b, which significantly increased Rv (Figure 14), with approximately 40%, for the feed speed

v_{f2} in comparison with v_{f1} (Table 4, Figure 14). Wood pores went beyond the marks left by the tool on the wood, and this is observed by a negative Rsk and a subunitary ratio Rpk/Rvk. The same is true for the ratio A1/A2, which indicates a larger share of the area of the valleys compared to the area of the peaks (Table 4). An increase in the rotation speed from n1 to n2 has significantly reduced Rv (Figure 14) with approximately 33% for the feed speed v_{f1} (ANOVA and Dunnett T3).
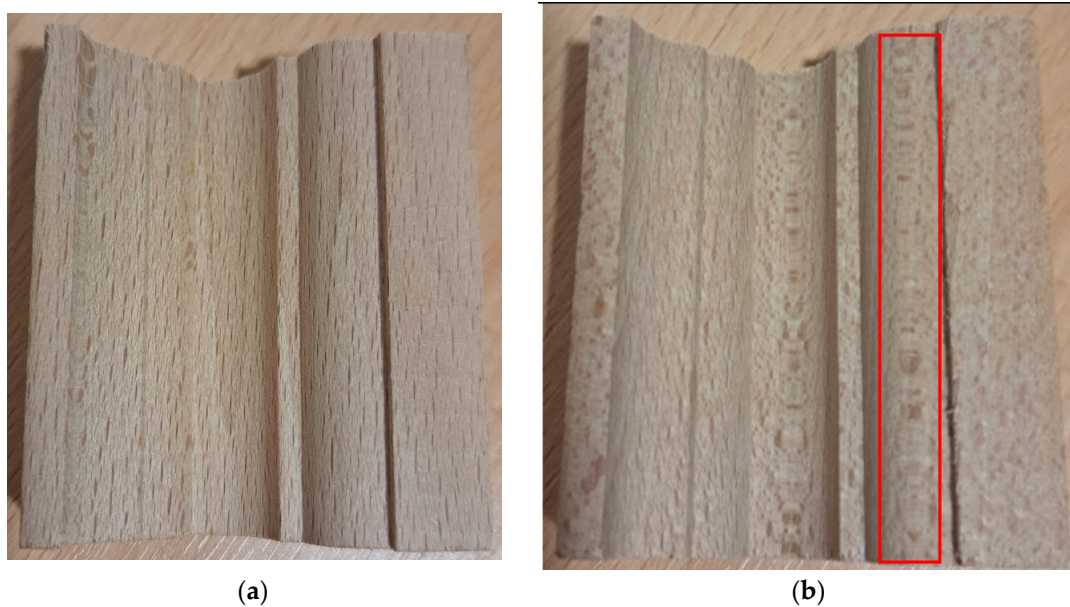

(**a**) (**b**)

Figure 13. Samples processed by milling with n_2 rotation speed. (**a**) Feed speed v_{f1}; (**b**) feed speed v_{f2}. The red rectangle exemplifies a radially cut surface which contains detached ray tissues.
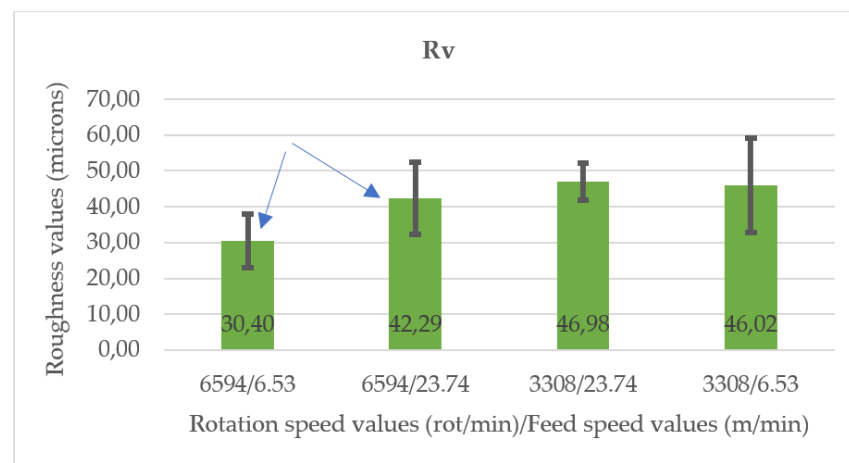

Figure 14. The variation of the deepest valley, Rv, with combinations of the rotation speed with the feed speed. With blue arrows, pair means that differ statistically are marked.

Interpretation of surface quality in the case of wood is complex. For optimization of the cutting quality and selection of the best working parameters, the tool marks are of interest. From this perspective, Rk parameter is representative and has shown it is significantly influenced by the feed speed and was less affected by the selection of the rotation speed. The surface fuzziness and accidental material detachment will be species-dependent and of wood local anatomy. However, their effect on the overall surface quality cannot be neglected. A statistical analysis ANOVA followed by Dunnett T3 test performed on the cumulative effect of processing plus the raised fiber (Rk+Rpk) has led to the same

conclusions as in the case of Rk alone: the feed speed was the most important factor affecting the surface quality by milling. Although the surface quality has improved by increasing the rotation speed, its effect was not significant (Tables 9 and 10). The best surface quality was obtained when combining n_2 (6594 rot/min) with v_{f1} (6.53 m/min) and the worst when the rotation speed n_1 (3308 rot/min) was combined with the high feed speed v_{f2} (23.74 m/min), as shown in Figure 15.

Table 9. Dependent variable Rk+Rpk—Test between groups' effects.

Source	Sum of Squares	df	Mean Square	F	Sig
Groups	1541.92	3	513.97	30.7	0.000

Table 10. Dependent variable Rk+Rpk—Dunnet T3 Post Hoc Test for multiple comparisons between groups' rotation speed–feed speed.

Group		Mean Difference	Std. Error	Sig
n_1-v_{f1}	n_1-v_{f2}	−12.59 [1]	513.97	0.000
	n_2-v_{f1}	1.17	1.26	0.921
n_2-v_{f2}	n_1-v_{f2}	−4.80	1.99	0.134
	n_2-v_{f1}	8.96 [1]	1.55	0.000

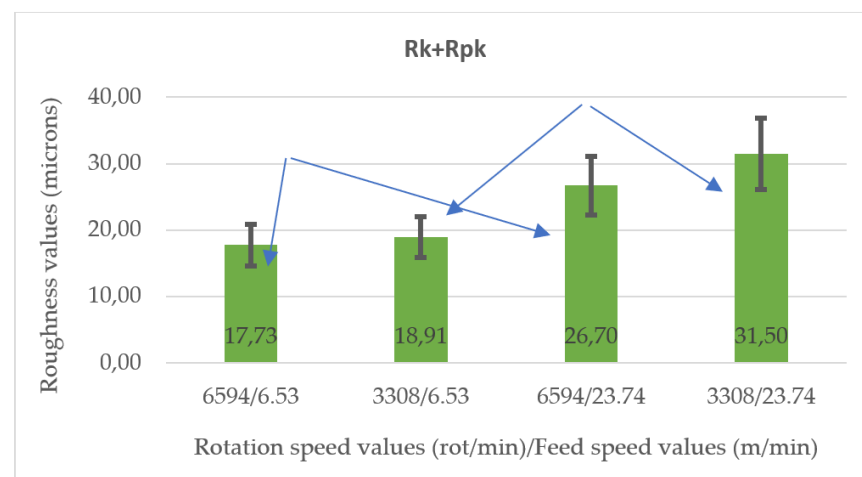[1] The error term is Mean Square (Error) = 16.738. The mean difference is significant at the 0.05 level.

Figure 15. The variation of the cumulative parameter Rk+Rpk with combinations of the rotation speed with the feed speed. With blue arrows, pair means that differ statistically are marked.

When the surface isolated gaps were included, together with the tool marks and the raised fiber, not only the feed speed was a significant factor, but also the rotation speed, the surface quality improving for the highest rotation speed n_2 in comparison with n_1 (Figure 16, Tables 11 and 12).

Another test was conducted to monitor the surface quality after the tool has milled 600 m of the same profile and species, in order to see which is the effect of the tool condition.

Comparative profiles when the tool was sharpened and profiles after the tool milled 600 m are displayed in Figure 17.

Table 11. Dependent variable Rk+Rpk+Rvk—Test between groups' effects.

Source	Sum of Squares	df	Mean Square	F	Sig
Groups	3350.23	3	1116.74	36.49	0.000

Table 12. Dependent variable Rk+Rpk+Rvk—Dunnet T3 Post Hoc Test for multiple comparisons between groups' rotation speed–feed speed.

Group		Mean Difference	Std. Error	Sig
n_1-v_{f1}	n_1-v_{f2}	-14.93 [1]	2.28	0.000
	n_2-v_{f1}	7.97 [1]	2.30	0.015
n_2-v_{f2}	n_1-v_{f2}	-9.18 [1]	2.20	0.002
	n_2-v_{f1}	13.72 [1]	2.00	0.000

[1] The error term is Mean Square (Error) = 30.6. The mean difference is significant at the 0.05 level.
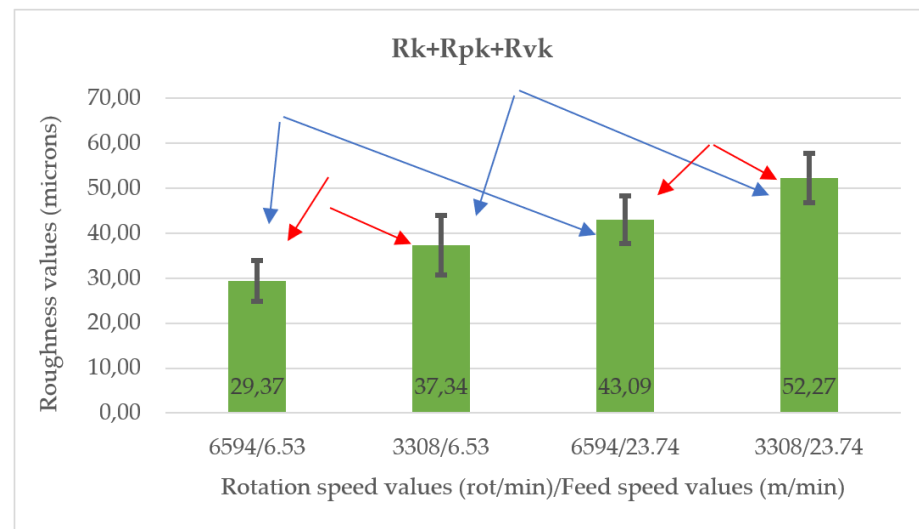
Figure 16. The variation of the cumulative parameter Rk+Rpk+Rvk with combinations of the rotation speed with the feed speed. With blue and red arrows, pair means that differ statistically are marked.

From the profiles presented in Figure 17, it can be observed that after using the tool by continuous processing for 600 m cutting distance, the surface quality improved (Figure 18). The surface improvement was also sensed by touch, but it is visible also in Figure 18c,d taken as example.

A statistical comparison of the composed parameter Rk+Rpk+Rvk was performed in order to obtain a global evaluation of the surface improvement. The ANOVA test followed by a Post Hoc test Games–Howell (groups had unequal number of measurements) indicated a surface improvement after the tool was working 600 m, which was significant when the high feed speed was used (v_{f2} = 23.74 m/min). The improvement was quantified to 30% roughness decrease for the rotation speed n_2 and to 34% when the rotation speed n1 was used.

This result is an indication that the surface quality is not only dependent on the wood material and the processing parameters, but also on the tool working load, which is expected to vary with the milling parameters as well as with the species. It will be interesting, in further tests, to explore the surface quality from the moment the tool is sharpened to the moment when it is worn out, together with microscopic observations regarding the state of the tool cutting edge. This may help establish an ideal working interval for the tool before it needs resharpening or replacement. A worn tool will increase the surface roughness and the occurrence of surface defects, such as pull-out material and fiber detachment.

Finally, another analysis addressed the surface quality at the four profile depths (from Figure 3), in order to see if the variation of the local cutting speed, v_c, implicitly of the feed per tooth, f_z, has a significant impact on the processing roughness quantified by the Rk parameter. The analysis was made for all combinations of rotation speed–feed speed. An

ANOVA single factor test was performed, with a level of significance $p < 0.05$. The results are presented in Table 13.
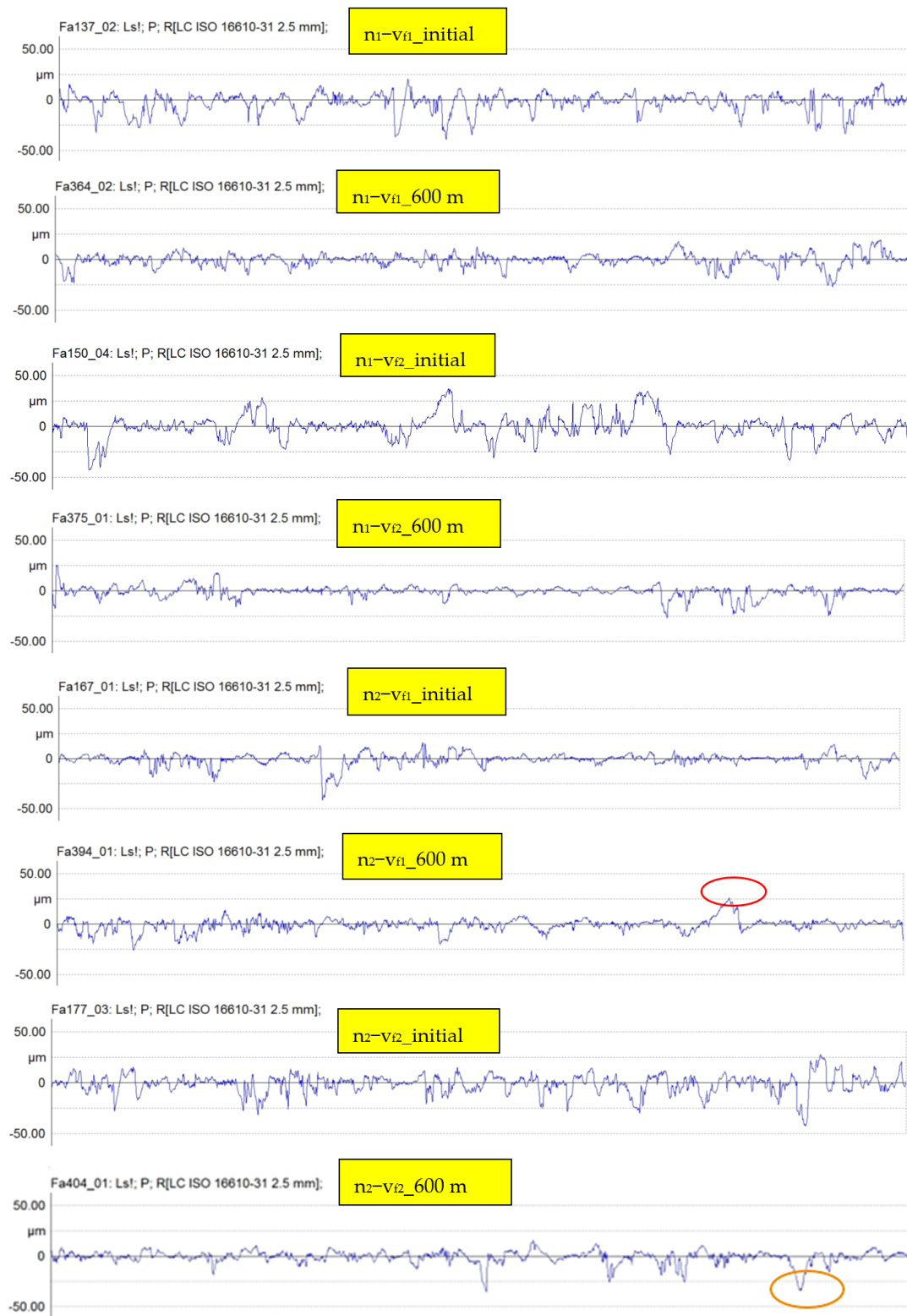

Figure 17. Roughness profiles of each group combination, rotation speed–feed speed comparing the effect of tool condition (when new and sharpened and after 600 m cutting distance). Raised fibers are marked with red; deep isolated valleys are marked with yellow ellipse.
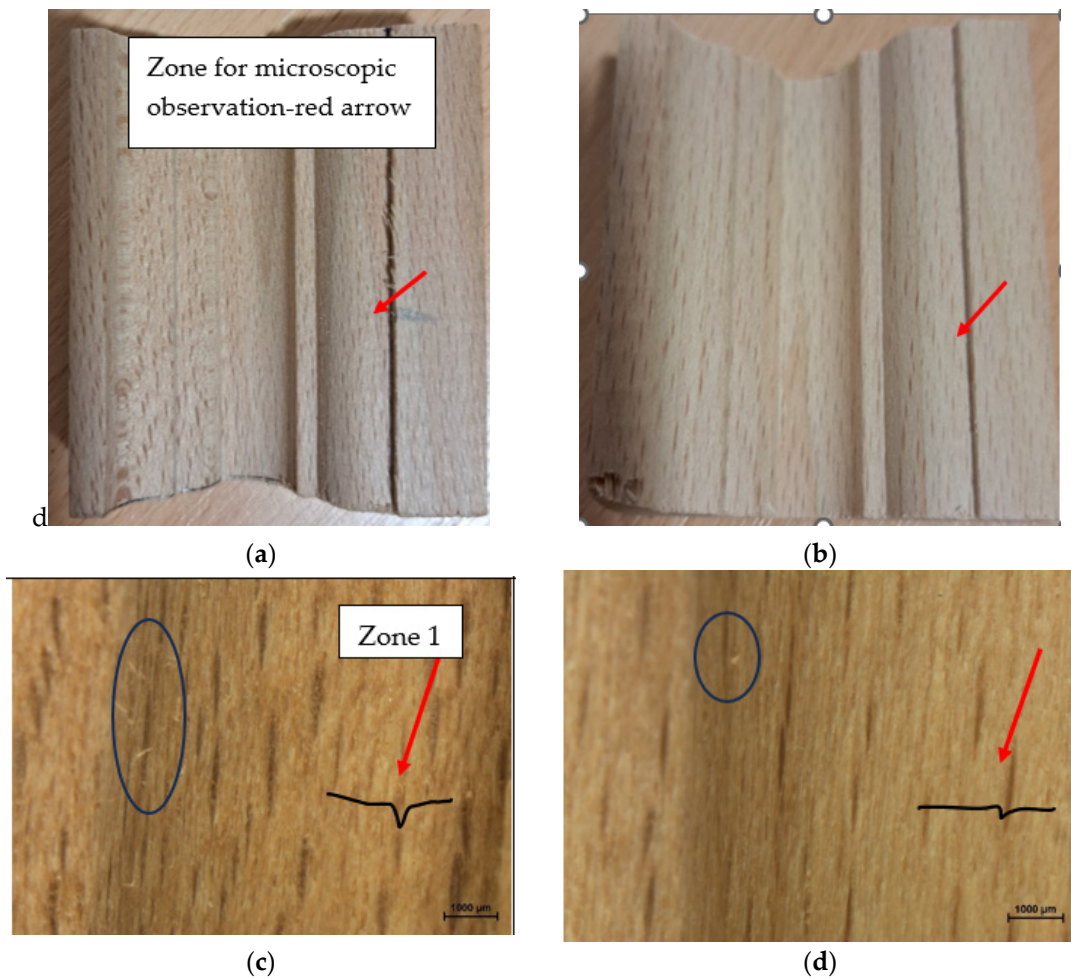
Figure 18. Images of beech milled profiles (**a**,**b**) and microscopic details (**c**,**d**) at magnification 22.5×. (**a**,**c**) Processing by n_1-v_{f2}, sharpened tool; (**b**,**d**) processing by n_1-v_{f2} after 600 m profile milling. Raised fibers are encircled with blue.

Table 13. Rk mean values at the four measured profile depths and the analysis of their statistical difference. Standard deviation in parentheses.

Parameters Combination	*p*-Value	Depth 1	Depth 2	Depth 3	Depth 4	Overall Mean
n_1-v_{f1}	0.04	13.84 (0.05) A	12.83 (1.67) AB	11.05 (1.61) B	10.69 (0.77) B	12.10 (1.70)
n_1-v_{f2}	0.21	11.64 (0.48) A	14.82 (1.52) A	17.02 (4.70) A	16.49 (3.59) A	14.99 (3.41)
n_2-v_{f1}	0.51	9.77 (3.12) A	9.17 (1.21) A	11.62 (0.94) A	10.21 (1.93) A	10.19 (1.94)
n_2-v_{f2}	0.20	17.91 (1.43) A	13.76 (1.66) A	16.06 (2.29) A	16.34 (2.84) A	16.02 (2.38)

Note: Values on the same row with the same letter do not differ statistically.

From Table 13, it can be concluded that the processing quality measured at different depths does not differ statistically, in spite of the local differences in the cutting speed.

There are different opinions in the literature regarding the effect of the cutting speed during machining processes. Some researchers found that the cutting speed has no effect on the surface quality, while others found that the cutting speed has a slight effect depending on process conditions [15].

The results regarding the effect of milling parameters on the wood surface quality are not surprising and are expected, but in comparison with other studies from the literature bring a novel approach to the evaluation of the surface quality, regarding wood as a stratified material. A stratified analysis of surface roughness parameters can not only clarify the surface complex morphology, but it is helpful to determine the contribution of processing parameters to the overall surface quality and their significance.

4. Conclusions

This study has shown that the surface quality should be analyzed on stratified levels of irregularities differentiating between, waviness, tool marks, fuzzy grain, and accidental surface gaps overlapped onto the deep anatomical cavities of the wood, such as pores from earlywood. This is because the milling quality will be dependent not only on the processing parameters and tool characteristics, but also on the wood species and its anatomical structure.

The interpretation of the results was focused on variations in v_f, respectively n, since f_z is directly influenced by the feed speed v_f, for a constant n and for the same number of cutters (a single type of tool was used in this research), while the cutting speed, v_c, differs very slightly with the local tool diameter (depth of cut, respectively), for a given rotation speed, n.

An increase in the feed speed, v_f, increases tool vibration, which leaves deeper waves in the surface. The surface waviness measured by Wa increased more than double when the feed speed increased approximately 3.6 times, from v_{f1} = 6.53 m/min, to v_{f2} = 23.74 m/min. Increasing the rotation speed from n_1 to n_2 (double) has decreased Wa with 20%, but without statistical support.

An increase in the feed speed increases the toolmarks approximated by Rk which are more pronounced as the rotation speed becomes higher. Rk increased with the feed speed (respectively, f_z for a constant n and number of cutters) for n_2 = 6594 rot/min by a significant 57%. An increase in the rotation speed from n_1 to n_2 has reduced Rk, but the effect was not significant. For example, an increase in the rotation speed from n_1 to n_2 decreased Rk by approximately 16% for the v_{f1} feed speed. Similar behavior was noticed for the Ra parameter. The processing quality (Rk) measured at different depths did not differ statistically, in spite of the local differences in the cutting speed.

An increase in the feed speed raises the wood fiber. Therefore, the Rpk parameter increased 2.4 times when the feed speed increased 3.6 times. The increase in the rotation speed does not produce any significant effect regarding fuzziness or raised fiber.

Wood pores were deeper than the marks left by the tool on the wood and their effect on surface quality was disregarded in the above conclusions. However, some gaps deeper than the core roughness and caused by material detachment were noticed when the milling encountered radial surfaces, thus affecting the ray tissues. This did not change the conclusion that the smoothest beech surface is obtained when the smallest feed speed (6.53 m/min) is used. However, by including the surface gaps in the analysis by referring to the parameter Rk+Rpk+Rvk, it attributed a significance to the rotation speed as well, such as the higher rotation speed (6594 rot/min) also contributing to the surface quality improvement.

The processing quality measured at different depths does not differ statistically, in spite of the local differences in the cutting speed.

The statistical analysis helped us to understand the hierarchy of influence factors and their significance. In this respect, the most important factor affecting the surface quality was the feed speed.

The moment of measuring the surface roughness, such as immediately after sharpening or after a working period, influences the result of the surface quality. Measurements

of surface quality after the tool processed 600 m of beech material improved the surface quality by 30%.

In further work, such stratified analysis will provide a more in-depth understanding and quantification of the tool interaction with the wood material and will help the selection of the most appropriate processing parameters as a function of the tool and species variables.

References

1. Thoma, H.; Peri, L.; Lato, E. Evaluation of Wood Surface Roughness Depending on Species Characteristics. Maderas. *Cienc. Tecnol.* **2015**, *17*, 285–292. [CrossRef]
2. Hazir, E.; Koc, K.H. Optimization of wood surface machining parameters in CNC routers: Response surface methodology (RSM) approach. *Int. J. Sci. Res. Eng. Technol.* **2016**, *5*, 494–501.
3. Hazir, E.; Koc, K.H. Optimization of wood machining parameters in CNC routers: Taguchi orthogonal array based simulated angling algorithm. *Maderas Cienc. Tecnol.* **2019**, *21*, 493–510. [CrossRef]
4. Westkämper, E.; Riegel, A. Qualittskriterien fur Geschlieffene Massivholzoberflchen. *Holz Roh Werkst.* **1993**, *51*, 121–125. [CrossRef]
5. Krisch, J.; Csiha, C. Analysing wood surface roughness using an S3P Perthometer and computer based data processing. In Proceedings of the XIII Sesja Naukowa Badania dla Meblarstwa, Poznan, Poland, 26 November 1999.
6. Magoss, E.; Sitkei, G. Influence of wood structure on the surface roughness at milling operations. In Proceedings of the 4th ICWSF, Missenden Abbey, UK, 14–16 July 1999.
7. Gurău, L. The Roughness of Sanded Wood Surfaces. Ph.D. Thesis, Forest Products Research Centre, Buckinghamshire Chilterns University College, Brunel University, London, UK, 2004.
8. Thibaut, B.; Denaud, L.; Collet, R.; Marchal, R.; Beauchêne, J.; Mothe, F.; Méausoone, P.J.; Martin, P.; Larricq, P.; Eyma, F. Wood machining with a focus on French research in the last 50 years. *Ann. For. Sci.* **2016**, *73*, 163–184. [CrossRef]
9. Gurău, L.; Irle, M. Surface roughness evaluation methods for wood products: A review. *Curr. For. Rep.* **2017**, *3*, 119–131. [CrossRef]
10. Gawronski, T. Optimisation of CNC routing operations of wooden furniture parts. *Int. J. Adv. Manuf. Technol.* **2013**, *67*, 2259–2267. [CrossRef]
11. Sutcu, A. Investigation of parameters affecting surfaces roughness in CNC Routing operation on Wooden EGP. *Bioresources* **2013**, *8*, 795–805.
12. Koc, K.H.; Erdinler, E.S.; Hazir, E.; Öztürk, E. Effect of CNC application parameters on wooden surface quality. *Measurement* **2017**, *107*, 12–18. [CrossRef]
13. Gürgen, A.; Çakmak, A.; Yldiz, S.; Malkoçoğlu, A. Optimization of CNC operating parameters to minimize surface roughness of pinus sylvestris using integrated artificial neural network and genetic algorithm. *Maderas Cienc. Tecnol.* **2022**, *24*, 5. [CrossRef]
14. Jiang, S.; Buck, D.; Tang, Q.; Guan, J.; Wu, Z.; Guo, X.; Zhu, Z.; Wang, X. Cutting Force and Surface Roughness during Straight-Tooth Milling of Walnut Wood. *Forests* **2022**, *13*, 2126. [CrossRef]
15. Costes, J.P.; Larricq, P. Towards high cutting speed in wood milling. *Ann. For. Sci.* **2002**, *59*, 857–865. [CrossRef]
16. Piernik, M.; Pinkowski, G.; Krauss, A. Effect of chip thickness, wood cross-sections, and cutting speed on surface roughness and cutting power during up-milling of beech wood. *BioResources* **2023**, *18*, 6784–6801. [CrossRef]
17. Pakzad, S.; Pedrammehr, S.; Hejazian, M. A Study on the Beech Wood Machining Parameters Optimization Using Response Surface Methodology. *Axioms* **2023**, *12*, 39. [CrossRef]

18. Rabiei, F.; Yaghoubi, S. A comprehensive investigation on the influences of optimal CNC wood machining variables on surface quality and process time using GMDH neural network and beest optimization algorithm. *Mater. Today Commun.* **2023**, *36*, 106482. [CrossRef]

19. Zhu, Z.; Jin, D.; Wu, Z.; Xu, W.; Yu, Y.; Guo, X.; Wang, X. Assessment of Surface Roughness in Milling of Beech Using a Response Surface Methodology and an Adaptive Network-Based Fuzzy Inference System. *Machines* **2022**, *10*, 567. [CrossRef]

20. Kilic, M.; Hiziroglu, S.; Burdurlu, E. Effect of machining on surface roughness of wood. *Build. Environ.* **2006**, *41*, 1074–1078. [CrossRef]

21. Magoss, E. General regularities of wood surfaces roughness. *Acta Silv. Lignaria Hung.* **2008**, *4*, 81–93.

22. Gurău, L.; Coşereanu, C.; Paiu, L. Comparative Surface Quality of Larch (*Larix decidua* Mill.) Fretwork Patterns Cut through by CNC Routing and by Laser. *Appl. Sci.* **2021**, *11*, 6875. [CrossRef]

23. *ISO 4287*; Geometrical Product Specifications (GPS)—Surface Texture—Profile Method—Terms, Definitions and Surface Texture Parameters. International Organization for Standardization: Geneva, Switzerland, 2009.

24. *ISO 13565-2*; Geometrical Product Specifications (GPS)—Surface Texture: Profile Method; Surfaces Having Stratified Functional Properties. Part 2: Height Characterisation Using the Linear Material Ratio Curve. International Organization for Standardization: Geneva, Switzerland, 1998.

25. *ISO/TS 16610-31*; Geometrical Product Specification (GPS)—Filtration—Part 31: Robust Profile Filters: Gaussian Regression Filters. International Standards Organisation: Geneva, Switzerland, 2010.

26. *EN ISO 683-1*; Heat-Treatable Steels, Alloy Steels and Free-Cutting Steels. Part 1: Non-Alloy Steels for Quenching and Tempering. International Organization for Standardization: Geneva, Switzerland, 2016.

27. *EN ISO 4957*; Tool Steel. International Organization for Standardization: Geneva, Switzerland, 2018.

28. Rolleri, A.; Burgos, F.; Aguilera, A. Surface Roughness and Wettability Variation: The effect of Cutting Distance during Milling of Pinus Radiata Wood. *Drv. Ind.* **2016**, *67*, 223–228. [CrossRef]

29. Fujiwara, Y.; Fujii, Y.; Sawada, Y.; Okumura, S. Assessment of wood surface roughness: A comparison between tactile roughness and three-dimensional parameters derived using a robust gaussian regression filter. *J. Wood Sci.* **2004**, *50*, 35–40. [CrossRef]

30. Gurău, L.; Mansfield-Williams, H.; Irle, M. Filtering the Roughness of a Sanded Wood Surface. *Holz Roh Werkst.* **2006**, *64*, 363–371. [CrossRef]

31. Piratelli-Filho, A.; Sternadt, G.H.; Arencibia, R.V. Removing deep valleys in roughness measurement of soft and natural materials with mathematical filtering. *Ciência Eng.* **2012**, *21*, 29–34. [CrossRef]

32. Tan, P.L.; Sharif, S.; Sudin, I. Roughness models for sanded wood surfaces. *Wood Sci. Technol.* **2012**, *46*, 129–142. [CrossRef]

33. Wagenführ, R. *Holzatlas*, 5th ed.; Fachbuchverlag: Leipzig, Germany, 2000; p. 707.

Article

Comparative Study on Wood CNC Routing Methods for Transposing a Traditional Motif from Romanian Textile Heritage into Furniture Decoration

Antonela Lungu [ID], Mihai Ispas, Luminiţa-Maria Brenci, Sergiu Răcăşan and Camelia Coşereanu *

Faculty of Furniture Design and Wood Engineering, Transilvania University of Brasov, B-dul Eroilor, nr. 29, 500036 Brasov, Romania; antonela.petrascu@unitbv.ro (A.L.); ispas_m@unitbv.ro (M.I); brenlu@unitbv.ro (L.-M.B.); sergiu.racasan@unitbv.ro (S.R.)
* Correspondence: cboieriu@unitbv.ro

Abstract: This paper presents experimental research on the Computer Numerical Control (CNC) routing of a traditional motif collected from Ţara Bârsei (Transylvania region) using two methods, namely, engraving (Engrave) and carving (V-Carve). The analysis of the CNC router processes includes the calculation of the path lengths, an assessment of the processing time and wood mass loss, and an evaluation of the tool wearing by investigating the tool cutting edge on a Stereo Microscope NIKON SMZ 18 before and after processing the ornament on wood. An aesthetic evaluation of the ornament routed on wood, using both the engraving and carving methods, is also conducted, whilst a microscopic analysis of the processed areas highlights the defects that occurred on the wood surface depending on the tool path.

Keywords: CNC router; textile heritage; stereo-microscopy investigation; traditional motif

1. Introduction

As in many other cultures in the world, the textile heritage from Romania is proof of cultural expression, and it has to be well preserved for the next generations. Unfortunately, the objects in this category may be subjected to degradation risks due to their advanced age and sometimes improper conservation [1]. Actual digital technologies supported by graphics programs, computer-aided design (CAD), and computer-aided manufacturing (CAM) allow for the replication and transfer of valuable motifs found on old textiles onto modern ones [2], thus contributing to their preservation. In light of the Framework Convention on the Value of Cultural Heritage for Society (Faro Convention), a "New heritage" is about to rise up, and it pertains to the use of the past in the present and its renewal into the future [3]. Taking advantage of modern technologies, creative industries, such as fashion, ceramics, the textile industry, the furniture industry, and others, are able to transpose old traditional motifs onto new objects, preserving them in new forms.

Computerized Numerical Control (CNC) routers in the furniture industry offer the possibility of milling decorations on the wood surface, importing the vector file made with graphic software, which renders the drawing of the original motif, or by converting 2D digital images into 3D representation through developed applications, such as Visual C++ software [4]. The sculpting process on a CNC router is based on optimization of the milling parameters, selection of the right tool, and the processing method. The majority of scientific papers investigate the quality of routed surfaces by measuring the roughness parameters [5–9] or by applying a mathematical model to adjust the feed rate depending on the surface quality along with the cutting direction and species of wood [10], or genetic algorithms on CAM software [11]. The spindle speed of 14,500 rpm and feed speed of 2 m/min for CNC routing birch and beech wood had as low effect values for the roughness parameter Ra (average surface roughness measured as the arithmetic averages of the absolute values for all deviations of peaks and ridges) for

a conventional way of cutting [5]. In the case of CNC milling of spruce and chestnut wood, 10,000 rpm for spindle speed and 5 m/min for feed speed were recommended for a minimum value of Rz (the average maximum peak to valley of five consecutive sampling lengths within the measuring length) roughness parameter, whilst for larch wood, a feed speed of 7 m/min and spindle speed of 18,000 rpm were found to be optimal [6]. Minimum Ra and Rz values were obtained for a spindle speed of approx. 17,000 rpm and a feed speed of 2 m/min in the case of CNC milling of Cedar of Lebanon pine [7].

Numerous studies were conducted to evaluate the tool wear or the effect of tool wear on the machining process for various species of wood or wooden-based materials [12–17]. Tool wear has a great influence on the quality of the product, its accuracy, and productivity. The measurement of the cutting edge profile gives indications about the tool wear level. It can be performed automatically [12] or by chemical, microscopic, and hardness analysis of the cutting knife. Indirect methods can also be used, such as the measurement of the electrical current consumption or the measurement of the sound pressure during processing. Both are higher when the tool wear increases [13]. Measuring Ra and Rz roughness parameters after successive CNC milling of pine wood, it was determined that, for the anti-wear coated tools, the values of the roughness parameters are higher in the phase of initial wear than those of an uncoated tool, but with increased wear, the situation is reserved and the roughness parameters for coated tools decreased to lower values than the initial ones [14]. Research on the correlation between the tool wear and cutting forces in the machining process of the Aleppo pine have shown that the edge recession occurred at a cutting length of 850 m, with abrupt wear at about 200 m [17].

The research presented in this paper shows the process of transposing a traditional motif taken from the textile heritage originating from the SE region of Transylvania from Romania (named Țara Bârsei) on the wood surface, as decoration such as for furniture, using a three-axis CNC router for the milling process. Two methods of transposing the motif were applied: engraving (Engrave) and carving (V-Carve), using V-Grooving Router Bit tool with an angled tip of 90°. Linux CNC version 2.7.0. software was used to simulate the machining process and the tool path for the two variants of the ornament. Maple wood was used for the experiment, and twenty successive ornaments were machined and executed for each variant of the model. The wear of the tools was determined by scanning electron micocopy of the tool cutting edge before starting the CNC milling process and after the ornaments were processed twenty times both by engraving and carving. A visual evaluation of the processed ornaments was conducted from the aesthetic and qualitative points of view, and details of the areas where wood fuzziness occurred were highlighted by stereo-microcopy analysis.

2. Materials and Methods

The traditional Romanian ornamentation is rich in geometric representations, characterized by a delicate refinement. The present research uses the plant motif from Figure 1 for the experiment, which is originally stitched in a cross technique on the sleeve of a traditional woman's blouse from the village of Bran, where Dracula's castle is located. The ornamental composition, subjected to the laws of symmetry and alternation, contains the motif of the clover leaf, the "water wave" pattern, and the fir leaf. All traditional motifs in Romania have a symbolic value. Thus, the clover suggests the magic number three, which exists in many ritual practices and generally protects human life, and the four-leaf clover is considered to bring luck [18]. Flowing water means a crossing, a test, and thus represents the passage, the flow of life, and the flow of time [19]. The fir tree can be assimilated with the tree of life, which is the backbone of the world. It is present at weddings and funeral rituals, and when it is represented with seven rows of branches, those are the seven heavens [20]. This popular motif with symbolic value was collected as a picture from the particular owner of the original blouse (Figure 1a) and then rendered in vector format using the professional vector graphics software CorelDRAW X17 (Figure 1b). The file was

then imported in AutoCAD LT 2017 (Figure 1c) and transferred to the 3-axis CNC router, ISEL GFV type, German production, with a maximum spindle speed of 15,000 rpm.
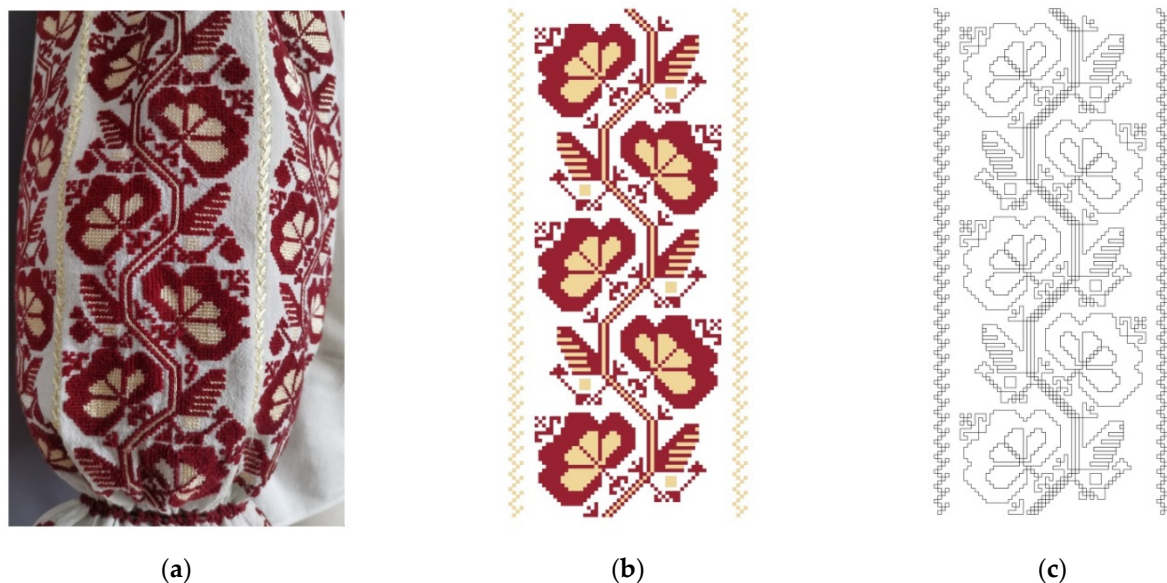
Figure 1. Traditional motif from Țara Bârsei subjected to the present research: (**a**) the picture of the textile object, (**b**) the digital vector format drawing, and (**c**) the contour of the ornament used by the CNC router for milling the maple wood surface.

The contour of the ornament (Figure 1c) was CNC machined in two ways: the first one was the engraving method (Engrave), for which a constant depth of the cut at 3 mm was applied to both closed contours and open contours of the drawing; the second one was the carving method (V-Carve), which can be applied only for closed contours, with variable depths between 1 mm to 3 mm for the surface and 3 mm for the contour. The other processing parameters of the CNC router were the spindle speed of 15,000 rpm and feed speed of 6 m/min.

Twenty maple (*Acer pseudoplatanus* L.) wood panels with dimensions of 300 mm × 200 mm × 11 mm, a moisture content of 11%, and a mean density of 615 kg/m^3 were used for the experiment. Due to its homogeneous structure and color compared to other species of wood, maple wood is recommended for carving.

The tool type chosen for the experiment is CMT Orange V-Grooving Router Bit angled 90° (Figure 2). These double cutting edge CMT bits offer a large range of woodworking possibilities, making clean cuts in the panels. They are made of super strength Fatigue Proof® steel with Tungsten carbide-tipped cutting edges [21].
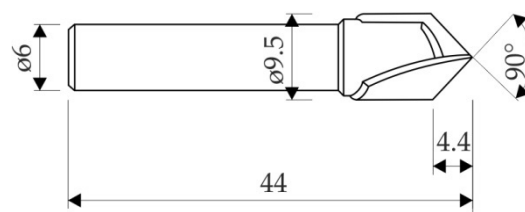
Figure 2. CMT Orange tool, V-Grooving Router Bit 90°, code 715.095.11.

2.1. Method to Analyse Tool Wear

In order to study the initial (abrupt) tool wear, twenty panels were used for CNC routing the ornament on the surface, and for each panel, the Engrave method was applied on one face and V-Carve on the other face. Two new V-Grooving 90° router bits were used for CNC milling of the wood surface: one for the Engrave method and the other for the V-Carve method. Before starting to process the ornaments on wood panels, the cutting

edge was studied using the stereo-microscope NIKON SMZ 18, with a zoom ratio of 18:1 and zooming range between 0.75× and 13.5×. The total magnification of the microscope used to investigate the tool cutting edge was 120×.

The stereo microcopy investigation was repeated after each new milling operation of the ornament on the wood surface for both CNC machining methods.

2.2. Simulation of Tool Path

The tool path was automatically calculated by the software Linux CNC version 2.7.0., a free software that runs under the Linux operating system. It was used together with the 3-axis CNC router. The software offers the possibility to simulate the machining process and to visualize the tool path and the data related to it: the length of the trajectory and the estimated processing time.

2.3. Method to Analyze the Wood Ornaments Produced

An investigation of the wood ornaments was conducted by comparing the two variants obtained by the Engrave and V-Carve methods from two points of view: the aesthetic one, following similarity with the original motif, and the quality of the processed surface analyzed by stereo-microscopy in the areas where wood fuzziness occurred. Wood mass loss after CNC machining the ornaments with the Engrave and V-Carve methods was also determined by weighing each panel before and after milling the wood. Wood mass loss may be correlated with the processing time in terms of productivity.

3. Results

The results obtained in the experiment are presented in Table 1.

Table 1. Recorded results for the Engrave and V-Carve methods.

No.	Method	Mass of Removed Wood [1], in kg/Panel	Tool Path, in m/Panel	Processing Time, in min:s/Panel
1	Engrave	0.038 (0.005)	19.165	39:03
2	V-Carve	0.014 (0.002)	49.741	59:48

[1] Average value calculated for the 20 panels on which experiment has been conducted. Values in the parenthesis are standard deviations.

3.1. Tool Wear

The wear occurred after processing the ornament twenty times on maple wood. This aspect was highlighted by the stereo-microscopy investigations. The tool cutting edge wear was not visible at the stereo-microscope after processing the ornament three times, but after milling the fourth panel, small changes were observed on the tool cutting edge (zone W, Figure 3; zone W rotated by 90°, Figure 4). Comparing the initial aspect of the tool cutting edge and the final one (after twenty uses), visible modifications occurred, both when the Engrave method (Figures 5 and 6) and the V-Carve method (Figures 7 and 8) were applied. A and B circled areas in Figures 5–8 were identified as the more affected zones of the cut edge, where its shape was modified as the result of the wear process.

Figure 3. Zone W of the investigation on the wear of the tool cutting edge.
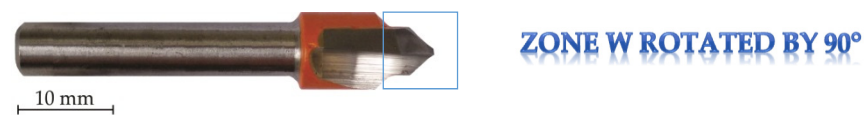
Figure 4. Zone W rotated by 90° for the investigation of the wear of the tool cutting edge.

(**a**)   (**b**)
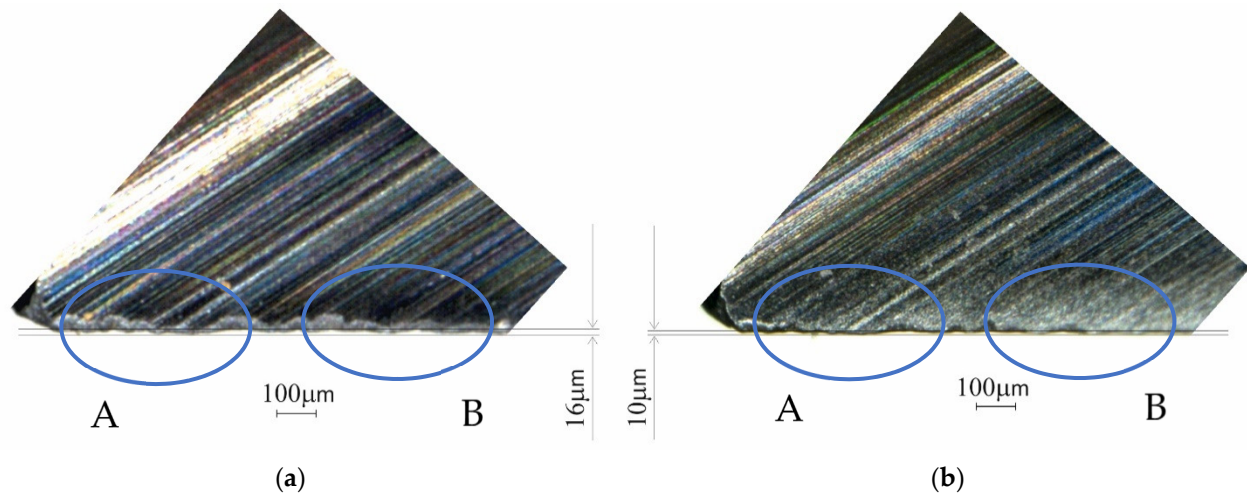
Figure 5. Zone W of the Engrave tool (120× magnification) on a stereomicroscope: (**a**) initial; (**b**) after twenty uses. A and B circled areas are the more affected one because of the wear process.

(**a**)   (**b**)
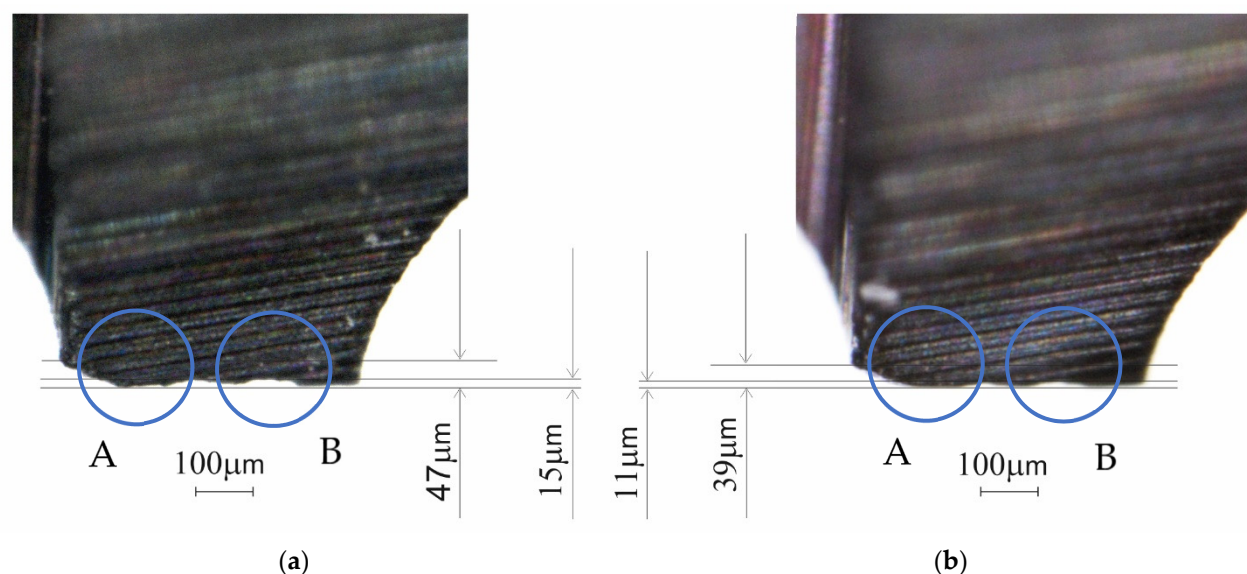
Figure 6. Zone W rotated by 90° of the Engrave tool (120× magnification) on a stereo-microscope: (**a**) initial; (**b**) after twenty uses. A and B circled areas are the more affected one because of the wear process.

The circles in Figures 5–8 indicate the zones where the differences are more visible (A and B circled areas). After twenty uses, the tools used for engraving and carving have blunt and rounded edges compared with their initial states in zone W and zone W rotated by 90°, especially for the tool tip area.

The wear process looks more pronounced for the second case, where the tool cutting edge was used for carving (V-Carve), as seen in Figures 7 and 8. Even if the tools were new, irregular contour of the cutting edge was noticed at the microscopic level before starting to use the tools for CNC routing the maple wood panels. Instead, the traces of sharpening the cutting edge were visible at this stage for zone W (Figures 5 and 7). The contour of the cutting edge became more regular after twenty uses of the tools, especially

when the V-Carve method was applied (Figures 7 and 8), but the traces of sharpened knife disappeared, replaced by a blunt-knife appearance.

(**a**)

(**b**)
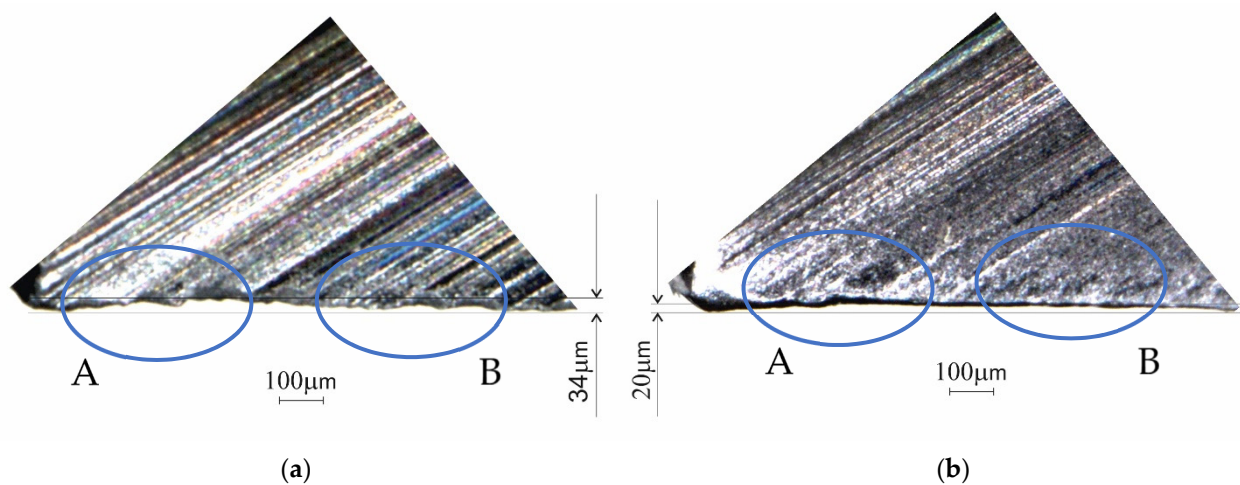
Figure 7. Zone W of the V-Carve tool (120× magnification) on a stereo microscope: (**a**) initial; (**b**) after twenty uses. A and B circled areas are the more affected one because of the wear process.

(**a**)

(**b**)
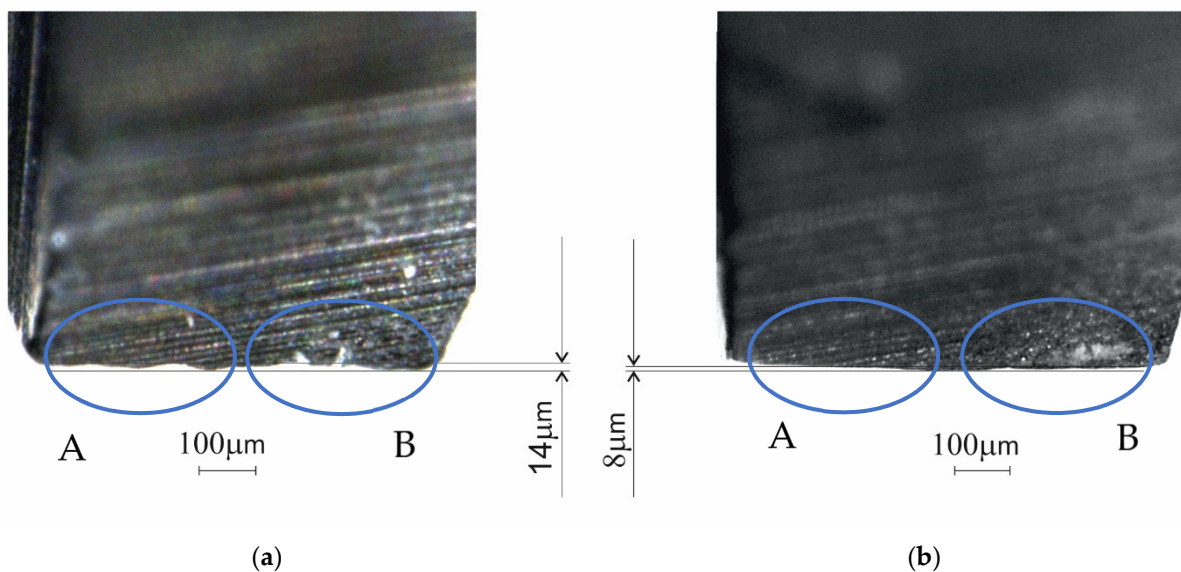
Figure 8. Zone W rotated by 90° of the V-Carve tool (120× magnification) on a stereo-microscope: (**a**) initial; (**b**) after twenty uses. A and B circled areas are the more affected one because of the wear process.

3.2. Tool Path

In Figures 9 and 10, the tool path simulated by Linux CNC version 2.7.0. software is represented. The dashed line represents the trajectory traveled when idling, and a continuous line represents the path traveled during processing. With an interrupted red line, the shape and dimensions of the wooden piece are presented.
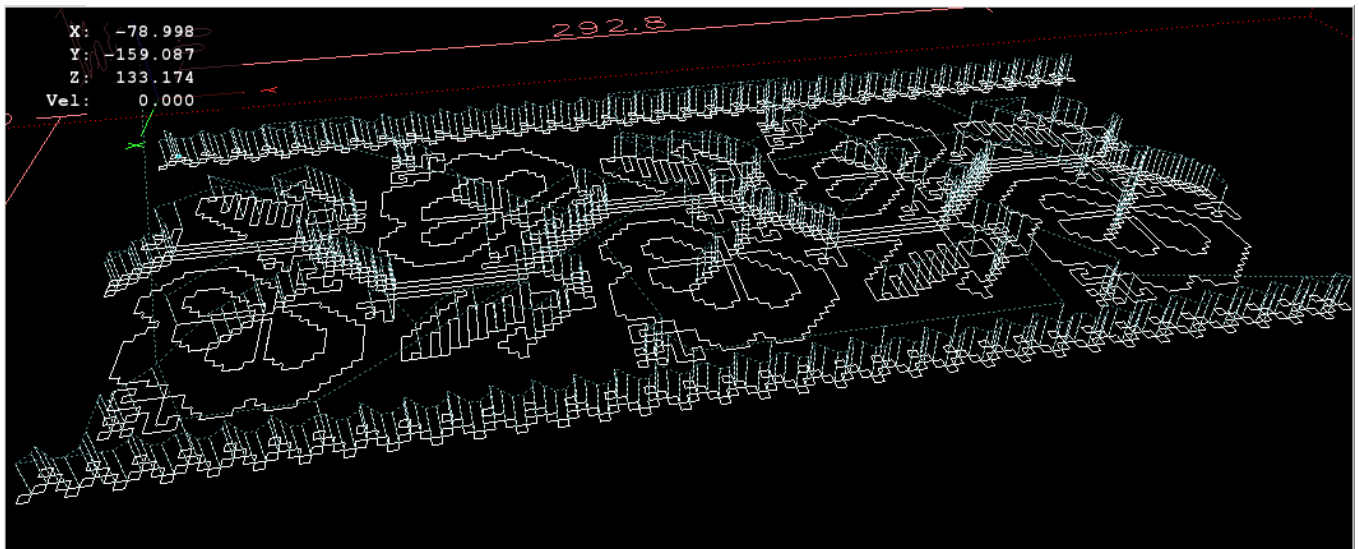
Figure 9. Tool path when milling with the Engrave method is applied.
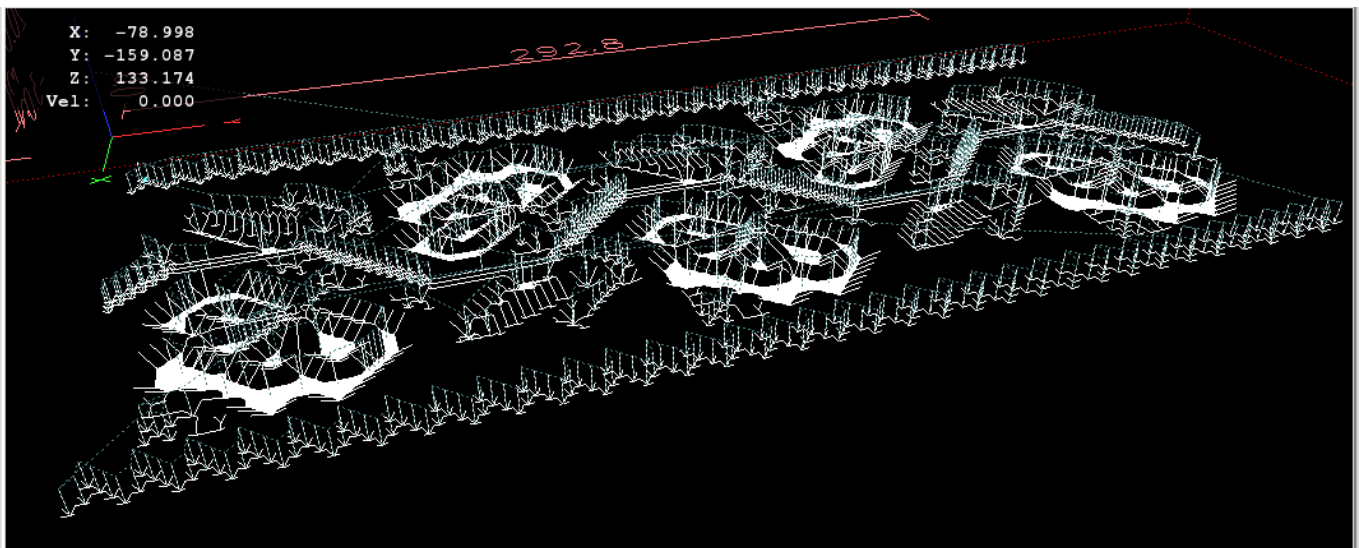
Figure 10. Tool path when milling with the V-Carve method is applied.

The calculated tool path by the Linux CNC software was 19,165.4 mm when the Engrave method was applied and 49,741.4 mm when the V-Carve method was applied for CNC routing. Calculating the whole length of the paths for the twenty processed ornaments, there was a route with 383.3 m length for engraving and 994.8 m length for carving. Similar research on Aleppo pine concluded that dge recession occurred at a cutting length of 850 m, with abrupt wear at about 200 m [17].

3.3. Wood Ornaments Investigation

A first evaluation of the ornaments was conducted by comparing the two variants transposed onto the wood surface with the original motif. The visual investigation revealed that the textile motif transferred by CNC milling on the maple wood surface looks different depending on the method applied: Engrave or V-Carve. In Figure 11a, the ornament looks crowded when applying the Engrave method. In the second case, when the V-Carve method was used (Figure 11b), the ornament processed on the wood surface resembled the original motif more.

(**a**)   (**b**)
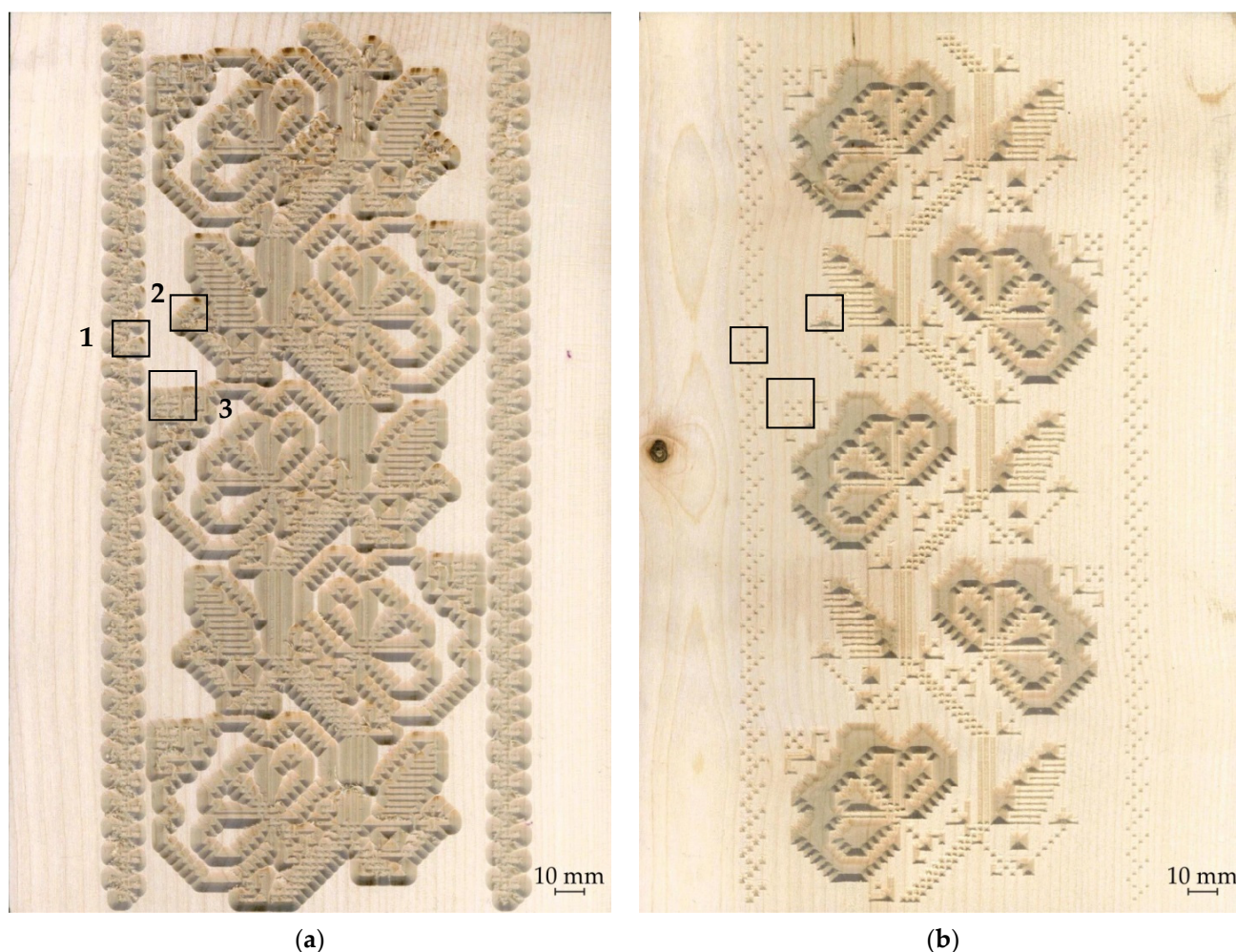
Figure 11. The CNC routed ornaments: (**a**) using the Engrave method; (**b**) using the V-Carve method. Areas marked with 1, 2 and 3 were identified to be characterized by pronounced wood fuzziness.

Studying the ornaments processed by the two methods, three zones where wood fuzziness occurred after processing the ornament by the Engrave method on the wood surface were highlighted. These zones are marked in Figure 11a, and they were assigned the numbers 1, 2, and 3. These zones were subjected to a stereo-microscopy analysis with $22.5\times$ magnification and compared to similar zones of the V-Carved ornament. The images are presented in Figures 12–14 for the Engrave method (a) and for the V-Carve method (b). The arrows indicate fuzzy grains on the wood surface, more numerous and larger in size than on the variant of the ornament for which the Engrave method was used.
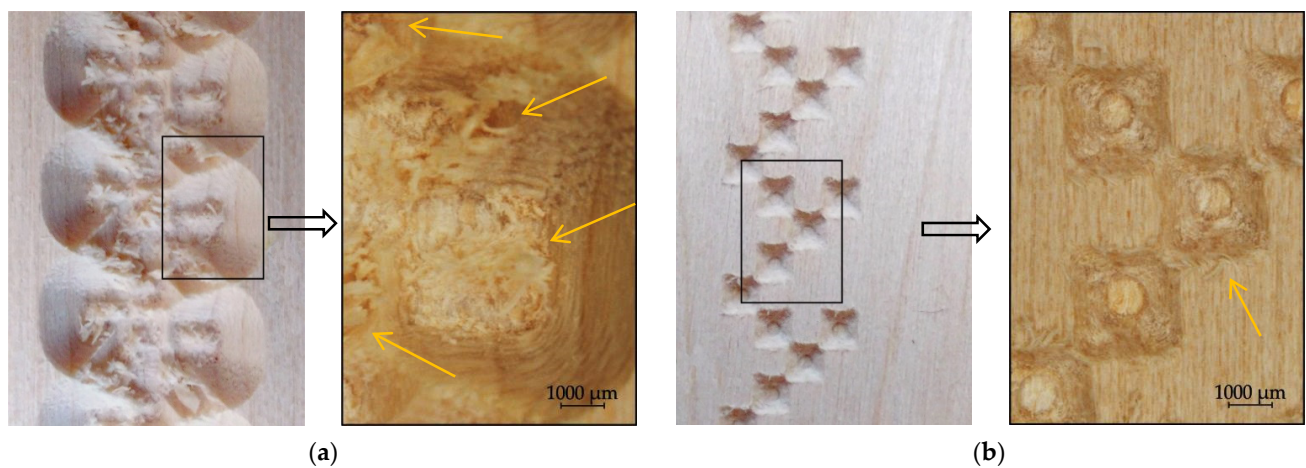
Figure 12. Detail 1 from Figure 8 subjected to stereo-microscopy analysis with 22.5× magnification: (**a**) ornament obtained by the Engrave method: detail from the picture (**left**) and the image with 22.5× magnification (**right**); (**b**) ornament obtained by the V-Carve method: detail from the picture (**left**) and the image with 22.5× magnification (**right**).
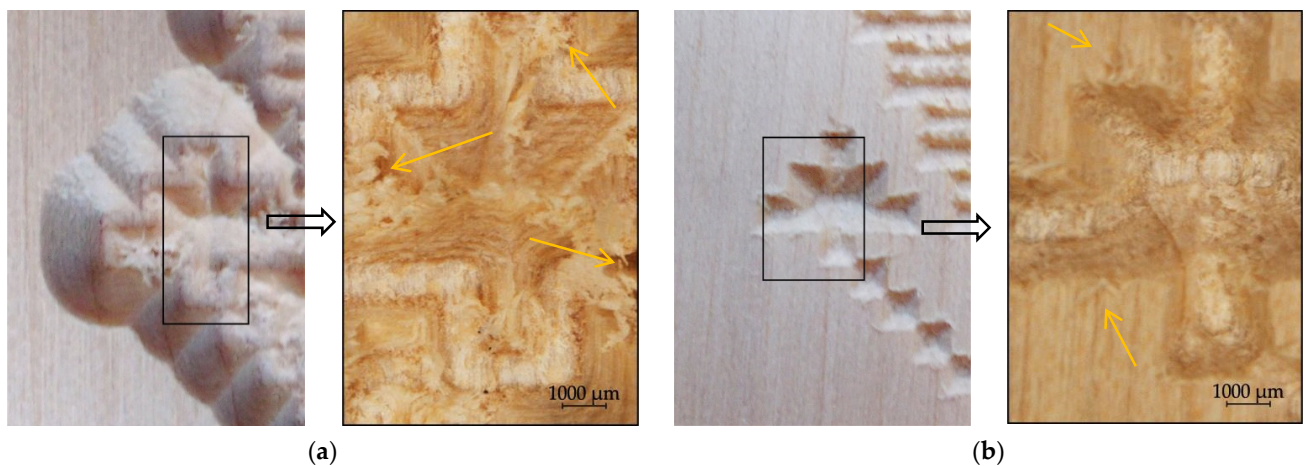
Figure 13. Detail 2 from Figure 8 subjected to stereo-microscopy analysis with 22.5× magnification: (**a**) ornament obtained by the Engrave method: detail from the picture (**left**) and the image with 22.5× magnification (**right**); (**b**) ornament obtained by the V-Carve method: detail from the picture (**left**) and the image with 22.5× magnification (**right**).
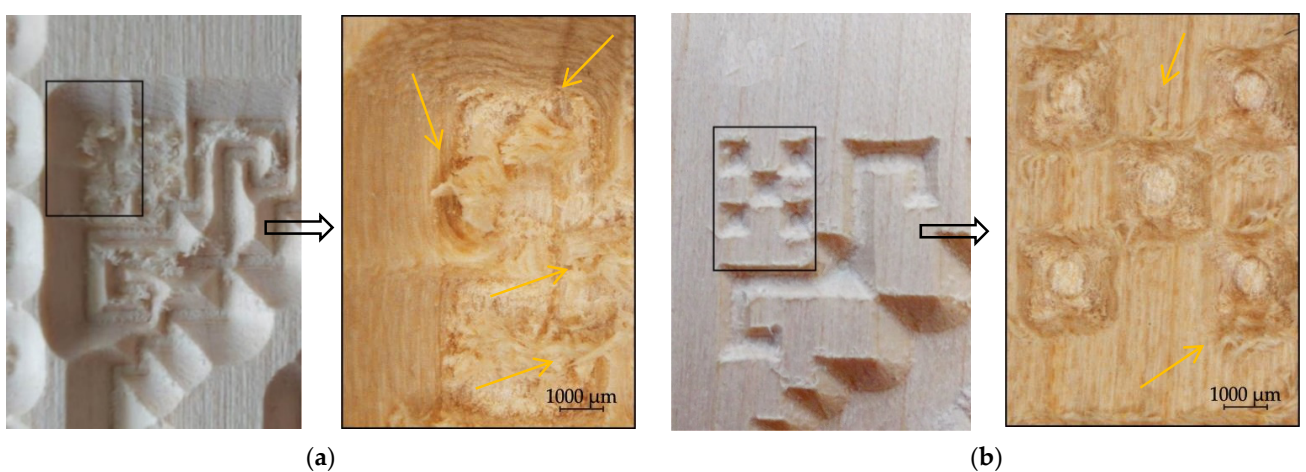
Figure 14. Detail 3 from Figure 8 subjected to stereo-microscopy analysis with 22.5× magnification: (**a**) ornament obtained by the Engrave method: detail from the picture (**left**) and the image with 22.5× magnification (**right**); (**b**) ornament obtained by the V-Carve method: detail from the picture (**left**) and the image with 22.5× magnification (**right**).

4. Discussion

For this research, a traditional Romanian motif taken from textile heritage was transposed as an ornament on maple wood panels by CNC machining with two different methods: engraving (Engrave) and carving (V-Carve) using the V-Grooving Router Bit angled at 90°. The comparison between the two processing methods included a visual analysis of the appearance of the processed ornament in the two variants, followed by a stereo-microscopy of the areas where fuzzy grains occurred after milling the wood; a tool wear assessment by microscopic investigation of the tool cutting edge after twenty successive millings of ornaments; and a calculation of the tool path and of the mass of the removed wood during the milling process and their correlation with the processing times.

The visual analysis revealed that the ornament looked totally different when it was engraved or carved by the CNC router. The carved ornament looked more similar the original motif. In addition, the microscopic investigation showed large and numerous wood fuzzy grains on the engraved surfaces, thus bringing another advantage to the V-Carve method.

The tool wear was highlighted by microscopic analysis of the tool cutting edge, where blunt and rounded edges were compared with their initial state after the ornament had been processed twenty times.

It is found that the wear of the tool used for engraving is 37.5% for the cutting area (see Figure 5) and 26.7% for the tip area (Figure 6). For the tool used for V-Carve milling, the wear is 41.2% for the cutting area (Figure 7), while for the tip, it was 42.8% (Figure 8). These data show that, in the case of milling with the Engrave method, the wear of the tool was less pronounced than that in the case of V-Carve milling. The explanation is related to the length of the tool path for the two applied methods (approx. 19.2 m when the Engrave method was applied and 49.7 m when the V-Carve method was applied).

It was also noticed that, when milling with the Engrave method, the wear affects the cutting edge area more, while when milling with the V-Carve method, the wear percentage of the tool tip is higher. This can be explained by the different contact areas between the tools and wood for the two cases, with the difference being the interior surface of the ornament, where the cutting depth varies between 1 mm to 3 mm, and the tip of the tool is involved in the milling process.

Correlations between tool path lengths calculated for twenty processed ornaments, their corresponding processing times, and masses of the removed wood are presented in Figure 15.

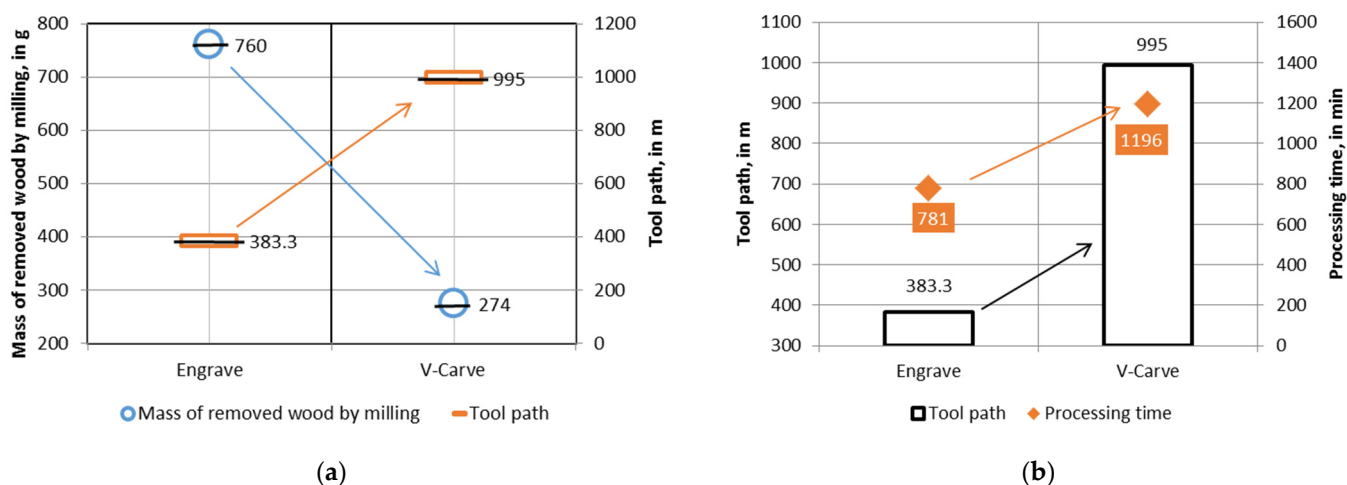
(a)　　　　　　　　　　　　　　　　　　　　　　　　　(b)

Figure 15. Comparison between the Engrave and V-Carve methods applied to CNC routing of an ornament on a maple wood surface: (**a**) correlation between the mass of removed wood and tool path length; (**b**) correlation between the tool path length and processing time.

5. Conclusions

The results of the present research show that the tool path is longer when applying the V-Carve method than for the Engrave method, and this aspect resulted in a longer processing time for the V-Carve method, as seen in Figure 15b. Instead, the mass of the wood removed during the routing process is higher when applying the Engrave method than when applying the V-Carve method. This can be explained by the constant cut depth of 3 mm for the Engrave method compared with the variable cut depth between 1 mm and 3 mm for the V-Carve method (3 mm only for the contour), resulting in a higher volume of wood removed in the first case. The longer tool path in the case of applying the V-Carve method, correlated with a longer processing time, is a drawback of this method in terms of productivity. Choosing the right method to be applied in CNC routing of ornaments similar to that used as an example in this research is a compromise between appearance, surface quality, and productivity. Being a furniture ornament, the aesthetic and the quality of the processed surface should be considered, so the V-Carve method is more advantageous from these points of view.

References

1. Ilieş, D.C.; Herman, G.V.; Caciora, T.; Ilieş, A.; Indrie, L.; Wendt, J.; Axinte, A.; Diombera, M.; Lite, C.; Berdenov, Z.; et al. Considerations Regarding the Research for the Conservation of Heritage Textiles in Romania. In *Waste in Textile and Leather Sectors*; Körlü, A., Ege University, Eds.; IntechOpen Limited: London, UK, 2020. [CrossRef]
2. Doble, L.; Stan, O.; Suteu, M.D.; Albu, A.; Bohm, G.; Tsatsarou-Michalaki, A.; Gialinou, E. Romanian traditional motif—element of modernity in clothing. *IOP Conf. Ser. Mater. Sci. Eng.* **2017**, *254*, 172009. [CrossRef]
3. Fairclough, G. The Value of Heritage for the Future. In *Heritage in Society. Cultural Policy and Management (KPY)*; Yearbook 3; Ünsal, D., Ed.; Istanbul Bilgi University Press: Istanbul, Turkey, 2012; pp. 34–41.
4. Sood, S.; Duvedi, R.K.; Bedi, S.; Mann, S. 3D representation and CNC machining of 2D digital images. *Procedia Manuf.* **2018**, *26*, 10–20. [CrossRef]
5. Pinkowski, G.; Szymanski, W.; Nosowski, T. Analyses of surface roughness in selected wood species after machining on a CNC woodworking centre. *Ann. WULS SGGW For. Wood Technol.* **2012**, *79*, 164–169.
6. Çakiroğlu, E.O.; Demir, A.; Aydin, I. Determination of the Optimum Feed Rate and Spindle Speed Depending on the Surface Roughness of Some Wood Species Processed with CNC Machine. *J. Anatol. Environ. Anim. Sci.* **2019**, *4*, 598–601. [CrossRef]
7. Hazir, E.; Koc, K.H. Optimization of wood machining parameters in CNC Routers: Taguchi orthogonal array based simulated angling algorithm. *Maderas Cienc. Tecnol.* **2019**, *21*, 493–510. [CrossRef]
8. Sütcü, A.; Karagöz, Ü. Effect of machining parameters on surface quality after face milling of MDF. *Wood Res.* **2012**, *57*, 231–240.
9. Supadarattanawong, S.; Rodkwan, S. An Investigation of the Optimal Cutting Conditions in Parawood (*Heavea Brasiliensis*) Machining Process on a CNC Wood Router. *Kasetsart J. (Nat. Sci.)* **2006**, *40*, 311–319.
10. Gawronski, T. Optimisation of CNC routing operations of wooden furniture parts. *Int. J. Adv. Manuf. Technol.* **2013**, *67*, 2259–2267. [CrossRef]
11. Krimpenis, A.A.; Fountas, N.A.; Mantziouras, T.; Vaxevanidis, N.M. Optimizing CNC wood milling operations with the use of genetic alghorithms on CAM software. *Wood Mater. Sci. Eng.* **2014**, *11*, 102–115. [CrossRef]

12. Ohuchi, T.; Murase, Y. Milling of wood and wood-based materials with a computerized numerically controlled router V: Development of adaptive control grooving system corresponding to progression of tool wear. *Wood Sci.* **2006**, *52*, 395–400. [CrossRef]
13. Aguilera, A.; Meausoone, P.J.; Rolleri, A.; Barros, J.L.; Burgos, F.; Aguilar, C. Advances on indirect methods to evaluate tool wear for Radiata pine solid wood molding. *Wear* **2016**, *350–351*, 27–34. [CrossRef]
14. Pinkowski, G.; Szymanski, W.; Gilewicz, A.; Krauss, A. Impact of the wear of the cutting edge on selected parameters of the surface geometric structure after wood milling. *Ann. WULS SGGW For. Wood Technol.* **2009**, *69*, 187–191.
15. Keturakis, G.; Lisauskas, V. Influence of the Sharpness Angle on the Initial Wear of the Wood Milling Knives. *Mater. Sci. (Medžiagotyra)* **2010**, *16*, 205–209.
16. Porankiewicz, B. Theoretical simulation of cutting edge wear when milling wood and wood based products. *Wood Sci. Technol.* **2006**, *40*, 107–117. [CrossRef]
17. Aknouche, A.; Outahyon, A.; Nouveau, C.; Marchal, R.; Zerizer, A.; Butaud, J.C. Tool wear effect on cutting forces: In routing process of Aleppo pine wood. *J. Mat. Process. Technol.* **2009**, *209*, 2918–2922. [CrossRef]
18. Antonescu, R.B. *Dicţionar de Simboluri şi Credinţe Tradiţionale Româneşti*; Ediţie digitală, Direcţia de cercetare, evidenţă a patrimoniului cultural mobil, imaterial şi digital; Institutul Naţional al Patrimoniului: Bucureşti, România, 2016; p. 661.
19. Semne Cusute. Available online: https://semne-cusute.blogspot.com/2012/07/motive-unda-apei.html (accessed on 5 June 2021).
20. Semne Cusute. Available online: https://semne-cusute.blogspot.com/2012/07/bradutul.html (accessed on 5 June 2021).
21. CMT Orange Tools. Available online: https://www.cmtorangetools.com/eu-en/industrial-router-bits/v-grooving-router-bits-90deg (accessed on 5 June 2021).

Influence of Adhesive Type and Content on the Properties of Particleboard Made from Sunflower Husks

Octavia Zeleniuc, Luminita-Maria Brenci,* Camelia Cosereanu, and
Adriana Fotin

The suitability of using milled sunflower husks as a wood substitute for producing medium-density particleboard was investigated. Additionally, the impact of the adhesive type and the amount used on the properties of the panels were evaluated. Urea-formaldehyde (UF) in three commercial variants (UCL, U96, and AG), phenol-formaldehyde (PF), modified melamine urea-formaldehyde (VM), and polymeric diphenylmethane diisocyanate (pMDI), as well as mixtures of VM/AG and of PF/pMDI, were used to manufacture the panels. The adhesive content was varied between 3% and 6% for pMDI, and from 9% and 12% for the other adhesives. Higher thickness swelling (TS) and water absorption (WA) values were observed with the UF panels compared with the PF and pMDI panels. The lowest mechanical strength properties were observed for the UF panels, with the commercial variants ranking (from highest to lowest): UCL > VM/AG > U96. Increasing the adhesive content level resulted in better dimensional stabilities and mechanical properties for the pMDI and PF panels, which met some of the performance requirements for interior uses prescribed by the relevant standard.

*Contact information: Department of Wood Processing and Wood Products Design, Faculty of Wood Engineering, University Transilvania Brașov, Brașov, Romania; *Corresponding author: brenlu@unitbv.ro*

INTRODUCTION

Forests not only supply wood for the rapidly growing composite industry, but they also help to support a healthy ecosystem and a sustainable environment. Hence, it is important to preserve forest resources while at the same time to develop new building products.

Global wood panel production has increased rapidly, with a 123% increase in 2016 (416 million m^3) when compared with 2000 (FAO 2017). China, the USA, Russia, Canada, and Germany represented the five largest producers and consumers, which accounted for 69% of global output in 2016 (FAO 2016). In Europe, wood-based panel production grew after 1990, from approximately 30 million m^3 to 86 million m^3 because of the development of new products, such as medium-density fiberboard (MDF) and oriented strand board (OSB), as well as new investments made in Eastern Europe. These investments have contributed to a 70% increase in Eastern Europe's panel production in 2017 when compared with 2000 (FAO 2017).

Romania is one of the Eastern European countries that have made significant investments in wood-based panels after 2008. In the last few years, new capacities were developed, which increased wood panel production to 6 million m^3 (2016), compared with 1.5 million m^3 in 2008 (FAO 2017). This increased production has placed some strain on

bioresources.com

the existing forest resources. In the near future, it is anticipated that available forest resources will be insufficient to satisfy all the wood demands while maintaining requirements for forest sustainability. This would require the promotion of new raw materials, such as agro-waste resources.

Short rotation wood could compensate for the forest resource deficits in Romania, but the areas harvested with these plantations at the national level represent less than 5% (Nicolescu and Hernea 2018). A more preferable alternative to wood is renewable agricultural residues. Currently, Romania has the potential for high-yield agricultural production; Romania is a typical agricultural country, with 62% of the arable land area (8.8 million ha) dedicated to agricultural activities (UNECE 2012). The most important agricultural crops are maize (corn), wheat, barley, sunflower, and soybean (soya). Agricultural residue wastes, such as straw, stalks, stems, and corn cobs, have the potential to be used as raw material for wood-based composites.

In Romania the annual crop residue amounts are between 10.2 and 27.0 dry Mt/year, of which approximately 4.7 to 12.6 dry Mt/year are collected (Scarlat *et al.* 2011). More than 50% of these unused residues are disposed into landfills, which contributes to environmental pollution. Another proportion of the unused residuals (approximately 46%) are used in animal feed and as fuel pellets for heat production. Sunflower (*Helianthus annuus* L.) has relatively a short growth cycle and it is easy to adapt at different soil conditions, thus is cultivated worldwide on a surface of 26.2 million hectares, reaching a production of 47.34 million tons in 2016 (Soare and Chiurciu 2018). Sunflower is the most important agricultural crop cultivated in Romania over 1 million hectares, followed by rapeseed and soybean. Sunflower production has increased in recent years, which has made Romania a leader in the European Union (EU); it accounted for approximately 24% of the total EU production in 2016 and 2017 (*i.e.*, 1.95 to 2.25 million metric tons) (Dobrescu 2017). In 2018 Romania has maintained its first place in the harvested sunflower production, with 1.785 million tons from 7.906 million tons of EU 28 production. At the world level, Romania contributed with 4.29% to the world production, being on the 5th place among Ukraine, Russia, Argentina and China (Eurostat 2019). The sunflower is basically used for the oil production, in EU amounting about 7.6 million tons of the crushed seed (Nazlin *et al.* 2017). The sunflower oil produced in Romania is expected to increase slightly, reaching 0.338 million metric tons (2017/2018) (Dobrescu 2017) and 3.800 million tons in Europe, in 2019 (Krautgartner *et al.* 2019). The percentage of husks in sunflower seeds varies between 10% and 30%, which depends upon the dehulling process used (Wan *et al.* 1979; Isobe *et al.* 1992; Heinrich 2017; Kumar 2018). The density of the husks is very low (212 kg/m^3 at 10% moisture content) (Gamea 2013). Based on the husks ratio in the seeds it can be estimated that approximately 3.42 million tons of husks annually become available from the dehulling process in EU. As a consequence, a large area of storage is necessary for oil producers, therefore the wastes of sunflower husks could be degraded in time and pollute the environment. Generally, these husks are used for fuel pellets, briquettes, xylose extraction, fertilizer, and animal feed. The husks are high in fiber and low in protein, and therefore have a very low commercial feed value (Le Clef and Kemper 2015). Their use in the particleboard production is very scarce. Taking in consideration the pressure put on the forest resources, the intensifying of trees harvesting to meet the production demand, these husks (by-products) could be a potential new resources for the particleboard production. The principal constituents of the husks are cellulose (27.43%), lignin (24.23%), hemicellulose (29.04%), and extractives (9%) (Popescu *et al.* 2013), similar to those of hardwood species.

A literature review indicates that research has been conducted to make composites from sunflower residues (*e.g.*, stalk, husks, and by-products obtained after oil extraction from the seeds). These residuals have been combined with aspen wood particles (Gertjejansen *et al*. 1972), cement (Sisman and Gezer 2013), cotton waste (Binici and Aksogan 2014), Calabrian pine, poplar wood particles (Bektas *et al*. 2005; Guler *et al*. 2006), polypropylene (Kaymakci *et al*. 2013), and chitosan (Mati-Baouche *et al*. 2014) to form composites. Most of the developed composite panels that utilize sunflower wastes are combined with a variety of other raw materials, such as agricultural wastes (corn, rice, wheat), wood particles (poplar, pine, aspen), and inorganics (plaster and concrete). The use of these raw material mixtures in particleboard manufacturing involves the time and cost for collecting, storing, milling, defibration, sorting, heat-treating, and pressing operations.

According to recent data it could be estimated that the adhesives used in Europe for particleboard production are: ureo-formaldehidic (UF) (90 to 92%), melamino-ureo-formaldehidic (6 to 7%), and polymeric diphenylmethane diisocyanate (pMDI) (1 to 2%) (Kutnar and Burnard 2013). Phenolic resin (PF) is the second important bonding adhesive after UF, employed in the manufacture of wood based panels (Athanassiadou *et al*. 2015; Sandberg 2016). Their amount required by technology is between 9 and 12% (Ayrilmis and Nemli 2017; Laskowska and Mamiński 2018). The physical and mechanical properties of sunflower-based particleboard are lower than those of wood particleboard when UF and PF adhesives are used (Bektas *et al*. 2005; Kwon *et al*. 2014; Guler 2017). PMDI and emulsified pMDI in water (EMDI) have been found to be good substitutes for formaldehyde-based adhesives, leading to improved mechanical properties for the panels formed (Franke *et al*. 1994; Tongboon *et al*. 2002; Papadopoulos *et al*. 2002; Preechatiwong *et al*. 2007; Garay *et al*. 2009; Dukarska *et al*. 2017).

The objectives of this research were to produce particleboards made from 100% sunflower husks that possessed physical and mechanical properties approaching that of wood particleboards, as well as to evaluate how various adhesives and their usage levels affect the physical and mechanical properties of the resulting panels.

EXPERIMENTAL

Lignocellulosic Material

Sunflower husks (*Helianthus annuus* L.*)* were used as a raw lignocellulosic material to manufacture particleboards. The husks from the sunflower seed dehulling process were obtained from a Romanian sunflower oil manufacturer. The hammer-milled husks were sieved through 4- and 0.5-mm mesh screens to remove oversized and undersized particles. The accepted fraction had particles with lengths from 2.55 to 4.76 mm, widths from 1.05 to 2.3 mm, and thicknesses of 0.2 mm. The screened husks were dried to 4% moisture content.

Adhesives

The following adhesives were used to manufacture sunflower husk particleboards: urea-formaldehyde (UF), phenol formaldehyde (PF), modified melamine-formaldehyde (VM), and polymeric diphenylmethane diisocyanate (pMDI). Three commercial variants of UF were tested (UCL, U96, and AG); these variants differed from one another regarding the synthesis method and the formaldehyde/urea (F/U) molar ratio (1.15, 0.96, and 1.09, respectively). Mixtures of VM/AG (20:80 wt. ratio) and PF/pMDI (70:30 wt. ratio) were

also used. PMDI today is generally applied in the European OSB industry (Stroobants and Grunwald 2014). The level applied is different depending on the product. In the OSB manufacturing the adhesive content ranges between 1.5% to 5%, and for particleboard an accelerator is added to the UF, and the combination in the core layer amounts to a percentage of 0.3% to 0.5% (Mantanis *et al*. 2017). Some research employed pMDI at rates of 1%, 2%, 3%, 4% and 6% for particleboard manufacturing (Papadopoulos *et al.* 2002; Korai and Ling 2011). Generally the hot pressing temperature varies from 180 °C to 240 °C (Papadopoulos *et al.* 2002) and the pressure time from 3 min to 6 min (Papadopoulos *et al* 2002; Korai and Ling 2011; Dukarska *et al*. 2017; Solt *et al*. 2019). A higher temperature was used for boards with pMDI, to reach sufficient temperature to allow the resin to cure. PMDI provides high bond strength, faster reaction time and superior resistance to water (Dunky 2003), thus it was employed beside UF adhesives. The choice of adhesives for the experimental tests was based on the data provided by the literature (Papadopoulos *et al*. 2002; Ressel 2008; Mendes *et al*. 2009; Korai and Ling 2011; Ayrilmis and Nemli 2017; Dukarska *et al*. 2017; Laskowska and Mamiński 2018; Solt *et al*. 2019). The adhesive types and the pressing schedule are presented in Table 1.

The solid resin content was based on the oven-dry weight of the husk particles. Ammonium chloride (NH_4Cl) was used a hardener for urea-formaldehyde resins and was added at 1.5% (based on the weight of the dry resin). All adhesives were obtained from Viromet SA (Victoria, Romania).

Table 1. Adhesive Content Level and Pressing Parameters

Board code	Adhesive content level (%)		Pressing parameters	
			Temperature (°C)	Pressing time (min)
UCL	9	12	150	7
U96	9	12	150	7
VM/AG	9	12	150	7
PF	9	12	160	7
pMDI	3	6	180	4
PF/pMDI	9	-	180	7

Panel Forming and Pressing

The milled husk particles were weighed and mixed with the selected adhesive in a blender. Panels with lateral dimensions of 420 mm x 420 mm were manually formed with a homogenous single-layer structure. Panels were hot-pressed at 2.45 N/mm^2 to obtain a target density of 600 kg/m^3. The pressing conditions are presented in Table 1. Two replicates were made for each panel type. After pressing, the panels were conditioned at 20 °C and 65% relative humidity until they reached equilibrium moisture content; the conditioned panels were trimmed to nominal lateral dimensions of 400 mm x 400 mm, with a thickness of 16 mm.

Physical and Mechanical Strength Characterization

Water absorption (WA) and thickness swelling (TS) tests were performed in accordance with the EN 317 (1993) standard. The density of the panels was measured in accordance with the EN 323 (1993) standard. The density profile was measured using a compact X-ray density profile analyzer (DPX300; Imal S.R.; Modena, Italy). The mechanical tests were performed using a Zwick/Roell Z010 universal-testing machine (Zwick/Roell; Kennesaw, GA) that was equipped with a ±10-kN load cell. The modulus of

bioresources.com

rupture (MOR), modulus of elasticity (MOE), and internal bond strength (IB) were evaluated in accordance with the EN 310 (1993) and EN 319 (1993) standards, respectively. Ten measurements were performed for each property tested; the reported values are the average of the measurements. One-way analysis of variance (ANOVA, using Microsoft Excel) was performed to evaluate the statistical effects of adhesive type and content level on the properties of the panels. A statistical significance level of $\alpha \leq 0.05$ was selected.

RESULTS AND DISCUSSION

Morphological Characterization

The panels produced with sunflower husk particles appeared rigid and strong. The particles showed good cohesion and were not easily detached (Fig. 1).

Fig. 1. Outside appearance of the experimental panels

More compact structures and uniform distributions of particles were observed for the panels made with 6% pMDI, 12% PF, and 12% VM/AG. It appeared that these adhesives were uniformly distributed over the surface of the particles and filled the voids between the particles to provide adequate adhesion among the particles. Moreover, pMDI penetrated into the amorphous components of the husk cell wall at the molecular level and led to plasticization, improving the thickness swelling resistance of panels (Frazier 2003). The internal morphologies of the various panels are more clearly observed in the high-definition photographs shown in Fig. 2 (originally 4800 dpi resolution).

For 3% pMDI, the panel structure was less compact and the adhesive partially adhered to some particles, resulting in the formation of localized agglomerations. The heterogeneous distribution of husk particles and adhesive led to more voids in the structure when urea-formaldehyde adhesives were used.

Physical and Mechanical Characterization

Figure 3 shows the vertical density profile (VDP) of the panels. These graphs exhibited a typical density profile caused by mat densification. A higher peak density was found 1 mm and 3 to 4 mm from the surface areas for the UF panels and PF/pMDI panels, respectively (Fig. 3; a through f, g through k). The core of the panels had a more pronounced U-shaped profile in the cases of UCL and U96 adhesives (Fig. 3; a, b, d, and e.).

bioresources.com
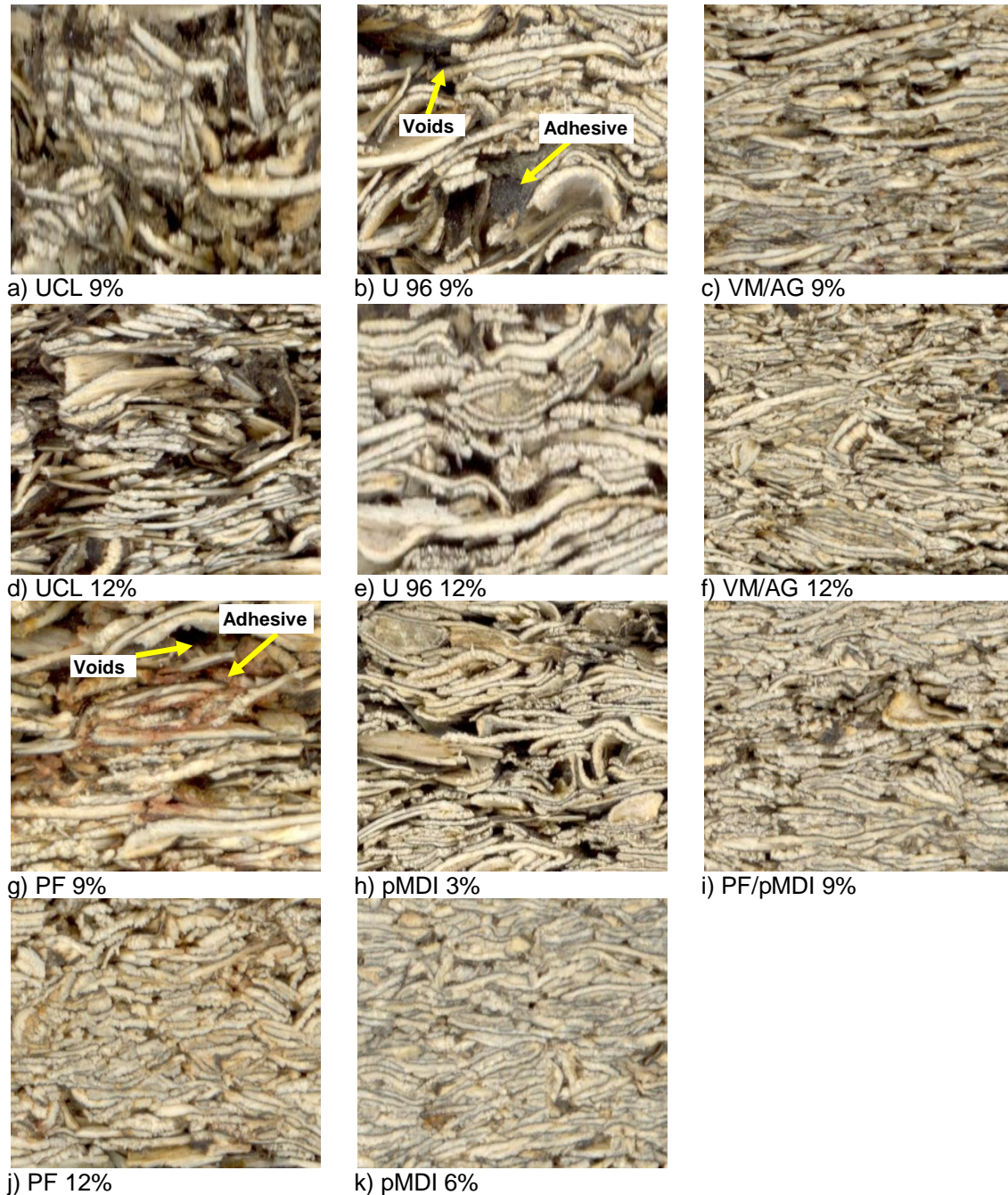
Fig. 2. Morphological details of the experimental panels (originally 4800 dpi resolution)

The mean densities of the panels (approximately 550 kg/m^3) were similar to one another except for the pMDI panels, which exhibited the lowest density (490 kg/m^3) (Fig. 3; h and i).

Panels made with pMDI had a relatively flat-shaped density profile (Fig. 3; h and k). In these cases, the pressing time was shorter when compared with the other panels; this may have affected the surface density by minimizing the differences between the lateral edges and the core.
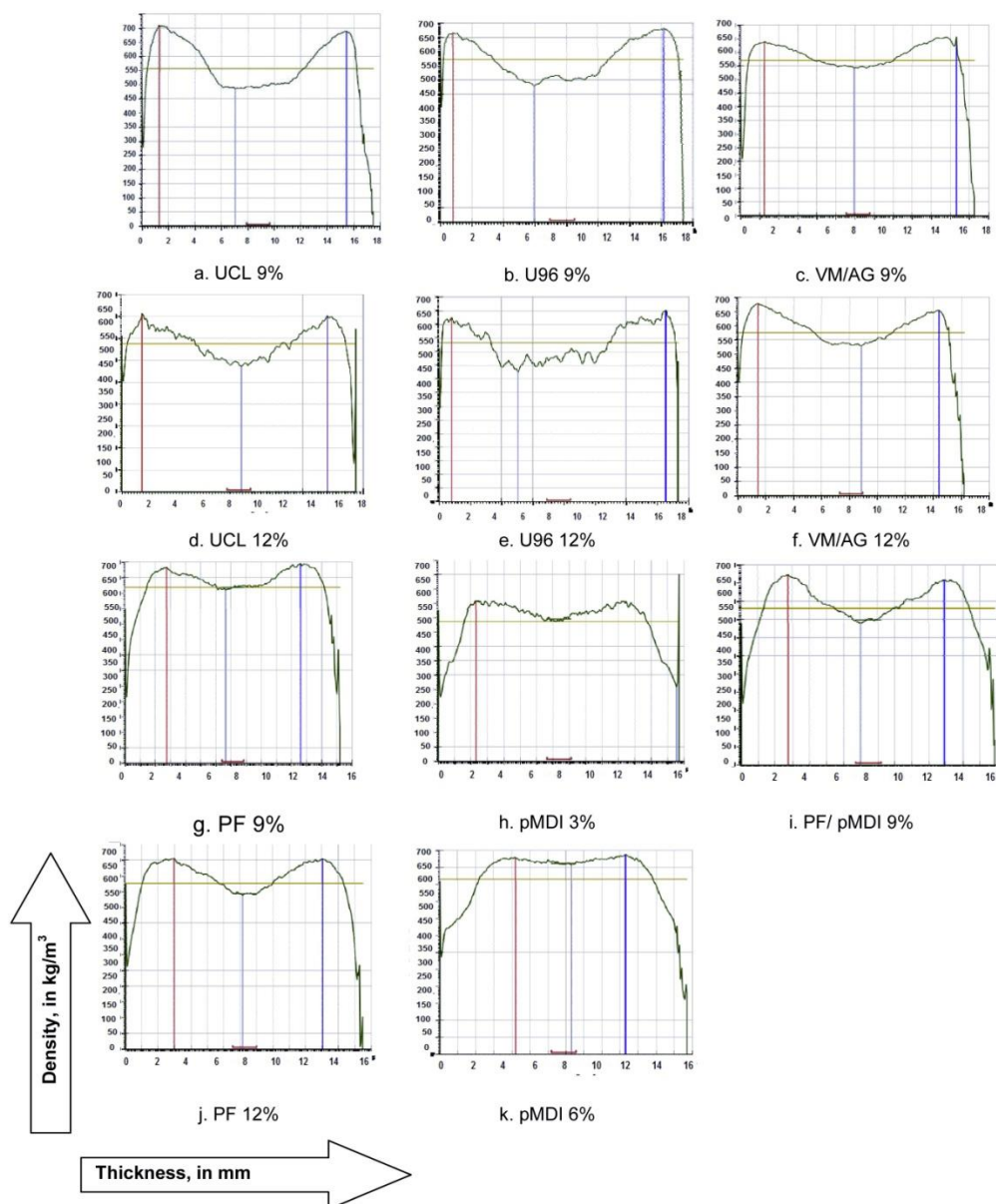
Fig. 3. Vertical density profiles of the experimental panels

The experimental panels can be classified as medium-density particleboard (below 600 kg/m^3). The lowest density was obtained for pMDI panels because of the low specific gravity of the adhesive (Rachtanapun *et al.* 2012). The average values of the physical properties are presented in Table 2. The moisture content of all panels was approximately 6.3%. The highest thickness swelling (TS) and water absorption (WA) values after 24 h of water immersion were observed for the panels made with UF adhesives; such adhesives are known to have low water resistance. Similar results in thickness swelling (TS 24h 49% ÷ 44%) were observed in the research made by Melo *et al.* (2014), who also observed a highest instability of particleboards that used only rice husk with urea-formaldehyde adhesive. The panels made with PF had the lowest TS and WA values (20% and 69%, respectively); these values were almost one-half the values observed for the UF panels. This behavior is attributed to the high water resistance of the methylene carbon-carbon bonds linking the aromatic nuclei of PF (Dunky 2003). A differential decrease in WA and

bioresources.com

TS values was noted as the adhesive content increased for all panels, except for the PF panels. The lower density of the PF panels made with 12% adhesive could have induced more water penetration into the panel structure when compared with the 9% adhesive panel.

Table 2. Physical Properties of the Experimental Panels

Properties	Adhesive content (%)	Density (kg/m^3)	TS 24h (%)	WA 24h (%)
UCL	9	556 (27.8)	41.2 (6.1)	125.3 (11.6)
	12	573 (21.6)	38.4 (5.6)	110.5 (13.3)
U96	9	577 (39.0)	44.5 (1.5)	140.2 (3.1)
	12	580 (21.0)	41.2 (6.1)	126.4 (10.1)
VM/AG	9	570 (40.0)	40.3 (0.6)	124.9 (3.4)
	12	574 (23.8)	32.2 (1.2)	106.9 (15.4)
PF	9	570 (16.7)	19.9 (3.3)	69.5 (6.2)
	12	524 (29.3)	20.8 (3.7)	68.7 (6.0)
pMDI	3	495 (20.9)	56.0 (3.6)	131.7 (6.4)
	6	535 (19.3)	29.7 (1.6)	76.0 (14.4)
PF/pMDI	9	520 (16.5)	31.4 (0.6)	81.3 (4.9)
The numbers in parentheses are the standard deviations				

A slight decrease in TS and WA (of approximately 7% and 10%, respectively) was observed for the 12% UF adhesive panels (UCL and U96) *versus* the 9% UF adhesive panels. These results are consistent with those of sugar cane bagasse particleboards reported by Mendes *et al.* (2009). Garay *et al.* (2009), registered a higher level of TS 24h and WA 24h (over 60% and 100% respectively), even when UF was increased from 10% to 15%, by using rice and wheat husk in different proportion with wood, for particleboard manufacturing. Klimek *et al.* (2016) observed that TS 24h of sunflower stalk particleboards did not show significant differences when increases the dosage of UF from 8% to 10%. They reported similar values compared to the present data for UF and MDI adhesives. Better results were recorded for VM/AG and pMDI panels, for which TS and WA decreased by 24% to 47% and 24% to 42%, respectively. The melamine resin and polyisocyanate components of these adhesives form strong bonds, conferring stability to the formed panels. Similar results were reported by Hse and Choong (2002) and Klimek *et al.* (2016) for rice hull-wood and sunflower stalks particleboards with polyisocyanate adhesive. Unexpectedly, the 3% pMDI panels had the highest TS and WA values (56.6% and 131.7%, respectively). It seemed that the adhesive was heterogeneously distributed onto the surfaces of the husk particles, which also led to a decrease in internal cohesion. All panels had TS values that were higher than the 14% limit recommended for P3 type panels (EN 312 (2013)). The present results on TS and WA were relatively high but are consistent with literature (Hse and Chong 2002; Guntekin and Karakus 2008; Garay *et al.* 2009; Melo *et al.* 2014; Guler 2015; Kord *et al.* 2016) and can be explained by the fact that no paraffin or other hydrophobic substances were added in the boards. Additionally, the complex interrelation between chemical composition, the size of particles, and their interaction with adhesives influenced the performance of the boards.

As expected, the use of pMDI and PF adhesives resulted in better panel stability regarding water penetration (*i.e.*, lower TS and WA) and higher IB than did the use of UF adhesives (Fig. 4). In general, the IB value increased in a somewhat linear fashion as the TS and WA values decreased. The highest IB values were observed for the pMDI and PF panels.
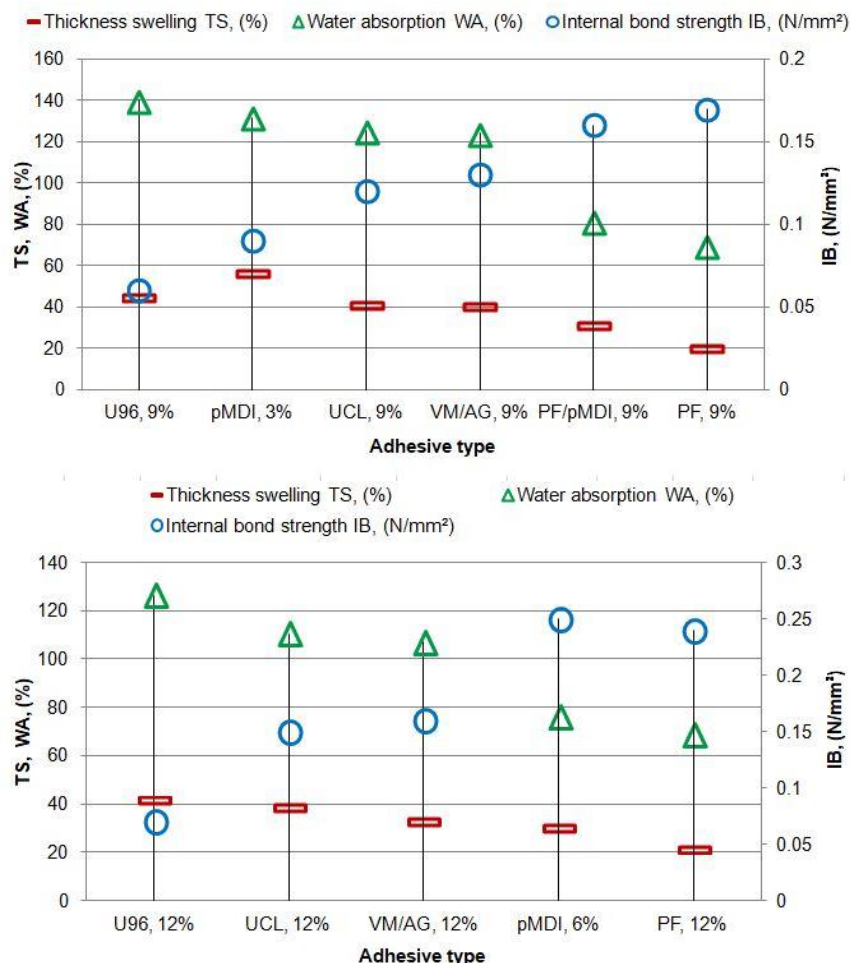
Fig. 4. Effect of adhesive type and its content level on the thickness swelling (TS), water absorption (WA), and internal bond strength (IB) of the panels

The adhesive type was found to have a significant influence on the measured TS and WA values at the 95% confidence level. The statistical impact of adhesive content level was more evident for pMDI (*p*-value less than 0.0001) than for UF (*p*-value of 0.004).

Mechanical Properties

The MOR and MOE values are presented in Fig. 5. The highest strength values were noted for PF and pMDI panels at the highest adhesive content level.

The UF panels had the lowest mechanical strength. Depending on the UF type, the average decrease in strength varied from 32% to 43% for MOR and 29% to 58% for MOE when compared with panels utilizing PF and pMDI at high adhesive content levels. Greater decreases, from 32% to 58% for MOR and 46% to 68% for MOE, were also observed at low adhesive content levels. The lowest strength results were noted for U96 panels and for 3% PMDI panels.

U96 adhesive had the lowest F/U ratio among the UF adhesives used; U96 is generally used to manufacture high-density fiberboards. This explained U96's poor performance with respect to the sunflower husk particles. An insufficient amount of adhesive in the case of 3% pMDI resulted in the lower mechanical properties of the resulting panel. The combination of UF with modified melamine-formaldehyde adhesive

bioresources.com

(VM/AG) slightly improved the mechanical properties *versus* the other urea adhesives. Low MOR and MOE values were reported by Guler (2015) and Melo *et al.* (2014) when using other agricultural residues (hazelnut husk, peanut hull, and rice husk) combined with UF adhesive.
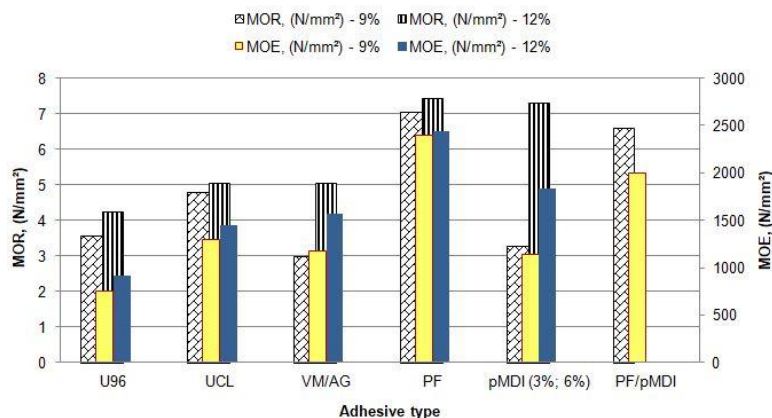
Fig. 5. Effect of adhesive type and its content level on MOR and MOE

All panels examined in this study failed to meet the minimum MOR requirements of EN 312 (2013). An increase in the percentage of agro wastes in the particleboard is expected to lead to a decrease in breaking strength and rigidity parameters (Ndazi *et al.* 2006; Melo *et al.* 2014; Klimek *et al.* 2016), and the boards generally failed to meet MOR standard P1 limits (Ndazi *et al.* 2006; Keskin *et al.* 2015; Klimek *et al.* 2016). The experimental boards had a density lower than 580 kg/m^3 and easily could be included in the low density category (Rowell 2014) where MOR, MOE and IB values are ranging from 3 N/mm^2 to 5.0 N/mm^2, 550 N/mm^2 to 1025 N/mm^2 and 0.1 N/mm^2 to 0.15 N/mm^2, respectively.

The effect of pMDI adhesive on MOR and MOE was obvious; therefore, the values obtained for 6% pMDI panels were comparable with those of 12% PF panels. This observation is similar to the results reported by Hse and Choong (2002) for 5.5% polyisocyanate adhesive used in particleboards made from rice hull mixed with wood particles. Only the PF and pMDI panels fulfilled the requirements for MOE (>1600 N/mm^2) in accordance with EN 312 (2013) for P2-type particleboard.

The average IB values ranged from 0.06 N/mm^2 (9% U96) to 0.25 N/mm^2 (12% PF and 6% pMDI). All panels bonded with UF adhesives had the lowest IB strengths at both adhesive content levels (Fig. 4). An increase in adhesive content from 9% to 12% improved the IB for all panels, which was more evident for PF (40% higher) than for UF panels (23% higher). The IB values of pMDI panels were significantly affected by adhesive content level. An IB increase of 177% was observed when the pMDI level increased from 3% to 6%; the IB values at 6% pMDI were comparable with those at 12% PF. The mixed resin system, pMDI/PF, was noted to have a lower IB than that of 6% pMDI panels, but it was comparable to those of 9% PF panels. A minimum IB value of 0.24 N/mm^2 is required for P1-type particleboards, according to EN 312 (2013); this requirement was met by 12% PF and 6% pMDI panels.

Statistical analyses showed that the mechanical properties of the experimental panels, in terms of MOR, MOE, and IB, were significantly influenced by the adhesive type (*p*-value of 0.0009). The statistical impact of adhesive content level on these values was

more evident for pMDI (p-value less than 0.0001) than for UF and PF panels (p-value of 0.04).

CONCLUSIONS

1. Adhesive type had a significant influence on the physical and mechanical properties of experimental composite panels made from sunflower hulls.

2. The adhesive content level had a significant effect on the properties of the panels, with a more notable effect observed for pMDI panels than for UF and PF panels.

3. Higher TS and WA values were noted for UF panels at the two adhesive content levels, with the commercial variants ranking (from highest to lowest) U96 > UCL > VM/AG. Slightly improved properties were observed for the VM/AG panels as a result of the addition of melamine to the UF adhesive.

4. Panels with 3% pMDI adhesive content exhibited lower mechanical properties than UF panels; this was attributed to low density and low bonding efficiency when using 3% pMDI.

5. The best panel dimensional stabilities and mechanical properties were observed for PF panels at both adhesive content levels, followed by PF/pMDI (9%) and pMDI (6%). These results indicate stronger bonds between husk particles and adhesive. PF and pMDI panels were found to comply with the MOE and IB strength requirements for general use as prescribed by the EN 312 (2013) standard.

6. The results obtained revealed that sunflower husks are compatible with UF, PF and pMDI adhesives and represent an alternative material to wood in particleboard manufacturing. The performance of boards was influenced by the adhesive type and content and the low density (below 580 kg/m^3), which contributed to a decrease in strength. The experimental particleboard presents a potential for indoor use as light panels for paneling or other decorative products.

ACKNOWLEDGMENTS

REFERENCES CITED

Athanassiadou, E., Markessini, C., and Tsiantzi, S. (2015). "Industrial amino adhesives satisfying stringent formaldehyde limits," in: *Melamine 2015 Conference*, 15-16 November, Dubai.

Ayrilmis, N., and Nemli, G. (2017). "Effect of adhesive type on the quality properties of particleboard," in: *Scientific Proceedings XIV of the Machines. Technologies. Materials - Innovations from Science to Industry 2017 International Congress*, summer session, Varna, pp. 519-520.

Bektas, I., Guler, C., Hulya, K., Mengeloglu, F., and Nacar, M. (2005). "The manufacture of particleboards using sunflower stalks (*Helianthus annuus* L.) and poplar wood (*Populus alba* L.)," *Journal of Composite Materials* 39(5), 467-473. DOI: 10.1177/0021998305047098

Binici, H., and Aksogan, O. (2014). "Engineering properties of insulation material made with cotton waste and fly ash," *Journal of Material Cycles and Waste Management* 17(1), 157-162. DOI: 10.1007/s10163-013-0218-6

Dobrescu, M. (2017). *Oilseeds Update - Romanian Sunflowers Shine* (GAIN Report No. RO1726/12/12/2017), U. S. Department of Agriculture, Foreign Agricultural Service, Washington, DC, USA, (https://gain.fas.usda.gov/Recent%20GAIN%20Publications/Oilseeds%20Update%20-%20Romanian%20Sunflowers%20Shine%20_Bucharest_Romania_12-12-2017.pdf).

Dukarska, D., Czarnecki, R., Dziurka, D., and Mirski R. (2017). "Construction particleboards made from rapeseed straw glued with hybrid pMDI/PF," *European Journal of Wood and Wood Products* 75(2), 175-184. DOI: 10.1007/s00107-016-1143-x

Dunky, M. (2003). "Adhesives in the wood industry," in: *Handbook of Adhesive Technology, Revised and Expanded*, Second Edition, A. Pizzi and K. L. Mittal (eds.), CRC Press, Boca Raton, FL, 872-931. DOI: 10.1201/9780203912225.ch47

EEA (2012). *Climate Change, Impacts and Vulnerability in Europe 2012 - An Indicator-based Report* (EEA Report No. 12), European Environment Agency, Copenhagen.

EN 310 (1993). "Wood-based panels. Determination of modulus of elasticity in bending and of bending strength," European Committee for Standardization, Brussels, Belgium.

EN 312 (2013). "Particleboards – Specifications," European Committee for Standardization, Brussels, Belgium.

EN 317 (1993). "Particleboards and fibreboards. Determination of swelling in thickness after immersion in water," European Committee for Standardization, Brussels, Belgium.

EN 319 (1993). "Particle boards and fibreboards. Determination of tensile strength perpendicular to the plane of the board," European Committee for Standardization, Brussels, Belgium.

EN 323 (1993). "Wood based panels. Determination of density," European Committee for Standardization, Brussels, Belgium.

Eurostat (2019). "Main annual crop statistics," Statistics Explained (https://ec.europa.eu/eurostat/statistics-explained/pdfscache/28946.pdf)

FAO (2016). "Global forest products. Facts and figures 2016," Food and Agricultural Organization (FAO) of the United Nations (UN), Rome, Italy, (http://www.fao.org/3/I7034EN/i7034en.pdf).

FAO (2017). "Global wood production growth accelerates," Food and Agricultural Organization (FAO) of the United Nations (UN), Rome, Italy, (http://www.fao.org/news/story/en/item/1073713/icode/).

Franke, J., Kappe, M., Recker, K., Reipf, H., Rliprecht, H. D., and Sachs, H. I. (1994). "Polyurethane (PUR) systems and polyisocyanates as starting materials for binders," in: *Polyurethane Handbook*, G. Oertel (ed.), Hanser Publisher, New York, NY, 615-628.

Frazier, C. E. (2003). "Isocyanate wood binders," in: *Handbook of Adhesive Technology, Revised and Expanded*, Second Edition, A. Pizzi and K. L. Mittal (eds.), CRC Press, Boca Raton, FL, USA, 674-686. DOI: 10.1201/9780203912225.ch33

Gamea, G. R. (2013). "Physical properties of sunflower seeds components related to kernel pneumatic separation," *International Journal of Engineering and Technology* 13(1), 103-114.

Garay, R. M., MacDonald, F., Acevedo, M. L., Calderón, B., and Araya, J. E. (2009). "Particleboard made with crop residues mixed with wood from *Pinus radiata*," *BioResources* 4(4), 1396-1408. DOI: 10.15376/biores.4.4.1396-1408

Gertjejansen, R. O., Haygreen, J. G., and French, D. W. (1972). *Particleboard from Aspen Flakes and Sunflower Hulls* (Technical Bulletin 290), University of Minnesota Agricultural Experiment Station, St. Paul, MN, 6 pp., http://hdl.handle.net/11299/108509

Guler, C., Bektas, I., and Kalaycıoğlu, H. (2006). "The experimental particleboard manufacture from sunflower stalks (*Helianthus annuus* L.) and Calabrian pine (*Pinus brutia* Ten.)," *Forest Products Journal* 56(4), 56-60.

Guler, C. (2015). "Research on the production of the composite panels from some agricultural residues," *Pro Ligno* 11(4), 187-191.

Guler, C. (2017). "Sunflower stalks as an alternative source of raw material in composite panel production," in: *Proceedings of the 5th International Conference on Advances in Science Engineering, Technology and Natural Resources,* Bangkok, Thailand, pp. 87-89. DOI: 10.17758/URUAE.AE0817110

Guntekin, E., and Karakus, B. (2008). "Feasibility of using eggplant (*Solanum melongena*) stalks in the production of experimental particleboard," *Industrial Crops and Products* 27(3), 354-358. DOI: 10.1016/j.indcrop.2007.12.003

Heinrich, D. (2017). "Comparison of hulling systems - Preparation of sunflower and double zero rapeseed," in: *17th Practical Short Course: Advanced Technologies in Oilseed Processing, Edible Oil Refining and Oil Modification - Focus On Sunflower Seed*, ID&A Ignace Debruyne & Associates VOF, Izegem, Belgium, (http://www.ofievents.com/turkey/contentimages/wygwam/9._Dirk_Heinrich.pdf).

Hse, C., and Choong, E. T. (2002). "Modified formaldehyde-based resin adhesives for rice hull-wood particleboard," in: *Wood-Cement Composites in the Asia-Pacific Region,* ACIAR Proceedings No. 107, P. D. Evans (ed.), Australian Centre for International Agricultural Research (ACIAR), Canberra, Australia, pp. 81-86.

Isobe, S., Zuber, F., Uemura, K., and Noguchi, A. (1992). "A new twin-screw press design for oil extraction of dehulled sunflower seeds," *Journal of the American Oil Chemists' Society* 69(9), 884-889. DOI: 10.1007/BF02636338.

Kaymakci, A., Ayrilmis, N., and Gulec, T., (2013). "Surface properties and hardness of polypropylene composites filled with sunflower stalk flour," *BioResources* 8(1), 592-602. DOI: 10.15376/biores.8.1.592-602.

Keskin, H., Kucuktuvek, M., and Guru, M. (2015). "The potential of poppy (*Papaver somniferum* L.) husk for manufacturing wood-based particleboards," *Construction and Building Materials* 95, 224-231. DOI: 10.1016/j.conbuildmat.2015.07.160

Klimek, P., Meinlschmidt, P., Wimmer, R., Plinke, B., and Schirp, A. (2016). "Using sunflower (*Helianthus annuus* L.), topinambour (*Helianthus tuberosus* L.) and cup-plant (*Silphinum perfoliatum* L.) stalks as alternative raw materials for particleboards," *Industrial Crops and Products* 92, 157-164. DOI: 10.1016/j.indcrop.2016.08.004

Korai, H., and Ling, N. (2011). "Effects of sealed press on improving the properties of particleboard," *Journal of Wood Science* 57, 208-213. DOI: 10.1007/s10086-010-1162-x

Kord, B., Zare, H., and Hosseinzadeh, A. (2016). "Evaluation of the mechanical and physical properties of particleboard manufactured from canola (*Brassica napus*) straws," *Maderas. Ciencia y Tecnología* 18(1), 9-18. DOI: 10.4067/S0718-221X2016005000002

Krautgartner, R., Golya, G., Rehder, L. E., Boshnakova, M., Dobrescu, M., Flach, B., Wilson, J., Faniadis, D., Guerrero, M., and Bolla, S. (2019). *EU-28 Oilseeds and Products Annual* (GAIN Report Number: AU1904), USDA Foreign Agricultural Service, Vienna.

Kumar, S. (2018). "Sunflower is a good source of animal feed," *International Journal of Current Microbiology and Applied Sciences* SI7, 2812-2816.

Kutnar, A., and Burnard, M. D. (2013). "The past, present and future of EU wood adhesive research and market," in: *Proceedings of Wood Adhesives 2014 Conference*, 9–11 October, Toronto, pp. 22-35.

Kwon, J. H., Ayrilmis, N., and Han, T. H. (2014). "Combined effect of thermoplastic and thermosetting adhesives on properties of particleboard with rice husk core," *Material Research* 17(5), 1309-1315. DOI: 10.1590/1516-1439.286314

Laskowska, A., and Mamiński, M. (2018). "Properties of particleboard produced from post-industrial UF- and PF bonded plywood," *European Journal of Wood and Wood Products* 76(2), 427-435. DOI: 10.1007/s00107-017-1266-8

Le Clef, E., and Kemper, T. (2015). "Sunflower seed preparation and oil extraction," in: *Sunflower Chemistry, Production, Processing, and Utilization,* E. Martínez-Force, N. T. Dunford, J. J. Salas (ed.), Academic Press and AOCS Press, DOI: 10.1016/C2015-0-00069-7

Mantanis, G. I., Athanassiadou, E. Th., Barbu, M. C., and Wijnendaele, K. (2017). "Adhesive systems used in the European particleboard, MDF and OSB industries," *Wood Material Science & Engineering* 13(2), 1-13, DOI : 10.1080/17480272.2017.1396622

Mati-Baouche, N., Baynast, H., Lebert, A., Sun, S., Lopez-Mingo, C. J. S., Leclaire, P., and Michaud, P. (2014). "Mechanical, thermal and acoustical characterizations of an insulating bio-based composite made from sunflower stalks particles and chitosan," *Industrial Crops and Products* 58(1), 244-250. DOI: 10.1016/j.indcrop.2014.04.022

Melo, R. R., Stangerlin, D. M., Santana, R. R. C., Pedrosa, T. D. (2014). "Physical and mechanical properties of particleboard manufactured from wood, bamboo and rice husk," *Materials Research* 17(3), 682-686, DOI: 10.1590/S1516-14392014005000052

Mendes, R. F., Mendes, L. M., Guimarães Júnior, J. B., Cavalcante dos Santos, R., and Bufalino, L. (2009). "The adhesive effect on the properties of particleboards made from sugar cane bagasse generated in the distiller," *Revista de Ciências Agrárias* 32(2), 209-218.

Nazlin, I., Kamar, N. A. K. Z., and Balu, N. (2017). "Competitiveness of the rapeseed industry in the European Union," *Oil Palm Industry Economic Journal* 17(1), 32-50.

Ndazi, B., Tesha, Ć. J. V., Karlsson, Ć. S., and Bisanda, Ć. E. T. N. (2006). "Production of rice husks composites with *Acacia mimosa* tannin-based resin," *Journal of Materials Science* 41, 6978-6983. DOI: 10.1007/s10853-006-0220-7

Nicolescu, V. N., and Hernea, C. (2018). "Romania," in: *Coppice Forests in Europe,* A. Unrau, G. Becker, R. Spinelli, D. Lazdina, N. Magagnotti, V. N. Nicolescu, P. Buckley, D. Bartlett, and P. D. Kofman (eds.), Albert Ludwig University Freiburg Printing Press, Freiburg, Germany, pp. 313-317, (https://www.eurocoppice.uni-freiburg.de/intern/coppiceineurope-volume/coppiceforestsineurope-6-25-romania-sept2018.pdf).

Papadopoulos, A. N., Hill, C. A. S., Traboulay, E., and Hague, J. R. B. (2002). "Isocyanate resins for particleboard: PMDI vs. EMDI," *Holz als Roh- und Werkstoff* 60(2), 81-83. DOI: 10.1007/s00107-001-0275-8

Popescu, B., Șenilă, L., Vărăticeanu, C., and Șimon G. N. (2013). "Cellulosic bioethanol from sunflower seed hulls - A renewable energy source," *Studia Universitatis Babes-Bolyai Ambientum* 58(1-2), 105-110.

Preechatiwong, W., Yingprasert, W., and Kyokong, B. (2007). "Effects of phenol-formaldehyde / isocyanate hybrid adhesives on properties of oriented strand lumber (OSL) from rubberwood waste," *Songklanakarin Journal of Science and Technology* 29(5), 1367-1375.

Rachtanapun, P., Sattayarak, T., and Ketsamak, N. (2012). "Correlation of density and properties of particleboard from coffee waste with urea–formaldehyde and polymeric methylene diphenyl diisocyanates," *Journal of Composite Materials* 46(15), 1839-1850. DOI: 10.1177/0021998311426624

Ressel, J. (2008). "Adhesive application," in: *Presentation during the 3rd International Wood Academy*, Feb. 25 – March 7, University of Hamburg, Hamburg, Germany.

Rowell, R. M. (2014). "The use of biomass to produce bio-based composites and building materials," in: *Advances in Biorefineries. Biomass and Waste Supply Chain Exploitation*, K. Waldron (ed.), Woodhead Publishing, Elsevier. DOI: 10.1533/9780857097385.2.803

Scarlat, N., Blujdea, V., and Dallemand, J. F. (2011). "Assessment of the availability of agricultural and forest residues for bioenergy production in Romania," *Biomass and Bioenergy* 35(5), 1995-2005. DOI: 10.1016/j.biombioe.2011.01.057

Sisman, C. B., and Gezer, E. (2013). "Sunflower seed waste as lightweight aggregate in concrete production," *International Journal of Environment and Waste Management* 12(2), 203-212. DOI: 10.1504/IJEWM.2013.055594

Sandberg, D. (2016). "Additives in wood products - Today and future developments," in: *Environmental Footprints and Eco-design of Products and Processes*, A. Kutnar, and S. Muthu (eds.), Springer, Singapore. DOI: 10.1007/978-981-10-0655-5

Soare, E., and Chiurciu, I. A. (2018). "Considerations concerning worldwide production and marketing of sunflower seeds," *Scientific Papers Series Management, Economic Engineering in Agriculture and Rural Development* 18(3), 421-427.

Solt, P., Konnerth, J., Gindl-Altmutter, W., Kantner, W., Moser, J., Mitter, R., and van Herwijnen, H. W. G. (2019). "Technological performance of formaldehyde-free adhesive alternatives for particleboard industry," *International Journal of Adhesion and Adhesives* 94, 99-131. DOI 10.1016/j.ijadhadh.2019.04.007

Stroobants, J., and Grunwald, D. (2014). "Wood based panels with enhanced properties: what is possible with MDI today?," in: *European Wood Based Panels 2014 Symposium*, 10th of October, Hanover.

Tongboon, S., Kiatkamjornwong, S., Prasassarakicht, P., Oonjittichai, W. (2002). "Particleboard from rubber wood flakes with polymeric MDI binder," *Wood and Fiber Science* 34(3), 391-397.

UNECE (2012). "Environmental performance reviews, Romania Second review," United Nations Economic Commission for Europe, New York, NY, USA., 247 pp., (http://www.unece.org/fileadmin/DAM/env/epr/epr_studies/Romania_II.pdf).

Wan, P. J., Baker, G. W., Clark, S. P., and Matlo, S. W. (1979). "Characteristics of sunflower seed and meal," *Cereal Chemistry* 56(4), 352-355.

Experimental thermal characterization of timber frame exterior wall using reed straws as heat insulation materials

Sergiu-Valeriu Georgescu[1] · Camelia Coşereanu[1] · Adriana Fotin[1] · Luminiţa-Maria Brenci[1] · Liviu Costiuc[1]

Abstract

The research presented in this paper proposes structures of timber frame exterior walls using reed straws as insulation materials. Having thicknesses of 175 mm and designed for exterior building walls, the proposed structures are composed of 12-mm-thick oriented strand board, 150-mm-thick insulation material with and without air layers, a vapour barrier foil and 12.5-mm-thick gypsum board for the interior face of the wall. The insulation materials used as reference for the proposed structures are polystyrene and rock wool. Reed straws used as insulation material for the tested wall structures formed insulation layers of 150 mm thickness in five configurations: 150-mm loose-fill reed straws without air layer and other four variants with loose-fill reed straws and 100-, 50-, 20- and 10-mm-thick air layers, respectively. The air layer was placed at the contact with gypsum board for all configurations. The reference structures (rock wool and polystyrene as insulation materials) followed three of the configurations set-up, namely 150-mm-thick insulation material (rock wool or polystyrene) only and insulation materials with air layers thicknesses of 100 and 50 mm, respectively. The eleven tested structures were subjected to thermal conductivity coefficient (λ) measurements. The tests were performed on HFM436 Lambda equipment. The structures were tested for an entire cycle of temperatures varying between -10 and $30\,°C$ and thus simulating summer and winter climate conditions. The thermal conductivity coefficient of the exterior walls filled with loose reed straws as insulation material was recorded between mean values of 0.076 and 0.077 W m^{-1} K^{-1}, except the structure with an air layer of 100 mm, for which a value of 0.120 W m^{-1} K^{-1} was registered.

Keywords Wood frame · Wall structure · Thermal conductivity · Reed straws

List of symbols

λ Thermal conductivity (W m^{-1} K^{-1})
T   Temperature (°C)
ρ Density (kg m^{-3})
ΔT Temperature difference (°C)
T_m Mean temperature (°C)
u Reed moisture content (mass%)

Subscripts

EPS   Polystyrene
RW   Rock wool
RS   Reed straws
OSB   Oriented strand board

GB   Gypsum board
VB   Vapour barrier
x   Air layer thickness

✉ Camelia Coşereanu
   cboieriu@unitbv.ro

1   Department of Wood Processing and Wood Products Design, Faculty of Wood Engineering, Transylvania University of Brasov, B-dul Eroilor 29, 500036 Brasov, Romania

Introduction

Building energy use accounts for about 40% of the total energy consumption in EU and the USA, and in European countries, the building space heating represents the most part of the energy consumption, namely 50% of the primary energy demand [1]. In this respect, building insulation materials have a major contribution to the reduction in the heating and cooling energy consumptions of buildings. Wood houses and timber frame walls filled with various thermal insulation materials play an important role in reducing the heating energy consumption level and CO_2 emissions. The comparison of different types of insulation materials should consider both the building energy

consumption and CO_2 emissions [2]. Commercial building insulation materials such as polystyrene (EPS), rock wool (RW) are used largely nowadays, but have the main drawback that they negatively affect the environment, especially due to their long time necessary to biodegrade.

The sustainability concept in building design encouraged researches in developing thermal and acoustic insulators using natural materials [3]. Several researchers focused on using small wood particles or shavings [4–6] in timber frame wall structures as loose-fill materials. Wood frame wall system with spruce bark fill material [4] proved to have low thermal conductivity values between 0.062 and 0.096 W m^{-1} K^{-1}. Other studies investigated the thermal transmittance of the building walls insulated with straw bales and reed straws as sustainable materials [7–10], recording low values of thermal transmittance for considerable thicknesses in the range of 420 to 580 mm and for the horizontally arrangement of the reed straws in the structure. Straw bales with a thickness of 50 cm proved to have low thermal conductivity of 0.067 W m^{-1} K^{-1} [10]. Wood frame walls with layers of paper spaced at 3, 5 and 7 mm were investigated for their heat insulation capacity, and thermal conductivity coefficients between 0.047 and 0.059 W m^{-1} K^{-1} were recorded. Lower thermal conductivity coefficients are obtained for the thinner air layers in the structure, due to the reduced impact of the convective heat transmittance [11]. Cellulose loose-fill material obtained from recycled paper is also studied as heat insulation material [12, 13], in wood frame wall structures registering low thermal conductivity coefficient values up to 0.050 W m^{-1} K^{-1} [12]. Flax and jute are also promising for this category of materials [14–16].

Thermal conductivity coefficient (λ) is one of the material's properties that characterize the heat insulation performance, and it is often used to select the appropriate material for building envelopes or thermal insulators [17]. Experimental methods of measuring λ are based on using heat flow meters with flux sensors and temperature control systems [6, 18] and in situ measurements using sensors for the determination of temperatures and relative humidity [19–21]. Experimental research is accompanied in several scientific papers by theoretical analysis using numerical methods [22] and computational models, such as finite methods [23–25]. An actual modern non-destructive method used to analyse the structures is the X-ray computed tomography which allows structure-based thermal modelling, applied by few researchers to investigate low-density bark-based panels as promising insulation materials [26].

This study presents an experimental approach to the thermal performance of timber frame exterior walls filled with reed straws as heat insulation materials and the comparison to similar structures where common insulation materials such as rock wool (RW) and polystyrene (EPS) were used. The thermal conductivity coefficient (λ) was measured on eleven types of wall structures including the reference ones. The study includes also an investigation on the influence of the air layer thickness on the thermal conductivity coefficient values and the variation of λ as function of density (ρ). The experiment was carried out in laboratory conditions using HFM436 Lambda apparatus (Netzsch, Selb, Germany) for the measurements.

Experimental

Materials

The core of the experimental exterior walls includes three types of thermal insulation materials (Fig. 1), namely loose bulk reed straws (RSs), rock wool (RW) and expanded polystyrene (EPS). Commercial RW and EPS having thicknesses of 50 mm were used as reference to compare the thermal insulation performance of reed straws. RS had initial moisture content (u) of 11%, bulk density (ρ) of 79.43 kg m^{-3} and a measured thermal conductivity coefficient (λ) of 0.054 W m^{-1} K^{-1}. The measured mean diameter of the reed straws was of 5 mm. RW batt (fireproof Baudeman Izo 42 Duo-Euroclass A1) with thickness of 50 mm, density of 30 kg m^{-3} and λ of 0.04 W m^{-1} K^{-1} and Baudeman EPS 50 mm (fire reaction class E1, water absorption $\leq$ 2.5%, compressive strength of 50 kPa), with density of 15 kg m^{-3} and $\lambda = 0.042$ W m^{-1} K^{-1} were used for the experimental structures. The 12-mm-thick oriented strand board (OSB 3) was used for the exterior face sheet, and commercial 12.5-mm gypsum board (GB) was used for the interior face sheet. OSB panels had a density of 600 kg m^{-3} and a thermal conductivity coefficient (λ) of 0.125 W m^{-1} K^{-1}, whilst the GB's density was 680 kg m^{-3} and measured λ was of 0.202 W m^{-1} K^{-1}. An aluminium-based foil (Isoflex Alu-PZ produced by S.C. Masterplast Romania S.R.L.) with a specific mass of 55 g m^{-2} was used as vapour barrier (VB).

Experimental Walls

The structures were formed as seen in Fig. 2, where (1) is the interior face sheet GB, (2) is the vapour barrier (VB), (3) represents the wall sides made from commercial 18-mm particleboard. Heat insulation materials (4) used for the experiment were RS, RW and EPS, respectively. The exterior face sheet of the experimental walls (5) shown in Fig. 2 is OSB 3. The wall frames were constituted from the particleboard sides which were connected with OSB

Fig. 1 Thermal insulation materials used for the experimental exterior walls; **a** reed straws; **b** rock wool; **c** polystyrene
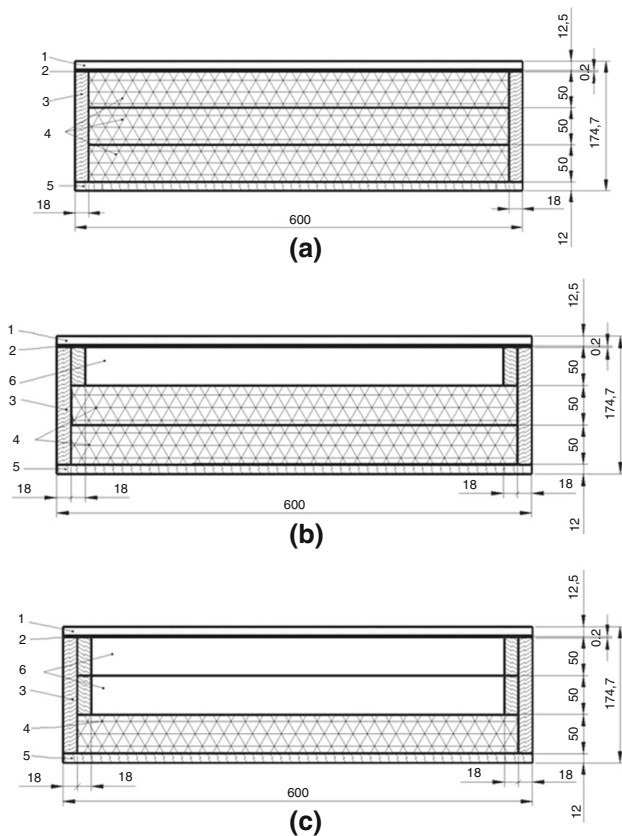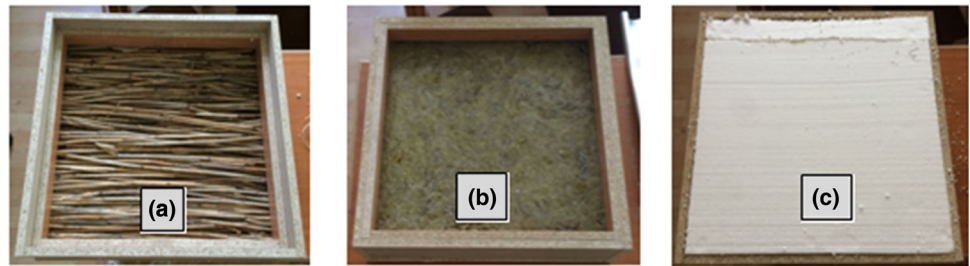

Fig. 2 Tested structures of the experimental exterior walls; **a** without air layer; **b** 50-mm air layer; **c** 100-mm air layer

exterior face sheet by screws and then filled with insulation materials.

First, the insulation materials were arranged in three layers, filling the entire interior space of the structure (Fig. 2a). Further experiments studied the influence of the thickness of the air layer upon the thermal conductivity coefficient of the structures. For this purpose, all three types of insulating materials were arranged inside the structure in one layer (50 mm thick) and two layers (100 mm thick), leaving air gaps of 100 mm (Fig. 2c) and 50 mm thick (Fig. 2b), respectively. Additional structures using reed straws as insulating materials were formed with air gaps of 20 mm and 10 mm, respectively. RSs were arranged in the structure in an uncompressed state. VB foil

and GB interior face sheet were afterwards mounted with the sides using screws.

Table 1 presents the components of the experimental walls. Structures from S1 to S6 are considered reference samples because they use common heat insulation materials and they have low thermal conductivity coefficients around 0.04 W m^{-1} K^{-1}. Eleven experimental wall structures with length × width × thickness of 600 × 600 × 174.5 mm were designed and built for thermal conductivity measurements. Two replicates of each structure type were made and tested. The mean value of the thermal conductivity coefficient for each ΔT was calculated with the recorded results of the two replicate panels. The mean value of λ for each tested structure was calculated with recorded values of λ for the nine temperatures configurations of the test, according to Table 2. Before testing, the structures were conditioned for one week to the experimental environmental conditions.

Methods

The experimental walls were subjected to thermal conductivity coefficient (λ) measurements using the hot plate technique according to ISO 8301:1991 [27] and DIN EN 12667:2001 [28].

The HFM436 Lambda apparatus (Netzsch, Selb, Germany) was used for the test. The plate temperature of this equipment ranges between − 20 and 70 °C, and the calibration curves are incorporated into the program. Lambda apparatus is provided with an external cooler, it has 10 programmable data points, and it has maximum specimen thickness of 200 mm and length × width of 610 × 610 mm. It measures thermal conductivity ranging between 0.002 and 1.0 W m^{-1} K^{-1} with an accuracy of 1 to 3%. A Peltier system is used for plate temperature control. The method is based on the determination of the heat that passes from the hot plate to the cold plate through the tested material or structure. The temperatures of the two plates and the thermal conductivity coefficient which is calculated based on Fourier's Law are automatically recorded by the software of the apparatus. The equipment was calibrated according to the temperature configuration

shown in Table 2 before starting the measurement of the thermal conductivity coefficients.

The experimental walls were installed into the Lambda apparatus so that the exterior face (OSB 3) was always placed on the cold plate. Density was introduced as input data in the apparatus software. The densities of the experimental walls were calculated as the ratio between their masses and volumes. The samples were placed between two heated plates, set at different temperatures, according to Table 2. The heat flow through the sample is measured by a calibrated heat flux transducer. After reaching a thermal equilibrium, the test is done. The sample centre (250 × 250 mm) is used for the analysis. The heat flow meter method applied for measurement is a standardized test technique [27, 28]. A calibration measurement is first taken, and then, the Q-LAB software displays three graphs that give the operator a visual indication of test progress: thermal conductivity, ΔT and mean temperature.

Results and discussion

Thermal conductivity coefficient

The experiment simulates the outdoor temperature (T_1), which varies from negative temperatures (for cold season) to positive temperatures (for warm and hot seasons) and the indoor temperature (T_2), which is a constant at value of 20 °C. Thermal conductivity coefficients were determined for each ΔT and each mean temperature T_m. The mean values and standard deviations of the measured λ for each structure are presented in Fig. 3. Standard deviations were

Table 2 Temperatures configuration set-up

| T_1*/°C	T_2**/°C	$\Delta T = T_2 - T_1$/°C	$T_m = \frac{T_1 + T_2}{2}$/°C
− 10	20	30	5
− 5	20	25	7.5
0	20	20	10
5	20	15	12.5
10	20	10	15
15	20	5	17.5
25	20	− 5	22.5
30	20	− 10	25
35	20	− 15	27.5

*Bottom plate temperature

**Upper plate temperature

calculated for each structure considering all the recorded values of λ for the two replicates and for all ΔT configurations (entire test cycle). The results show that the lowest value of the thermal conductivity coefficient λ was recorded for three-layer (150 mm thick) RW insulation material (0.049 W m^{-1} K^{-1}), followed by the wall structure having three layers of EPS heat insulation material (0.055 W m^{-1} K^{-1}). All wall structures having RS as heat insulation material recorded higher values of λ than those of the similar structures with common heat insulation materials (RW and EPS).

The air layer with a thickness of 100 mm inside the wall structures favoured the occurrence of other phenomena such as heat transfer by convection and circulation of humid air with negative effects on the heat thermal insulation performance of the structure. These phenomena are

Table 1 Components of the experimental walls

Type of insulation material	Structures	Density ρ/kg m^{-3}	Interior face sheet GB	VB	Air	EPS	RW	RS	Exterior face sheet OSB 3
			Thickness/mm						
					Core layer				
Polystyrene (EPS)	S1	94.85	12.5	0.2	100	50	–	–	12
	S2	98.80	12.5	0.2	50	100	–	–	12
	S3	102.75	12.5	0.2	–	150	–	–	12
Rock wool (RW)	S4	99.14	12.5	0.2	100	–	50	–	12
	S5	107.39	12.5	0.2	50	–	100	–	12
	S6	115.63	12.5	0.2	–	–	150	–	12
Reed straws (RSs)	S7	113.29	12.5	0.2	100	–	–	50	12
	S8	135.68	12.5	0.2	50	–	–	100	12
	S9	158.07	12.5	0.2	–	–	–	150	12
	S10	149.11	12.5	0.2	20	–	–	130	12
	S11	153.59	12.5	0.2	10	–	–	140	12

Fig. 3 Mean values and standard deviations of the thermal conductivity coefficients measured for the tested structures during the entire test cycle
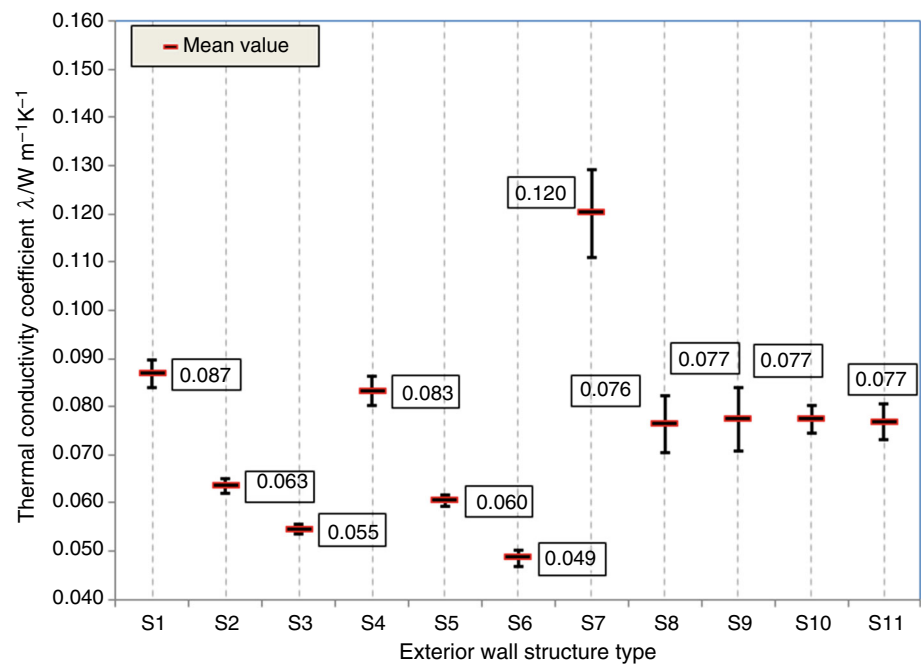
more pronounced in the case of reed structure, where the initial measured moisture content was of 11% and rise in temperature during the test led to water evaporation and increase in humidity in the air layer accompanied by the occurrence of heat transfer by convection. The result is a diminished thermal insulation capacity of this structure and a high mean value of λ, namely 0.120 W m^{-1} K^{-1} compared to 0.087 W m^{-1} K^{-1} for S1 (EPS as heat insulation material) and 0.083 W m^{-1} K^{-1} for S4 (RW as heat insulation material).

Reducing the thickness of the layer of air to 50 mm had as a result the improvement in thermal insulation capacity of all structures as follows: λ decreased by 28% for structures using EPS and RW and 38% for the structure using reed straws.

It has to be noticed that reducing the layer of air to 20 mm and 10 mm, respectively, in the case of wall structures with reed straws, the measured thermal conductivity coefficient λ remained almost constant around the value of 0.077 W m^{-1} K^{-1}.

Considering the initial measured values of λ for RW (0.04 W m^{-1} K^{-1}), EPS (0.042 W m^{-1} K^{-1}) and RS (0.054 W m^{-1} K^{-1}), the performance of the wall structures proved to be similar to the performance of the insulation material expressed by its λ. Thus, knowing the thermal conductivity coefficients of the thermal insulation materials the behaviour of the structures is predictable.

The diagrams in Fig. 4 show different values of measured λ for various ΔT. The diagrams are split into two parts according to the temperature configuration set-up shown in Table 2. Thus, ΔT with values between − 15 and

10 °C corresponds to the summer temperatures, whilst the values of ΔT higher than 10 °C correspond to winter season. As seen in Fig. 4, the thermal conductivity coefficients have higher values for temperatures corresponding to summer season (on the left side). It can be explained by the increase in temperature and occurrence of water evaporation phenomenon along with the increase in humidity inside the air cavities. Those factors led to the increase in thermal coefficient values because of the more intense movement of the humid air and the occurrence of the convection phenomenon.

The temperature environment conditions at which the structures are more stable from the thermal insulation point of view are the negative temperatures, for which the values of λ are closer. The impact of negative temperatures on the structures causes the probable occurrence of condensation inside them, and this may favour the slower movement of the humidity, resulting in less variation of thermal conductivity coefficient.

The λ measurement protocol of the wall structures was set to a continuous temperature variation from negative to positive values so that the structures are subjected to successive cooling and heating, leading to variations of thermal conductivity coefficient λ. The structures were not removed from the equipment, passing an entire cycle during testing period of time.
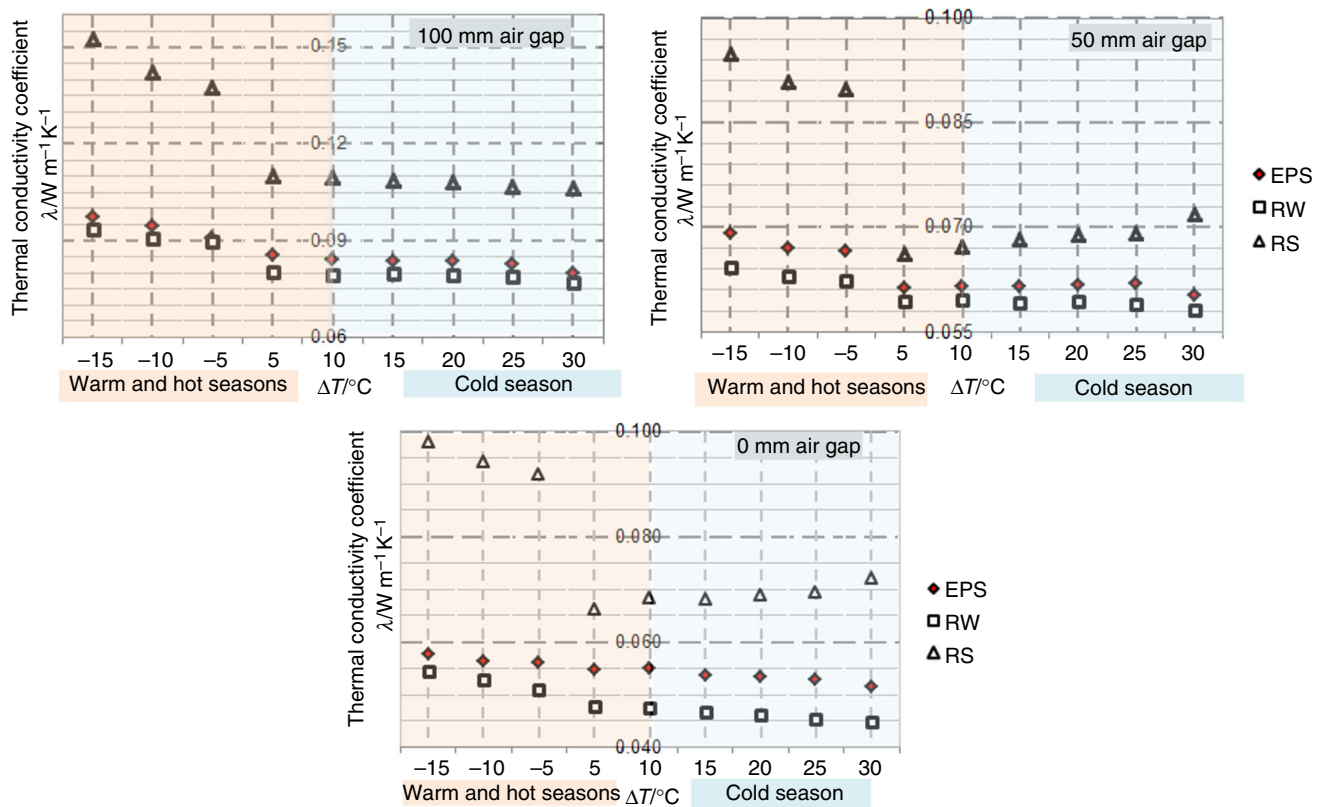
Fig. 4 Variation of thermal conductivity coefficient for similar wall structures with tested heat insulation materials: EPS, RW, RS

The influence of the air layer thickness in the case of reed straws wall structures

The graphical representation of the dependence between the thermal conductivity coefficient λ and the thickness of the air layer for wall structures with reed straws is shown in Fig. 5. As shown in Fig. 3, the mean values of thermal conductivity coefficients for this case are in a narrow range of values between 0.076 and 0.077 W m^{-1} K^{-1} for air gaps up to 50 mm thicknesses. Analysing the behaviour of the thermal conductivity coefficient for wall structures with reed straws (Fig. 5), it can be observed that the narrowest

values in the range were recorded for the walls with the air layer thicknesses of 10 and 20 mm and for the structures without air gap. Broader values in the range of measured λ were recorded for air layer thicknesses of 50 mm and 100 mm, respectively. The higher values of λ were recorded for the case when the thermal resistance of the structure was influenced by the convection heat losses because of the high temperatures specific to summer conditions and to the movement of the humid air inside the structure, namely for the structures with 100 mm air gap. As the diagram in Fig. 5 shows, these phenomena are more reduced for the structures where no air gaps or air

Fig. 5 Variation of thermal conductivity coefficient λ against the thickness of the air layer for the structures with reed straws
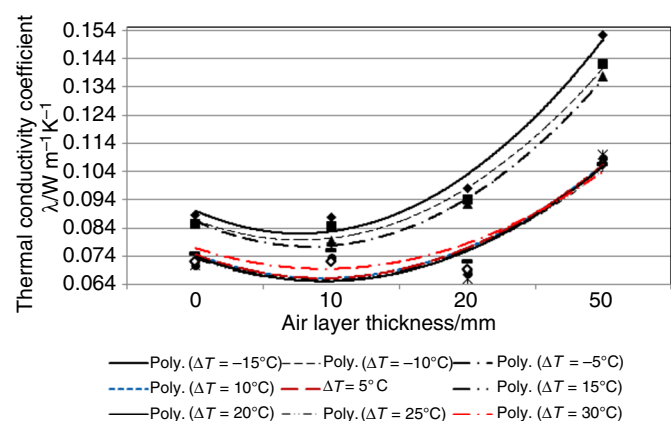
Table 3 Polynomial functions of λ against the air layer thickness inside the wall structure

ΔT/°C	T_1/°C	T_2/°C	Polynomial function (λ as a function of air layer thickness x)	R^2
30	− 10	20	$\lambda = 0.0042x^2 - 0.0184x + 0.0898$	0.77
25	− 5	20	$\lambda = 0.0048x^2 - 0.0214x + 0.0897$	0.79
20	0	20	$\lambda = 0.0049x^2 - 0.0221x + 0.0898$	0.79
15	5	20	$\lambda = 0.0048x^2 - 0.0211x + 0.088$	0.78
10	10	20	$\lambda = 0.0043x^2 - 0.0176x + 0.0835$	0.70
5	15	20	$\lambda = 0.0043x^2 - 0.0176x + 0.0835$	0.70
− 5	25	20	$\lambda = 0.009x^2 - 0.0444x + 0.1318$	0.93
− 10	30	20	$\lambda = 0.0091x^2 - 0.0443x + 0.1326$	0.93
− 15	35	20	$\lambda = 0.0101x^2 - 0.0492x + 0.1405$	0.93

thicknesses of 10 and 20 mm are present. The polynomial curves in Fig. 5 show a minimum point at an air gap of 10 mm. Figure 5 proposes a mathematical model to approximate the variation trend of λ. In fact, the experimental results for λ are not very far for air gaps up to 50 mm.

The polynomial variation of λ as a function of the air layer thickness (x) of the wall structures filled with reed straws is shown in Fig. 5, and the equations are given in Table 3, where the regression R^2 is between 0.70 and 0.79 for ΔT in the range between 5 and 30 °C and 0.93 for ΔT in the range of − 15 to − 5 °C. The weak fitting R^2 value for ΔT varying from 5 to 30 °C may be explained by collateral heat transfer phenomena that occurred when increasing the temperature of the lower plate from negative to positive values. After calibration, the lower plate reached a negative temperature of − 10 °C and the water inside the structure has frozen. With the increase in temperature, the water passed into the liquid phase and later in vapour phase, creating more numerous freely moving molecules and conferring internal mobility to water and vapours into the structure and occurrence of convective heat transfer in addition to conductive heat transfer, affecting thus the correlations with the pure conductivity phenomena.

The influence of the density on the thermal conductivity coefficient

The densities of the experimental wall structures are shown in Table 1 and Fig. 6. The highest values of the densities between 113.29 and 153.59 kg m^{-3} were recorded for the structures filled with reed straws.

Polynomial equations were found to predict the correlation between thermal conductivity coefficient and density of the structures (Fig. 6). The coefficient of determination (R^2) indicates that the predicted models completely fit for the structures filled with EPS and RW and the percentage of variations in the measured λ for the wall structures filled with RS indicates a good fit of the model.

Statistical ANOVA single-factor variance analysis was performed for the determination of the influence of the air layer thickness on the thermal conductivity coefficient value. The statistical analysis includes the mean values obtained in the experiment. Factors that significantly affect the thermal conductivity were determined using the reported p values. The thickness of the air layer was found to have a highly significant influence on the measured thermal conductivity at a 95% confidence level ($p \leq 0.05$) in the case of RW and EPS, whilst the air layer thickness in the case of RS was not statistically significant.

Conclusions

In this study, thermal conductivity of timber frame wall structures using reed straws as heat insulation materials was theoretically and experimentally investigated. Two directions were approached in the research: the first one was focused on comparing the thermal insulation capacity of reed straw (RS), as a renewable and natural resource, to that of common insulation materials such as RW and EPS; the second one investigated the influence of the wall air thickness on the performance of the thermal conductivity coefficient. With respect to the first direction, identical wall structures with RS, RW and EPS were made, tested and compared. The experimental results of λ showed best thermal performances for RW and EPS structures without air layer (0.049 and 0.055 W m^{-1} K^{-1}, respectively), compared to similar RS structures (0.077 W m^{-1} K^{-1}). Thermal conductivity ranged between 0.066 and 0.095 W m^{-1} K^{-1} for reed-filled wall structures. Similar results were recorded [4] for spruce bark (0.062 and 0.096 W m^{-1} K^{-1}) or for straw bales 50 mm thick [10]. With regard to the second research direction, the present experimental study shows that with the increase in the air layer thickness inside RW and EPS structures, λ increases by approx. 15% for the thickness of 50 mm and around 60% for the thickness of 100 mm. Similar results as for RW and EPS structures were presented by other
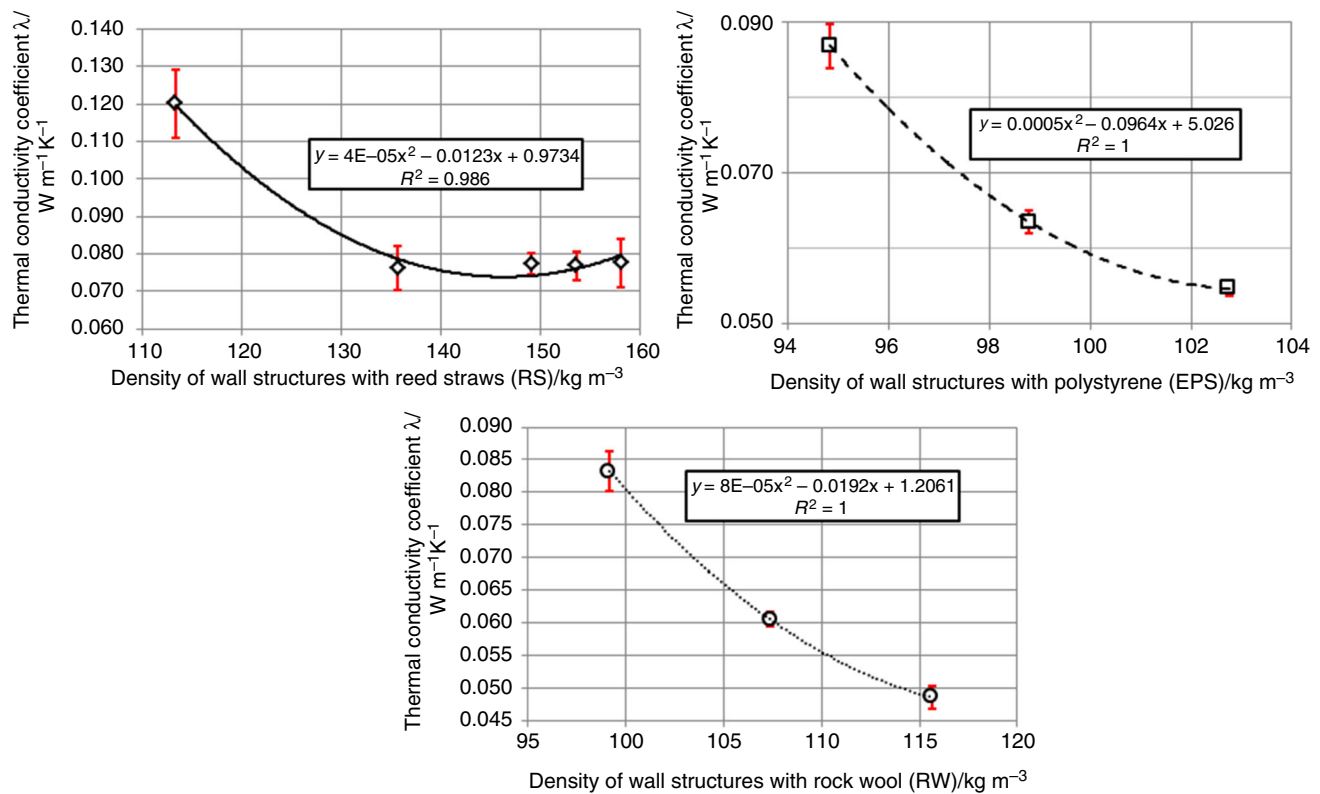
Fig. 6 Correlations between thermal conductivity coefficients and densities of the experimental wall structures

researchers [12] in case of using cellulose loose-fill material in the wood wall structure (0.050 W m^{-1} K^{-1}).

Less variation of thermal conductivity coefficient during the entire test cycle was reached by reed wall structures, for which λ was in the range of 0.076 to 0.077 W m^{-1} K^{-1} for the structures having the thicknesses of the air layer up to 50 mm. Instead, a value of 0.120 W m^{-1} K^{-1} was recorded for the structure with air layer thickness of 100 mm. The conclusion is that the same thermal performance is achieved by reed straws when the entire space inside the structures is filled with this material, or air gaps of 10, 20 or 50 mm thicknesses are left in the structure. The same trend of good thermal performance when the air gap in the structure is thinner was observed by other researchers, too [11]. Lower thermal conductivity coefficients were registered by reducing the air layer thickness from 7 to 3 mm between the layers of paper that formed the interior structure of the wood frame wall. This was explained by the reduced impact of the convective heat transmittance that occurred in the air gaps. The ANOVA single-factor variance analysis performed in the present study shows that the air gap thickness is highly significant for the thermal conductivity in the case of RW and EPS, whilst the air layer thickness in the case of RS is not statistically significant.

The present study also shows that the variation of temperatures from negative to positive ones during the test cycle together with the occurrence of water evaporation phenomenon along with the increase in humidity inside the air cavities increases the thermal conductivity coefficient values because of the more intense movement of the humid air and convection occurrence, as shown in other studies [29–31]. This assumption confirms the lower heat insulation performance of all structures having 100 mm air gap thickness.

Polynomial equations were found to predict the correlation between thermal conductivity coefficient and density of the structures. The analysis of λ values in the case of reed wall structures had as a result equations of the polynomial functions for the dependence between the thermal conductivity and the thickness of the air layer. In order to complete the conclusions of the present study, further research is planned to provide detailed information on the heat transfer phenomena inside the structures, by measuring temperature and humidity along the thickness.

References

1. Cao X, Liu J, Xilei D. Building energy-consumption status worldwide and the state-of-the-art technologies for zero-energy buildings during the past decade. Energy Build. 2016;128:198–213.
2. Su X, Luo Z, Li Y, Huang C. Life cycle inventory comparison of different building insulation materials and uncertainty analysis. J Clean Prod. 2016;112(1):275–81.
3. Asdrubali F, D'Alessandro F, Schiavoni S. A review of unconventional sustainable building insulation materials. Sustain Mater Technol. 2015;4:1–17.
4. Kain G, Barbu CM, Hinterreiter S, Richter K, Petutschnigg A. Using bark as heat insulation material. BioResources. 2013;8(3):3718–31.
5. Kain G, Lienbacher B, Barbu MC, Senck S, Alexander Petutschnigg A. Water vapour diffusion resistance of larch (*Larix decidua*) bark insulation panels and application considerations based on numeric modelling. Constr Build Mater. 2018;164:308–16.
6. Brenci LM, Cosereanu C, Zeleniuc O, Georgescu SV, Fotin A. Thermal conductivity of wood with ABS waste core sandwich composites subject to various core modifications. BioResources. 2018;13(1):555–68.
7. Miljan M, Miljan MJ, Miljan J, Akermann K, Karja K. Thermal transmittance of reed-insulated walls in a purpose-built test house. Mires Peat 2013/14;13(Article 07):1–12.
8. Miljan M, Miljan J. Thermal transmittance and the embodied energy of timber frame lightweight walls insulated with straw and reed. In: IOP conference series: Materials Science Engineering, vol. 96; 2015. p. 012076. https://doi.org/10.1088/1757-899x/96/1/012076.
9. Miljan MJ, Miljan M., Miljan J. Thermal conductivity of walls insulated with natural materials. In: 4th international conference civil engineering 13' proceedings, part I construction and materials, vol. 4; 2013. p. 175–79.
10. Ashour T, Georg H, Wu W. Performance of straw bale wall: a case of study. Energy Build. 2011;43(8):1960–7. https://doi.org/10.1016/j.enbuild.2011.04.001.
11. Pásztory Z, Horváth T, Glass SV, Zelinka SL. Thermal insulation system made of wood and paper for use in residential construction. Forest Prod J. 2015;65(7–8):352–7. https://doi.org/10.13073/FPJ-D-14-00100.
12. Nicolajsen A. Thermal transmittance of a cellulose loose-fill insulation material. Build Environ. 2005;40(7):907–14. https://doi.org/10.1016/j.buildenv.2004.08.025.
13. Zheng C, Li D, Ek M. Mechanism and kinetics of thermal degradation of insulating materials developed from cellulose fiber and fire retardants. J Thermal Anal Calorim. 2018. https://doi.org/10.1007/s10973-018-7564-5.
14. Samal S, Stuchlík M, Petrikova I. Thermal behavior of flax and jute reinforced in matrix acrylic composite. J Therm Anal Calorim. 2018;131(2):1035–40. https://doi.org/10.1007/s10973-017-6662-0.
15. Jiang Y, Lawrence M, Hussain A, Ansell M, Walker P. Comparative moisture and heat sorption properties of fibre and shiv derived from hemp and flax. Cellulose. 2018. https://doi.org/10.1007/s10570-018-2145-0.
16. Stevulova N, Estokova A, Cigasova J, Schwarzova I, Kacik F, Geffert A. Thermal degradation of natural and treated hemp hurds under air and nitrogen atmosphere. J Therm Anal Calorim. 2017;128(3):1649–60. https://doi.org/10.1007/s10973-016-6044-z.
17. Roberts BC, Webber ME, Ezekoye OA. Development of a multi-objective optimization tool for selecting thermal insulation materials in sustainable designs. Energy Build. 2015;105(15):358–67. https://doi.org/10.1016/j.enbuild.2015.07.063.
18. Kain G, Lienbacher B, Barbu M-C, Richter K, Petutschnigg A. Larch (*Larix decidua*) bark insulation board: interactions of particle orientation, physical–mechanical and thermal properties. Eur J Wood Wood Prod. 2018;76:489–98. https://doi.org/10.1007/s00107-017-1271-y.
19. Labat M, Woloszyn M, Garnier G, Roux JJ. Dynamic coupling between vapour and heat transfer in wall assemblies: Analysis of measurements achieved under real climate. Build Environ. 2015;87:129–41.
20. Durica P, Juras P, Gaspierik V, Rybarik J. Long-term monitoring of thermo-technical properties of lightweight constructions of external walls being exposed to the real conditions. Procedia Eng. 2015;111:176–82.
21. Briga-Sá A, Nascimento D, Teixeira N, Pinto J, Caldeira F, Varum H, Paiva A. Textile waste as an alternative thermal insulation building material solution. Constr Build Mater. 2013;38:155–60. https://doi.org/10.1016/j.conbuildmat.2012.08.037.
22. Vakili M, Karami M, Delfani S, Khosrojerdi S, Kalhor K. Experimental investigation and modeling of thermal conductivity of CuO–water/EG nanofluid by FFBP-ANN and multiple regressions. J Therm Anal Calorim. 2017;129(2):629–37. https://doi.org/10.1007/s10973-017-6217-4.
23. Balaji N, Mani M, Venkatarama Reddy BV. Thermal performance of the building walls. In: Preprints of the 1st IBPSA Italy conference Free University of Bozen-Bolzano, vol. 346; 2013. p. 1–7.
24. Bassiouny R, Ali MRO, NourEldeen E-SH. Modeling the thermal behavior of Egyptian perforated masonry red brick filled with material of low thermal conductivity. J Build Eng. 2016;5:158–64.
25. Czajkowski Ł, Olek W, Weres J, Guzenda R. Thermal properties of wood-based panels: thermal conductivity identification with inverse modelling. Eur J Wood Wood Prod. 2016;74:577–84. https://doi.org/10.1007/s00107-016-1021-6.
26. Kain G, Lienbacher B, Barbu MC, Plank B, Richter K, Petutschnigg A. Evaluation of relationships between particle orientation and thermal conductivity in bark insulation board by means of CT and discrete modelling. Case Stud Nondestr Test Eval. 2016;6:21–9.
27. ISO 8301. Thermal insulation—determination of steady-state thermal resistance and related properties—heat flow meter apparatus. International Organization for Standardization, Geneva, Switzerland 1991.
28. DIN EN 12667. Thermal performance of building materials and products—determination of thermal resistance by means of guarded hot plate and heat flow meter methods—products of high and medium thermal resistance. German Institute for Standardization, Berlin, Germany 2001.
29. Bedane AH, Afzal MT, Sokhansanj S. Simulation of temperature and moisture changes during storage of woody biomass owing to weather variability. Biomass Bioenergy. 2011;35:3147–51.
30. Bryś A, Bryś J, Ostrowska-Ligeza E, Kaleta A, Górnicki K, Glowacki S, Koczon P. Wood biomass characterization by DSC or FT-IR spectroscopy. J Therm Anal Calorim. 2016;126(1):27–35. https://doi.org/10.1007/s10973-016-5713-2.
31. Modarresifar F, Bingham PA, Jubb GA. Thermal conductivity of refractory glass fibres. J Therm Anal Calorim. 2016;125(1):35–44. https://doi.org/10.1007/s10973-016-5367-0.

Thermal Conductivity of Wood with ABS Waste Core Sandwich Composites Subject to Various Core Modifications

Luminita-Maria Brenci, Camelia Cosereanu, Octavia Zeleniuc,
Sergiu-Valeriu Georgescu,* and Adriana Fotin

Five types of alternative sandwich composite structures designed for building walls were investigated in this study using various core materials such as wood shavings, recycled acrylonitrile butadiene styrene panels, and rock wool. The sandwich structures were designed for exterior walls with a thickness of 175 mm. The experiment simulated the conditions for inside and outside temperatures during winter and summer seasons. The thermal conductivity coefficient associated with winter was lower by about 55% than those registered for summer. Wood shavings and one ABS panel as core components led to the most thermally stable structure. The best insulation solutions were the rock wool core structures with a mean thermal conductivity coefficient between 0.0564 W/mK and 0.0605 W/mK for the entire testing cycle. The two ABS panels from the core configurations had a negative impact on the thermal performance. The lowest thermal performance was recorded by the pure wood shavings core structure, with a maximum value of thermal conductivity coefficient of 0.150 W/mK. Compressed wood shaving core structures can compete with rock wool as thermal insulation solution.

Contact information: Transylvania University of Brasov, Faculty of Wood Engineering, Department of Wood Processing and Wood Products Design, 29 Eroilor Blvd, 500036 Brasov, Romania;
 * Corresponding author: sergiu.georgescu@unitbv.ro

INTRODUCTION

The thermal conductivity of an insulating material is an important thermal property to be considered when rating the materials for building construction. A high resistance to heat flow and a low thermal conductivity coefficient is recommended for materials that are utilized as thermal insulators. The most commonly used building insulation materials are polystyrene (extruded and expanded), rock wool and glass wool, polyurethane, and foam glass. The possibility of high CO_2 emissions during production and their short life cycle make them less desirable as building materials (Su *et al.* 2016). Carbon reduction is an important advantage of wood buildings because only one cubic meter of structural lumber stores 0.9 tons of CO_2 from the atmosphere (Asdrubali *et al.* 2017).

New raw materials, such as cellulose loose-fill (Nicolajsen 2005), wood wastes (Agoua *et al.* 2013), hemp (Benfratello *et al.* 2013; Zach *et al.* 2013; Latif *et al.* 2014), bark wastes (Kain *et al.* 2013), olive seeds (Binici and Aksogan 2016), cork (Limam *et al.* 2016), and palm tree surface fibers (Ali and Alabdulkarem 2017) have been investigated in recent years, especially with regard to their thermal insulating properties.

These innovative insulation materials are currently studied as alternative solutions to traditional insulators. Some modern cellulose insulation materials are made from recycled newspaper, such as soft fiber pulp spray-applied product and cellulose loose-fill insulation material, which have thermal conductivity values of 0.040 W/mK (Roberts *et al.* 2015) and 0.050 W/mK (Nicolajsen 2005), respectively. Straw bales with a thickness of 50 cm have also been investigated (Ashour *et al.* 2011). These experimental samples show a low thermal conductivity of 0.067 W/mK. Panels made from olive seeds, wood shavings, PVC grounds, and epoxy resin, at various rates and with densities around 1000 kg/m^3 have a thermal conductivity coefficient in the range of 0.0742 W/mK to 0.145 W/mK. A low density in samples results in lower heat transfer coefficients (Binici and Aksogan 2016). Natural insulation materials made only from pure untreated wood fibers have low thermal conductivity coefficients (0.04363 W/mK dried-up samples) (Zach *et al.* 2013).

Most studies dealing with insulation materials (cork, bark, rice straw, hemp, *etc.*) report low densities between 170 kg/m^3 and 260 kg/m^3 and low thermal conductivity coefficients between 0.0475 W/mK and 0.0697 W/mK (Kain *et al.* 2013; Wei *et al.* 2015; Ali and Alabdulkarem 2017). In contrast, a low-density board of 212 kg/m^3 made from corn cob had a higher thermal conductivity coefficient of 0.139 W/mK (Pinto *et al.* 2012).

Sandwich structures are more and more used for their various applications, having the advantage of light weight without affecting the level of performance and their mechanical responses change with the variation of thermal conductivity and density. (Mehar *et al.* 2017). Wood frame wall systems are considered better alternatives for fire resistant and hygro-thermal performant walls. In these cases, the heat transfer coefficient ranges between 0.204 W/m^{2}K and 0.30 W/m^{2}K for structural wood-paper frame wall of 185 mm thick (Pásztory *et al.* 2015) and for a wood frame with hemp and stone wool insulations 100 mm thick (Latif *et al.* 2014), respectively. A similar heat transfer coefficient of about 0.200 W/m^{2}K was obtained for a wall system made of 5 cm-thick reinforced concrete and 80 cm-thick glulam studs filled with polystyrene foam with a 3-cm air gap (Destro *et al.* 2015). Bark fill material at a density of 250 kg/m^3 for bark loose bulks was used in a wood frame wall system (Kain *et al.* 2013) and showed low thermal conductivity values in the range of 0.062 W/mK and 0.096 W/mK. The performance of the bark fill was not as good as light insulation materials such as polystyrene or rock wool because of the relatively high density of bark loose bulks. The methods for measuring thermal parameters are generally based on sensors and monitors placed in the wall structure to hourly record the temperature, moisture content, and relative humidity in order to assess the influence of these parameters on the heat transfer (Kain *et al.* 2013; Wang *et al.* 2013; Latif *et al.* 2014; Pásztory *et al.* 2015). Besides density, an increase in temperature and moisture content in wall panels causes an increase of thermal conductivity influenced by the porous structure and the different intermolecular distances of matter at different states (Latif *et al.* 2014; Wei *et al.* 2015). The use of wooden elements in wall structures improves their thermal performances compared with masonry and concrete systems (Destro *et al.* 2015).

This study focused on creating wooden sandwich composite structures for walls with different cores design at the laboratory level. The thermal conductivity coefficient was measured on five types of structures. Spruce wood (*Picea abies*) was used for frame and wood shavings, and rock wool and hot pressed acrylonitrile butadiene styrene (ABS)

panels constituted the core. The thermal conductivity was automatically measured based on thickness, density, temperature gradient, and mean temperatures.

EXPERIMENTAL

Materials

The experimental walls included acrylonitrile butadiene styrene (ABS) wastes as manufactured panels, and wood shavings (WS) and rock wool (RW) as loose bulk for the core. The wastes used for the core (ABS and WS) were provided by the small scale furniture production site at Faculty of Wood Engineering in Romania. The oriented strand board (OSB) and commercial gypsum board (GB) were used for the face sheets. OSB panels had a density of 660 kg/m^3 and a thermal conductivity coefficient (λ) of 0.125 W/mK, whilst the GB's density was 650 kg/m^3 and measured λ was 0.225 W/mK. The polyethylene foil (P) with a specific weight of 195 g/m^2 was used as a vapor barrier in the sandwich structure.

Mixed spruce (80% share in the mat) and beech (20% share in the mat) wood shavings (WS) collected from milling machines and planer were used in the sandwich composite cores. The initial moisture content of wood shavings (before forming the structures) ranged between 8.2% and 8.7% (greater for the softwood). Few days after, the structures were constituted and they were conditioned to stable conditions at a relative humidity of 65% and temperature of 20 ℃, before installation and starting the tests. WS are relatively thin and wide and occupy a large unit of space, so it constituted the porous structure of the wall. The loose bulk density for the WS was approximately 135 kg/m^3 (for S2), whilst the compacted bulk density was 160 kg/m^3 (for a compaction ratio of 1.2 for structures S1 and S3). The shavings length varied from 12 mm to 38.7 mm for flakes and from 1.2 mm to 12 mm for particles, with a thickness between 0.2 mm and 0.5 mm. The shares of flakes and particles into the WS were 25% and 75% respectively (Fig. 1a). Curled flakes create large voids, which could be filled by mixing them with particles from milling, thus intending to improve the thermal insulation of WS. Even so, a definitive pattern of variation of thermal coefficient with particle sizes it is difficult to be established, because of the heterogeneous structure of wood (Oluyamo and Bello 2014).
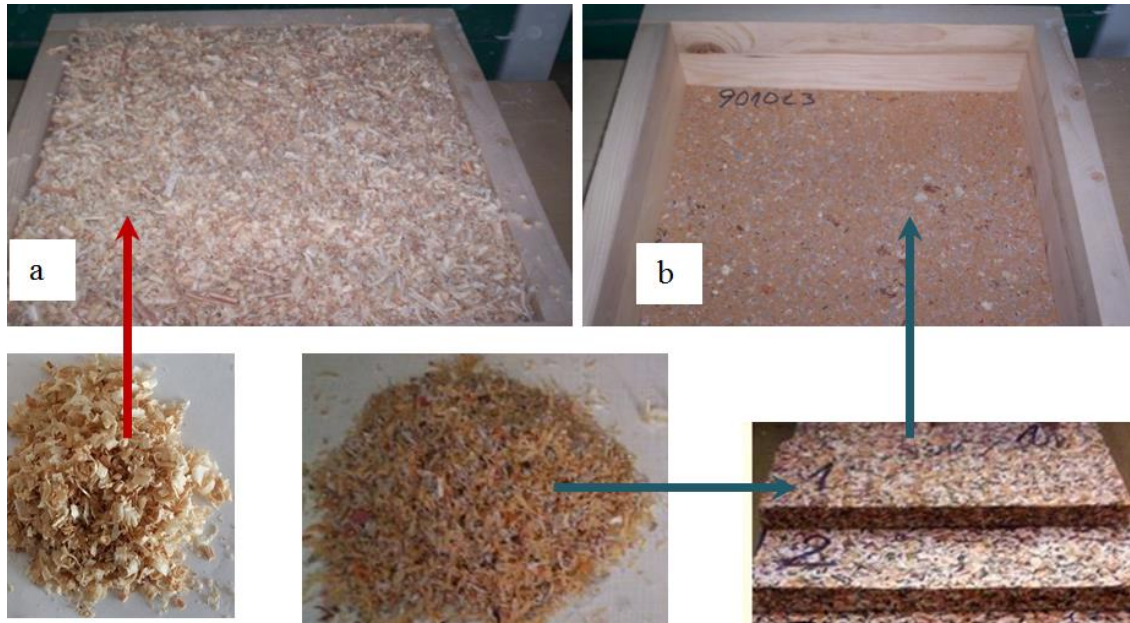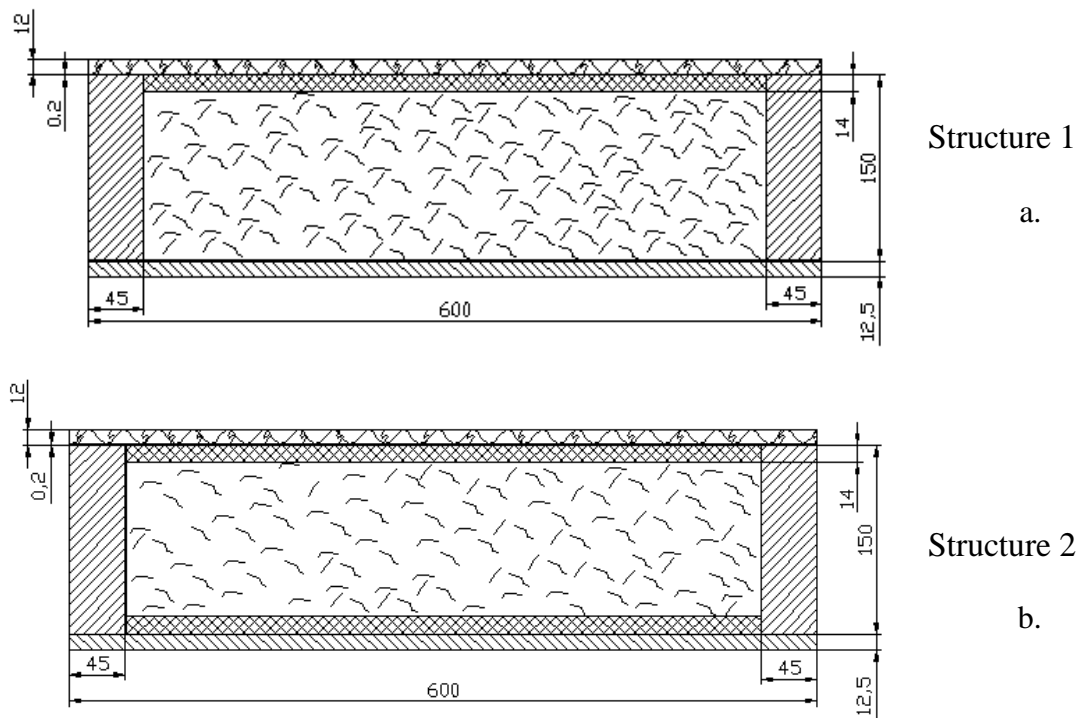
Fig. 1. Wood shavings (a) and ABS panel (b) used for the core experimental wall structures
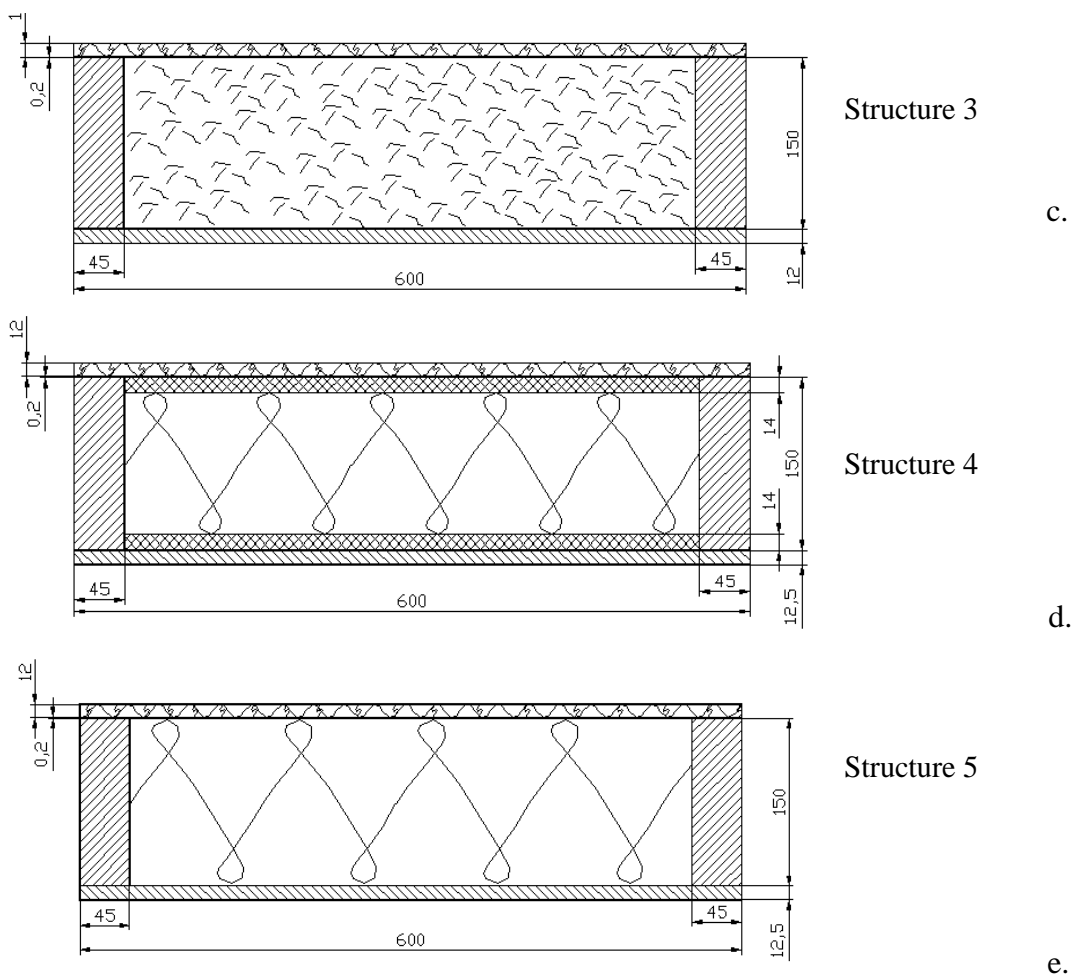

Structure 1

a.

Structure 2

b.

Fig. 2. Designed sandwich composite structures of the experimental walls

ABS was collected as waste and removed from the edge of the banding operation. The wastes were collected in a special bag attached to the machine exhaust outlet. ABS particles with lengths between 2 mm and 20 mm, widths between 0.5 mm and 3 mm, and with a 0.2 mm thickness formed a mat, which was hot pressed for 20 min at a temperature of 130 °C and a pressure of 20 bar (Cosereanu and Lica 2014). ABS panels (Fig. 1b) with the dimensions 600 mm x 600 mm and density of 240 kg/m^3 were obtained. They were then sized to the final dimensions of 510 mm x 510 mm x 14 mm and used for the core of the experimental walls.

Experimental Walls

Five experimental wall structures with a length of 600 mm, a width of 600 mm, and a thickness of 175 mm were designed and built for thermal conductivity measurements. The designed structures of the walls are presented in Fig. 2. The walls were designed as sandwich structures (Table 1), composed of wooden frames, cores, and two face sheets. The wood frames were made from spruce wood (*Picea abies*) with a thickness of 45 mm. Each wood frame was planked with a 12.5 mm gypsum board (GB) on one side and a 12 mm OSB panel on the other side. The experimental walls were designed with various core compositions, as specified in Table 1.

bioresources.com

Structure S5 was considered a reference sample because of the low thermal conductivity coefficient of rock wool core, which had a measured thermal conductivity coefficient of 0.037 W/mK at a density of 30 kg/m^3, and it is a material generally used for insulations.

Table 1. Components of Designed Walls

Structures and Materials	Inside Face Sheet		Core				Outside Face Sheet
	GB	P	ABS	WS	RW	ABS	OSB
Structure 1 (S1)	x	x	-	x	-	x	x
Structure 2 (S2)	x	x	x	x	-	x	x
Structure 3 (S3)	x	x	-	x	-	-	x
Structure 4 (S4)	x	x	x	-	x	x	x
Structure 5 (S5)	x	x	-	-	x	-	x
x – raw material used in the structure							

Methods

The five structures of the experimental walls were subjected to thermal conductivity coefficient (λ) measurements. The tests were performed on HFM436 Lambda equipment (Netzsch, Selb, Germany), according to ISO 8301 (1991) and DIN EN 12667 (2001). This testing method is based on the determination of the quantity of heat that is passed from a hot plate to a cold plate through the sandwich composite structure.

The temperature difference between the two plates is registered, and the thermal conductivity coefficient is automatically calculated based on Fourier's Law. Before the samples were tested, the equipment was calibrated depending on the temperature differences (ΔT) and mean temperatures (T_m). Table 2 presents the values set for temperature configuration.

Table 2. Temperatures Configuration Set Up

ΔT = T$_1$-T$_2$ in °C	$T_m = \frac{T_1+T_2}{2}$ in °C												
	-5		0		5		10		15		20		25	
	T$_1$	T$_2$	T$_1$	T$_2$	T$_1$	T$_2$	T$_1$	T$_2$	T$_1$	T$_2$	T$_1$	T$_2$	T$_1$	T$_2$
10	0	-10	5	-5	7.5	2.5	15	5	20	10	25	15	30	20
15	2.5	-12.5	7.5	-7.5	12.5	-2.5	17.5	2.5	22.5	7.5	27.5	12.5	32.5	17.5
20	5	-15	10	-10	15	-5	20	0	25	5	30	10	35	15
25	7.5	-17.5	12.5	-12.5	17.5	-7.5	22.5	-2.5	27.5	2.5	32.5	7.5	37.5	12.5
30	10	-20	15	-15	20	-10	25	-5	30	0	35	5	40	10

(T$_1$) upper plate temperature
(T$_2$) bottom plate temperature

Density was introduced as input data in the equipment software. The density was calculated as the ratio between mass and volume of the tested structure. Two specimens of each structure were built and tested, and the results presented are the mean values.

RESULTS AND DISCUSSION

The experiment simulates the outdoor temperatures (T_2), indoor temperatures (T_1), and differences between them (ΔT). Thermal conductivity coefficients were determined for each ΔT and each mean temperature T_m. The results are presented in the histograms in Fig. 3.

The mean temperature values used in the experimental measurements were characterized by two intervals: T_m of -5 °C, 0 °C, and 5 °C for the winter season, and T_m of 15 °C, 20 °C, and 25 °C for the summer season.

The structures are not homogeneous, so they did not have a predictable behavior (increase or decrease), of thermal coefficient considering the variation of the experimental setup conditions. The impact of negative temperatures on the structures caused the probable occurrence of condensation inside the structures.

The sudden rise in temperature (in the case of ΔT = 10 °C) in structures 3 and 5 (the simplest ones), for T_m between 5 °C and 10 °C favored the humidity circulation inside the structure, which led to a sudden increase of thermal coefficient. Inside the structures, pure thermal conductivity along with other phenomena associated with moisture and heat transfer occurs. Moreover, heat transfer by convection and capillarity takes place. These phenomena lead to an increase in the thermal coefficient value, observed mainly with the structures having loose bulk wood shavings as core.

For all structures, as can be observed in Fig. 4, when ΔT increases (from ΔT = 10 °C to ΔT = 30 °C), the negative temperature field of T_2 (blue area) extends from T_m = 5 °C to 15 °C. The conditions at which the structures are subjected, are more stable (negative temperatures) for a longer period of time, between ΔT = 20 °C and ΔT = 30 °C. This may have favored the conditions of thermal and humidity transfer determining a slower reaction of the structures components, resulting in a less variation of thermal conductivity coefficient.
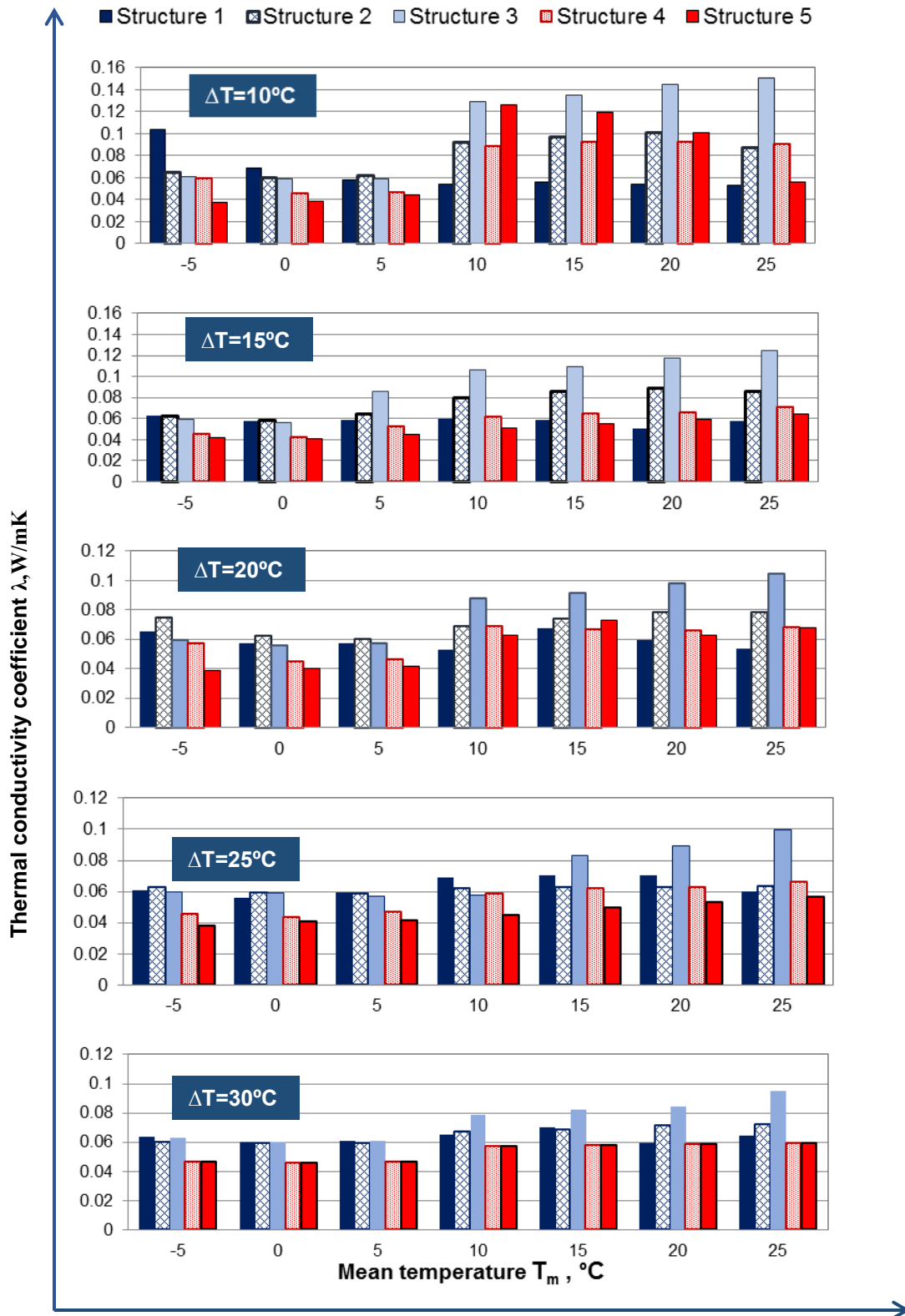
Fig. 3. Thermal conductivity coefficient values at various temperature differences between equipment hot plate and cold plate (ΔT) and at different mean temperatures T_m
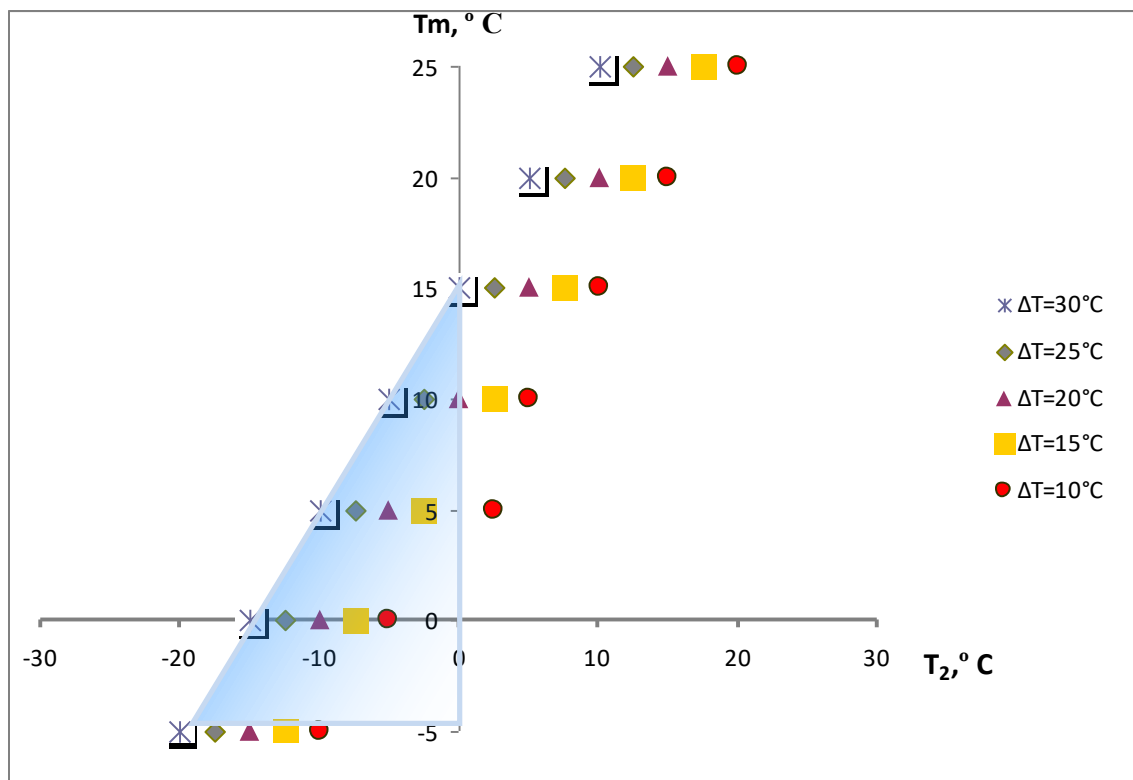
Fig. 4. The evolution of negative and positive temperature zones according to variation of ΔT

For each structure, the same measurement protocol was used. The test consisted of a continuous passage of structures from negative to positive values of temperature T_2. The structures had undergone through successive cooling and heating, which influenced the core thermal behavior, leading to oscillatory variation of thermal conductivity coefficient λ (*i.e.* S5 at $\Delta T = 10$ °C and $\Delta T = 15$ °C). During the testing time the structures were not removed from the equipment, passing an entire cycle testing period.

The structures are defined in two categories based on the core components: one filled with wood shavings (S1, S2, and S3) and the other one with rock wool (S4 and S5). Analyzing the behavior of the first category, it can be observed that the structure S3 (the simplest one) does not provide the required thermal resistance to reduce convection heat losses due to the local temperature differences appeared in the structure during the summer. In summer time, accumulated heat was higher than in winter, S3 recording the highest thermal coefficient of 0.150 W/mK.

The same trend can be observed in structures S1 and S2, but the phenomenon is less amplified due to the presence of the ABS layer acting as a moisture barrier. Generally, structure S1 had the lowest λ coefficient compared to S3 and S2 in both seasons (below 0.063 W/mK) (Fig. 5), showing a smaller variation related to T_m and ΔT. On the other hand, reducing voids by compaction of shavings, the convective loops are eliminated and convection heat losses are diminished.

The gaps between flakes for S2 with loose bulk core shavings favor the heat flow, resulting in convective heat transfer and a higher λ.
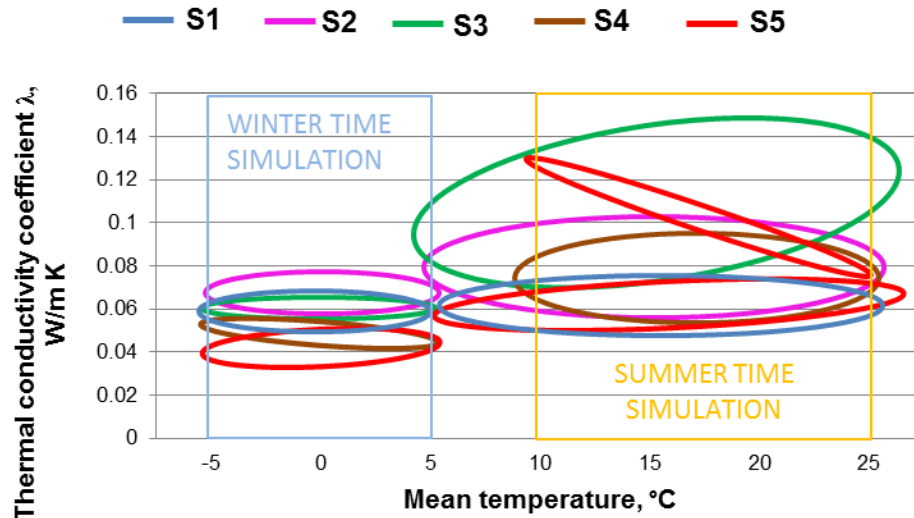
Fig. 5. Comparison between thermal conductivity coefficient limits of investigated structures in the conditions of both winter and summer season simulation

Structure S5 had a lower thermal conductivity compared to S4 (both with rock wool core). The mean values for the entire testing cycle were 0.0564 W/mK for S5 and 0.0605 W/mK for S4 (Fig. 6). The differences between these structures are attributed to core structure, S4 including ASB layers on both sides. The upper layer (from the exterior) might control the interior humidity to lower level during cold periods, thermal coefficient reaching values below 0.06 W/mK. During summer time the ABS bottom layer (from the interior) favored the increasing of λ to values ranging from 0.090 W/mK (ΔT=10 ℃) to 0.071 W/mK (ΔT=15 ℃) and 0.059 W/mK (ΔT=30 ℃).

From the analyzed structures, it can be seen that S5 and S1 had a better performance compared to the other structures with the lowest values of λ throughout the test cycle (0.0564 W/mK for S5 and 0.0614 W/mK for S1) (Fig 6).
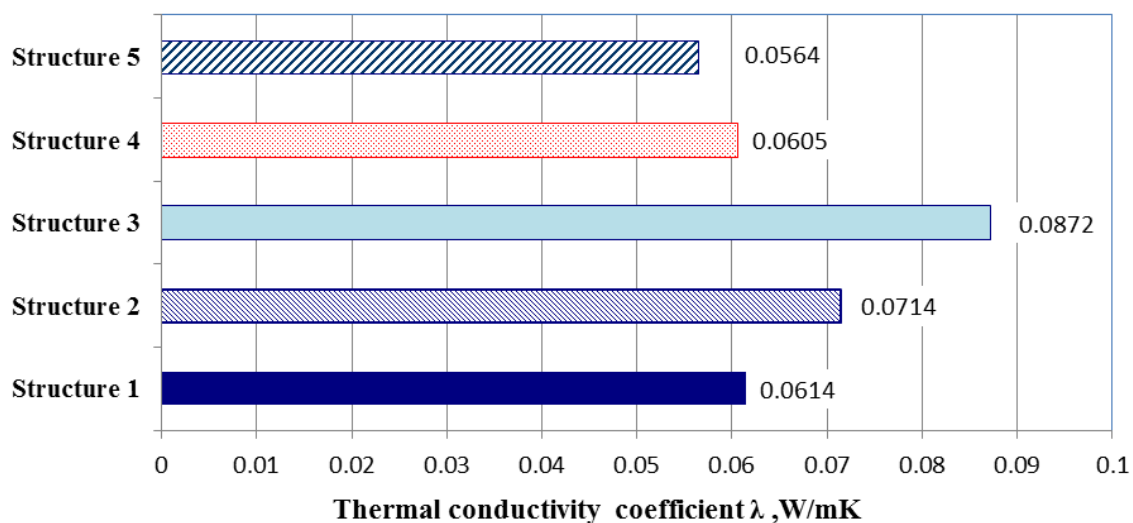

Fig. 6. Mean values of thermal conductivity coefficient for the entire test cycle

The densities of the experimental wall structures and standard deviations are shown in Fig. 7. The highest density (299 kg/m^3) was recorded for S2, having a core composition of wood shavings and two panels made from ABS wastes.
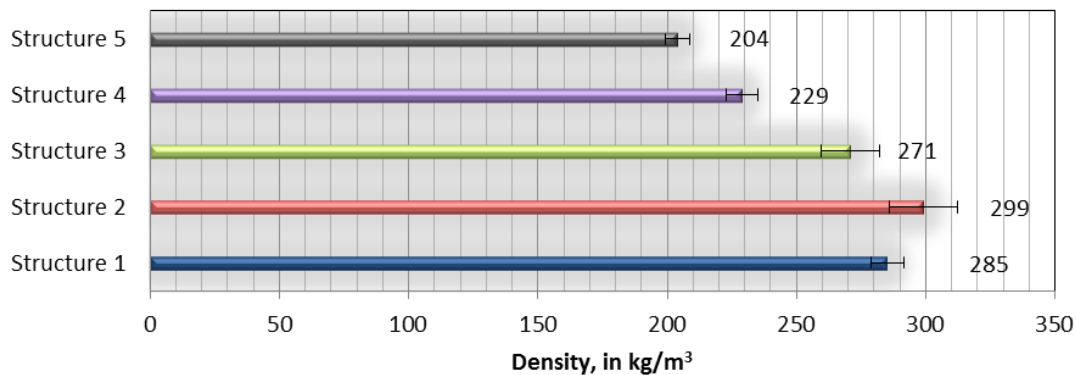

Fig. 7. Histogram of densities of the experimental wall structures

The lowest density value (204 kg/m^3) was in S5 (reference) witch was composed only of rock wool core and OSB/ GB faces. The spread values of the λ at different densities and the ΔT limits are shown in the left panel in Fig. 8. The mean values of λ and standard deviations of all structures are shown in the right panel in Fig. 8.
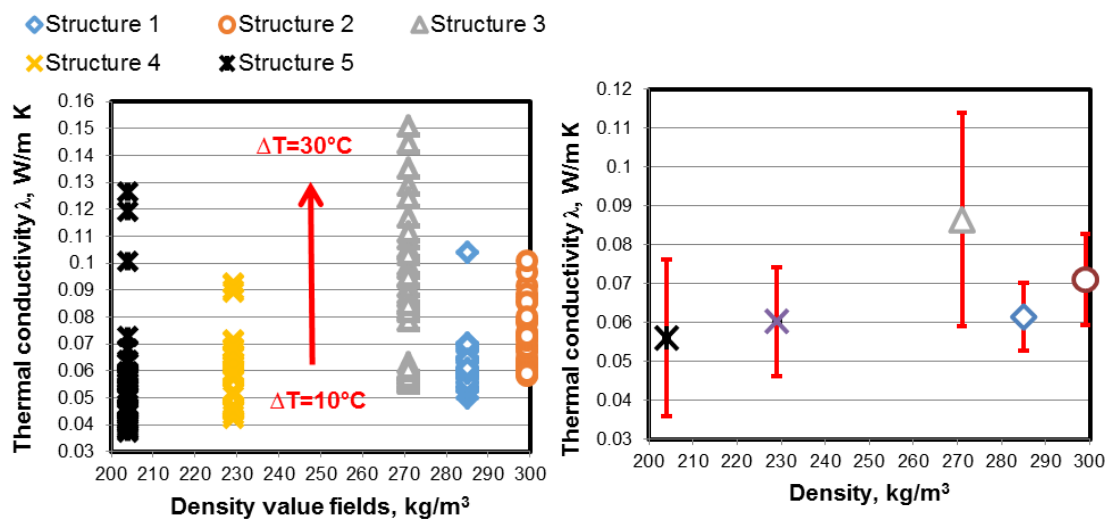

Fig. 8. Histogram of thermal conductivity against structure density for all ΔT (left) and mean values of thermal conductivity coefficient (right)

The influence of the interaction of factors on the thermal conductivity coefficient was performed using the statistical ANOVA single-factor variance analysis. Differences were considered statistically significant at p ≤ 0.05. Factors that significantly affect the thermal conductivity were determined using the reported p-values. After performing the statistical analysis of the mean values obtained in the experiment, ΔT and density were found to have a highly significant influence on the measured thermal conductivity at a 95% confidence level (p ≤ 0.05), whilst the mean temperature was not statistically significant.

CONCLUSIONS

1. The best thermal performance was recorded for S5 followed by S4, rock wool core as low density fibrous insulation layer reaching the lowest thermal conductivity coefficient compared to wood shaving core structures.

2. Less variation of thermal conductivity coefficient during the entire testing cycle was reached by S1. This structure registered a better thermal behavior compared to structures containing in their core wood shavings (S2 and S3).

3. The successive cooling and heating phases during the testing cycle influenced the thermal behavior of structures, perceived as oscillatory variation of thermal conductivity. Inside the structures there is not only pure thermal conductivity, others phenomena associated to moisture and heat transfer occurred.

4. The ABS layer applied above the gypsum board didn't improve the insulation behaviour of S2 and S4 structures.

5. Both density and ΔT influenced to a greater extend the thermal conductivity coefficient than the mean temperature T_m

6. Wood shavings compressed to a lower density, as an ecological and inexpensive material could represent a viable solution for thermal insulation compared with rock wool.

ACKNOWLEDGMENTS

REFERENCES CITED

Agoua, E., Allognon-Houessou, E., Adjovi, E., and Togbedji, B. (2013). "Thermal conductivity of composites made of wastes of wood and expanded polystyrene," *Construction and Building Materials* 41(109), 557-562. DOI: 10.1016/j.conbuildmat.2012.12.016

Ali, M. E., and Alabdulkarem, A. (2017). "On thermal characteristics and microstructure of a new insulation material extracted from date palm trees surface fibers," *Construction and Building Materials* 138(52), 276-284. DOI: 10.1016/j.conbuildmat.2017.02.012

Asdrubali, F., Ferracuti, B., Lombardi, L., Guattari, C., Evangelisti, L., and Grazieschi, G. (2017). "A review of structural, thermo-physical, acoustical, and environmental properties of wooden materials for building applications," *Building and Environment* 114(March 2017), 307-332. DOI: 10.1016/j.buildenv.2016.12.033

Ashour, T., Georg, H., and Wu, W. (2011). "Performance of straw bale wall: A case of study," *Energy and Buildings* 43(8), 1960-1967. DOI: 10.1016/j.enbuild.2011.04.001

Benfratello, S., Capitano C., Peri, G., Rizzo G., Scaccianoce, G., and Sorrentino, G. (2013). "Thermal and structural properties of a hemp-lime biocomposite,"

Construction and Building Materials 48(November 2013), 745-754. DOI: 10.1016/j.conbuildmat.2013.07.096

Binici, H., and Aksogan, O. (2016). "Eco-friendly insulation material production with waste olive seeds, ground PVC and wood chips," *Journal of Building Engineering* 5(March 2016) 260-266. DOI: 10.1016/j.jobe.2016.01.008

Cosereanu, C., and Lica, D. (2014). "Wood-plastic composites from waste materials resulted in the furniture manufacturing process," *Pro Ligno* 10(2), 26-33.

Destro, R., Boscato, G., Mazzali, U., Russo, S., Peron, F., and Romagnoni, P. (2015). "Structural and thermal behaviour of a timber-concrete prefabricated composite wall system," *Energy Procedia* 78(November 2015), 2730-2735. DOI: 10.1016/j.egypro.2015.11.614

DIN EN 12667 (2001). "Thermal performance of building materials and products - Determination of thermal resistance by means of guarded hot plate and heat flow meter methods - Products of high and medium thermal resistance," German Institute for Standardization, Berlin, Germany.

ISO 8301. (1991). "Thermal insulation - Determination of steady-state thermal resistance and related properties - Heat flow meter apparatus," International Organization for Standardization, Geneva, Switzerland.

Kain, G., Barbu, C. M., Hinterreiter, S., Richter, K., and Petutschnigg, A. (2013). "Using bark as heat insulation material," *BioResources* 8(3), 3718-3731. DOI: 10.15376/biores.8.3.3718-3731

Latif, E., Ciupala, M. A., and Wijeyesekera, D. C. (2014). "The comparative in situ hygrothermal performance of hemp and stone wool insulations in vapour open timber frame wall panels," *Construction and Building Materials* 73(30 December 2014), 205-213. DOI: 10.1016/j.conbuildmat.2014.09.060

Limam, A., Zerizer, A., Quenard, D., Sallee, H., and Chenak, A. (2016). "Experimental thermal characterization of bio-based materials (Aleppo Pine wood, cork and their composites) for building insulation," *Energy and Buildings* 116(15 March 2016), 89-95. DOI: 10.1016/j.enbuild.2016.01.007

Mehar, K., Panda, S. K., and Patle, B. K. (2017). "Stress, deflection, and frequency analysis of CNT reinforced graded sandwich plate under uniform and linear thermal environment: A finite element approach," *Polymer Composites,* Version of Record online 17 May 2017, available on http://onlinelibrary.wiley.com. DOI: 10.1002/pc.24409

Nicolajsen, A. (2005). "Thermal transmittance of a cellulose loose-fill insulation material," *Building and Environment* 40(7), 907-914. DOI: 10.1016/j.buildenv.2004.08.025

Oluyamo, S. S., and Bello, O. R. (2014). "Particle sizes and thermal insulation properties of some selected wood materials for solar device applications," *IOSR Journal of Applied Physics* 6(2) Ver.I, 54-58. DOI: 10.9790/4861-06215458

Pásztory, Z., Horváth, T., Glass, S. V., and Zelinka S. L. (2015). "Thermal insulation system made of wood and paper for use in residential construction," *Forest Products Journal* 65(7-8), 352-357. DOI: 10.13073/FPJ-D-14-00100

Pinto, J., Cruz, D., Paiva, A., Pereira, S., Tavares, P., Fernandes, L., and Varum, H. (2012). "Characterization of corn cob as a possible raw building material," *Construction and Building Materials* 34(September 2012), 28-33. DOI: 10.1016/j.conbuildmat.2012.02.014

bioresources.com

Roberts, B. C., Webber, M. E., and Ezekoye, O. A. (2015). "Development of a multi-objective optimization tool for selecting thermal insulation materials in sustainable designs," *Energy and Buildings* 105(15), 358-367. DOI: 10.1016/j.enbuild.2015.07.063

Su, X., Luo, Z., Li, Y., and Huang, C. (2016). "Life cycle inventory comparison of different building insulation materials and uncertainty analysis," *Journal of Cleaner Production* 112(Part 1), 275-281. DOI: 10.1016/j.jclepro.2015.08.113

Wang, X., Fei, B., and Ni, J. (2013). "Experimental assessment of hygrothermal performance of wood frame wall system in Suzhou's Lake Tai climate zone," *BioResources* 8(3), 4702-4710. DOI: 10.15376/biores.8.3.4702-4710

Wei, K., Lv, C., Chen, M., Zhou, X., Dai, Z., and Shen, D. (2015). "Development and performance evaluation of a new thermal insulation material from rice straw using high frequency hot-pressing," *Energy and Buildings* 87(1 January), 116-122. DOI: 10.1016/j.enbuild.2014.11.026

Zach, J., Hroudová, J., Brožovský, J., Krejza, Z., and Gailius, A. (2013). "Development of thermal insulating materials on natural base for thermal insulation systems," *Procedia Engineering* 57(2013), 1288-1294. DOI: 10.1016/j.proeng.2013.04.162

Effect of Particle Size and Geometry on the Performance of Single-layer and Three-layer Particleboard Made from Sunflower Seed Husks

Camelia Cosereanu,* Luminita-Maria Brenci, Octavia Zeleniuc, and Adriana Fotin

The effects of particle size and geometry on the physical (density, water absorption, and thickness swelling), thermal, and mechanical (modulus of elasticity, bending strength, internal bond strength, and screw holding strength) properties of single-layer and three-layer particleboards made from sunflower seed husks were investigated. Panels manufactured from particles with various sizes using a urea-formaldehyde adhesive had densities ranging from 535 to 682 kg/m³. The adhesive ratio was at a level of 16% for the single-layer mat configuration; for the three-layer structure, levels of 14% for the core and 16% for the faces were used, based on the weight of particles. The best results occurred in single-layer particleboard made from fine particles, which nearly met the general purpose requirements of the EN 312 Standard. Determination of the thermal conductivity coefficient demonstrated good insulation properties of all panels and their potential use for different structural configurations which are not subjected to strong stresses, suitable for interior design.

INTRODUCTION

Agro-residues (AGs) and biomass, such as sunflower stalk, corn stalk, cotton stalk, walnut shell, peanut hull, bagasse fiber, luffa fiber, coconut fiber, kenaf, giant reed, eucalyptus, and grass, have been investigated as possible raw materials for particleboard manufacture, in actual conditions of high demand for wooden materials and decrease in world forest resources (Guler *et al.* 2008; Garay *et al.* 2009; Nemli *et al.* 2009; Ashori and Nourbakhsh 2010; Fiorelli *et al.* 2012). Thus, the application of AGs for sustainable construction materials provides a solution that offers a reduction in natural resource use (Mangesh *et al.* 2013). Particleboards are generally made of wood chips bonded by adhesives, being pressed under heat. Basically, the wood chips can be replaced by any lignocellulosic material, as the chemical composition of that material is similar to that of wood, containing cellulose, hemicellulose, and lignin (Barros Filho *et al.* 2011; Fiorelli *et al.* 2012). The chemical composition of sunflower husks: 21.85% lignin (Carre 2009), or hemicellulose 24%, lignin 23.2%, and cellulose 42.7% (Saura-Caligsto 1983) is similar with that of wood, as found in the literature: 40-50% cellulose, 20-25% lignin, and 25-35% hemicellulose (Hayes 2010). These data show that, from this point of view, the sunflower husks can replace the wood in a particleboard structure.

The percentage of husks in sunflower seeds is in the range of 21.1% to 29.8% (Wan *et al.* 1979; Carre 2009); thus, the manufacturers of sunflower oil are faced with a

high stock of residues, taking into consideration also the low husks bulk density, which varies between 150 and 200 kg/m^3 (Carre 2009). Generally, these residues are used for making pellets and briquettes, but the high content of silicon in sunflower husks creates problems, such as wear to the machines making the pellets. At the same time, compared to wood, sunflower husks contain much more nitrogen, which produces strong pollutants (nitrogen oxides) during combustion. A better solution may be the incorporation of husks in structures of boards with improved properties for furniture or building applications.

Some researchers have shown that the presence of sunflower residues (husks or stalks) in particleboard panels decreased the mechanical resistance and dimensional stability. Incorporation of sunflower residues up to 50% led to properties which met the requirements of standards such as CS 236-66 (1968) or EN 312 (2003) (Gertjejansen *et al.* 1972; Guler *et al.* 2006). The same results were obtained by researchers who investigated the properties of particleboards made from other agro-wastes and wood particles. Up to 25% peanut hull mixed with European black pine (Guler *et al.* 2008), a mixture of at least 30% almond shell particles with wood (Pirayesh and Khazaeian 2012), mixtures of up to 30% wheat and corn incorporated with pine (Garay *et al.* 2009), and up to 30% kenaf in combination with rubber wood, have shown good performance in mechanical properties (Abdul Halip *et al.* 2014).

Other researchers have investigated the possibility of using 100% agro-wastes in particleboards manufacturing and their impact on the board properties. The effects of panel density and adhesive ratio on some physical and mechanical properties of peanut hull particleboard were investigated (Güler and Buyuksari 2011), and the results showed that only the panels with high density (800 kg/m^3) almost met the requirements of the EN 312 (2003) Standard for general purposes (P1). Attempts to reduce the panels' density to 400 kg/m^3 succeeded and also fulfilled the internal bond requirement (EN 312 - P2) by using only agro-wastes, such as miscanthus, topinambur, and sunflower stalks, for single-mat configurations. The same requirements were unfortunately not met for three-layer particleboard (Balducci *et al.* 2008). Additional promising results of three-layer particleboard made from fast-growing willow and black locust with low densities (600 to 660 kg/m^3) have been obtained (Kowaluk *et al.* 2011).

The quality of the final product and its strength is influenced by the quality, size, geometry, and location of particles in the panel structure. Some researchers found differences in the properties of particleboards, with the best results being obtained for those manufactured with medium sized particles (Lee *et al.* 2006; Pan *et al.* 2007; Garcia-Ortuño *et al.* 2011). Two types of particles are generally prepared: fine and coarse. In mixtures of pine, sawdust, shavings, and chips, the fine particles were in the range of 1 to 3 mm long, 0.5 to 1 mm wide, and 0.1 to 0.3 mm thick. The more coarse particles had a length between 10 to 20 mm, width between 3 and 5 mm, and thickness between 0.3 and 0.5 mm (Garay 2012). In the case of three-layer particleboard, the fine particles (32% to 35%) are used for faces and coarse particles are used for the core layer. The most used adhesive is urea-formaldehyde (UF), the content of which is recommended to be about 8 to 9% for the core and 10 to 12% for the face layers (Buyuksari *et al.* 2010; Güler and Buyuksari 2011; Kowaluk *et al.* 2011; Garay 2012). Sieving, microscopy or mathematical distribution functions are methods described in the literature for determining the particle size distribution (Vitez and Travnicek 2010).

According to the literature (Gertjejansen *et al.* 1972), sunflower seed husks are valorised in particleboard manufacture and have good performance only when they

constitute up to 50% of the raw material used. Therefore, particleboards made from 100% sunflower seed husks need to be improved to increase their performance.

The main objective of this research was to obtain particleboards made only from sunflower seed husks, without adding any other lignocellulosic materials, keeping at the same time the board properties at the level of a wood particleboard. Their performance was investigated by testing the density, water absorption (WA), thickness swelling (TS) after 24-h water immersion, thermal properties, bending strength (BS), modulus of elasticity (MOE), internal bond strength perpendicular to the plane of the board (IB), and screw holding strength (HS). These properties were related to board structure, size and geometry of the sunflower husks particles, respectively. Using wastes such as sunflower husks can decrease the consumption of wood, leading to wood savings and forest preservation. Thus, an increase of adhesive ratio up to 16% is economically affordable considering that wood cost (as raw material) was replaced by some low cost wastes.

EXPERIMENTAL

Materials

Particle size analysis

Two categories of the sunflower husks were used in the boards manufacturing. The first category included the uncrushed sunflower husks as coarse particles, and the second one was represented by crushed husks as fine particles. The fine particles were obtained by hammer milling of the coarse particles. The moisture contents were approximately 8.6% and 7.6% for coarse and fine particles, respectively. The coarse (sunflower husks) and fine particles were separately screened using a horizontal screen shaker with sieves of 4, 3, 2, 1, and 0.5 mm to remove undersized particles (dust) and obtain the fractions necessary for the mat formation. Three samples of 25 g each was weighed and screened. The mass fractional shares of different particle sizes within samples of coarse and fine particles are shown in Fig.1.
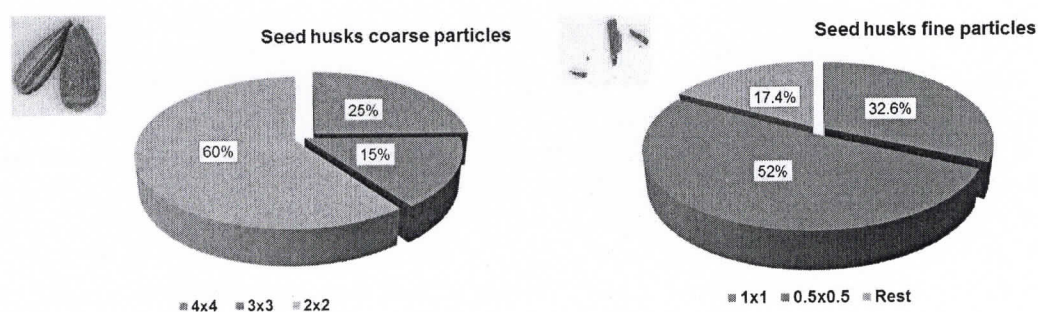
Fig. 1. Average mass fraction share of coarse particles (sunflower husks) and fine particles retained on sieves of 4, 3, 2, 1, and 0.5 mm

The majority of the coarse particles (59 to 61%) passed through the 4.0-mm and 3.0-mm sieves and settled on the 2.0-mm sieve. The coarse particles were from 4.0-mm, 3.0-mm, and 2.0-mm sieves and their dimensions varied between 2.91 and 12.7 mm in length, widths from 2 to 7 mm and thicknesses from 0.2 to 0.5 mm (Fig. 2). The husk

thicknesses were measured with calliper and were in the range found also in the literature (Wan *et al.* 1979). The aspect ratio (length to width ratio) varied from 1.07 to 4.9. The measurements were carried out in AutoCAD (Autodesk), version 2007. The particles were first scanned, imported in AutoCAD, then adjusted to 1:1 scale and measured.
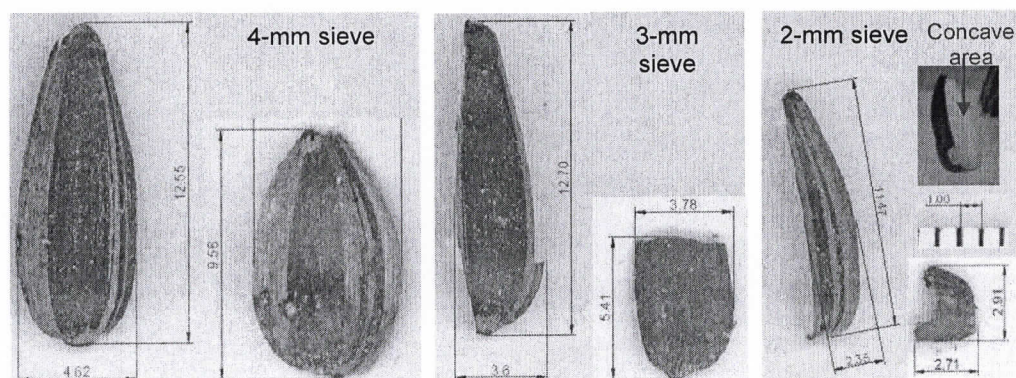

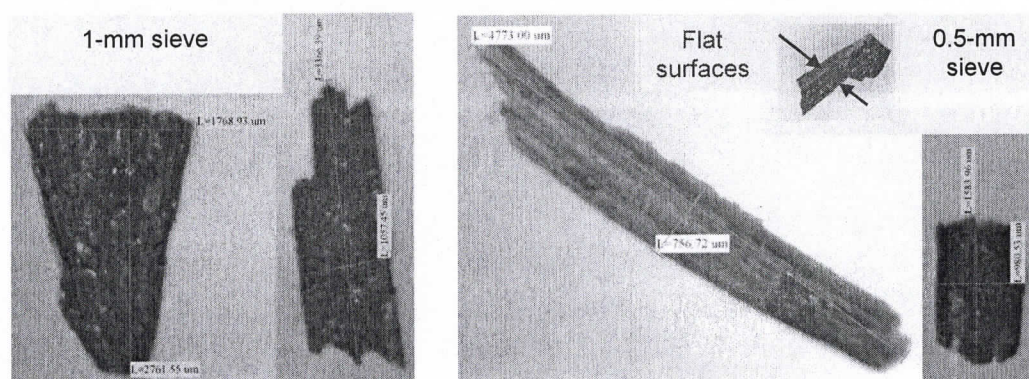**Fig. 2.** Geometry and size of coarse particles measured in AutoCAD program, in mm

Fig. 3. Geometry and size of fine particles measured in microscopic examination, in microns

For the fines, 51 to 53% of the particles were retained on the 0.5-mm sieve and 31.2% to 33.8% of them on the sieve of 1 mm. These fractions were used as the faces of three-layer particleboard and as a single-layer mat configuration. The fine particle dimensions, from the sieves 1.0-mm and 0.5-mm, were in the range of 0.98 to 4.77 mm for length, 0.7 to 1.7 mm width, and thickness from 0.2 to 0.5 mm. The aspect ratio (length to width ratio) was 1.03 to 6.3 for the fine particles. The fine particles were measured by an Optika microscope (SZM-2; Italy), as can be seen in Fig. 3. The ocular stereomicroscope is equipped with an Optika PRO 3 high resolution digital video camera and Optika vision software package that provides linear in-scale measurements.

Methods

Single-layer and three-layer particleboard manufacture

Seven types of particleboards in two configurations were manufactured: single-layer particleboards made from 100% fine particles (SLFP), 100% coarse particles (SLCP), 50% coarse with 50% fine particles (1/2SLC-FP), 50% fine with 50% wood particles (1/2SLF-WP), 50% coarse with 50% wood particles (1/2SLC-WP), and 100% wood particles (WP). The second configuration was the three-layer particleboard (TLP)

in a ratio 30:70 (fine for faces: coarse for core). Urea-formaldehyde resin with a solid content of 66± 1% was added to the single-mat configuration at a level of 16%, based on the weight of the particles. For the three-layer structure, the ratios were 14% for the core and 16% for the faces. Preliminary tests made in our laboratory showed that lowering the adhesive consumption below 12% led to inadequate results of bonding strength. As a consequence, an amount of maximum 16% urea-formaldehyde adhesive was considered suitable for all tested particleboards. Higher UF adhesive ratios resulted in an increase of bond strength levels, as found in the literature (Ferra *et al.* 2011). Ammonium chloride 1%, based on the weight of dry resin, was added as a hardener. No wax or other hydrophobic substances were used. The adhesive and particle mixture was blended for 3 min to obtain a homogenised mixture. The particleboards were manually formed in dimensions of 620 mm x 620 mm (length x width) and thicknesses from 50 mm to 60 mm (the lowest value for fines and the highest value for the coarse structures) and hot-pressed; after the edge trimming, the panels' final dimensions were 600 mm x 600 mm x 16 mm. The experimental design for the single-layer and three-layer particleboards is shown in Table 1.

Table 1. Experimental Design for Single-layer and Three-layer Particleboards

Board type	Type of particles	Adhesive (UF) resin (%)	Press temperature (°C)	Pressing time (min)	Press pressure (bar)	Final dimensions (mm)
SLFP	fines	16	180	6	30	600x600x16
SLCP	coarses	16	180	6	30	600x600x16
TLP	30% fines (faces) 70% coarses (core)	16 (faces) 14 (core)	180	6	30	600x600x16
1/2SLC-FP	50% fines 50% coarses	16	180	6	30	600x600x16
1/2SLF-WP	50% fines 50% wood particles	16	180	6	30	600x600x16
1/2SLC-WP	50% coarses 50% wood particles	16	180	6	30	600x600x16
WP	100% wood particles	16	180	6	30	600x600x16

After pressing, the particleboards were conditioned at 20 °C and 65% relative humidity for approximately 2 weeks before evaluating the properties. Five replicate panels were made for each board type; two were tested for thermal conductivity using a heat flow meter (HFM 436/6/1 Lambda; Germany) and three were cut to obtain samples for mechanical and physical testing.

Physical and mechanical testing

The physical properties were determined as follows: density (EN 323 1993), water absorption (WA) and thickness swelling (TS) after 24 h of water immersion (EN 317 1993), and thermal conductivity coefficient (λ) (DIN EN 12667 2001 and ISO 8301 1991). Bending strength (BS), modulus of elasticity (MOE) (EN 310 1993), internal bond strength (IB) perpendicular to the plane of the board (EN 319 1993), and screw holding strength (SH) (EN 320 1993) were determined using a universal testing machine (Zwick/Roell Z010, Germany). Testing was performed according to each standard methodology. Density, IB, SH, MOE, and BS were each measured on six specimens. For MOE and BS, the panel length depended on the panel thicknesses. Five panels were

tested for WA and TS tests, and two panels tested for the thermal properties. Panels for thermal testing had dimensions of 600 mm x 600 mm x 16 mm, and they were measured at eight points for a difference of temperature (ΔT) of 30 °C between upper and lower plates. The water absorption and thickness swelling tests were performed by submerging the specimens in water at room temperature (20 °C) for 2 h and 24 h, and calculated based on weight and thickness measurements respectively, before and after immersion in water. The results reported were the average of specimens tested, both for mechanical and physical properties.

RESULTS AND DISCUSSION

The panels' characteristics are presented in Table 2. The best results were obtained for SLFP, which had properties that were nearest to the EN 312 (2003) Standard requirements, compare to the other investigated panels.

Table 2. Physical and Mechanical Properties of Investigated Particleboards

Type	Density (kg/m³)	WA 24 h (%)	TS 24 h (%)	BS (N/mm²)	MOE (N/mm²)	IB (N/mm²)	SH (N/mm)	λ (W/mK)
SLFP	682 (14.5)	55.4 (2.7)	10.2 (1.3)	5.82 (0.26)	1703 (141)	0.24 (0.017)	31.33 (1.50)	0.079 (0.001)
SLCP	587 (15.7)	60.7 (2.3)	11.9 (0.7)	5.33 (0.99)	2030 (125)	0.11 (0.010)	31.47 (1.30)	0.077 (0.006)
TLP	555 (14.83)	53.4 (11.8)	9.2 (0.9)	4.89 (0.50)	1645 (192)	0.18 (0.014)	25.15 (1.42)	0.076 (0.002)
1/2SLC-FP	605 (12.58)	74.5 (13)	14.8 (0.7)	4.15 (0.68)	1718 (159)	0.09 (0.006)	21.93 (1.21)	0.086 (0.001)
1/2SLF-WP	672 (24.8)	46.4 (6.5)	9.9 (1.0)	6.46 (0.49)	1566 (107)	0.18 (0.031)	37.68 (5.00)	0.077 (0.001)
1/2SLC-WP	535 (5.68)	65.2 (2.4)	8.50 (0.5)	4.39 (0.86)	1515 (71)	0.07 (0.004)	17.12 (0.95)	0.079 (0.007)
WP	653 (16.9)	50.6 (7.0)	6.4 (0.9)	10.29 (0.84)	2103 (191)	0.26 (0.023)	41.06 (7.70)	0.075 (0.001)
EN *			14[c]	11.5[a]	1600[b]	0.24[a]		

* Minimum requirements according to EN 312 (2003):
[a] Requirements for particleboards for general uses (P1)
[b] Requirements for furniture manufacturing (P2)
[c] Requirements for moisture resistant particleboards (P3)
Values in parentheses are standard deviations

The results of the most important tested properties of the investigated particleboards are shown in Fig. 4. The density varied within the boards' group, the higher values being noticed for SLFP, 1/2SLF-WP, and WP. The density of the single-layer particleboard decreased with increasing particle size (SLCP compared to SLFP), because of the higher compaction ratio of fine particles compared to the coarse ones. The fine particles are easy to press at high temperature, resulting in higher density panels (Cai *et al.* 2004). The internal bond strength (IB) of SLFP was superior to that of SLCP (0.24 compared to 0.11 N/mm²) and TLP (0.18 N/mm²). Corn and rice stubbles mixed with pine wood in various ratios led to similar IB values ranging between 0.11 N/mm² to 0.29 N/mm² (Garay *et al.* 2009).
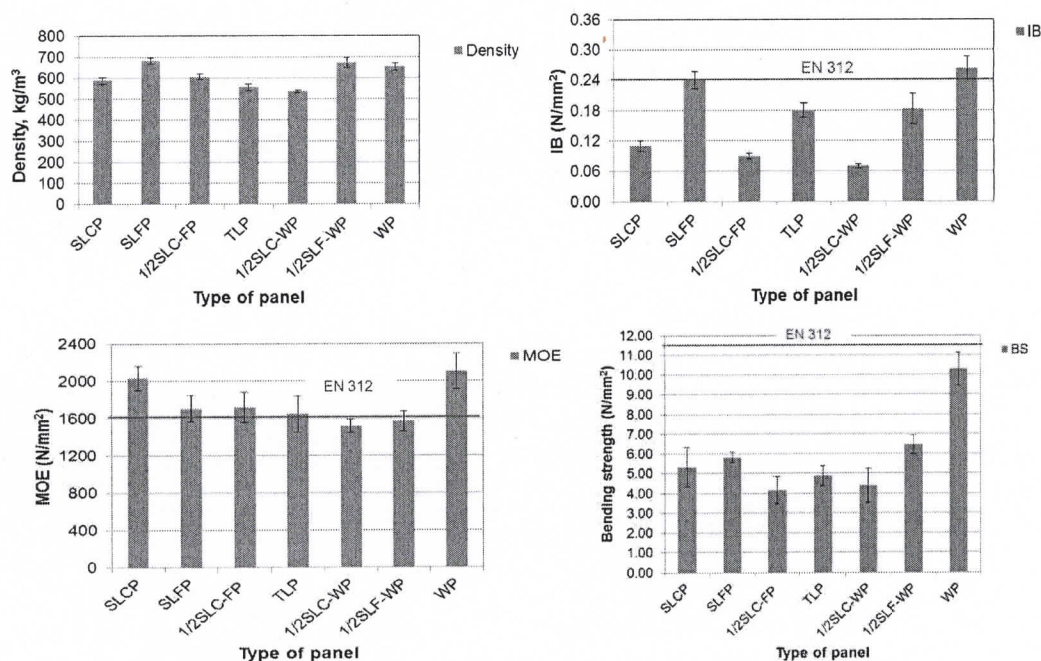
Fig. 4. Density, internal bond strength (IB), MOE and bending strength (BS) for the tested particleboards.

Higher screw holding strengths (SH) were obtained for SLCP, SLFP, and 1/2SLF-WP, as seen in Table 2. It seems that the particles' size and geometry had an important influence on both IB and SH strengths. The fine particles, with their flat surfaces and fusiform appearance, achieved a better bonding contact, so the obtained structure was more compact and homogenous. Coarse particles, with their concave geometry, produced local agglomerations of adhesive with a reduced compactness, lowering the internal bond strength. The highest MOE value was obtained for SLCP, the coarse particles increasing the stiffness of the board (Fig. 4). The values of BS were below the EN 312 (2003) standard limit for all boards. Lower values of WA and TS were obtained for all particleboards. The structures with coarse particles had the highest WA values, explained by the porosity caused by the concavity and variation in shapes of the husks. All the boards with fine particles in the outer layers (TLP, SLFP) had low WA and TS values, because of the higher compactness and low wettability. Similar results were obtained for peanut hulls and pine particleboards (Guler *et al.* 2008; Güler and Büyüksari 2011) and almond shells mixed with wood (Pirayesh *et al.* 2013). Three-layer particleboard (TLP) has similar performance with 1/2SLC-WP board, except IB. Based on the EN Standard (EN 312 2003), SLFP nearly met the minimum requirements for MOE, TS, and IB, but not for BS. Mechanical properties of the tested boards can be compared with those made from grass clipping mixed with wood (Nemli *et al.* 2009). Thermal conductivity coefficients (0.075 to 0.079 W/mK), as shown in Table 2, indicated good thermal insulating properties for all panels. The normal range of insulation materials is between 0.035 W/mK and 0.160 W/mK (Panyakaew and Fotios 2008), agro-wastes boards being included with the following thermal conductivity coefficients: 0.046 W/mK (coconut husks), 0.096 W/mK (bagasse) (Panyakaew and Fotios 2008), 0.0764-0.1254 W/mK

(durian peel and coconut coir) (Madurwar *et al.* 2013) and 0.051 W/mK for rice straw (Wei *et al.* 2015).

CONCLUSIONS

1. The size and geometry of particles influenced the performance of studied particleboards. The fusiform shape of fine particles and their homogeneous distribution in the structure improved the performance of single-layer and three-layer particleboards made from sunflower husks. The concave geometry of the coarse particles led to a more porous structure affecting WA and internal bond strength.

2. Better performance was obtained for single-layer particleboards made from fine particles (SLFP) compared to the other panels.

3. Three-layer particleboards had a lower density with negative influence on the bending strength (BS). The boards made from sunflower husks and wood did not exceed the performances of those made only from sunflower husks.

4. The boards are recommended for paneling structures and furniture components which are not subjected to bending stresses.

ACKNOWLEDGMENTS

REFERENCES CITED

Abdul Halip, J., Tahir, P. Md., Choo, A. C. Y., and Ashaari, Z. (2014). "Effect of kenaf parts on the performance of single-layer and three-layer particleboard made from kenaf and rubberwood," *BioResources* 9(1), 1401-1416. DOI: 10.15376/biores.9.1.1401-1416

Ashori, A., and Nourbakhsh, A. (2010). "Bio-based composites from waste agricultural residues," *Waste Management* 30(4), 680-684. DOI: 10.1016/j.wasman.2009.08.003

Balducci, F., Harper, C., Meinlschmidt, P., Dix, B., and Sanasi, A. (2008). "Development of innovative particleboard panels," *Drvna Industrija* 59(3), 131-136.

Barros Filho, R. M., Mendes, L. M., Novack, K. M., Aprelini, L. O., and Botaro, V. R. (2011). "Hybrid chipboard panels based on sugarcane bagasse, urea formaldehyde and melamine formaldehyde resin," *Industrial Crops and Products* 33(2), 369-373. DOI: 10.1016/j.indcrop.2010.11.007

Cai, Z., Wu, Q., Lee, J.N., Hiziroglu, S. (2004). "Influence of board density, mat construction, and chip type on performance of particleboard made from eastern redcedar," *Forest Products Journal* 54(12), 226-232.

Carre, P. (2009). WP2 Report of the SUSTOIL Project, Deliverable D2.1. Review and Evaluation Major and Most Promising Processing Technologies for Oil Seed Pre-

treatment and Extraction FP7-Energy, http://www.york.ac.uk/res/sustoil/Pages/Deliverable%202-5.pdf, Accessed March 6, 2014.

CS 236-66 (1968). "Commercial Standard. Mat formed Wood particleboard."

DIN EN 12667. (2001). "Thermal performance of building materials and products - Determination of thermal resistance by means of guarded hot plate and heat flow meter methods - Products of high and medium thermal resistance," *British Standards*, London.

EN 310. (1993). "Wood-based panels. Determination of modulus of elasticity in bending and of bending strength," *British Standards*, London.

EN 312. (2003). "Particleboards. Specifications," *British Standards*, London.

EN 317. (1993). "Particleboards and fibreboards. Determination of swelling in thickness after immersion in water," *British Standards*, London.

EN 319. (1993). "Particleboards and fibreboards. Determination of tensile strength perpendicular to the plane of the board," *British Standards*, London.

EN 320. (1993). "Fibreboards. Determination of resistance to axial withdrawal of screws," *British Standards*, London.

EN 323. (1993). "Wood-based panels. Determination of density," *British Standards*, London.

Ferra, J. M. M., Ohlmeyer, M., Mendes, A. M., Costa, M. R. N., Carvalho, L. H., and Magalhães, F. D. (2011). "Evaluation of urea-formaldehyde adhesives performance by recently developed mechanical tests," *International Journal of Adhesion & Adhesives* 31, 127-134. DOI: 10.1016/j.ijadhadh.2010.11.013

Fiorelli, J., Curtolo, D. D., Barrero, N. G., Savastano Jr., H., Pallone, E. M. J. A., and Johnson, R. (2012). "Particulate composite based on coconut fiber and castor oil polyurethane adhesive: An eco-efficient product," *Industrial Crops and Products* 40, 69-75. DOI: 10.1016/j.indcrop.2012.02.033

Garay, R. M., MacDonald, F., Acevedo, M. L., Calderon, B., and Araya, J. E. (2009). "Particleboard made with crop residues mixed with wood from *Pinus radiata*," *BioResources* 4(4), 1396-1408. DOI: 10.15376/biores.4.4.1396-1408

Garay, R. M. (2012). "Lab testing for P3 moisture resistant overlaid particleboards made from wood residues," *BioResources* 7(3), 3093-3103. DOI: 10.15376/biores.7.3.3093-3103

Garcia-Ortuño, T., Andreu-Rodriguez, J., Ferrandez-Garcia, M. T., Ferrandez-Villena, M., and Ferrandez-Garcia, C. E. (2011). "Evaluation of the physical and mechanical properties of particleboard made from giant reed (*Arundo donax* L.)," *BioResources* 6(1), 477-486. DOI: 10.15376/biores.6.1.477-486

Gertjejansen, R. O., Haygreen, J. G., and French, D. W. (1972). "Particleboard from aspen flakes and sunflower hulls," *Technical Bulletin* 290, Forestry Series TU, University of Minnesota, http://digitalcommons.usu.edu/aspen_bib/5418, Accessed March 6, 2014.

Güler, C., and Büyüksari, Ü. (2011). "Effect of production parameters on the physical and mechanical properties of particleboards made from peanut (*Arachis hypogaea* L.) hull," *BioResources* 6(4), 5027-5036. DOI: 10.15376/biores.6.4.5027-5036

Guler, C., Bektas, I., and Kalaycioglu, H. (2006). "The experimental particleboard manufacture from sunflower stalks (*Helianthus annuus* L.) and Calabrian pine (*Pinus brutia* Ten.)," *Forest Products Journal* 56(4), 56-60.

Guler, C., Kopur, Y., and Tascioglu, C. (2008). "The manufacture of particleboards using mixture of peanut hull (*Arachis hypogaea* L.) and European black pine (*Pinus nigra* Arnold) wood chips," *Bioresource Technology* 99(8), 2893-2897. DOI: 10.1016/j.biortech.2007.06.013

Hayes, D. (2010). "Chemistry and properties of woods-Carbolea," *DAFF RSF Project Database*, University of Limerick, www.carbolea.ul.ie/wood.php, Accessed November 14, 2014.

ISO 8301 (1991). "Thermal insulation - Determination of steady-state thermal resistance and related properties - Heat flow meter apparatus," *International Organization for Standardization*, Geneva, Switzerland.

Kowaluk, G., Fuczek, D., Beer, P., and Grzeskiewicz, M. (2011). "Influence of the raw materials and production parameters on chosen standard properties for furniture panels of biocomposites from fibrous chips," *BioResources* 6(3), 3004-3018. DOI: 10.15376/biores.6.3.3004-3018

Lee, S., Shupe, T. F., and Hse, C. Y. (2006). "Mechanical and physical properties of agro-based fibreboard," *Holz als Roh- und Werkstoff* 64(1), 74-79. DOI: 10.1007/s00107-005-0062-z

Madurwar, V. M., Ralegaonkar, R. V., and Mandavgane, S. A. (2013). "Application of agro-waste for sustainable construction materials: A review," *Construction and Building Materials* 38, 872-878. DOI: 10.1016/j.conbuildmat.2012.09.011

Nemli, G., Demirel, S., Gümüşkaya, E., Aslan, M., and Acar, C. (2009). "Feasibility of incorporating waste grass clipping (*Lolium perenne* L.) in particleboard composites," *Waste Management* 29(3), 1129-1131. DOI: 10.1016/j.wasman.2008.07.011

Pan, Z., Zheng, Y., Zhang, R., and Jenkins, B. M. (2007). "Physical properties of thin particleboard made from saline eucalyptus," *Industrial Crops and Products* 26(2), 185-194. DOI: 10.1016/j.indcrop.2007.03.006

Panyakaew, S., and Fotios, S. (2008). "Agricultural waste materials as thermal insulation for dwellings in Thailand: Preliminary results," PLEA 2008 – 25th Conference on Passive and Low Energy Architecture, Dublin.

Pirayesh, H., and Khazaeian, A. (2012). "Using almond (*Prunus amygdalus* L.) shell as a bio-waste resource in wood-based composite," *Composites: Part B: Engineering* 43(3), 1475-1479. DOI: 10.1016/j.compositesb.2011.06.008

Pirayesh, H., Khanjanzadeh, H., and Salari, A. (2013). "Effect of using walnut/almond shells on the physical, mechanical properties and formaldehyde emission of particleboard," *Composites Part B: Engineering* 45(1), 858-863. DOI: 10.1016/j.compositesb.2012.05.008

Vitêz, T., and Travnicek, P. (2010). "Particle size distribution of sawdust and wood shavings mixtures," *Research in Agricultural Engineering* 56(4), 154-158.

Wan, P. J., Baker, G. W., Clark, S. P., and Mattock, S. W. (1979). "Characteristics of sunflower seed and meal," *Cereal Chemistry* 56(4), 352-355.

Wei, K., Lv, C., Chen, M., Zhou, X., Dai, Z., Shen, D. (2015). "Development and performance evaluation of a new thermal insulation material from rice straw using high frequency hot-pressing," *Energy and Buildings* 87, 116-122. DOI: 10.1016/j.enbuild.2014.11.026

EVALUATION OF TENSILE AND COMPRESSION BENDING MOMENT OF L-TYPE JOINTS WITH 3D PRINTED CONNECTORS

Antoniu NICOLAU[1]   **Camelia COȘOREANU**[1]
Luminița M. BRENCI[1]
Mihai A. POP[2]   **Cătălin CIOACĂ**[3]

Abstract: *The paper investigates the bending moments under diagonal tensile and diagonal compression loads of L-type corner joints made of three wooden parts corresponding to the leg and the two stretchers used in chair construction. The wooden parts were jointed together with a 3D printed connector made of polylactic acid (PLA) filaments using Filament Fused Fabrication (FFF) as additive manufacturing technology. Larch (Larix decidua Mill.) wood was used to manufacture the wooden elements. In order to assess how the model orientation on the build platform influences the mechanical performance of the printed connector, two print positions were taken into account during the additive manufacturing (AM) process, namely horizontal and vertical. Mechanical testing under diagonal tensile and compression loads of the L-type corner joints, followed by the microscopic investigation of the fractured connectors with magnifications 50X, 80X, 100X were employed in this study. The results were compared with those of the reference L-type corner joint consisting of common mortise-tenon jointed wooden elements. The results show that the vertical orientation of the model on the build platform of the 3D printer is preferred for a better mechanical performance. The microscopy of the fractured connectors revealed the interlayer delamination of the filaments, especially in the case of the horizontal orientation of the model, which caused the wooden parts to slide out of the connector and record low values of the maximum failure loads.*

Key words: *Polylactic acid (PLA), additive manufacturing, larch wood, connector, L-type corner joint.*

---

[1] Faculty of Furniture Design and Wood Engineering, Transilvania University of Brasov, B-dul Eroilor, no. 29, 500036 Brasov, Romania;
[2] Faculty of Materials Science and Engineering, Transilvania University of Brasov, B-dul Eroilor, nr. 29, 500036 Brasov, Romania;
[3] Department of Management and Military Sciences, "Henri Coanda" Air Force Academy, Street Mihai Viteazul 160, 500183, Brasov, Romania;
Correspondence: Camelia Coșereanu; email: cboieriu@unitbv.ro.

1. Introduction

Filament fused fabrication (FFF), as a part of AM, has a multitude of applications, being one of the most accessible and inexpensive 3D printing technologies. PLA filaments are often used for large applications, being manufactured in a variety of colours that can bring an attractive design to 3D printed objects [8, 25]. In the traditional furniture manufacturing industry, the possibilities of designing wooden components generate a series of constraints on the production in this field, limited by the execution of the joints between the wooden parts to 90º angles, rarely connecting more than two pieces in the same joint [5]. The use of 3D printed parts in the structure of furniture allows the design without the limitations of wood jointing and avoids the difficult technological processes of wood [14]. By using AM, functional structures with difficult geometries can be obtained through the deposition of successive layers of extruded thermoplastic filament [21]. There are several advantages of using AM in the production of furniture parts: improving the degree of fit, reducing the difficulty of parts manufacturing and the production time, easing the assembly process, allowing the secondary recycling of furniture and prolonging its service life with a positive impact on the environment [16, 27].

The creation of a 3D model is the first step before 3D printing an object. Computer-aided design (CAD) software, such as AutoCAD, Rhino, SolidWorks, Autodesk 3ds Max, and Maya, is used for this purpose. The 3D model is saved as a (.stl) file and then transferred to the printer software. The software slices the

data file into individual layers which are sent as instructions to the printing device that adds overlapping layers of material, until the object is printed completely.

The most used materials for printed parts in furniture manufacturing are the filaments made of acrylonitrile butadiene styrene (ABS) and PLA, and FFF technology is employed to print them. The costs of these two materials are similar, but the filaments made of ABS have a slightly toxic exudate and they are sensitive to thermal deformation, whilst the PLA filaments are safer and more environmentally friendly [5]. Based on the literature review, some researchers [18] reached the conclusion that layer thickness and raster width should be minimal for improving the mechanical strength of the specimens and temperature plays a significant role in PLA filament bonding. The increased thickness of the printed layer decreases the manufacturing time of the specimen [4], but it has a negative impact on the quality of the printed surface, by increasing its roughness [22]. PLA filaments have similar mechanical properties with the printed specimens, so an assessment of the filament could predict the behaviour of the specimen [7]. The SEM examination of printed specimens with different coloured PLA filaments [26] indicated that colorant additives could play a role in the size of the inter-layer gaps, due to the fact that some colorants restrict heat flow and could lower the ultimate tensile strength, as in the case of white PLA, which had larger gaps in its structure compared to the natural material. In order to support the piece, in the case of complex geometries, it is necessary to add material to create a structure that supports the geometry of the piece in the correct

position during the printing process [2]. Once the object is created, a variety of finishing activities are needed [19, 24].

Several attempts are presented in the literature related to the manufacture of 3D printed connectors for furniture, using FFF or the selective laser sintering (SLS) method of AM technology [1, 2, 5, 9, 10]. The application of AM in the development and research of furniture parts relies on a comprehensive analysis based on evaluation tests. There are few methods applied in the literature for the assessment of the mechanical strength of the assembly with 3D printed connectors, or of the product itself. The corner joint is often used to assemble chair parts using mortise-tenon joints [17] and one evaluation method is to subject the L-type corner jointed parts to diagonal compression and diagonal tensile loads [3, 6, 13, 15, 23] and to calculate the bending moments. Another method is to assess the strength and durability of the chair seat and back by applying perpendicular forces to their middle points [1, 9].

There are not many studies available regarding the assessment of the mechanical strength of 3D printed connectors for furniture. The present paper investigates the behaviour under diagonal compression and diagonal tensile loads of L-type joints between wooden elements assembled with a 3D printed connector made of white PLA. The experimental research reveals the influence of the orientation of the model on the build platform of the 3D printer upon the bending moment of the tested L-type corner joints under diagonal compression and diagonal tensile loads. Larch wood (*Larix Decidua* Mill.) was selected for the experiment, which is a species with moderate resistance used in

the construction of chairs. This choice is intended to allow for a gradual progression in the research, avoiding the oversizing of the connector, as would be the case when joining more resistant wood species like beech or oak.

2. Materials and Methods
2.1. L-type Corner Joints

Larch (*Larix decidua* Mill.), wood with a moisture content of 9.2% and density of 607 kg/m^3 was used as raw material for the wooden parts. Two different L-type corner joints were designed for the mechanical tests: the first one included a 3D printed connector, and the second one was a common mortise-tenon joint between the three wooden elements, and was taken as reference sample. The adhesive used for the mortise-tenon joint was the commercial Novobond D2 polyvinyl acetate. The construction types and sizes of the L-type corner joints are presented in the cross sections from Figures 1a and 1b.

The density of the larch wood, determined by the calculation of the moisture content of 9.2%, was 607 kg/m^3. An adherent joint was used between the wooden parts and the 3D printed connector, and no adhesive was used. The piece of wood corresponding to the leg of the chair was completely inserted into the square section of the connector, and the stretchers were inserted 30 mm into the void spaces designed for them. The 3D model of the connector was designed using the SolidWorks 3D CAD software, version 2016, developed by Dassault Systèmes, France, and exported to the printer software as a (.stl) file.
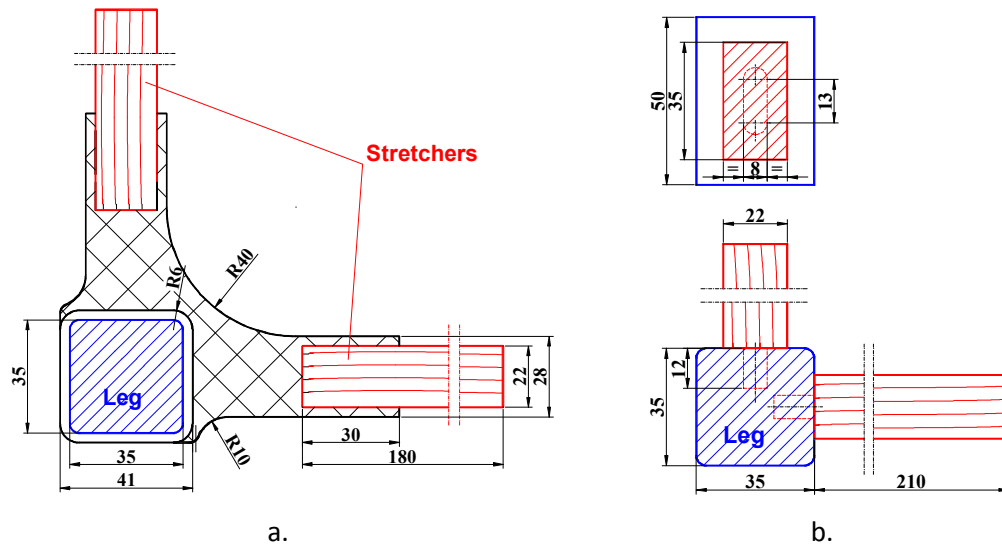
Fig. 1. *L-type corner joints used for the experimental work with:*
a. a 3D printed connector; b. a common mortise-tenon joint

2. Additive Manufacturing

FFF technology was employed to print the connectors, and white PLA filament (S.C. Atelier Concept&Design Studio, Bucharest, Romania) was used as material for the 3D print. The characteristics of the filament, as resulted from the technical data sheet of the supplier, are presented in Table 1.

Table 1

Characteristics of the white PLA filament used to print the experimental connectors

Characteristics	Value	Test method
Thickness [mm]	2.85 ± 0.10	
Print temperature [°C]	180 – 220	
Build platform temperature [°C]	60 – 70	
Print speed [mm/s]	40 – 80	
Impact strength [kJ/m^2]	7.5	ISO 180/A
Tensile strength [MPa]	110 (MD)	ASTM D882
Tensile modulus [MPa]	3310 (MD)	ASTM D882
Elongation at break [%]	160 (MD)	ASTM D882
Flexural modulus [MPa]	±2392.5	

The initial filament deposition is the perimeter, which defines a closed contour for the deposition of the subsequent layers of the 3D printed connector. The infill pattern, alternating in the X and Y direction at an inclination angle of 45º relative to the direction of the perimeter and perpendicular to the previous layer, was selected according to the literature recommendation, in order to obtain superior results concerning the compressive or tensile properties [11, 20]. The parameters used to print the connectors were, as follows:

• Print speed of 50 mm/s;

• Print temperature of 250°C;
• Layer height of 0.2 mm;
• 100% filling density.

Two orientations of the model on the build platform were considered, as shown in Figure 2. In "position 1" from Figure2a, the part is printed horizontally and does not need a support material. In "position 2" from Figure 2b, the connector is printed in a vertical position and the deposition of the layers needs a support material which is removed after the printing process is over. As seen in Figure 2b, a set of three pieces were printed at the same time.
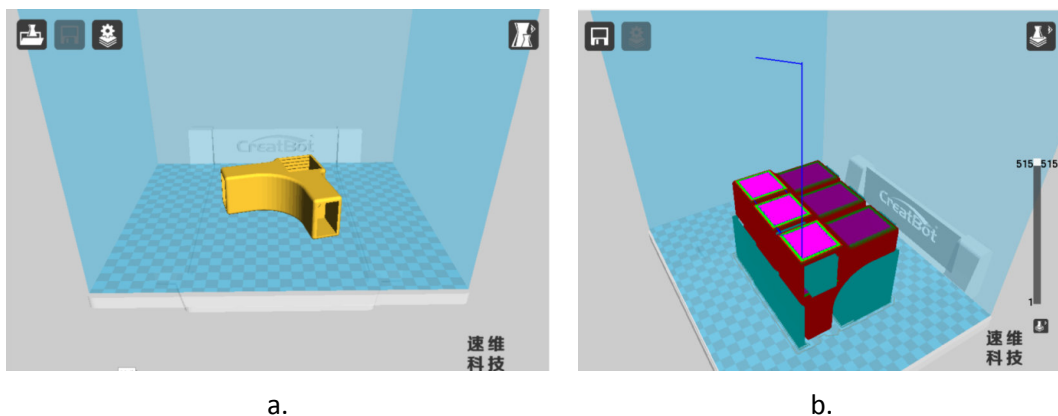

a.   b.

Fig. 2. *Orientation of the model on the build platform: a. Position 1 (horizontally); b. Position 2 (vertically) with support material, colored in green*

The printer used to manufacture the connectors was CreatBot DX Plus-3D (manufacturer Henan CreatBot Technology Limited, Zhengzhou City, Henan Province, China). This printer has the following characteristics: filament diameter of 2.85 mm, nozzle temperature up to 260°C, open filament system, maximum print speed of 200 mm/s, build area of 250 mm x 300 mm x 520 mm, layer height between 0.05 and 0.5 mm, and resolution of 0.05 mm.

3. Mechanical Strength of the L-Type Corner Joints

The L-type corner joints were tested for both diagonal compression and diagonal tensile loads using models described in the literature [3, 12, 28]. The tests were performed on the Zwick/Roell Z010 universal testing machine (Ulm, Germany) for five samples of each category. The compression loads tend to open the joint, while the tensile forces tend to close the

joint, and bending moments occur in the corner joints under these loads.

The bending moments under the tensile (M_t) and compression (M_c) loads were calculated using Equations (1) and (2), respectively:

$$M_t = \frac{F}{2} \cdot L_t \quad [\text{N·m}] \tag{1}$$

$$M_c = F \cdot L_c \quad [\text{N·m}] \tag{2}$$

where:

L_t and L_c are the moment arms under tensile and compression loads [m];

F – the maximum failure load [N].

Figure 3a shows how the test was conducted under tensile load in the case of the white PLA connector and Figure 3b shows the test under compression load for the reference L-type corner joint.

The same test speed of 7 mm/min was applied both for the L-type corner joint with connector and for the reference sample.
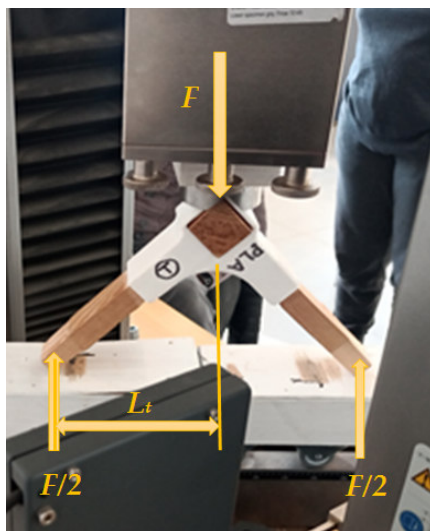
a.   b.

Fig. 3. *Mechanical tests: a. under diagonal tensile load;*
b. under diagonal compression load

4. Microscope Investigation

The microscope investigation of the fractured connector after testing under diagonal tensile and compression loads was conducted on two microscopes: the optical microscope OmniMetBuehler (Tokyo, Japan) with 50x and 100x magnification power and the Emspira 3 Digital Microscope (Leica Microsystems,

Danaher Corporation, Washington DC, USA) with 26×, 40×, and 80× magnification power. The optical microscope was used to investigate the cracks occurred in the connectors printed in position 1, and the Emspira 3 Digital Microscope with an 8:1 zoom ratio with 26×- 206× magnification range was used to analyse the damage of the connectors printed in position 2. The micrographs were taken on the

longitudinal and crosscut sections of the 3D printed connectors where cracks and fractured areas occurred after mechanical testing.

5. Results and Discussion
5.1. Strength of the L-Type Corner Joints

Both the reference and L-type corner joints with 3D printed connectors were subjected to diagonal compression and tensile tests and afterwards the results were compared for the maximum failure loads (Table 2) and for the bending moments calculated using Equations (1) and (2) together with the recorded displacements during the test (Figure 4). The average values of the results recorded for five samples and the standard deviations (values in the parentheses) are presented in Table 2 and in the graph from Figure 4.

Table 2

Average values of maximum failure loads,
recorded for all experimental L-type corner joints

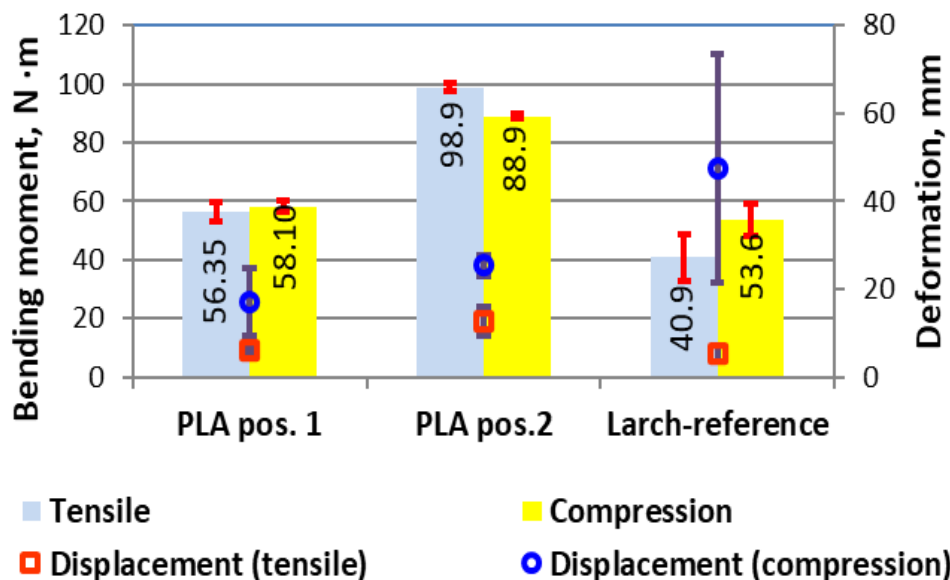| L-type corner joint/print position	Maximum failure tensile loads (F) [N]	Maximum failure compression loads (F) [N]
White PLA connector/position 1	613.5 (92.3)[1]	377.0 (30.1)
White PLA connector/position 2	1124.0 (161)	592.7 (27)
Reference (mortise-tenon joint)	464.6 (91.8)	357.4 (36)

Fig. 4. *Bending moments and displacements under tensile and compression loads for the L-type corner joints with 3D printed connectors made from white PLA in position 1 (PLA pos.1) and position 2 (PLA pos.2), and for the common mortise-tenon joint made of larch wood, taken as reference (Larch-reference)*

The behaviour of the reference L-type corner joint during the test is highlighted in Figure 5a for the tensile load and in Figure 5b for the compression load.
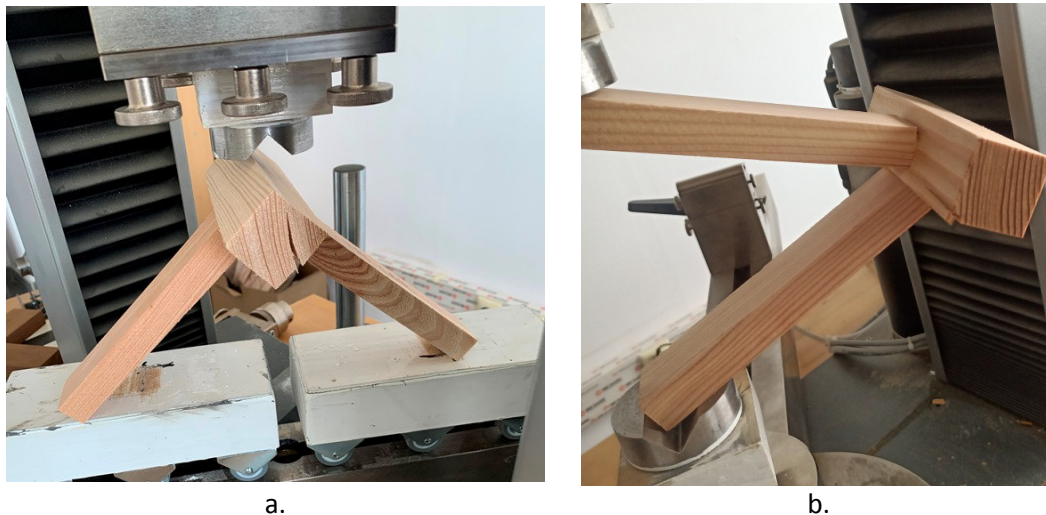

a.   b.

Fig. 5. *Behavior under tensile (a.) and compression (b.) loads*
of the reference L-type corner joints

The lowest F value was recorded for the reference sample under compression load (357.4 N), and the highest was recorded for the L-type corner joint with the connector printed in position 2 under the tensile load (1124 N), as seen in Table 2. The data in Table 2 show that the recorded *F* values were higher under tensile than under compression loads, whilst the displacements had an opposite trend (Figure 4), namely lower under tensile than under compression loads. The same trend of the displacements was noticed for the L-type corner joints made of wood-based panels [23], approximately 1.5 times higher under compression load compared to tensile load. The lowest value is accompanied by the highest displacement value (47.3 mm) of the reference sample under compression load, as the diagram in Figure 4 and the image from Figure 5b show. In this case, the higher deformation of the L-type corner joints under compression load resulted in the occurrence of cracks, both on the piece of leg and on the stretchers, seriously affecting the mortise-tenon joint (Figure 6b) and ultimately the low recorded *F* values. In Figure 6, the marked circles marked with 1 show the deep cracks that occurred on the leg and the circles numbered with 2 highlight the fracture mode of the mortise and tenon joint.

While the mechanical tests damaged the wooden elements in the case of the reference sample, they remained unaffected after testing the L-type corner joints with the connectors (Figure 7). During the tests, the cracks occurred at the edges of the connectors, because of the forces exerted by the stretchers on the connectors.

Overall, the bending moment capacities of the L-type corner joints with connectors were higher than those of the reference, both under tensile and compression loads, as can be seen in the diagram in Figure 4. These findings highlight the benefit of using connectors instead of common mortise-tenon joints for chair production, because in addition to the other advantages related to the reduced production times and ease of manufacturing [16, 27] they also bring the advantage of higher strength than the wood itself.
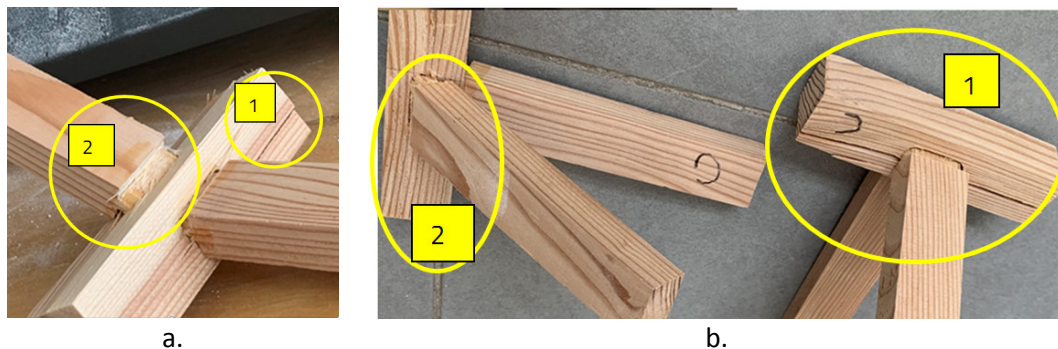

a.   b.

Fig. 6. *The fracture mode of the reference L-type corner joint under tensile (a.) and compression (b.) loads*

The results presented in the diagram from Figure 4 clearly show that the orientation of the model in position 2 is preferable for a better mechanical performance of the L-type corner joint with a 3D printed connector. Thus, for the connector printed in position 2, *F* was 1.8 times higher for tensile load and 1.6 times higher for compressive load, compared to the L-type corner joint with the connector printed in position 1. The M_c value for the L-type corner joint with the connector in position 2 was 88.9 Nm, very close to the value of 95.54 Nm obtained in a previous study [3] for the mortise-tenon corner joint (250 mm x 250 mm long and 20 mm thick made of beech wood) used in the construction of a chair.

In the present research, no adhesive was used to bond the wooden parts to the 3D printed connector. In this case, the mechanical strength was based only on the friction forces and the assembly forces, but failed because of delamination which occurred between the 3D printed layers at the connection with the wooden stretchers, as can be seen in Figure 7, where these types of fractures are circled.

Cracks at the edge of the connectors caused the stretcher to slide out of the joint more quickly in the event of a larger delamination or fracture. The delamination between the printed layers in position 1 was deeper than in position 2, because the deposition of layers in position 1 was in the same direction as the length of the stretcher, so the forces applied by the stretcher inside the connector could strain easily, affecting the adhesion between the printed layers. A similar conclusion was presented in the study [13] for fasteners used for corner jointing wood and wood-based composites, which showed that the main reason for joint damage was fasteners slipping out of sockets. When bonding 3D

printed connectors (made of ABS filament) to join two beech wood rails with the intention to use these connectors in the construction of a chair [9], maximum failure loads between 790 N and 905 N were recorded, which were higher than those recorded in the present study, but 2.5 times smaller than the wooden mortise and tenon joint taken as reference. Even though the tests of the assembled chair showed that the seat was strong enough, the 3D-printed connectors at the back ended up breaking. So it is possible that the solution of gluing the connector to the wooden parts increases the strength of the corner joint and implicitly the strength of the chair produced with these joints. This solution can be considered for the continuation of the present research.
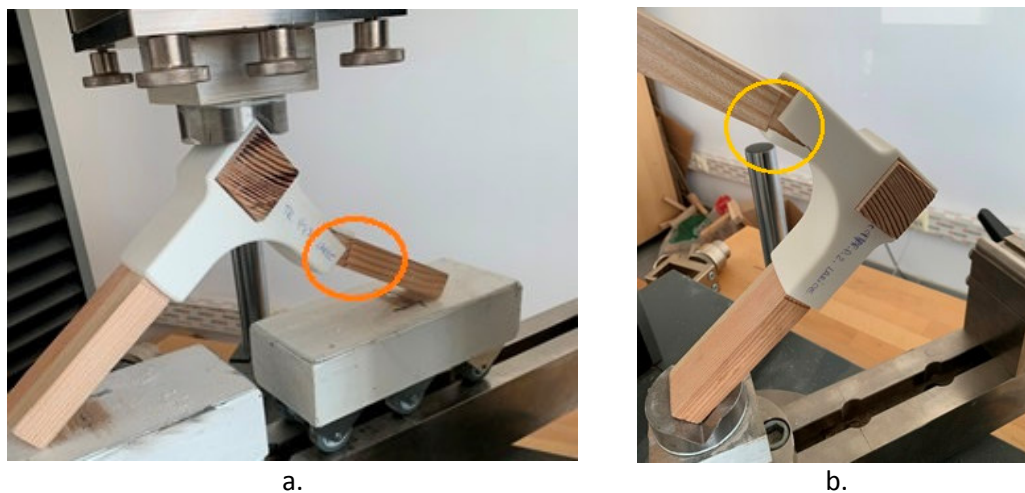

a.   b.

Fig. 7. *The fracture mode of the connectors after mechanical testing: a. under tensile load, print position 2; b. under compression load, print position 2*

5.2. Microscope Investigation

The microscope investigation was conducted in order to better highlight the fracture mode of the connectors after mechanical testing.

The pictures were taken in the longitudinal direction, considered to be along the direction of the stretchers and transverse, which means perpendicular to the direction of the stretcher. The 100x magnification images shown in Figure 8 are illustrative of the connector fractures after testing under tensile load in the longitudinal (Figure 8a) and transverse (Figure 8b) directions. The pictures showed that the connectors failed by delamination

In Figure 8a, the delamination process in the longitudinal direction is highlighted. The delamination propagation continues in the transversal direction (Figure 8b) and the circled area indicates the protrusions caused by the overlap of the material during the AM process and the deformation of the deposition layers in this area. It is possible that the surplus of accumulated material in this area determined the stress of the upper deposition layer, which is why delamination occurred between the layers in this area, as a result of the tensile stress

accumulated. The cause of this excess material may be the inertia generated by the print speed.
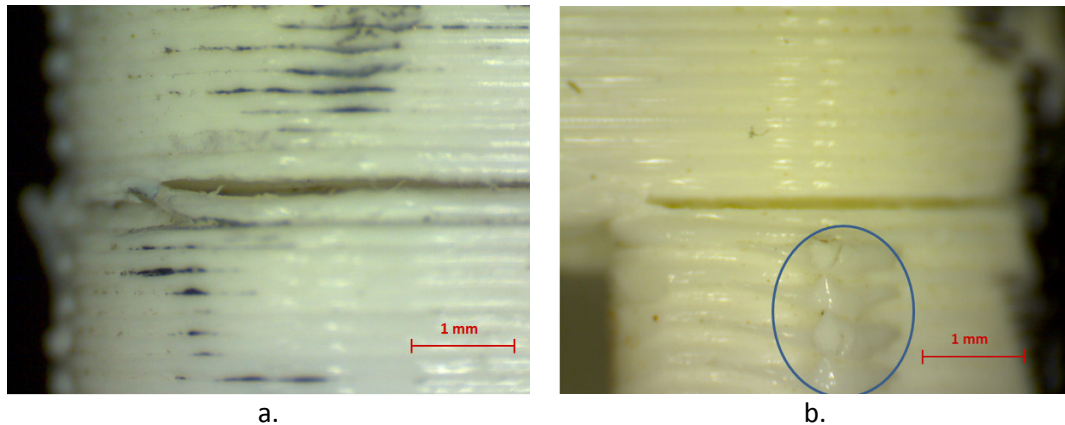

a.   b.

Fig. 8. *Process of delamination propagation in the connector printed in position 1, under tensile load: a. in the longitudinal direction, magnification 100X; b. in the transverse direction, magnification 100X*

The delamination of the filament layers in the longitudinal direction particularly affects the edges of the opening where the stretcher exits the connector, due to the fact that the filament layers are oriented parallel to the length of the stretcher. Also, a component of the tensile load acts perpendicularly, tending to detach first the layers near the opening edge and continuing the delamination both longitudinally and transversely over large distances, producing structural failure and sliding of the stretcher outside the connector.

In Figure 9a it can be seen that the delamination propagates over a measured length of 6.624 mm in the longitudinal direction and continues in the transverse direction for another 3.728 mm (Figure 9b). The details in Figures 9c and 9d show that the delamination affected only two adjacent layers and the stresses did not fracture the filament layer.

In the case of the connectors printed in position 1 and subjected to both compression and tensile loads, the failures were influenced by the insufficient adhesion between two adjacent layers, capable of resisting the forces that push the layers in a perpendicular direction from the inside to the outside. These forces tend to first detach the layers near the edge of the connector where the stretchers are inserted and then continue to propagate the delamination over several centimeters. The failure loads in this case recorded low values, but the wooden parts remained undamaged, and no fractures of the PLA layers were observed.

When changing the orientation of the model on the build platform in position 2 (Figure 2b), the maximum failure tensile loads were 1.83 times higher than those recorded for the printed connector in position 1, and the maximum failure compression loads were 1.57 times higher than the previous ones. The printed layers subjected to high tensile and shear stresses failed, and the delamination

propagated over short distances accompanied by local fractures of the material, as seen in Figure 10a for the diagonal tensile test and in Figure 10b for the diagonal compression test. The local fractures allowed the tests to continue without slippage of the stretchers, so the strength contribution of the PLA material resulted in increased connector strength.
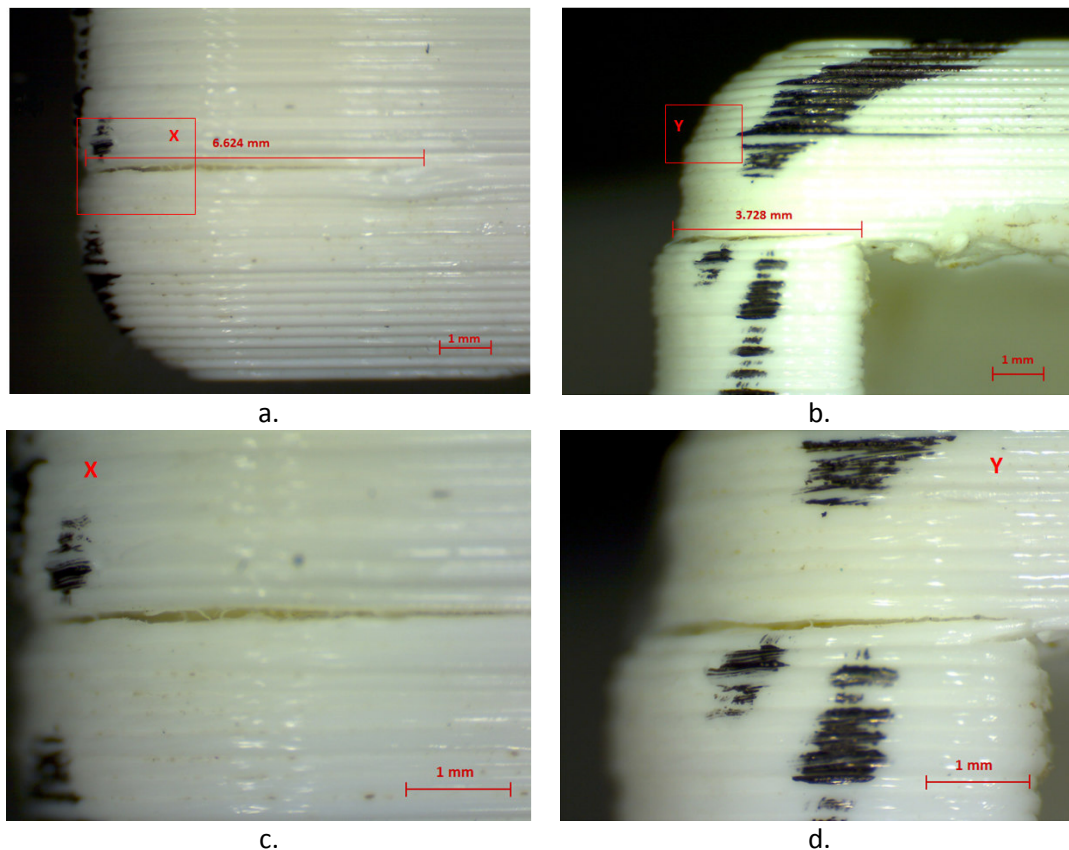

a.

b.

c.

d.

Fig. 9. *Process of delamination propagation in the connector printed in position 1,
under compression load; a. in the longitudinal direction, magnification 50X;
b. in the transversal direction, magnification 50X; c. detail of the delamination in the
longitudinal direction, magnification 100X; d. detail of the delamination in the transverse
direction, magnification 100X*

The L-type corner joints with the 3D printed connector made of white PLA filaments recorded better results compared to the common mortise and tenon joint taken as reference. None of the tests performed on the L-type joints with 3D printed connectors affected the wooden parts of the assembly. Only connectors failed into delamination and fractures, but higher values of the maximum failure forces were recorded for these L-type corner joints compared to the one made of larch wood parts, mortise and tenon jointed, taken as reference. In contrast, the wooden parts of the L-type reference corner joint were partially or

completely broken during the tests. This is the main advantage of using 3D printed connectors for L-type corner joints in chair production, as the wooden parts remain unaffected if the chair is overloaded and the connectors are damaged. The connectors can be replaced and the chair can be easily rebuilt by reusing the wooden elements. This is not the case with the wooden chair if the parts of the chair are broken, because the reconstruction of the chair with the same wooden elements is not possible.
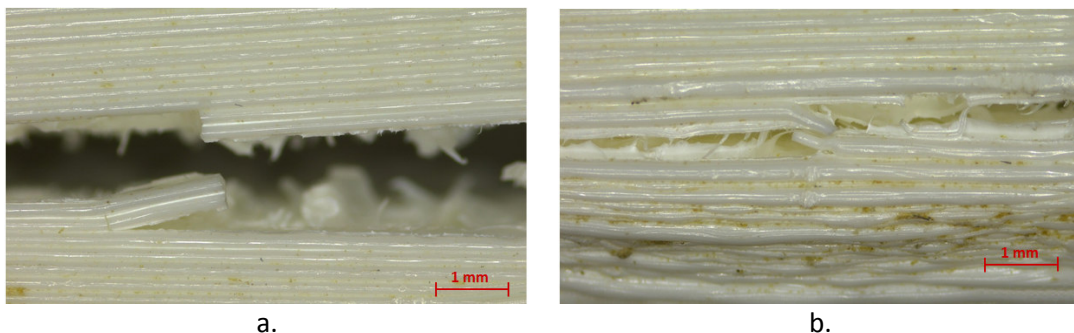

a.   b.

Fig.10. *Fracture mode of the connectors printed in position 2, magnification 80X:*
a. under tensile load; b. under compression load

The connector presented in this research is the first design concept. Based on the actual results obtained, further research will be done by changing the shape and size of the connector or using a different filament to increase its mechanical performance. The use of other wood species instead of larch is another direction of research. Finally, an optimized connector shape and size will be used to produce a chair and to test it for strength.

6. Conclusions

L-type corner joints with 3D printed connectors are potential solutions that can be applied in chair manufacturing.

In the L-type corner joint, the stresses under diagonal tensile and diagonal compression loads are transmitted to the connectors, which fail in delamination and fracture, protecting the wooden parts, which remain unaffected.

If larch is used for the wooden parts, the maximum tensile and compression failure loads of L-type corner joints with 3D printed connectors are higher than those of the common mortise and tenon joint.

Changing the print orientation of the connector from the horizontal position (position 1) to the vertical position with support (position 2) resulted in improved strength of the L-type corner joint under diagonal tensile and diagonal compression loads.

Diagonal tensile and compression loads applied to the L-type corner joint with 3D printed connector in the vertical position typically fracture multiple layers of the part with partial interlayer delamination, resulting in a tendency to maintain strength in the affected area and increase maximum failure loads.

The cost of the 3D printed connectorjoint may be covered by saving wood, due to shorter stretchers, by eliminating machining mortises and

tenons for adhesive joints, eliminating gluing times and time for assembly, which is transferred to the client. In addition, the package will be smaller because of the dismountable construction, and implicitly, the cost of transportation will be lower compared to the adhesive jointed chair.

Further research will be conducted to adjust the size of the 3D printed connector for jointing beech wood partsand to build a chair using 3D printed connectors and assess its strength.

References

1. Aiman, A.F., Sanusi, H., Haidiezul, A.H.M. et al., 2020. Design and structural analysis of 3D-printed modular furniture joints. In: IOP Conference Series: Materials Science and Engineering, vol. 932(1), ID article 012101. DOI: 10.1088/1757-899X/932/1/012101.
2. Aydin, M., 2015. Additive manufacturing: Is it a new era for furniture production? In: Journal of Mechanics Engineering and Automation, vol. 5(6), pp. 338-347. DOI: 10.17265/2159-5275/2015.06.002.
3. Ayrilmis, N., As, N., Dündar, T. et al., 2020. Determination of bending moment of L-type corner joints used in chair production and their effects on mechanical performance of chairs. In: Materials International, vol. 2(3), pp. 318-323. DOI: 10.33263/MATERIALS23.318323.
4. Chacón, J.M., Caminero, M.A., García-Plaza, E. et al., 2017. Additive manufacturing of PLA structures using fused deposition modelling: Effect of process parameters on mechanical properties and their optimal selection. In: Materials and Design, vol. 124, pp. 143-157. DOI: 10.1016/j.matdes.2017.03.065.
5. Chen, C., Yang, W., Teng, H. et al., 2023. Study on the application of 3D printing to wooden furniture connectors. In: Journal of Physics: Conference Series, vol. 2631(1), ID article 012006. DOI: 10.1088/1742-6596/2631/1/012006.
6. Derikvand, M., Eckelman, C.A., 2015. Bending moment capacity of L-shaped mitered frame joints constructed of MDF and particleboard. In: BioResources, vol. 10(3), pp. 5677-5690. DOI: 10.15376/biores.10.3.5677-5690.
7. Dizon, J.R.C., Espera, A.H., Chen, Q. et al., 2018. Mechanical characterization of 3D-printed polymers. In: Additive Manufacturing, vol. 20, pp. 44-67. DOI: 10.1016/j.addma.2017.12.002.
8. Felek, S.Ö., 2020. A new era in furniture production: 3D printer. In: International Conference on Knowledge & Innovation in Engineering, Science & Technology, 6-8 March, 2020, Budapest, Hungary.
9. Hajdarevic, S., Kuzman, M.K., Obucina, M. et al., 2023. Strength and stiffness of 3D-printed connectors compared with the wooden mortise and tenon joints for chairs. In: Wood Material Science and Engineering, vol. 18(3), pp. 870-883. DOI: 10.1080/17480272.2022.2086065.
10. Jarža, L., Čavlović, A.O., Pervan, S. et al., 2023. Additive technologies and their applications in furniture design and manufacturing. In: Drvna Industija, vol. 74(1), pp. 115-128. DOI: 10.5552/drvind.2023.0012.
11. Kadhum, A.H., Al-Zubaidi, S., Abdulkareem, S.S., 2023. Effect of the

infill patterns on the mechanical and surface characteristics of 3D printing of PLA, PLA+ and PETG. In: Chemengineering, vol. 7(3), ID article 46. 10.3390/chemengineering7030046.

12. Kasal, A., Smardzewski, J., Kuşkun, T. et al., 2023. Analyses of L-type corner joints connected with auxetic dowels for case furniture. In: Materials, vol. 16(13), ID article 4547. DOI: 10.3390/ma16134547.

13. Krzyźaniak, Ł., Kuşkun, T., Kasal, A. et al., 2021. Analysis of the internal mounting forces and strength of newly designed fastener to joints wood and wood-based panels. In: Materials, vol. 14(23), ID article 7119. DOI: 10.3390/ma14237119.

14. Magrisso, S., Mizrahi, M., Zoran, A., 2018. Digital joinery for hybrid carpentry. In: Proceedings of the 2018 CHI Conference on Human Factors in Computing Systems, 21-26 April, 2018, Montreal, Canada, ID article 167, pp. 1-11. DOI: 10.1145/3173574.3173741.

15. Majewski, A., Krystofiak, T., Smardzewski, J., 2020. Mechanical properties of corner joints made of honeycomb panels with double arrow-shaped auxetic cores. In: Materials, vol. 13(18), ID article 4212. DOI: 10.3390/ma13184212.

16. Nicolau, A., Pop, M.A., Coşereanu, C., 2022. 3D printing application in wood furniture components assembling. In: Materials, vol. 15(8), ID article 2907. DOI: 10.3390/ma15082907.

17. Nicolau, A., Pop, M.A., Georgescu, S.V. et al., 2023. Application of additive manufacturing technology for chair parts connections. In: Applied Sciences, vol. 13(21), ID article 12044. DOI: 10.3390/app132112044.

18. Popescu, D., Zapciu, A., Amza, C. et al., 2018. FDM process parameters influence over the mechanical properties of polymer specimens: A review. In: Polymer Testing, vol. 69, pp. 157-166. DOI: 10.1016/j.polymertesting.2018.05.020.

19. Saad, R.M., 2016. The revolution of materials used in 3D printing applications in furniture & interior design. In: International Design Journal, vol. 6(3), 19, pp. 143-163. DOI: 10.12816/0036501.

20. Sandanamsamy, L., Harun, W.S.W., Ishak, I. et al., 2023. A comprehensive review on fused deposition modelling of polylactic acid. In: Progress in Additive Manufacturing, vol. 8, pp. 775-799. DOI: 10.1007/s40964-022-00356-w.

21. Shahrubudina, N., Leea, T., Ramlana, R., 2019. An overview on 3D printing technology: Technological, materials, and applications. In: Procedia Manufacturing, vol. 35, pp. 1286-1296. DOI: 10.1016/j.promfg.2019.06.089.

22. Simion, I., Arion, A.F., 2016. Dimensioning rules for 3D printed parts using additive technologies (FDM). In: University Politechnica of Bucharest Scientific Bulletin, Series D, vol.78(2), pp. 79-92.

23. Smardzewski, J., Rzepa, B., Kılıç, H., 2016. Mechanical properties of externally invisible furniture joints made of wood-based composites. In: BioResources, vol. 11(1), pp. 1224-1239. DOI: 10.15376/biores.11.1.1224-1239.

24. Top, N., Şahin, I., Gökçe, H., 2019. Topology optimization for furniture connection part and production with 3D printer technology. In: Proceedings of the 29th International Conference on

Research for Furniture Industry, September 2019, Ankara, Turkey, pp. 671-677.

25. Valiyousefi, M., Alihedarloo, A., 2019. A Study the impact of 3D-printed joints on the complex wooden structures. In: Proceedings of International Congress on Science and Engineering, 14-15 October, 2019, University of Tokio, Japan.

26. Wittbrodt, B., Pearce, J.M., 2015. The effects of PLA color on material properties of 3D printed components. In: Additive Manufacturing, vol. 8, pp. 110-116. DOI: 10.1016/j.addma.2015.09.006.

27. Yang, S., Du, P., 2022. The application of 3D printing technology in furniture design. In: Scientific Programming, vol. 43(7), ID article 437. DOI: 10.1155/2022/1960038.

28. Yerlikaya, N.C., 2013. Failure load of corner joints, which are reinforced with glass-fiber fabric in case-type furniture. In: Scientific Research and Essays, vol. 8(8), pp. 325-339. DOI: 10.5897/SRE12.419.

ECO-COMPOSITES DESIGNED FOR THERMAL AND ACOUSTIC INSULATION OF BUILDINGS

Luminița-Maria BRENCI[1]

Abstract: *The paper aims to present a series of new composites that may be used for the thermal and acoustic insulation of buildings. The new composite structure is made from glued chips and wood fibres, hemp flakes, wool and reed fibres. The paper describes how the composites were made, and the methods used to determine the heat transfer coefficient and the acoustic absorption. The main purpose of this article is to promote these types of ecological materials which may replace in the near future, the materials that damage the human health and the environment.*

Key words: *ecological composites, thermal conductivity, sound absorption, insulation.*

1. Introduction

The "green" planet we live on has to be maintained by eliminating the most disturbing elements with unwanted "domino" effects on both human health and the environment.

At European level, buildings account for approximately 40% of the final energy consumption, and 36% of the emissions of greenhouse gases [14]. The consequence of this fact has led to the imposition of measures by the European Union, which stipulates that the Member States should ensure that "by 31 December 2020 all new buildings are buildings whose energy consumption is nearly zero" and " after 31 December 2018, new buildings occupied and owned by public authorities are buildings whose energy consumption is

nearly zero" [14].

According to the World Health Organization, noise is considered to be a stress factor that severely affects the health of humans [11] being responsible for the occurrence of sleep disorders, cardiovascular disease, high blood pressure, myocardial infarction and tinnitus.

The centralized global medical data indicate that 12% of deaths are caused by ischemic heart disease, 9.6% of them by cerebrovascular disease and 1.6% of them by hypertension [12]. As regards the children of school age, the prolonged exposure to noise causes cognitive disorders [12]. The excessive exposure to noise also leads to the occurrence of tinnitus, which can cause sleep disturbances, depression, inability to work,

---

[1] Faculty of Wood Engineering, Transilvania University of Brașov, B-dul Eroilor, no. 29, 500036, Brasov, Romania.
Correspondance: Luminița M. Brenci, e-mail: brenlu@unitbv.ro.

frustration etc. [12].

In order to mitigate these undesirable effects, a possible solution to be applied is to insulate the buildings by using materials with high thermal and acoustic performances. Polystyrene is a thermal insulating material typically used for buildings, due to its affordable price and the low density, compared to other materials.

The World Health Organization Report in 2007 labeled polystyrene as a possible carcinogenic material, placed in the third risk group. According to the "Norms of fire safety of buildings", polystyrene is in "E" risk group, defined as a highly flammable material, which can withstand the maximum temperature of 75°C. Another drawback is that of not being a recyclable material, its degradation period being up to 400 years [1].

These drawbacks have determined the researchers to find new insulating products made from environmentally friendly materials that neither affect the health of humans, nor intervene as pollutants to the environment.

Studies on the composites containing hemp in their structure have shown that their acoustic properties [3], improve as the particle size decreases. For the composites having wood chips and fibers mixed with wool and jute in their structure [2], the sound absorption capability proved to be superior to other wood-based materials.

In the case of studies on the thermal insulation capacity of various materials, it has been demonstrated that an increase in the density of the composites made from bamboo fibers, leads to the determination of a higher thermal conductivity coefficient [6].

Other studies have shown that eco-materials can be successfully used in both acoustic and thermal insulation of buildings. Thus, research on biodegradable composites [5] showed that the panels containing textile fibers, wood chips and wood fibers in their structure performed on low values of the coefficient of thermal conductivity ($\lambda = 0.0412 W/mK$).

This article presents a series of research works performed with a view to developing new composite materials for thermal and acoustic insulation, intended to replace traditional materials.

2. Objective

The main objective of the paper refers to the method to obtain new structures of composite using eco-materials such as: reed, wood fibres, wood chips, hemp particles, and also to determine both the coefficient of the thermal conductivity and the sound absorption of these composites, as well as to show whether or not they can be used as building materials for thermal insulation and sound absorption.

3. Method, Material and Equipment

The composite panels were made from the following environmentally friendly materials: wood chips and fibres, hemp and reed particles, wool waste, embedded in cement dissolved in water (Table 1).

The materials were mechanically mixed for a better homogenization of the structure; they were afterwards placed in wooden forms of 450mm x 450mm x 30mm and cold pressed for 24 hours. The composites thus obtained were heat dried for 5 hours in a press whose platens were heated in a range between 40°C and 50°C.

The equipment used to determine the coefficient of thermal conductivity was HFM436 Lambda (Figure 1) and the other one used to determine the sound absorption coefficient was Kundt tube (Figure 1b).

Eco-materials used for manufacturing environmentally friendly composites

Code no.	Eco-materials [%]	Adhesive [%]	Density [kg/m^3]
P1	8.8% wood chips and 4.4% wool waste (total = 13.2%)	cement 47.3% dissolved in water 39.5%	729.16
P2	7.2% wood fibers and 3.5% wool waste (total = 10.7%)	cement 38.3% dissolved in water 54%	677.08
P3	4.4% wood chips, 4.4% wood fibers and 4.4% wool waste (total = 13.2%)	cement 47.3% dissolved in water 39.5%	733.33
P4	2.5% wood chips, 6.3% hemp particles and 4.4% wool waste (total = 13.2%)	cement 47.3% dissolved in water 39.5%	718.75
P5	6.3% wood chips, 2.5% hemp particles and 4.4% wool waste (total = 13.2%)	cement 47.3% dissolved in water 39.5%	708.33
P6	4.4% wool waste and 8.8% reed particles (total = 13.2%)	cement 47.3% dissolved in water 39.5%	716.33

Fig. 1. *Equipment used for experiment: a – HFM436 Lambda; b – Kundt tube*

In order to determine the coefficient of thermal conductivity, the panels were cut at dimensions of 400mm x 400mm x 30mm, and the sound absorption coefficient of the panels was obtained using samples cut at a diameter of 100mm.

The measurement of the thermal conductivity was done according to ISO 8301/1991 [8] and DIN EN 12667:2001 [9]. Thus, all the panels were tested for six values of the external temperature (T1) and a constant temperature difference, ΔT=20°C (Table 2).

In order to determine the sound absorption coefficient, a noise level of 75dB and a band of low frequencies in the range of 50-1390Hz were used.

4. Results and Discussion

The coefficients of thermal conductivity and sound absorption are analysed bellow.

Measurement points of the thermal conductivity   Table 2

Temperature of the bottom plate T1 [^{0}C]	Temperature of the upper plate T2 [^{0}C]	$\Delta T = T2\text{-}T1$ [^{0}C]	Temperature average $\frac{T1+T2}{2}$ [^0C]
-20	0		-10
-15	5		-5
-10	10	20	0
-5	15		5
5	25		15
10	30		20

4.1 Coefficient of Thermal Conductivity

The results of the thermal conductivity coefficient determined from the experiments are shown in Table 3 and Figure 2. Following the results of the thermal conductivity coefficient of the six panels (Figure 2), each measured in six points (measuring conditions), one can notice that the lowest values of the coefficient of thermal conductivity were obtained for the composites P2 and P5, which means that they perform better as insulators.

The presence of the wood fibres in the structure of P2 panel determines a better insulation capacity than in the case of mixing wood chips and hemp particles (P5 panel).

For the composites P1 and P4 were recorded the highest values of the thermal conductivity coefficient, suggesting the lowest thermal insulation properties. Comparing the experimental results of the panels P3 and P6, one can notice that wood fibers and chips are not as good as reed particles for the performance of the thermal insulation of the resulted composites. Comparing panels P4 and P5, one can see that the structures are similar, except the amounts of wood chips and hemp particles. One can also notice that a greater amount of wood chips (panel P5) improves the thermal insulation property compared to the panel P4. Comparing the results of thermal conductivity coefficient (Figure 2) with density of all tested panels (Table 1), it can be noticed that a decreased density is usually but not necessarily associated to an increase of thermal insulation performance.

Table 3

Variation of the values of the thermal conductivity coefficients for the different types of experimental panels in the six measuring points (representing different measuring conditions as detailed in Table 2)

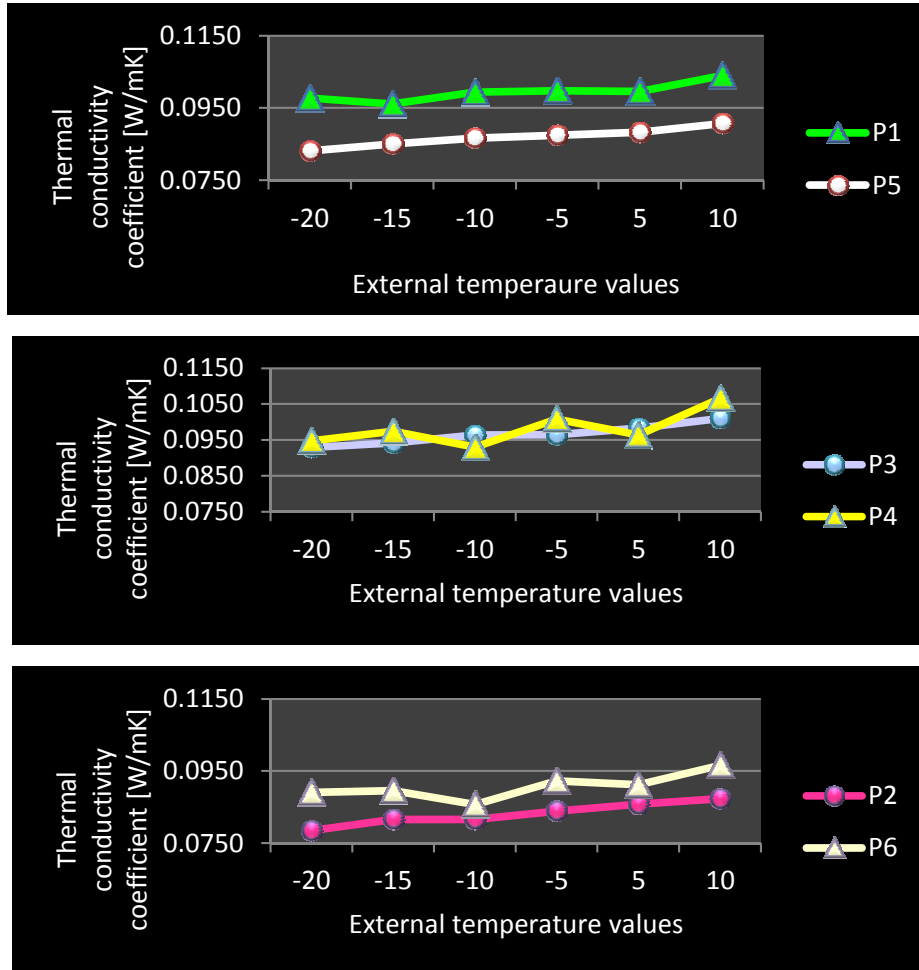| Panel type	Thermal conductivity coefficient λ [W/m*K] / measuring points					
	1	2	3	4	5	6
P1	0.097699	0.096065	0.099344	0.099790	0.099596	0.104011
P2	0.078481	0.081599	0.081575	0.083904	0.085780	0.087307
P3	0.092939	0.094164	0.096357	0.096435	0.098301	0.101044
P4	0.094784	0.097396	0.092992	0.100848	0.096339	0.106589
P5	0.083116	0.085049	0.086681	0.087484	0.088299	0.090738
P6	0.089080	0.089561	0.085723	0.092258	0.091153	0.096599

Fig. 2. *Diagram of the thermal conductivity coefficient*

4.2. Sound Absorption Coefficient

Analyzing the graphs in Figure 3, one can see that the panels P1, P2 and P3 have the average value of sound absorption coefficient in the range of 0.8 ÷ 0.9, the highest value being recorded for composite P3 (α = 0.870212) in the frequency range of 650 ÷ 950Hz.

In case of panel P4, the average sound absorption coefficient varies between 0.7 ÷ 0.8 for the frequency range of 650 ÷ 1050Hz. For panel P5, a higher value of the sound absorption coefficient was registered in the frequency range of 600 ÷ 850Hz, with a maximum value of 0559. In

the frequency range of 850-1150Hz, a declined curve is observed, but for a frequency above 1150Hz, a peak of 0.649297 is reached. The explanation for such a situation can be attributed to the heterogeneity of the considered composite structure.

For the composites having in their structure the same materials (wood chips, hemp particles and wool) one can notice that a larger amount of wood chips and a smaller amount of hemp particles (in case of panel P5) provides a smaller acoustic insulation capacity than that of panel P4, which has a lower content of wood chips and a higher content of hemp particles.
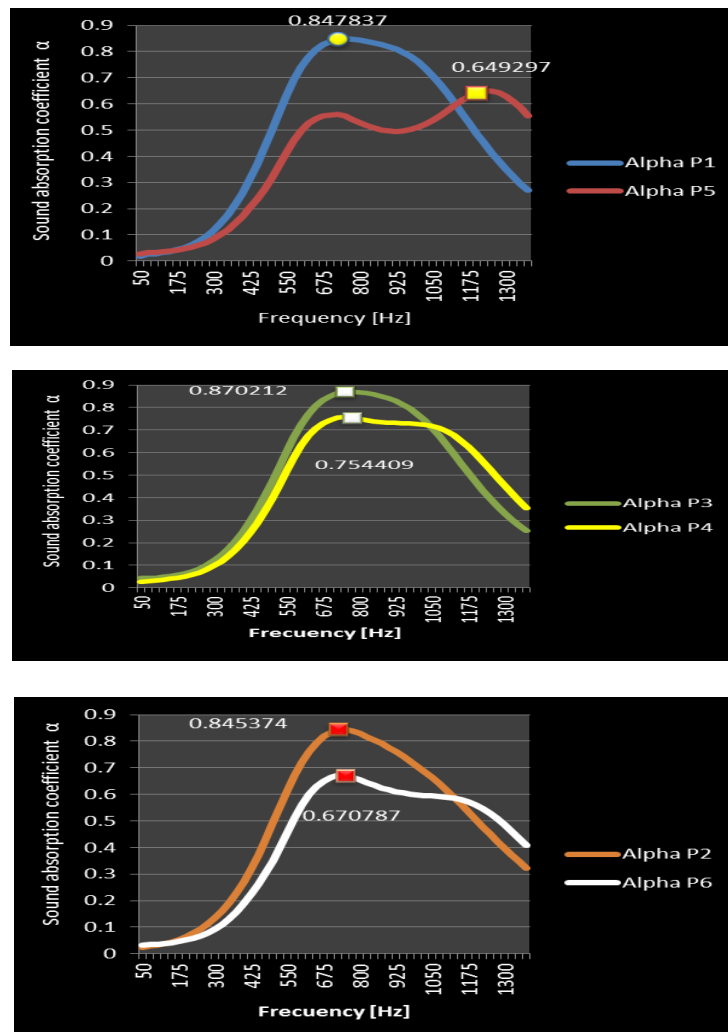
Fig. 3. *Measured values of the sound absorption coefficients*

The provisions of SR EN ISO 11654 [10], impose a classification of sound insulating materials. Thus, the composites analyzed in the paper may be classified as follows: panels P1, P2 and P3 in class B and panels P4, P5 and P6 in class C.

5. Conclusions

The analysis of the results of the two investigations, leads to the following conclusions:

- with a view to manufacturing a series of new eco-composite materials, the research presented in this paper, submits green products with higher coefficients of thermal conductivity, than those of polystyrene ($\lambda = 0.036 \div 0046$ W/mK) [7], but preferably to be used in the thermal insulation of buildings and civil engineering, because of the polystyrene drawbacks;
- the presence in the composite structures of the wood chips, wood fibres, wool and hemp particles led to good results

of the thermal conductivity coefficient, the top panel being P2;
- the determined values of the acoustic absorption coefficient resulted in the highest values recorded at 750Hz for both P1 and P3 structures;
- for panel P5, which has the lowest value of the acoustic absorption coefficient, the structure consisting of a higher amount of wood particles and a lower value of hemp particles proved to be non-efficient;
- a decreased density is usually but not necessarily associated to an increase of thermal insulation performance, and such comparison should be made on panels with similar composition;
- taking into account that the materials having the thermal conductivity coefficient up to 0.1W/mK are considered to be good thermal insulators, it can be concluded that all the panels studied in this paper meet this requirement [11];
- using ecological materials (wood chips and fibres, wool waste, hemp and read particles) in proportions of 10.7-13.2% in the composites structure, resulted in acceptable values of the thermal conductivity coefficient (λ = 0.078-0.089 W/mK), which is a clear positive result compared to other composites which had only 5% of hemp particles (λ=0.130-0.142 W/mK) [4];
- among the six composite materials presented in this paper, the composite panel P2 proved to be a possibly successful material to be used for thermal and acoustic insulation of industrial and civil buildings.

The results presented in the paper are a part of the research area covered by the author, and the analyses carried out have shown that the main disadvantage of these panels, is the high density. A solution for a further research is to use other than ceramic adhesives, obtaining thus lighter panels.

Acknowledgements

References

1. Coşereanu C., Lăzărescu C-tin, Olărescu C., Laurenzi W., 2012. Ecological solution for low building walls. In: Pro Ligno, vol. 8(1), pp, 28-34.
2. Curtu I., Stanciu M.D., Coşereanu C., Vasil O., 2012. Assessment of acoustic properties of biodegradable composite materials with textile inserts. In: Materiale Plastice, no. 49(1), pp. 68-72.
3. Gle P., Gourgon E., Armand L., 2011. Acoustical properties of material made of vegetal particles with several scales of porosity. In: Applied Acoustic Journal, vol. 72(5), pp. 249-259.
4. Gherghişan A.M., Cismaru I., 2013. Research concerning the influence of matrix in hemp hurds composites on thermal conductivity. In: Pro Ligno, vol. 9(3), pp. 26-33.
5. Olărescu C.M., Coşereanu C., 2011. Research on the thermal insulation potential of some composites made of biodegradable materials. In: Pro Ligno, no. 7(3), pp. 54-58.
6. Takagi H., Kako S., Kusano K., Oisaka A., 2007. Thermal conductivity of PLA-bamboo fiber composite. In: Advanced Composite Materials, no. 16(4), pp. 377-384.
7. Yucel K.T., Basyigit C., Ozel C., 2003. Thermal insulation of expanded

polystyrene as construction and insulation materials. In: Fifteenth Symposium on Thermophysical Properties, Boulder-Colorado, USA.

8. ***, 1981. ISO 8301/1991-08-01. Thermal insulation – Determination of state thermal resistance and related properties – Heat flow meter apparatus.

9. ***, 2001. DIN EN 12667/2001. Thermal performance of building materials and products – Determination of thermal resistance by of means of guarded hot plate and flow meter methods – Products of high and medium thermal resistance.

10. ***, 2002a. SR EN ISO 11654/2002 Acoustics. Acoustic absorbers for use in buildings. Evaluation of acoustic absorption.

11. ***, 2002b. C107/0-2002. Legal framework of the thermal insulation of buildings for design and execution.

12. ***, 2011a. Environmental burden of disease associated with inadequate housing. Methods for quantifying health impacts of selected housing risks in the WHO European Region. http://www.euro.who.int/__data/assets/ pdf_file/0003/142077/e95004.pdf.

13. ***, 2011b. Burden of disease from environmental noise. Quantification of healthy life years lost in Europe. http://www.euro.who.int/__data/assets/ pdf_file/0008/136466/e94888.pdf.

14. ***, 2013. The Report of the Commission to European Parliament and the Council on the progress of member states regarding to buildings whose energy consumption is nearly zero. http://eur-lex.europa.eu/LexUriServ/LexUriServ. do?uri=COM:2013:0483:FIN:RO:PD